ELECTROCHEMICAL CO_2 REDUCTION

AFROZA BEGUM

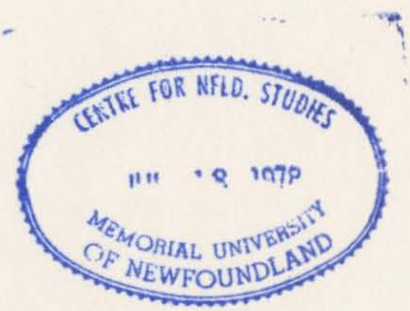
CENTRE FOR NFLD. STUDIES
MEMORIAL UNIVERSITY
OF NEWFOUNDLAND

Electrochemical CO_2 Reduction

by

© Afroza Begum

A thesis submitted to the School of Graduate Studies

in partial fulfillment of the requirements for the

degree of Doctor of Philosophy

Department of Chemistry

Memorial University of Newfoundland

April, 2011

St. John's Newfoundland

Abstract

Electrochemical methods for CO_2 reduction have been receiving continuous attention for the last few decades mainly for the conversion of CO_2 to fuels as an alternative global energy source and the inexpensive production of carboxylated products for industrial applications. CO_2 is considered as a greenhouse gas, whose increasing concentration in the atmosphere is a growing environmental concern. The main obstacle for the direct electrochemical reduction of CO_2 is the requirements of very high negative standard potential as high as -2.21 V vs SCE. Several transition-metal based molecular catalysts, for example, ruthenium polypyridyl complexes, were reported to convert CO_2 to fuels, such as methanol, formic acid, oxalic acid, methane etc., at a lower cathodic potential. On the other hand, electrocatalytic conversions of CO_2 using aromatic ketones were also found to be useful in the syntheses of medicinally useful materials, such as 2-arylpropanoic acids and α-oxocarboxylic acids (as anti-inflammatory drugs), agricultural chemicals and perfumes. A number of monometallic and bimetallic ruthenium benzimidazole and benzothiazole based polypyridyl complexes were synthesized in this work that were found to be operate as electrocatalysts for CO_2 reduction at reasonable cathodic potentials. These complexes were characterized by cyclic voltammetry (CV), electronic absorption (UV-Vis) and emission, X-ray diffraction (XRD) techniques.

Electrolysis of the complexes was performed to reveal their electrocatalytic effect on CO_2 reduction. Product analysis by high-performance liquid chromatography (HPLC)/UV-Vis methods revealed that formate and oxalate are detectable in addition to

some other products. In this study, it was found that structural variations in the electrocatalyst could influence the activity, however all benzothiazole containing complexes exhibited much higher activities than those of the corresponding benzimidazole complexes. Formate and oxalate were produced and detected at moderately low cathodic overpotentials for $[\{(bpy)_2Ru\}_2(\mathbf{py_2tbtz})]^{4+}$. This is an unprecedented result for benzothiazole complexes. In addition, the electrochemical reduction of CO_2 by fluorenone-9-one was found to produce 9-hydroxyfluorene and 9-hydroxyfluorene-9-carboxylic acid, in addition to formate and oxalate at a low cathodic overpotential.

Acknowledgements

I would like to acknowledge my deepest gratitude and appreciation to my supervisor Prof. Peter G. Pickup who helped my learning and played a key role at every stage in this study. I would like to thank him for his indispensable guidance, valuable suggestions, and constant inspirations in my journey towards this long awaited goal. I am greatly indebted to him for his innumerate brilliant ideas, creativity and lots of patience. But most importantly Dr. Peter G. Pickup is a nice person.

I am very much grateful to my beloved 4 year old daughter Sarah Hannah Mahmud, who is the source of all my inspirations. She is very loving, wonderful, and considerate baby and I am very fortunate for having her. I am very grateful to my parents and my husband for their unparalleled love. My husband Dr. Ilias Mahmud has been very encouraging and helpful in both academics and personal life.

I would like to thank to the members of my supervisory committee Profs. Graham Bodwell and David W. Thompson for their valuable suggestions and to Dr. Robert J. Helleur for his time and valuable suggestions especially in helping the product analyses. I would like to thank Dr. Louise N. Dawe for her help in solving the X-ray crystallography of some of my samples and Ms. Linda Windsor for her help during the product analysis.

I desire of to offer my respect and special thanks to all the honorable teachers of the Department of Chemistry, Memorial University. I also want to thank to the nice people especially to Ms. Viola Martin, Ms. Mary Flinn, Ms. Rosallind Collins, Ms. Linda Thompson and many others.

Last, but certainly not the least, I would like to thank my entire group mates. I feel very fortunate to have worked with them. I would like to say special thank to Ali Modir and Rodney Smith for their suggestions.

To everyone else I did not mention, thanks for making my time enjoyable at Memorial University. I wish everyone all the best in future.

Table of contents

Title..... i

Abstract..... ii

Acknowledgements..... iv

List of Figures..... xii

List of Schemes..... xxv

List of Tables..... xxvii

Glossary of Abbreviations..... xxix

Glossary of Symbols..... xxxi

Chapter 1 An introduction to electrochemical CO_2 reduction..... 1

1.1 Importance of CO_2 reduction..... 2

1.2 Electrocatalysis – kinetics..... 4

1.3 Review of electrochemical CO_2 reduction..... 7

1.3.1 Solubility of CO_2..... 9

1.3.2 Metal electrodes..... 10

1.3.3 Transition metal complexes..... 13

1.3.3.1 Metal complexes with macrocyclic ligands..... 14

1.3.3.2 Metal complexes with bpy and CO ligands..... 17

1.3.3.3 Ru complexes with bpy ligands..... 24

1.4 Ruthenium chemistry..... 30

1.4.1 Bimetallic Ru complexes and superexchange.....31

1.4.2 Review of a number of bimetallic Ru complexes 37

1.5 Objectives of the thesis work.....41

Chapter 2 Synthesis and characterization of some monometallic and bimetallic ruthenium polypyridyl complexes.....44

2.1 Instrumentation and starting materials.....45

2.2 Preparation of ligands.....47

2.2.1 1-Methyl-2-(pyridin-2-yl)-1H-benzo[d]imidazole [Me-pybim]..... 47

2.2.2 2,5-Bis(1-methyl-1H-benzo[d]imidazol-2-yl)pyrazine[Me_2-pzbbim]..48

2.2.3 3,3′-Dimethyl-2,2′-di(pyridin-2-yl)-5,6′-bi(3H-benzo[d]imidazole) [Me_2-py_2bbim].....49

2.2.4 2-(Pyridin-2-yl)benzo[d]thiazole [pybtz].....50

2.2.5 2,6′-Bis(2-pyridyl)-2,2′:6,2″-thiazolo[4,5-d]-benzothiazole [py_2tbtz].52

2.2.6 2,5-Di(benzo[*d*]thiazol-2-yl)pyrazine [pzbbtz] 53

2.2.7 2,5-Bis(1-methyl-1*H*-benzo[*d*]imidazol-2-yl)pyridine [Me_2-pybbim].54

2.3 Preparation of complexes.....55

2.3.1 [Ru(**Me-pybim**)$(bpy)_2$]$(ClO_4)_2$ 55

2.3.2 [Ru(**pybtz**)$(bpy)_2$]$(ClO_4)_2$ 56

2.3.3 [Ru(**Me_2-pybbim**)$(bpy)_2$]$(ClO_4)_2$ 58

2.3.4 [{(bpy)$_2$Ru}$_2$(**Me$_2$-pzbbim**)](ClO$_4$)$_4$ 59

2.3.5 [{(bpy)$_2$Ru}$_2$(**pzbbtz**)](ClO$_4$)$_4$ 61

2.3.6 [{(bpy)$_2$Ru}$_2$(**py$_2$tbtz**)](ClO$_4$)$_4$ 62

2.3.7 [{(bpy)$_2$Ru}$_2$(**Me$_2$-py$_2$bbim**)](ClO$_4$)$_4$ 64

2.4 X-ray crystallographic studies of some ruthenium polypyridyl complexes 65

2.5 X-ray diffraction studies 66

2.5.1 Crystal structure for Ru(**pybtz**)(bpy)$_2$(ClO$_4$)$_2$ 69

2.5.2 Crystal structure for Ru(**Me$_2$-pybbim**)(bpy)$_2$(ClO$_4$)$_2$ 71

2.5.3 Crystal structure for [{(bpy)$_2$Ru}$_2$(**pzbbtz**)](ClO$_4$)$_4$ 73

2.5.4 Crystal structure for [{(bpy)$_2$Ru}$_2$(**py$_2$tbtz**)](ClO$_4$)$_4$ 78

Chapter 3 Electrochemical and photophysical properties of the synthesized ruthenium polypyridyl complexes 81

3.1 Introduction 82

3.2 Electrochemical measurements 82

3.3 Electrochemistry under N_2 84

3.3.1 Monometallic complexes 84

3.3.1.1 Ru(bpy)$_3^{2+}$ 84

3.3.1.2 [Ru(**Me-pybim**)(bpy)$_2$]$^{2+}$ 85

3.3.1.3 [Ru(**pybtz**)(bpy)$_2$]$^{2+}$ 86

3.3.1.4 [Ru(**Me$_2$-pybbim**)(bpy)$_2$]$^{2+}$ 87

3.3.2 Bimetallic complexes 88

3.3.2.1 $[\{(bpy)_2Ru\}_2(\mathbf{Me_2\text{-}pzbbim})]^{4+}$ 88

3.3.2.2 $[\{(bpy)_2Ru\}_2(\mathbf{pzbbtz})]^{4+}$ 90

3.3.2.3 $[\{(bpy)_2Ru\}_2(\mathbf{py_2tbtz})]^{4+}$ 92

3.3.2.4 $[\{(bpy)_2Ru\}_2(\mathbf{Me_2\text{-}py_2bbim})]^{4+}$ 94

3.4 Summary of electrochemical characterization of Ru complexes 96

3.5 Photophysical properties 98

3.5.1 Monometallic complexes 99

3.5.2 Bimetallic complexes 106

3.5.2.1 $[\{(bpy)_2Ru\}_2(\mathbf{Me_2\text{-}pzbbim})]^{4+}$ and

$[\{(bpy)_2Ru\}_2(\mathbf{pzbbtz})]^{4+}$ 106

3.5.2.2 $[\{(bpy)_2Ru\}_2(\mathbf{py_2tbtz})]^{4+}$ and

$[\{(bpy)_2Ru\}_2(\mathbf{pzbbtz})]^{4+}$ 109

3.5.2.3 $[\{(bpy)_2Ru\}_2(\mathbf{Me_2\text{-}py_2bbim})]^{4+}$ 111

3.6 Conclusions 114

Chapter 4 Electrochemical CO_2 reduction by metal complexes and product analyses 116

4.1 Introduction 117

4.2 Electrochemical measurements under CO_2 118

4.2.1 Monometallic complexes 118

4.2.1.1 $Ru(bpy)_3^{2+}$ 118

4.2.1.2 [Ru(**Me-pybim**)(bpy)$_2$]$^{2+}$ 119

4.2.1.3 [Ru(**Me$_2$-pybbim**)(bpy)$_2$]$^{2+}$ 120

4.2.1.4 [Ru(**pybtz**)(bpy)$_2$]$^{2+}$ 123

4.2.2 Bimetallic complexes 124

4.2.2.1 [{(bpy)$_2$Ru}$_2$(**Me$_2$-py$_2$bbim**)]$^{4+}$ 124

4.2.2.2 [{(bpy)$_2$Ru}$_2$(**py$_2$tbtz**)]$^{4+}$ 127

4.2.2.3 [{(bpy)$_2$Ru}$_2$(**Me$_2$-pzbbim**)]$^{4+}$ 128

4.2.2.4 [{(bpy)$_2$Ru}$_2$(**pzbbtz**)]$^{4+}$ 130

4.3 Discussion 131

4.4 Electrolysis and product analysis of complexes under CO_2 134

4.4.1 Electrolysis of [{(bpy)$_2$Ru}$_2$(**py$_2$tbtz**)]$^{4+}$ under CO_2 134

4.4.2 Discussion 138

4.5 Conclusions 140

Chapter 5 Electrochemical reduction of CO_2 by fluorene-9-one..... 142

5.1 Overview of electrochemical reduction of CO_2 by aliphatic and aromatic ketones 143

5.2 Proposed mechanisms for electrochemical reduction pathways of CO_2 by aromatic and aliphatic ketones 143

5.2.1 Electrocarboxylation..... 144

5.2.2 Homogeneous catalysis 146

5.3 Goals 149

5.4 Electrochemical studies of fluorene-9-none 150

5.4.1 Under N_2 150

5.4.2 Under CO_2 152

5.5 Electrolysis of fluorene-9-one under CO_2 155

5.5.1 Current and charge during the electrolyses 155

5.5.2 Cyclic voltammetry of electrolysis solutions 158

5.5.3 Product analysis by ^{1}H NMR and GC-EIMS 164

5.5.4 Separation and quantification of 9-hydroxyfluorene and 9-hydroxyfluorene-9-carboxylic acid by HPLC 168

5.5.5 HPLC separation and quantification of oxalic and formic acid 176

5.5.6 Discussion 183

Chapter 6 Summary 188

References 192

Appendix A- IR spectra 210

Appendix B- ^{1}H-NMR spectra 225

Appendix C- ^{13}C-NMR spectra 240

Appendix D- X-ray Crystallography data 247

List of Figures

1.1 Schematic representation of the various types of molecular catalysis of electrochemical reactions.....6

1.2 Examples of some macrocyclic complexes..... 15

1.3 Example of electrocatalytic activity for a Ni cyclam^{2+} complex. Cyclic voltammetry under N_2 and CO_2 confirms the electrocatalytic activity of the complex on Hg electrode 16

1.4 Cyclic voltammograms of $[Ni_3(\mu_3\text{-}\mathbf{CNMe})(\mu 3\text{-}I)(\mathbf{dppm})_3][PF_6]$ in 0.1 M $NaPF_6$/MeCN, initial voltammogram of a solution under N_2 (solid); the same solution after exposure to CO_2 (dotted) (3 min). (Phenyl groups on P are omitted for clarity).....17

1.5 Cyclic voltammogram of $[\{Ru(\mathbf{tbbpy})_2\}_2(\mathbf{bibzim})][PF_6]_2$ in acetonitrile under an Ar atmosphere (upper) and under a CO_2 (lower) atmosphere..... 25

1.6 IR spectra of $[RuL\text{-}(\mathbf{napy\text{-}\kappa^2N,N''})(dmso)](PF_6)_2$ under controlled potential electrolysis in CH_3CN ((a) and (b)) or CD_3CN (a′): (a) The potential was swept from -0.95 to -1.45 V; (b) The potential was swept from -1.44 to -0.95 V (vs Fc/Fc^+). *denotes CH_3CN peaks. 26

1.7 Structures and cyclic voltammograms of $[(bpy)_2Ru(\mathbf{dmbbbpy})][PF_6]_2$ and $[\{(bpy)_2Ru\}_2(\mathbf{dmbbbpy})][PF_6]_4$ (0.3 mM) in 0.1 M Bu_4NBF_4/ MeCN at a glassy carbon electrode, under N_2 (——) and CO_2 (------) (scan rate = 50 mV/s). 28

1.8 IR spectra of $[(bpy)_2Ru(\mathbf{dmbbbpy})][PF_6]_2$ (0.8 mM) during thin-cell bulk electrolysis in CD_3CN with $LiBF_4$ (*a*) starting scans, (*b*) using $^{12}CO_2$, (*c*) using $^{13}CO_2$. 29

1.9 Overlap between: (a) a σ-donor bond of a ligand and the d_{z^2} or $d_{x^2-y^2}$ orbital of a metal and (b) π-donation from a ligand's π orbital to a d_{xy}, d_{xz} or d_{yz} orbital of the metal (c) back donation or back bonding from a metal to a ligand via overlap of a metal based d_{xy}, d_{xz} or d_{yz} orbital and a ligand π* orbital..... 32

1.10 Terminal coordinating and intervening fragments for bimetallic ruthenium complexes..... 33

1.11 Mechanisms for electron transfer between metal sites in bimetallic complexes. 34

1.12 (a) LUMO and (b) HOMO bridging ligand assisted superexchange..... 35

1.13 The Creutz–Taube ion. 37

1.14 Cyclic voltammogram for a 0.5 mM $[\{(bpy)_2Ru\}_2(2,3\text{-dpp})]^{4+}$ and $[\{(bpy)_2Ru\}_2(2,5\text{-dpp})]^{4+}$, 0.05 M Et_4NBF_4/DMF solution. Working electrode Pt; T = -54 °C; scan rate 0.1 V/s. 39

1.15 Examples of some imidazole/benzimidazole based ligands for bimetallic ruthenium complexes from Haga's papers. 40

1.16 A molecular switching device: proton transfer acts as a trigger signal..... 41

2.1 X-ray crystal structure for $[Ru(\mathbf{pybtz})(bpy)_2]^{2+}$. 30% probability ellipsoids; anions and hydrogen atoms omitted for clarity. 70

2.2 X-ray crystal structure for $[Ru(\mathbf{Me_2\text{-}pybbim})(\mathbf{bpy})_2]^{2+}$. 30% probability ellipsoids; anions and hydrogen atoms omitted for clarity.....73

2.3 X-ray crystal structure for $[\{(bpy)_2Ru\}_2(\mathbf{pzbbtz})]^{4+}$. 30% probability ellipsoids; anions and hydrogen atoms omitted for clarity..... 77

2.4 X-ray crystal structure for $[\{(bpy)_2Ru\}_2(\mathbf{py_2tbtz})\}]^{4+}$. 30% probability ellipsoids; anions and hydrogen atoms omitted for clarity.. 80

3.1 Cyclic voltammogram of 1 mM $Ru(bpy)_3^{2+}$ in CH_3CN/ 0.1 M Bu_4NBF_4 under N_2 at a glassy carbon electrode (at ν = 50 mV/s). (Inset: differential pulse voltammogram under N_2 at a glassy carbon electrode). 84

3.2 Cyclic voltammogram of 1 mM $[Ru(\mathbf{Me\text{-}pybim})(bpy)_2]^{2+}$ in CH_3CN/0.1 M Bu_4NBF_4 under N_2 at a glassy carbon electrode (at ν = 50 mV/s). (Inset: differential pulse voltammogram under N_2 at a glassy carbon electrode). 85

3.3 Cyclic voltammogram of 1 mM $[Ru(\mathbf{pybtz})(bpy)_2]^{2+}$ in CH_3CN /0.1 M Bu_4NBF_4 under N_2 at a platinum electrode (at ν = 100 mV/s). (Inset: differential pulse voltammogram under N_2 at a glassy carbon electrode). 86

3.4 The Cyclic voltammogram of 1 mM $[Ru(\mathbf{Me_2\text{-}pybbim})(bpy)_2]^{2+}$ in CH_3CN/0.1 M Bu_4NBF_4 under N_2 at a platinum electrode (at ν = 100 mV/s). (Inset: differential pulse voltammogram under N_2 at a glassy carbon electrode.) 88

3.5 The cyclic voltammogram of 1 mM $[\{(bpy)_2Ru\}_2(\mathbf{Me_2\text{-}pzbbim})]^{4+}$ in CH_3CN/0.1 M Bu_4NBF_4 under N_2 at a platinum electrode (at v = 100 mV/s). (Inset: differential pulse voltammogram under N_2 at a glassy carbon electrode). 89

3.6 The Cyclic voltammogram of 1 mM $[\{(bpy)_2Ru\}_2(\mathbf{pzbbtz})]^{4+}$ in CH_3CN/0.1 M Bu_4NBF_4 under N_2 at a platinum electrode (at v = 100 mV/s). (Inset: differential pulse voltammogram under N_2 at a glassy carbon electrode). 91

3.7 The cyclic voltammogram of 1 mM $[\{(bpy)_2Ru\}_2(\mathbf{py_2tbtz})\}]^{4+}$ in CH_3CN/0.1 M Et_4NClO_4 under N_2 at a glassy carbon electrode (at v = 50 mV/s). (Inset: differential pulse voltammogram under N_2 at a glassy carbon electrode). 92

3.8 The cyclic voltammogram of 1 mM $[\{(bpy)_2Ru\}_2(\mathbf{Me_2\text{-}py_2bbim})]^{4+}$ in CH_3CN/0.1 M Bu_4NBF_4 under N_2 at a glassy carbon electrode (at v = 100 mV/s). (Inset: differential pulse voltammogram under N_2 at a glassy carbon electrode). 94

3.9 Potential wells for a ground state and an excited state..... 99

3.10 Electronic absorption spectra of $[Ru(\mathbf{Me\text{-}pybim})(bpy)_2]^{2+}$, $[Ru(\mathbf{pybtz})(bpy)_2]^{2+}$, $[Ru(\mathbf{Me_2\text{-}pybbim})(bpy)_2]^{2+}$, and $Ru(bpy)_3^{2+}$ (ca. 7.5×10^{-6} M) in CH_3CN at ambient temperature..... 100

3.11 Electronic emission spectra of $[Ru(\mathbf{Me\text{-}pybim})(bpy)_2]^{2+}$, $[Ru(\mathbf{pybtz})(bpy)_2]^{2+}$, $[Ru(\mathbf{Me_2\text{-}pybbim})(bpy)_2]^{2+}$, and $Ru(bpy)_3^{2+}$

(ca. 7.5×10^{-6} M) in CH_3CN at ambient temperature. 101

3.12 Electronic absorption spectrum of $[Ru(\mathbf{Me_2\text{-}pybbim})(bpy)_2]^{2+}$ in acetonitrile under N_2 and in the presence and absence and presence of $HClO_4$ at ambient temperature. 102

3.13 Electronic absorption spectra of $[\{(bpy)_2Ru\}_2(\mathbf{Me_2\text{-}pzbbim})]^{4+}$, $[\{(bpy)_2Ru\}_2(\mathbf{pzbbtz})]^{4+}$, and $Ru(bpy)_3^{2+}$ in CH_3CN at ambient temperature. 107

3.14 Electronic emission spectrums of $[\{(bpy)_2Ru\}_2(\mathbf{pzbbtz})]^{4+}$, $[\{(bpy)_2Ru\}_2(\mathbf{Me_2\text{-}pzbbim})]^{4+}$ and $Ru(bpy)_3^{2+}$ in CH_3CN at ambient temperature. ... .108

3.15 Electronic absorption spectra of $Ru(bpy)_3^{2+}$, $[\{(bpy)_2Ru\}_2(\mathbf{py_2tbtz})]^{4+}$, and $[\{(bpy)_2Ru\}_2(\mathbf{pzbbtz})]^{4+}$ in CH_3CN at ambient temperature. 109

3.16 Electronic emission spectra of $Ru(bpy)_3^{2+}$, $[\{(bpy)_2Ru\}_2(\mathbf{py_2tbtz})]^{4+}$ and $[\{(bpy)_2Ru\}_2(\mathbf{pzbbtz})]^{4+}$ in CH_3CN at ambient temperature... 110

3.17 Electronic absorption spectra of $Ru(bpy)_3^{2+}$, $[Ru(\mathbf{Me\text{-}pybim})(bpy)_2]^{2+}$, $[Ru(\mathbf{Me_2\text{-}pybbim})(bpy)_2]^{2+}$, and $[\{(bpy)_2Ru\}_2(\mathbf{Me_2\text{-}py_2bbim})]^{4+}$ in CH_3CN at ambient temperature. 111

3.18 Electronic emission spectra of $Ru(bpy)_3^{2+}$, $[Ru(\mathbf{Me\text{-}pybim})(bpy)_2]^{2+}$, $[Ru(\mathbf{Me_2\text{-}pybbim})(bpy)_2]^{2+}$, and $[\{(bpy)_2Ru\}_2(\mathbf{Me_2\text{-}py_2bbim})]^{4+}$ in CH_3CN at ambient temperature. 112

3.19 Structures of $[\{(bpy)_2Ru\}_2(\mathbf{Me_2\text{-}py_2bbim})]^{4+}$ and $[Ru(\mathbf{Me\text{-}pybim})(bpy)_2]^{2+}$. 113

4.1 Cyclic voltammograms of 1 mM $Ru(bpy)_3(ClO_4)_2$ in CH_3CN/0.1 M Et_4NClO_4 containing 1% water under N_2 and CO_2 at a glassy carbon electrode (at v = 100 mV/s). 119

4.2 Cyclic voltammograms of 1 mM $[Ru(\mathbf{Me\text{-}pybim})(bpy)_2]^{2+}$ in CH_3CN /0.1 M Et_4NClO_4 containing 1% water under N_2 and CO_2 at a glassy carbon electrode (at v = 100 mV/s). 120

4.3 Cyclic voltammograms of 1 mM $[Ru(\mathbf{Me_2\text{-}pybbim})(bpy)_2]^{2+}$ in CH_3CN/ 0.1 M Et_4NClO_4 containing 1% water under N_2 and CO_2 at a glassy carbon electrode (at v = 100 mV/s). 121

4.4 Cyclic voltammograms of 1 mM $[Ru(\mathbf{pybbim})(bpy)_2]^{2+}$ in CH_3CN/ 0.05 M Et_4NClO_4 containing 1% water under N_2 and CO_2 at a platinum electrode (at v = 100 mV/s). 122

4.5 Cyclic voltammograms of 1 mM $[Ru(\mathbf{pybtz})(bpy)_2]^{2+}$ in CH_3CN/ 0.1 M Et_4NClO_4 containing 1% water under N_2 and CO_2 at a glassy carbon electrode (at v = 100 mV/s). 123

4.6 Cyclic voltammograms of 1 mM $[\{(bpy)_2Ru\}_2(\mathbf{Me_2\text{-}py_2bbim})]^{4+}$ in CH_3CN/0.1 M Bu_4NBF_4 containing 1% water under N_2 and CO_2 at a glassy carbon electrode (at v = 100 mV/s). 124

4.7 Structures and cyclic voltammograms of 0.3 mM **1** or **2** in 0.1 M Bu_4NBF_4/MeCN at a glassy carbon electrode (3.0 mm) under N_2 (—) and CO_2 (----) atmospheres. Scan rate = 50 mV/s. 125

4.8 Cyclic voltammograms of 1 mM $[\{(bpy)_2Ru\}_2(\mathbf{py_2bbim})]^{4+}$ in

CH_3CN/0.1 M Bu_4NBF_4 containing 1% water under N_2 and CO_2 at
a glassy carbon electrode (at ν = 100 mV/s). 126

4.9 Cyclic voltammograms of 1 mM $[\{(bpy)_2Ru\}_2(\mathbf{py_2tbtz})]^{4+}$ in
CH_3CN/0.1 M Et_4NClO_4 (1% water) under N_2 and CO_2 at
a glassy carbon electrode (at ν = 100 mV/s). 127

4.10 Cyclic voltammograms of 1 mM $[\{(bpy)_2Ru\}_2(\mathbf{Me_2\text{-}pzbbim})]^{4+}$
in CH_3CN/0.1 M Et_4NClO_4 containing 1% water under N_2 and CO_2
at a glassy carbon electrode (at ν = 100 mV/s). 129

4.11 Cyclic voltammograms of 1 mM $[\{(bpy)_2Ru\}_2(\mathbf{pzbbtz})]^{4+}$
in CH_3CN/0.1 M Bu_4NBF_4 containing 1% water under N_2 and CO_2
at a glassy carbon electrode (at ν = 100 mV/s). 130

4.12 Cyclic voltammograms of 1 mM $[(bpy)_2Ru(\mathbf{tz})]^{2+}$ in CH_3CN/
0.1 M Et_4NClO_4 containing 1% water under N_2 and CO_2
at a glassy carbon electrode (at ν = 100 mV/s). 132

4.13 Cyclic voltammograms of 1 mM $[Ru(\mathbf{tz})_3]^{2+}$ in CH_3CN/0.1 M
Et_4NClO_4 containing 1% water under N_2 and CO_2 at a glassy
carbon electrode (at ν = 100 mV/s). 133

4.14 HPLC chromatograms for separation of: A) standards;
B) formic acid, and C) oxalic acid from an electrolyzed solution
of $[\{(bpy)_2Ru\}_2(\mathbf{py_2tbtz})]^{4+}$ (1 mM) in CO_2 saturated CH_3CN
/0.1 M Bu_4NBF_4, under wet conditions at a Hg pool electrode..... 136

4.15 Standard addition plot for the quantification of formic acid in the

electrolyzed solution of $[\{(bpy)_2Ru\}_2(\mathbf{py_2tbtz})]^{4+}$.....137

4.16 Standard addition plot for the quantification of oxalic acid in the electrolyzed solution of $[\{(bpy)_2Ru\}_2(\mathbf{py_2tbtz})]^{4+}$.....137

5.1 Cyclic voltammogram of methyl benzoate (2.6 mM) in DMF/0.1 M n-Bu_4NClO_4 in the absence (dotted line) and presence (solid line) of CO_2 (26 mM). The current scale is normalized relative to the cathodic peak current in the absence of CO_2, i_p°. Scan rate 1 V/s. Temperature 25 °C. 148

5.2 Cyclic voltammogram of **Fl** (5 mM) in CH_3CN/0.1 M Et_4NBF_4, under N_2 at a glassy carbon electrode, (ν = 50 mV/s). Ag/AgCl (RE), Pt (CE). 150

5.3 Cyclic voltammograms of **Fl** (5 mM) in CH_3CN/0.1 M Et_4NBF_4 under CO_2 (.....) and N_2 (—) at a glassy carbon electrode, (ν = 50 mV/s), Ag/AgCl RE), Pt (CE) (Shows both peak). 152

5.4 Cyclic voltammograms of **Fl** (5 mM) in CH_3CN/0.1 M Et_4NBF_4, under CO_2 (.....) and N_2 (—) at a glassy carbon electrode (0.20 cm^2) at a scan rate of 50 mV/s (first peak). 153

5.5 Current vs time response during the electrolysis of 5 mM **Fl** in CH_3CN/20 mM Et_4NBF_4 (anhydrous), under CO_2, at -1.2 V vs Ag/AgCl at a Hg pool electrode (11.12 C passed). 156

5.6 Q vs t response during the electrolysis of 5 mM **Fl** in CH_3CN/20 mM Et_4NBF_4, under CO_2, at -1.2 V vs Ag/AgCl at a Hg pool

electrode A) anhydrous (11.12 C passed), B) 1% v/v water
(11.06 C passed). 157

5.7 Cyclic voltammograms of 5 mM **FI** in CH_3CN/0.1 M Et_4NBF_4
at a glassy carbon electrode (0.20 cm^2), scan rate of 50 mV/s
(before electrolysis) under N_2 and CO_2. 158

5.8 Cyclic voltammograms of 5 mM **FI** in CH_3CN/0.1 M Et_4NBF_4
at a glassy carbon electrode (0.20 cm^2), scan rate of 50 mV/s after
the electrolysis at a Hg pool electrode, at -1.2 V vs Ag/AgCl
(12.8 C passed) under N_2 and CO_2. 159

5.9 Cyclic voltammogram of an electrolyzed solution of 5 mM **FI** in
CH_3CN/0.1 M Et_4NBF_4 at glassy carbon electrode (0.20 cm^2),
scan rate of 50 mV/s, after the electrolysis under CO_2 at a Hg
pool electrode at -1.2 V vs Ag/AgCl (12.8 C passed). 160

5.10 Cyclic voltammogram of an electrolyzed solution (12.8 C) of
5 mM **FI** in CH_3CN/0.1 M Et_4NBF_4 at -1.2 V vs Ag/AgCl
at glassy carbon electrode (0.20 cm^2), scan rate of 50 mV/s,
after flushing with N_2 (ca. 2 h.). 161

5.11 Cyclic voltammogram of an electrolyzed solution (12.8 C) of
5 mM **FI** in CH_3CN/0.1 M Et_4NBF_4 at -1.2 V vs Ag/AgCl
at a glassy carbon electrode (0.20 cm^2), scan rate of 50 mV/s,
after exposure to air for several hours and then flushing with N_2. 162

5.12 Cyclic voltammogram of an electrolyzed solution (12.8 C)

of 5 mM **Fl** in CH_3CN/0.1 M Et_4NBF_4 at -1.2 V vs Ag/
AgCl at a glassy carbon electrode (0.20 cm^2), scan rate of
50 mV/s after expose to air for several hours, flushing with N_2
and then with CO_2 163

5.13 ^1H NMR spectrum (MeOD) of the middle chromatographic
band from the electrolysis of **Fl** under anhydrous conditions. 165

5.14 ^1H NMR spectra in MeOD of: 1) the solid residue from a
Fl/CO_2 electrolysis solution (1% water, 11.06 C passed);
2) 9-hydroxyfluorene; 3) **Fl**; 4) 9-hydroxyfluorene-9
-carboxylic acid; 5) a standard mixture (2 drops from each 5 mM
solution) of **Fl**; 9-hydroxyfluorene and 9-hydroxyfluorene-9
-carboxylic acid. 166

5.15 GC-EIMS separation of electrolyzed solutions of: A) 11.5 C passed,
hydrous systems; B) 12.7 C passed, anhydrous system for 5 mM **Fl**,
20 mM of Et_4NBF_4 under CO_2. 9-Hydroxyfluorene-9-carboxylic
acid, 9-hydroxyfluorene and **Fl** were identified as products. 167

5.16 Chromatographic separations of three standards: a) 9-hydroxyfluorene-
9-carboxylic acid; b) 9-hydroxyfluorene; c) **Fl** using CH_3CN/80 mM
aqueous CH_3COOH eluent. 170

5.17 Chromatographic separation of non-electrolyzed solution of **Fl** (5 mM)
in acetonitrile and 20 mM of Et_4NBF_4 using CH_3CN/80 mM aqueous
CH_3COOH as an eluent..... 171

5.18 Chromatographic separation of electrolyzed solutions of: (A) 8.6 C passed, hydrous system; and (B) 12.7 C passed, anhydrous system, of 5 mM **Fl**, 20 mM of Et_4NBF_4 in CH_3CN/80 mM aqueous CH_3COOH as an eluent. a) 9-hydroxyfluorene-9-carboxylic acid, b) 9-hydroxyfluorene, and c) **Fl**. 172

5.19 Calibration plots for A) 9-hydroxyfluorene, and B) 9-hydroxyfluorene -9-carboxylic acid obtained by using acetonitrile and aqueous 80 mM of acetic acid as gradient eluent. 173

5.20 Standard addition plot for the quantification of 9-hydroxyfluorene for the electrolysis (8.06 C) solution of **Fl** (5 mM) in 20 mM of Et_4NBF_4 (anhydrous conditions), by using acetonitrile and aqueous 80 mM of acetic acid as gradient eluent. 174

5.21 Standard addition plot for the quantification of 9-hydroxyfluorene -9-carboxylic acid for the electrolysis (8.6 C) solution of **Fl** (5 mM) in CH_3CN/20 mM of Et_4NBF_4 (hydrous conditions), by using acetonitrile and aqueous 80 mM of acetic acid as gradient eluent. 175

5.22 Standard addition plot for quantification of formic acid by GC-FID method in an electrolyzed solution (11.0 C passed, 1% water) of 5 mM **Fl**, 20 mM of Et_4NBF_4. 177

5.23 Chromatogram of a standard mixture of 5 mM oxalic and 5 mM formic acid using 50 mM KH_2PO_4/H_3PO_4 at pH = 2.45 and acetonitrile (95:5) as the eluent. 178

5.24 HPLC chromatogram of an electrolyzed solution (8.06 C, anhydrous system) of 5 mM **Fl** in CH_3CN containing 20 mM of Et_4NBF_4. The isocratic eluent was KH_2PO_4/H_3PO_4 at pH = 2.45 and acetonitrile (95:5). Peaks are identified as: a) oxalic acid; b) not identified; c) not identified; d) not identified; e) 9-hydroxyfluorene-9- carboxylic acid; f) Et_4NBF_4 (electrolyte); g) 9-hydroxyfluorene; h) **Fl** and i) not identified. 179

5.25 HPLC chromatogram of an electrolyzed solution (8.06 C, anhydrous system) of 5 mM **Fl** in CH_3CN containing 20 mM of Et_4NBF_4. The eluent was KH_2PO_4/H_3PO_4 at pH = 2.45 and acetonitrile (95:5) as isocratic eluent. 180

5.26 HPLC chromatogram of an electrolyzed solution (11.06 C, hydrous system) of 5 mM of **Fl** in CH_3CN containing 20 mM of Et_4NBF_4. The eluent was KH_2PO_4/H_3PO_4 at pH = 2.45 and acetonitrile (95:5) as isocratic eluent. 180

5.27 Standard addition plot for the quantification of formic acid for the electrolysis (11.06 C) solution of **Fl** (5 mM) in CH_3CN/20 mM of Et_4NBF_4 (hydrous conditions), by using 50 mM of KH_2PO_4/H_3PO_4 buffer (pH = 2.45) and acetonitrile (95:5) as an isocratic eluent. 181

5.28 Standard addition plot for the quantification of oxalic acid for the electrolysis (8.06 C) solution of **Fl** (5 mM) in CH_3CN/20 mM Et_4NBF_4 (anhydrous conditions), by using 50 mM of KH_2PO_4/H_3PO_4 buffer

(pH = 2.45) and acetonitrile (95:5) as an isocratic eluent. 182

5.29 Plot of percentage of charge consumed for each of the products relative to the total amount of charge passed for the electrolysis of **Fl** (5 mM) in CO_2-saturated acetonitrile and 20 mM of Et_4NBF_4 solutions under anhydrous and 1% water conditions at a Hg pool electrode at -1.2 V vs Ag/AgCl. 185

5.30 Plot of percentage of carboxylated products formed relative to faradaic yields of **Fl** (5 mM) at -1.2 V vs Ag/AgCl in CO_2-saturated acetonitrile and 20 mM of Et_4NBF_4 solutions under anhydrous and 1% water conditions at a Hg pool electrode. 187

List of Schemes

1.1 Electrocatalysis (homogeneous catalysis) process with an electron source..... 5

1.2 Reaction pathways in electrochemical reduction of CO_2 under various conditions. 12

1.3 Proposed mechanism for the Tanaka catalyst. 18

1.4 Proposed mechanism for the photochemical reduction of CO_2 by $[Re(bpy)(CO)_3Cl]$. 20

1.5 Possible mechanism products during electrochemical CO_2 reduction by $[Ru(bpy)(\mathbf{terpy})(CO)]^{2+}$. 21

1.6 Mechanism for metallacyclization on electrochemical reduction of CO_2 by $[Ru(bpy)(\mathbf{napy})_2(CO)_2]^{2+}$. 23

1.7 Structures of some of Tanaka's electrocatalysts. 24

1.8 Possible mechanism for formation of Ru-(η^1-CO_2) and Ru–CO complexes by $[RuL\text{-}(\mathbf{napy\text{-}\kappa^2N,N''})(dmso)](PF_6)_2$ in CO_2-saturated solution. 27

4.1 General cycle for the production of various products during electrochemical CO_2 reduction by metal complexes with acyclic ligands as electrocatalysts. 139

5.1 General mechanisms for the electrochemical carboxylation of aromatic ketones by CO_2 in non-aqueous solution. 145

5.2 Redox catalysis and quasi-redox catalysis processes for

electrochemical CO_2 reduction by esters. 147

5.3 Multiple competing pathways of product formation during the electrolysis of **Fl** in CO_2-saturated acetonitrile under both anhydrous and 1% water conditions. Percentage of charge was calculated based on the initial amount of charge passed and faradaic efficiency for each of the products. 184

List of Tables

1.1 Faradaic efficiencies for hydrocarbon preparation on copper: influence of solvent and supporting electrolyte. 8

1.2 Solubility of CO_2 in various solvents at 1 atm and 25 °C. 10

2.1 Summary of crystallographic data for $[Ru(\mathbf{pybtz})(bpy)_2]^{2+}$, $[Ru(\mathbf{Me_2pybbim})(bpy)_2]^{2+}$,$[\{(bpy)_2Ru\}_2(\mathbf{pzbbtz})]^{4+}$ 67

2.2 Summary of crystallographic data for $[\{(bpy)_2Ru\}_2(\mathbf{py_2tbtz})]^{4+}$ 68

2.3 Selected bond distances (Å) and angles (°) for $[Ru(\mathbf{pybtz})(bpy)_2]^{2+}$. 71

2.4 Selected bond distances (Å) and angles (°) for $[Ru(\mathbf{Me_2\text{-}pybbim})(bpy)_2]^{2+}$. 72

2.5 Selected bond distances (Å) and angles (°) for $[\{(bpy)_2Ru\}_2(\mathbf{pzbbtz})]^{4+}$ 75

2.6 Bond lengths (Å) and bond angles (°) for $[\{(bpy)_2Ru\}_2(\mathbf{py_2tbtz})]^{4+}$. 79

3.1 Formal potentials *vs.* Ag/AgCl of all the complexes in the presence of 0.1 M Bu_4NBF_4/CH_3CN 96

3.2 Separation between oxidation formal potentials, ΔE° (mV), and the corresponding comproportionation constant, K_c (eqn. 10, chapter 1, page 36), for all bimetallic complexes. 97

3.3 Absorption and emission maxima data for the monometallic and bimetallic complexes in acetonitrile at ambient temperature. 104

3.4 Absorption, emission maxima, excitation wavelength and HOMO-LUMO energy gap of some monometallic complexes. 104

3.5 Excitation wavelength, emission area, absorbance, and emission quantum yields of some monometallic complexes in CH_3CN at room temperature 105

5.1 Potentials and currents for the first two reduction peaks of **Fl** (5 mM) in CH_3CN/0.1 M Et_4NBF_4 at ν = 0.05 V/s in a N_2-saturated solution..... 151

5.2 HPLC gradients used for the separation and quantification of 9-hydroxyfluorene and 9-hydroxyfluorene-9-carboxylic acid in the electrolyzed solutions of **Fl** (5 mM) under CO_2..... 169

5.3 HPLC quantification of products from the electrolysis of 5 mM **Fl** in CH_3CN/20 mM Et_4NBF_4 in CO_2-saturated solution. The charge passed in these electrolyses corresponds to one-electron per **Fl** molecule..... 176

5.4 HPLC quantification of products from the electrolysis of 5 mM **Fl** in CO_2-saturated CH_3CN/20 mM Et_4NBF_4 solution. The charge passed in these electrolyses corresponds to one-electron per **Fl** molecule. 183

Glossary of Abbreviations

API-MS	atmospheric pressure ionization-mass spectrometry
APCI	atmospheric pressure chemical ionization
BL	bridging ligand
bpy	"2,2′- bipyridine"
Bu_4NBF_4	tetra-*n*-butylammonium fluoborate
cat.	catalyst
CV	cyclic voltammetry
CT	Creutz-Taube ion
DPV	differential pulse voltammetry
ESI-MS	electrospray ionization-mass spectrometry
EC_{cat}	catalytic regeneration of the electroactive species in a following homogeneous reaction
ECE	heterogeneous electron transfer, homogeneous chemical reaction, and heterogeneous electron transfer, in sequence
Fl	fluorene-9-one
GC	gas chromatography
HOMO	highest occupied molecular orbital
HPLC	high performance liquid chromatography
IT	intervalence charge transfer
FTIR	fourier transform infrared spectroscopy
LUMO	lowest unoccupied molecular orbital
MALDI TOF MS	matrix assisted laser desorption ionization time-of-flight mass spectrometry
MLCT	metal-to-ligand charge-transfer
Me-pybim	1-methyl-2-(pyridin-2-yl)-1H-benzo[d]imidazole
Me_2-pybbim	2,5-bis(1-methyl-1*H*-benzo[*d*]imidazol-2-yl)pyridine
Me_2-pzbbim	2,5-bis(1-methyl-1H-benzo[d]imidazol-2-yl)pyrazine
Me_2-py_2bbim	3,3′-dimethyl-2,2′-di(pyridin-2-yl)-5,6′-bi(3H-benzo[d]imidazole)
NMR	nuclear magnetic resonance
ORTEP	Oak Ridge thermal ellipsoid plot
PPA	polyphosphoric acid
ppm	parts per million
pybtz	2-(pyridin-2-yl)benzo[d]thiazole
pzbbtz	2,5-di(benzo[*d*]thiazol-2-yl)pyrazine
py_2tbtz	2,6′-bis(2-pyridyl)-2,2′:6,2″-thiazolo[4,5-d]-benzothiazole
P_2O_5	phosphorus pentaoxide
SCE	saturated calomel electrode
Et_4NClO_4	tetraethylammonium perchlorate
TLC	thin layer chromatography
tz	2,2′- bithiazole

TFA-*d*	deuterated trifluoroacetic acid
TMS	tetramethylsilane
UV-vis	ultraviolet-visible

Glossary of Symbols

Δ	chemical shift (in ppm)
ν	scan speed
Ag/AgCl	silver wire reference
C	coulomb
E	potential
E°	formal potential
$E^{\circ\prime}$	equilibrium potential
ΔE°	difference between the formal potentials
e^-	electron
$E_{1/2}$	half wave potential
$E_{p,a}$	anodic peak potential
$E_{p,c}$	cathodic peak potential
I	current
$i_{p,a}$	anodic peak current
$i_{p,c}$	cathodic peak current
m/z	mass-to-charge ratio
M	molarity
M^+	molecular ion
ε	extinction coefficient
λ	wavelength
Q	charge
K_c	comproportionation constant
E_{em}	emission maximum energy
E_{ab}	absorption maximum energy
φ	quantum yield
E_{00}	HOMO-LUMO energy gap
η	refractive index
J	coupling constant

Chapter 1

An introduction to electrochemical CO_2 reduction

1.1 Importance of CO_2 reduction

Our currently used global chemical energy sources are beginning to present serious challenges as a result of long-term exploitation. The comprehensively-used chemical energy sources, i.e., fossil fuels, are not sustainable resources and this urges us to break our dependence on them. Our future energy sources could be renewable (wind, hydroelectric, geothermal, solar, and biomass) and nuclear energy [1]. Nuclear energy is expensive and produces hazardous and persistent environmental pollution. Renewable energy seems insufficient for current global demand. Among the other alternatives, only biomasses (e.g., agricultural and forest products) produce fuels directly. However, for the production of biofuels, a significant amount of food resources (e.g., corn, sugar, crop oils etc.) is being used up, which has partially led sharply increased food prices [2] as well as environmental pollution (e.g., CO_2) [3, 4].

Among the greenhouse gases, CO_2 concentrations are continuously increasing in the atmosphere from various sources and is believed to be one of the major [5] contributors for global warming. Combustion of any carbon-containing material (e.g., fossil fuels) releases carbon dioxide and water. Synthetic liquid hydrocarbon production, which is done mainly by 'syn-gas' processes, also generates huge amounts of CO_2 and other byproducts. Additionally, electricity production (from fossil fuels), transportation, industrial sectors, and fermentation plants (from EtOH production) are major sources for CO_2 emissions [6]. In short, all of these factors contribute to the increase of atmospheric CO_2 levels, which are currently around 380 ppm [7]. Thus, processes that consume CO_2 are attractive, not only considering its continuous increase in the atmosphere, but also

considering the increasing utilization of carbon based energy sources [8].

The continuous increase in the atmospheric CO_2 concentration along with other gases in air impacts not only global warming, but also environmental concerns such as air pollution, acid rain, acidification of the oceans, deforestation, etc. It is a major challenge for humankind to overcome these harmful effects. In order to limit CO_2 emissions into the atmosphere, the "Kyoto agreement" and subsequent international efforts should be strictly implemented. In fact CO_2 is the most important and naturally abundant source of carbon available to mankind. Electrochemical reduction of CO_2 and subsequent conversion into fuels has been attracting enormous scientific attention and thus it has grown into a vast field of research over the last few decades. Nature uses CO_2 to produce carbohydrates and oxygen by the process of photosynthesis. Scientists are now looking for a type of "artificial leaf" that could efficiently produce a number of useful products similar to nature's photosynthetic processes. The ultimate goal of this kind of artificial photosynthesis is to produce liquid fuels such as methanol and formic acid [9]. Thus, the chemical and electrochemical recycling of CO_2 to carbon neutral fuels and useful chemicals are expected to appear as a practical step, which would possibly be a feasible and powerful new alternative to current energy sources.

Usually, the electrochemical reduction of CO_2 requires a high cathodic potential ca. -2.21 V vs SCE. An effective electrocatalyst can reduce this potential substantially, driving an electrochemical reaction at less cathodic potentials under mild and clean conditions.

1.2 Electrocatalysis - kinetics

Equilibrium potentials vs NHE for the electrochemical reduction of CO_2 to various products are shown below in equations (2-6). It is clear from these equations that the distribution of the reduction products has a strong influence on its thermodynamic accessibility from CO_2. As the number of participating protons and electrons increases, the potential becomes less negative.

$$CO_2 + e^- \rightarrow CO_2^{\bullet -} \qquad E^\circ = -2.21 \text{ V vs SCE} \quad \text{.....(1)}$$

$$CO_2 + 2H^+ + 2e^- \rightarrow HCOOH \qquad E^{\circ\prime} = -0.61 \text{ V} \quad \text{.....(2)}$$

$$CO_2 + 2H^+ + 2e^- \rightarrow CO + H_2O \qquad E^{\circ\prime} = -0.53 \text{ V} \quad \text{.....(3)}$$

$$CO_2 + 4H^+ + 4e^- \rightarrow HCHO + H_2O \qquad E^{\circ\prime} = -0.48 \text{ V} \quad \text{.....(4)}$$

$$CO_2 + 6H^+ + 6e^- \rightarrow CH_3OH + H_2O \qquad E^{\circ\prime} = -0.38 \text{ V} \quad \text{.....(5)}$$

$$CO_2 + 8H^+ + 8e^- \rightarrow CH_4 + H_2O \qquad E^{\circ\prime} = -0.24 \text{ V} \quad \text{.....(6)}$$

An effective electrocatalyst can drive a reduction (or oxidation) reaction of a substrate at modest potentials, highly efficiently, possibly close to the thermodynamic equilibrium potential (see Scheme 1.1). Thus, an electrochemical reaction can be favoured thermodynamically with substantial reaction kinetics towards the CO_2 conversion to highly selective products. In addition, Savéant [10] opined that, in an effective electrocatalytic process more than one reactant and one product would participate by several bond breaking and bond forming processes, which in turn opens

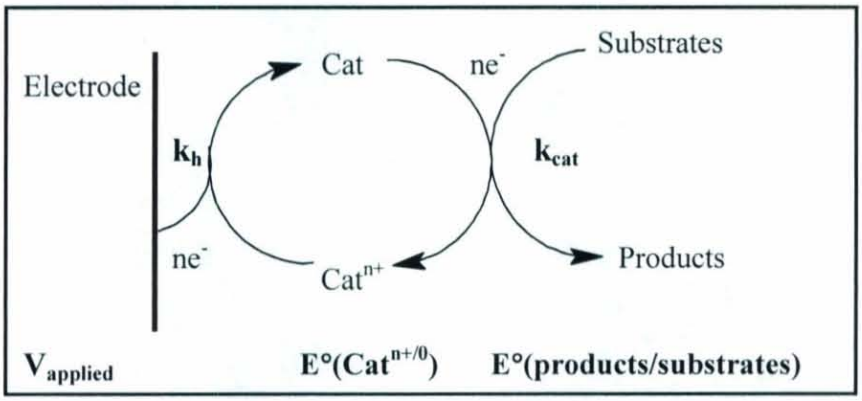

Scheme 1.1: Electrocatalysis (homogeneous catalysis) with an electron source. Reproduced with permission from *Chem. Soc. Rev.* 2009, 38, 89 [11]. Copyright © 2009 The Royal Society of Chemistry.

subsequent fast multi-electron reaction pathways during an electron transfer reaction. Therefore, an electrochemical reaction can be favored thermodynamically and energetically in multi-electron charge transfer pathways to a fuel forming process (Eqs. 2, 5, 6).

According to Benson et al. [11], an electrocatalytic process (for the electro-reduction of CO_2) can be identified by comparing the cyclic voltammetry in the presence and absence of CO_2. In the presence of CO_2, the potential may shift with an increase in the diffusion-limited current (can be a result of regeneration of catalysts) and generally the anodic wave disappears (an indication of a chemical reaction between CO_2 and an electrocatalyst). Also, the cyclic voltammogram will return to its original appearance after removal of CO_2 with N_2/Ar purge. All these things will be an indication of an

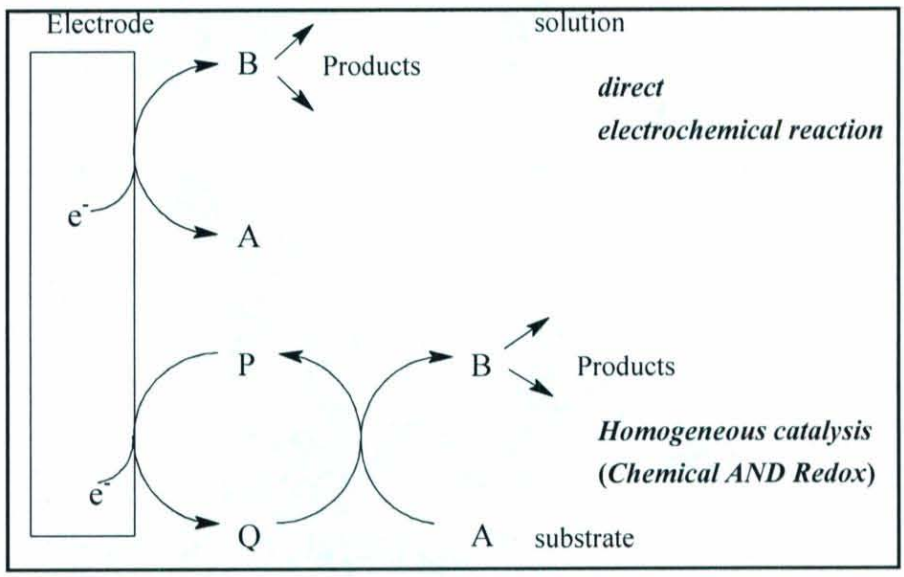

Figure 1.1: Schematic representation of the various types of molecular catalysis of electrochemical reactions. Reproduced with permission from *Chem. Rev.* 2008, 108, 2348 [10]. Copyright © 2008 American Chemical Society.

EC_{cat} mechanism [12]. The additional supporting evidence can be revealed by performing electrolysis and find out the electrocatalytic products with the regeneration of the electrocatalyst itself.

An electrocatalyst may function by a heterogeneous or homogeneous catalytic process. In general, homogeneous catalysis is a process where a catalyst can freely diffuse in the reaction medium along with the reactant. According to Savéant et al. [13], in a homogeneous system, transition metal electrocatalysts may perform either "redox" or "chemical" catalytic processes. In a "redox catalytic" process the redox reaction usually occurs solely by an outersphere electron transfer (fast) mechanism. Here the metal

complex acts as a mediator and transfers electrons from the electrode to the substrate A (see Figure 1.1) while maintaining its original coordination spheres. On the other hand, in the "chemical catalytic" process, a chemical reaction occurs between the electrocatalyst (metal complex) and the substrate by an inner-sphere electron transfer mechanism. This reaction involves both electron transfer and chemical reaction processes via the formation of a very active intermediate catalyst–substrate [MC–A] complex. Usually, the chemical step determines the selectivity for this kind of reaction mechanism.

1.3 Review of electrochemical CO_2 reduction

Electrochemical CO_2 reduction has been a field of paramount interest since the 20^{th} century. In recent years, extensive research in this field has further advanced, with numerous reports published during the last two decades. Different metals, metal oxides, metal alloys, nonmetals, metal complexes, polymers, and monomers along with some organic functional groups such as esters and ketones have been studied as electrocatalysts for CO_2 reductions.

Metal cathodes are heterogeneous catalysts that show selective product formation together with suitable mechanical, chemical, and thermal stability. On the other hand, transition metal complexes can be either homogeneous or heterogeneous (e.g., immobilization onto an electrode surface) catalysts with low operating potentials and high selectivities [14-15]. The use of metal complexes is advantageous over metal cathodes [16] and organic electrocatalysts [15] because they operate under milder conditions and have lower overpotentials for electrochemical CO_2 reduction. However,

metal complexes tend to have limited stabilities.

The product distributions and the faradaic efficiencies of electrochemical CO_2 reduction by different electrocatalysts can be influenced by several factors such as i) the electrocatalyst, ii) the supporting electrolyte, iii) the solvent, iv) temperature, and v) the applied potential/current of the electrolysis.

Table 1.1: Faradaic efficiencies for hydrocarbon preparation on a copper electrode: influence of solvent and supporting electrolyte [17]. Reproduced from *Journal of the University of Chemical Technology and Metallurgy,* 2007, 42, 4 [online].

Supporting salt, conditions	**Main products (faradaic efficiency, %)**
KOH/aq	CO (98), hydrocarbons(<2)
Benzalkonium chloride	CH_4 (42.5), C_2H_4 (2.4)
Tetraethylammonium perchlorate /MeOH	C_2H_4 (11.5)
CsOH (243 K)/MeOH	C_2H_4 (23.7-32.3), CH_4 (8.3)
$KHCO_3$ (298 K), aq.	CH_4 (16-17.8), C_2H_4 (12.7-14)
$KHCO_3$ (273 K), aq.	CH_4 (24.7), C_2H_4 (6.5)

Table 1.1 describes an example of how the faradaic efficiency and product selectivity of the electrochemical reduction of CO_2 at a copper electrode can be affected by the electrolytes and solvents. It is seen that, in the presence of benzalkonium chloride, the faradaic efficiency for the formation of methane is 42.5%, whereas for ethylene it is

only 2.4% [17]. However, when the electrolysis was performed in the presence of CsOH and at low temperature using methanol, the faradaic efficiency for ethylene formation can be increased up to 32.3%, whereas the faradaic efficiency for the formation of methane is only 8.3%. The formation of methane can be increased if aqueous $KHCO_3$ is used at a low temperature.

The most commonly reported products of electrochemical CO_2 reductions by different electrocatalysts are HCOOH, CO, and $H_2C_2O_4$ (oxalic acid) along with hydrocarbons, HCHO, and CH_3OH. According to Wong at al. [16], CO might be an important intermediate in the multi-step CO_2 reduction to hydrocarbons and could be a precursor to various other chemicals. The other possible paths are via formation of $CO_2^{\bullet-}$, $COOH^{\bullet}$ (ad) or, reduced CO_x^{y-}(ad) species to a variety of other electrochemically reduced CO_2 products [18]. In addition, the formation of oxalate dianion by reductive coupling of CO_2 can be accomplished by a number of metals (e.g., Hg, and Pd) with a outersphere electron transfer or by organic electrocatalysts (e.g., esters and ketones) via the formation of anion radicals or by transition metal complexes in a inner-sphere electron transfer processes [10,19]. Usually, a proton source is required to produce a formate anion.

1.3.1 Solubility of CO_2

Solubility of CO_2 is an important factor in the electrochemical reduction of CO_2. Usually the solubility of CO_2 is much higher in non-aqueous solvents than in aqueous systems (see Table 1.2). It can be observed that, among the non-aqueous solvents, CO_2 has the

Table 1.2: Solubility of CO_2 in various solvents at 1 atm and 25 °C [17]. Reproduced from *Journal of the University of Chemical Technology and Metallurgy,* 2007, 42, 4 [online].

Solvent	**Concentration (M)**
Water	0.033
Methanol	0.06
Tetrahydrofuran (THF)	0.205 ± 0.008
Acetonitrile (AN)	0.275 ± 0.008
Dimethylformamide (DMF)	0.199 ± 0.006
Dimethylsulfoxide (DMSO)	0.138 ± 0.003

highest solubility in acetonitrile. Acetonitrile can thus be considered as a good solvent for CO_2 reduction. If the reaction is to be performed in water or methanol, it usually requires high pressure of CO_2. The elevation of CO_2 pressure significantly enhances the solubility of CO_2 in H_2O. For example, the solubility of CO_2 at 25 °C is around 0.034 mol L^{-1} at 1 atm [20], which could be elevated 36-fold to 1.22 mol L^{-1} at 50 atm. On the other hand, for non-aqueous solvent systems, the electrochemical reduction can be performed at normal atmospheric pressure with good results.

1.3.2 Metal electrodes

Electrochemical CO_2 reduction has been performed by using a variety of metal electrocatalysts. Reaction conditions under aqueous media require continuous purging of

CO_2 due to the low solubility of CO_2 in water. During the electrochemical process, the diffusion of CO_2 from the bulk to the electrode surface usually limits the current density. Several approaches can be followed to avoid this limited mass transport by using either a low operating reaction temperature, high-pressure [21], ultrasonic radiation [22] or gas diffusion electrodes [23] all of which result in an increase of partial current densities for CO_2 electroreduction.

According to Hori et al. [24], Cu is the best electrode for the production of hydrocarbon based products such as, CH_4 and C_2H_4 along with EtOH and PrOH under aqueous conditions, while, CO was produced selectively by Au, Ag, Zn, Pd and Ga electrodes. In addition, Pb, Hg, In, Sn, Cd, Tl and Bi electrodes can selectively produce $HCOO^-$. It is interesting that Zr, Cr, Rh, W, Co, Ir, Ni, Fe, Pt, and Ti electrodes did not produce any reduction products under aqueous conditions and H_2 formed as the only product at 1 atm. However, at elevated pressure (ca. 30 atm) all these metal electrodes selectively produced CO and $HCOO^-$. Although high pressure improves the faradaic efficiency for the formation of CO/HCOOH, product selectivity remained unchanged. Scheme 1.2 shows the reaction pathways for the formation of various products in the electrochemical reduction of CO_2 under different reaction conditions.

The electrochemical reduction of CO_2 under non-aqueous conditions has been performed using a variety of solvents, such as propylene carbonate (PC), acetonitrile (ACN), dimethyl sulfoxide (DMSO), methanol (MeOH), dimethylformamide (DMF), and tetrahydrofuran (THF). According to Haynes and Sawyer [26], electrochemical CO_2 reduction at Hg and Au electrodes in DMSO can selectively produce $HCOO^-$ and CO as

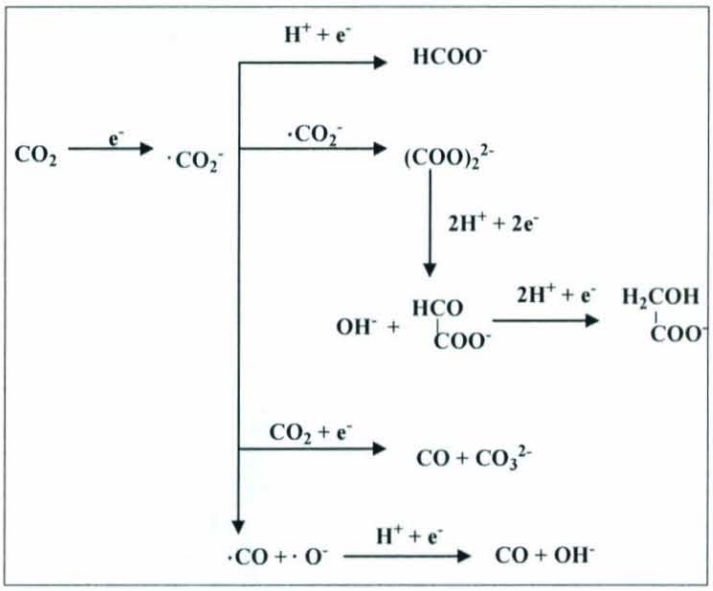

Scheme 1.2: Reaction pathways in electrochemical reduction of CO_2 under various conditions. Reproduced from *Bull. Chem. Soc. Jpn.* 1987, 60, 2517 [25]. [Online] Copyright © 1987 The Chemical Society of Japan.

the main catalytic products, whereas Tyssee et al. [27] reported the production of oxalate ($C_2O_4^{2-}$) in DMF at a Hg electrode. The electrochemical reduction of CO_2 on Pb and Hg electrodes in DMF-H_2O was studied by Savéant and coworkers [28], where CO, HCOOH and $(COOH)_2$ were found as the electrocatalytic products. Ito and coworkers [25] studied electrochemical CO_2 reduction in PC/0.1 M TEAP/H_2O (300 ppm) for different metal catalytic systems. For potentiostatic electrolysis at –2.8 V vs Ag/AgCl, $(COOH)_2$ was found as the main product for Pb, Hg and Tl electrodes, whereas for Cu, Ag, Au, Zn, In,

Sn, Ni, and Pt electrodes, CO was yielded selectively. On the other hand Fe, Cr, Mo, Pd, and Cd electrodes produced both CO and $(COOH)_2$ as the main products.

Some particular disadvantages to be noted here are that metal electrodes suffer from corrosion and passivation, particularly during long term electrolysis, which limits their use as electrocatalysts. Moreover, the product selectivity of a metal electrode is often severely affected by the presence of extremely small amounts of "ad-atoms" on the surface. In addition to that, surface contamination sometimes results in unexpected experimental results.

1.3.3 Transition metal complexes

Electrochemical CO_2 reduction catalyzed by transition metal complexes have been studied over the last 30 years for their excellent activities and selectivities, which make them good candidates to be used as electrocatalysts [11]. Transition metal complexes can be incorporated with different metals e.g., Ni, Re, Pd, Co, Cu, Ru, Rh, and Ir and ligands such as polypyridines, tetraazamacrocycles, porphyrins, phthalocyanines, and phosphines [29-39]. According to Sánchez-Sánchez et al. [40], square planar coordinated metal complexes work well under aqueous conditions, whereas a non-aqueous solvent is well suited for octahedral complexes. Mechanistically, for this kind of reaction, it is generally believed that a vacant coordination site (very active intermediate) is generated on the metal [18] during the CO_2 reduction, where CO_2 could bind and stimulate its activation within the metal coordination sphere. Thus the reduction reaction is assumed to be favored thermodynamically by creating an easy way to release products [10].

There is a strong influence on changing the central metal and/or the ligand for the electrochemical CO_2 reduction by metal complexes. For example, CO is produced selectively by Ni and Co macrocycles and Re, Ru and Rh pyridine complexes [41-46]. Alternatively, phthalocyanine, Co and Ni macrocycles, ruthenium bipyridine complexes and iron-sulphur clusters [47-49] have been reported for the formation of HCO_2^- during electroreduction of CO_2. Based on these results, it seems that the ligation characteristics as well as electron density on the metal are both essential parameters for the subsequent formation of a CO_2 adduct and the nature of the product distribution. However, compared to the variety of transition metal ions, there have been limited studies on the effect of ligands on the electrocatalytic activity of transition metal complexes. Two predominantly used polypyridyl ligands e.g., 2,2′-bipyridine and 1,10-phenanthroline are of special interest in this area because these ligands can play an impotant role in the electrochemical and photochemical reduction of CO_2 by serving as electron "reservoirs" [50] or, "promoters" [51].

1.3.3.1 Metal complexes with macrocyclic ligands

Meshitsuka and coworkers (in 1974) were the first to report the electrochemical reduction of CO_2 by a number of Co/Ni phthalocyanine complexes [52]. Although they did not elucidate any satisfactory results to support the mechanism for formation of the products, or current efficiency or even the turnover number, this result opened the first window for transition metal complexes as electrocatalysts for CO_2 reduction. After that, Eisenberg and coworkers in 1980 reported some Co and Ni tetraaza-macrocyclic complexes with

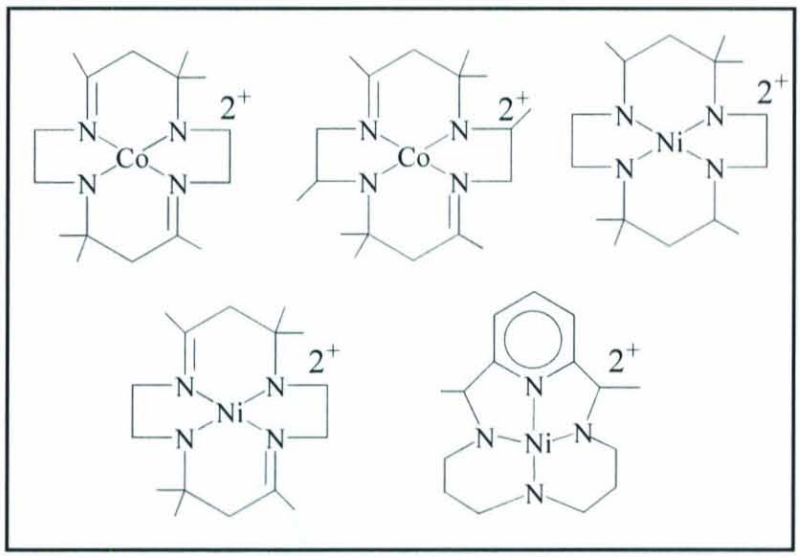

Figure 1.2: Examples of some macrocyclic complexes. Reproduced with permission from *Chem. Soc. Rev.* 2009, 38, 89 [11]. Copyright © 2009 The Royal Society of Chemistry.

high current efficiencies and turnover numbers [53]. These complexes were able to reduce CO_2 to CO from the potentials -1.3 to -1.6 V vs SCE with current efficiencies of up to 98%. However, they had low turnover numbers. Figure 1.2 shows a few examples of Ni and Co macrocyclic complexes that have been used as electrocatalysts.

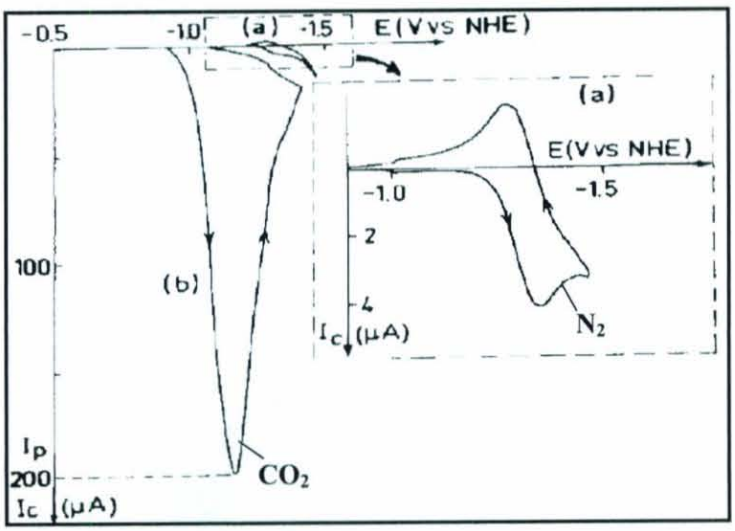

Figure 1.3: Example of electrocatalytic activity for a Ni cyclam^{2+} complex. Cyclic voltammetry under (a) N_2 and (b) CO_2 confirms the electrocatalytic activity of the complex on Hg electrode. Reproduced with permission from *J. Am. Chem. Soc.* 1986, 108, 7461 [41]. Copyright © 1986, American Chemical Society.

Sauvage and others found CO as the main product at a potential of -0.86 V vs SCE for Ni^{II} cyclam complexes [see Figure 1.3] with faradaic efficiencies of up to 96% even in the presence of water [41-42, 53-54]. Interestingly, it was found that complexes with open or unsaturated chains of similar moieties showed poor catalytic activities relative to cyclic forms. Moreover, studies showed that the catalytic activities of these complexes were dependent on their strong adsorption to the surface of the mercury electrode [42, 55].

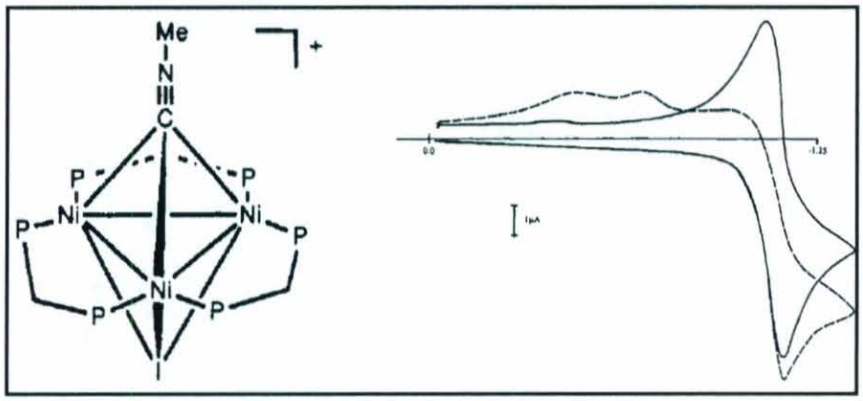

Figure 1.4: Cyclic voltammograms of $[Ni_3(\mu_3\text{-}\mathbf{CNMe})(\mu_3\text{-}I)(\mathbf{dppm})_3][PF_6]$ in 0.1 M $NaPF_6$/MeCN, initial voltammogram of a solution under N_2 (solid); the same solution after exposure to CO_2 (dotted) (3 min). (Phenyl groups on P are omitted for clarity). Reproduced with permission from *Organometallics* 1992, 11, 1986 [55]. Copyright © 1992 American Chemical Society.

Among the other types of promising macrocyclic complexes, Kubiak et al. [11] reported a Ni complex, $[Ni_3(\mu_3\text{-}\mathbf{CNMe})(\mu_3\text{-}I)(\mathbf{dppm})_3][PF_6]$ (**dppm** = bis(diphenyl-phosphino)methane) [see Figure 1.4] that provided a high activity in CO_2 reduction.

1.3.3.2 Metal complexes with bipyridynes (bpy) and CO ligands

$[Re(bpy)(CO)_3Cl]$ and $[Ru(bpy)_2(CO)X]^{n+}$ (X=CO, Cl, H ; n = 2 or 1) [44] are two important examples in this category and have been reported to be very successful electrocatalysts for the production of CO and $HCOO^-$. During the electrochemical CO_2

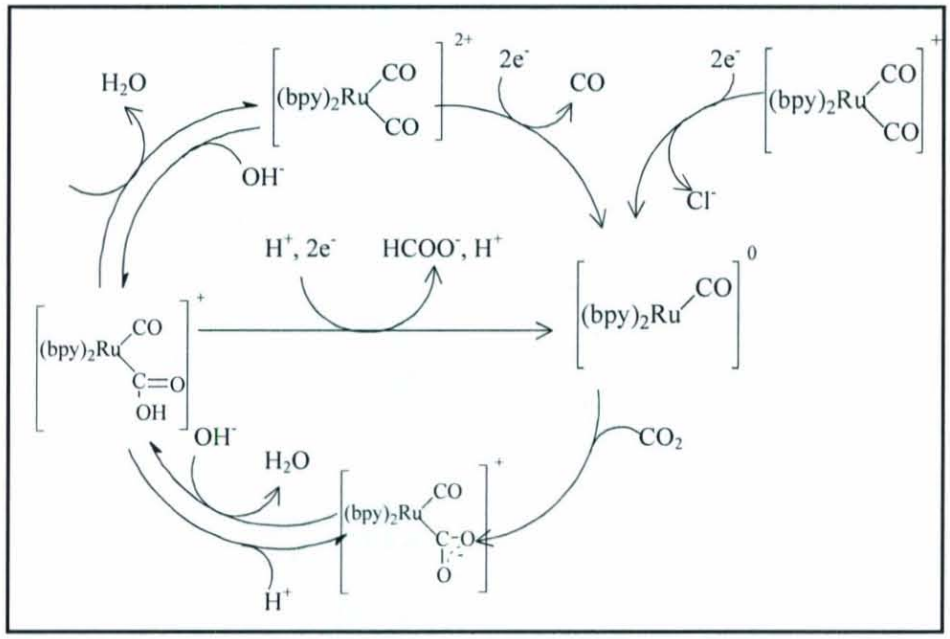

Scheme 1.3: Proposed mechanism for the Tanaka catalyst. Reproduced with permission from *Organometallics* 1987, 6, 181 [56]. Copyright © 1987 American Chemical Society.

reduction, these complexes showed exceptional stabilities, high efficiencies and reactivities. Among the ruthenium polypyridyl complexes, $[Ru(bpy)_2(CO)_2]^{2+}$ and $[Ru(bpy)(CO)Cl]^{+}$ [45, 48] have been studied most extensively. It was reported that, these complexes undergo reductive cleavage to form $[Ru(bpy)_2(CO)]^{o}$ which reacts with CO_2 to afford products and reform the original complex.

Scheme 1.3 illustrates the possible mechanism for the formation of products during electrochemical reduction of CO_2 by $[Ru(bpy)_2(CO)_2]^{2+}$ and $[Ru(bpy)(CO)Cl]^{+}$ as

proposed by Tanaka et al. [45, 48, 56-57]. According to the authors, upon electrolysis under CO_2 in the presence of aqueous DMF (10 vol. % H_2O) at a potential of -1.3 to -1.5 V (vs SCE), both complexes were able to produce CO, H_2 and $HCOO^-$. However, in the presence of anhydrous DMF, both complexes readily decomposed under similar reaction conditions. In spite of having low turnover numbers and low selectivities, these complexes have been used to reveal several of the key intermediates in course of the reduction of CO_2.

The mechanism proceeded through formation of an unstable five-coordinate neutral complex of $[Ru(bpy)_2(CO)]^o$ via two-electron reduction of both of the complexes with the loss of CO/Cl^- (see Scheme 1.3). Additionally, $[(bpy)_2Ru(CO)(COOH)]$ (a key intermediate in the formation of HCOOH) was produced upon two-electron reduction under acidic conditions with the regeneration of the five-coordinate $[Ru(bpy)_2(CO)]^o$.

Surprisingly, when aqueous acetonitrile was used as a solvent instead of DMF, the electrocatalytic reduction of CO_2 with $[Ru(bpy)_2(CO)_2]^{2+}$ [58] produced a polymeric electroactive film $[\{Ru^o(bpy)(CO)_2\}_n]$ during exhaustive electrolysis at -1.45 V. This film is believed to have formed during the two-electron reduction from the $[Ru(bpy)_2(CO)_2]^{2+}$ ion via the dechelation of one bpy ligand.

On the other hand, in the DMF/H_2O (9:1) system, when the complex $[Re(bpy)(CO)_3Cl]$ [43] was electrolyzed at -1.5 V vs SCE, CO_2 was electrochemically reduced to produce CO with a faradaic yield of 98% and several hundred turnover numbers. According to these reports, a five-coordinate complex of $[Re(bpy)(CO)_3Cl]^-$ was produced by an initial one-electron reduction via loss of a CO ligand (instead of Cl^-

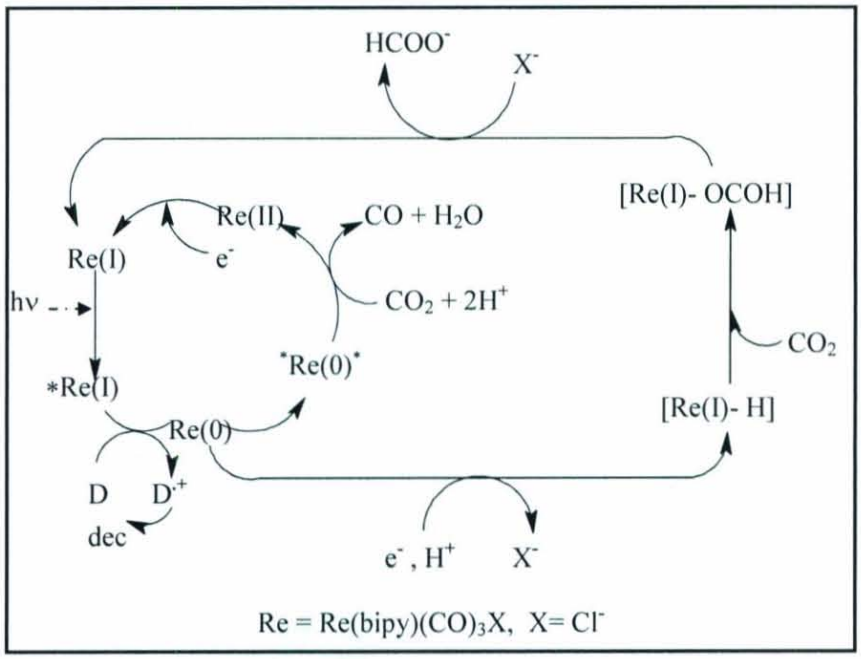

Scheme 1.4: Proposed mechanism for the photochemical reduction of CO_2 by $[Re(bpy)(CO)_3Cl]$. Reproduced with permission from *Coord. Chem. Rev.* 1989, 93, 245 [67]. Copyright © 1989 published by Elsevier Science B.V.

ion as with Tanaka's catalysts [45]), and thus was able to coordinate with CO_2 efficiently and thereby stimulated its reduction. It was mentioned that, to increase the efficiency and selectivity of the system, an excess of Cl^- ion as coordinating anion as well as the presence of water are both important factors [59-61].

Additionally, $[Re(bpy)(CO)_3Cl]$ was the first reported catalyst for photochemical CO_2 reduction [64 a]. Irradiation at 400 nm (MLCT band) caused this complex to reduce CO_2 and produce CO in the presence of an organic electron donor, which is oxidized

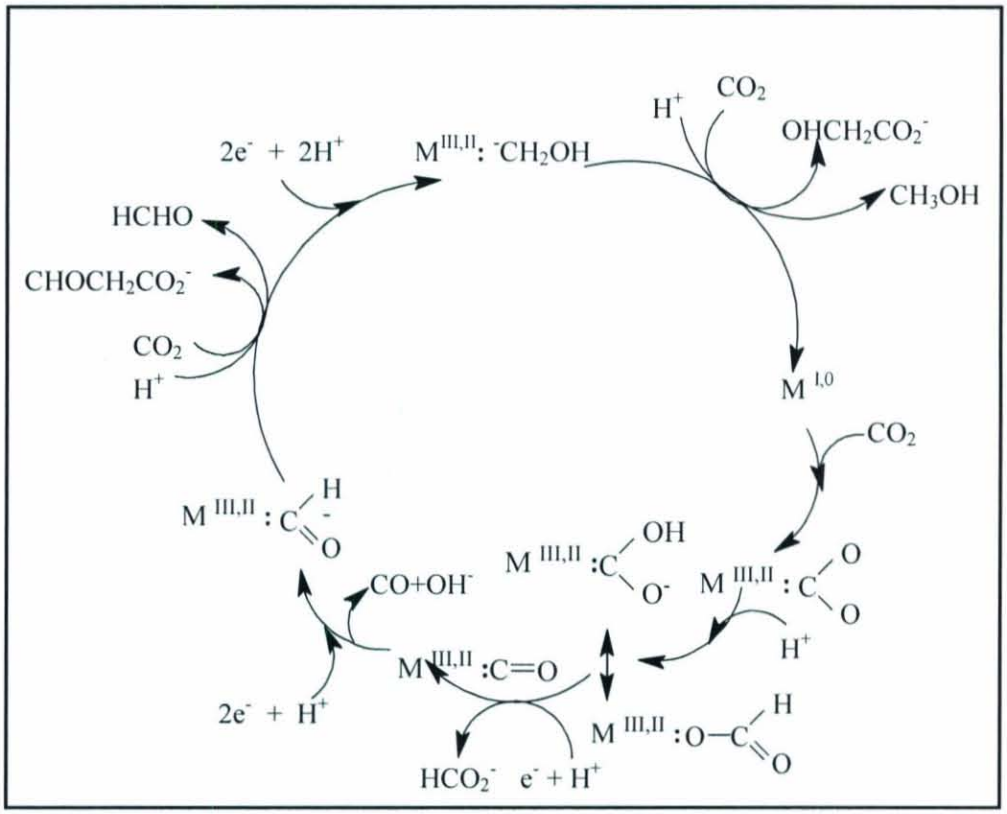

Scheme 1.5: Possible mechanism for the formation of products during electrochemical CO_2 reduction by $[Ru(bpy)(\mathbf{terpy})(CO)]^{2+}$. Reproduced with permission from *Chem. Rev.* 2008, 108, 2348 [10]. Copyright © 2008, American Chemical Society.

during the process. High quantum yields (up to 14%) were observed in the presence of Cl^- ion. The rhenium complex was reported to act simultaneously as a photoactive species and as a precursor to the catalytic centre in this photocatalytic process. Detailed studies

on the possible mechanism have been published by a number of research groups [54, 62-66] and the proposed mechanism is shown in Scheme 1.4. As our main interest here is on electrochemical CO_2 reduction, the photochemical reductions are not discussed in detail and discussions are limited solely to electrochemical methods.

Electrocatalyst $[Ru(bpy)(\mathbf{terpy})(CO)]^{2+}$ [65, 67-68] showed attractive results for the production of higher carbon number products via electrochemical CO_2 reduction. In a C_2H_5OH:H_2O (8:2) system at -20 °C with electrolysis at -1.75 V vs Ag/Ag^+, this complex produced $OHCCO_2H$ (glyoxylic acid) and $HOCH_2CO_2H$ (glycolic acid) in addition to CO, HCO_2H, HCHO, and CH_3OH [see Scheme 1.5]. It is interesting that electrolysis of this complex at room temperature produced only CO, HCO_2H, H_2, and traces of CH_3OH as the electrocatalytic products. The formation of $[Ru(bpy)(\mathbf{terpy})(CHO)]^+$ was believed to be the key step for the production of these multi-electron reduction products.

According to their report, low temperature could be a factor for the possible formation of four- and six-electron products, which in turn could be related to the formation of a stable M–CO adduct and its subsequent conversion to products [see Scheme 1.5]. In addition, the nature of the catalyst could be the another possibility for the formation of these multi-electron products, because of the fact that a similar complex $Ru(bpy)_2(CO)_2$ did not produce the above mentioned products under same experimental conditions (same medium, temperature). These results suggest that in order to accomplish a multi-electron transfer reduction, the reductive cleavage of the Ru–CO bond should be suppressed.

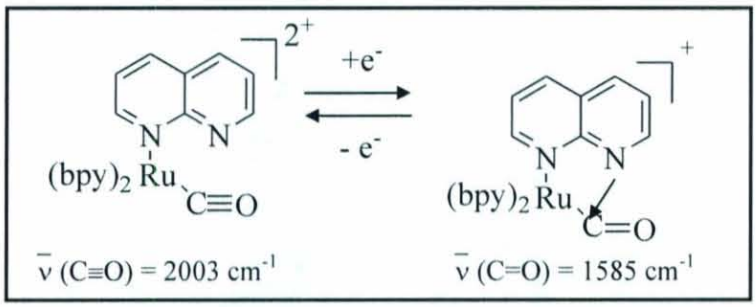

Scheme 1.6: Mechanism for metallacyclization on electrochemical reduction of CO_2 by $[Ru(bpy)(\mathbf{napy})_2(CO)_2]^{2+}$. Reproduced with permission from *Angew. Chem.*, 2005, 117, 2269 [74]. Copyright © 2005 Wiley-VCH Verlag GmbH & Co. KGaA.

The introduction of a naphthylpyridine (**napy**) ligand in $[Ru(bpy)(\mathbf{napy})_2(CO)_2]^{2+}$ [69-74] shows evidence of the production of a stable Ru–CO bond by forming a five-membered ring [see Scheme 1.6] and thus creates a possible new pathway for CO expulsion towards products. The formation of this "electroinduced metallacyclization" would possibly suppress the reductive cleavage of the Ru–CO bond and thereby influence the selective formation of ketone in the presence of a methylating agent. Electrochemical reduction of CO_2 by this complex selectively produced acetone via the formation of a Ru-$COCH_3$ complex upon two-electron reduction in DMSO in the presence of $(CH_3)_4NBF_4$. $(CH_3)_4N^+$ was believed to act as a methylating agent here and the current efficiency was found to be increased up to 70% at 100 °C. Thus, the use of the **napy** ligand as an electron reservoir also led to an excellent performance for the CO_2 reduction.

On the other hand, Meyer and coworkers have found that cis-$[Rh(bpy)_2X_2]^+$ (X is Cl or OTf) were able to reduce CO_2 at -1.55 V vs SCE to produce formic acid as the main

product with faradaic efficiencies of up to 64% [75]. However, for the $[M(bpy)_2(CO)H]^+$ (M = Os, Ru) system, the faradaic efficiency for formate production was only 25% (under "wet" conditions) and in anhydrous conditions, CO was the major product [76].

1.3.3.3 Ru complexes with bpy ligands

Very few electrocatalysts have been found under the criteria of Ru complexes with bpy ligands. Electrochemical reduction by $[Ru(bpy)_2\mathbf{L}]^{2+}$ (where, **L** = bpy or 2- pyridyl-1-methyl benzimidazole) did not produce any appreciable activity (in the CV in CH_3CN) towards CO_2 reduction. According to Tanaka et al. [77], these complexes are not able to reduce CO_2 under controlled potential electrolyses in CH_3CN (both aqueous and anhyderous conditions) even at -1.80 V.

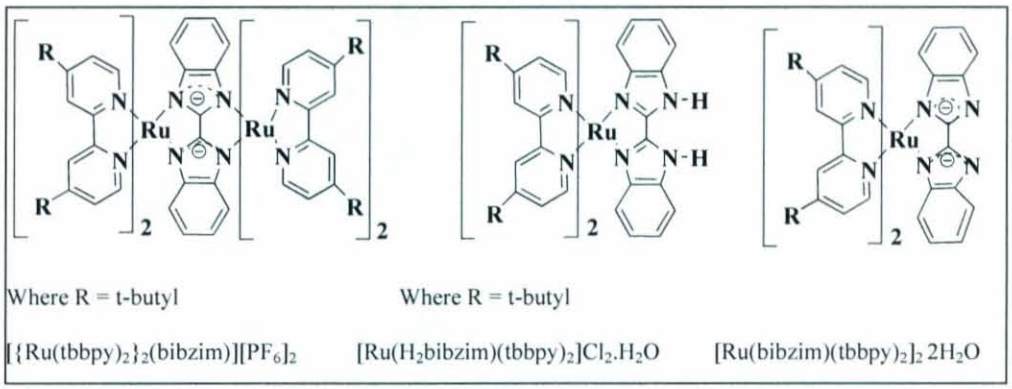

Scheme 1.7: Structures of some of Tanaka's electrocatalysts. Reproduced with permission from *Dalton Trans.* 2000, 3649 [78]. Copyright © 2000 Royal Society of Chemistry.

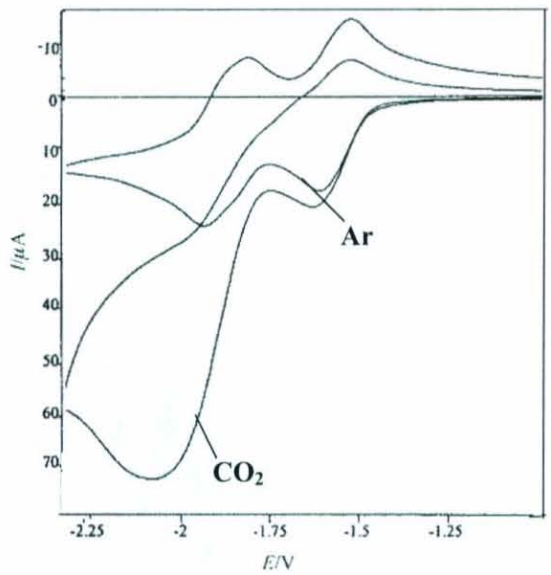

Figure 1.5: Cyclic voltammogram of $[\{Ru(\mathbf{tbbpy})_2\}_2(\mathbf{bibzim})][PF_6]_2$ in acetonitrile under an Ar atmosphere (upper) and under a CO_2 (lower) atmosphere. Reproduced with permission from *Dalton Trans.* 2000, 3649 [78]. Copyright © 2000 Royal Society of Chemistry.

In contrast, electrochemical reduction of CO_2 by $[Ru(\mathbf{H_2bibzim})(\mathbf{tbbpy})_2]Cl_2 \cdot H_2O$ (**H_2bibzim** = bibenzimidazole; **tbbpy** = 4,4′-di-*tert*-butyl-2,2′-bipyridine) [78] [see Scheme 1.7] produced CO (1-2%) and oxalate (up to 10%), while the deprotonated complex, $[Ru(\mathbf{bibzim})(\mathbf{tbbpy})_2]_2 \cdot 2H_2O$, produced oxalate with a current efficiency of 43% and some CO (1-2%) as well. The possible mechanism for catalytic activity of this complex was not clarified. However, it was reported that the protonated complex showed lower activities compared to that of the deprotonated one [see Figure 1.5].

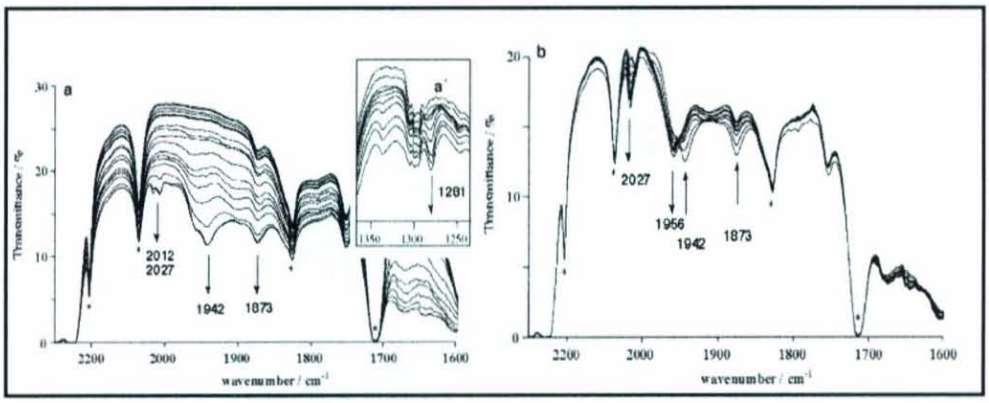

Figure 1.6: IR spectra of [RuL-(**napy-κ²N,N″**)(dmso)](PF$_6$)$_2$ under controlled potential electrolysis in CH_3CN ((a) and (b)) or CD_3CN (a′): (a) The potential was swept from -0.95 to -1.44 V; (b) The potential was swept from -1.44 to -0.95 V (vs Fc/Fc^+). *denotes CH_3CN peaks. Reproduced with permission from *J. Org. Chem.* 2005, 690, 4272 [79]. Copyright © 2005 published by Elsevier Science B.V.

Tanaka and coworkers first reported that the complex [RuL-(**napy-κ²N, N″**)(dmso)](PF$_6$)$_2$, (where, L= N″-methyl-4′-methylthio-2,2′:6′,4″-terpyridinium) is useful for the direct observation of Ru–CO complex formation by the electrochemical reduction of a CO-free ruthenium complex in a CO_2-saturated solution [79]. In the presence of CO_2, upon electrolysis at -1.44 V vs Fc/Fc^+ in CH_3CN, this complex was found to form Ru-(η^1–CO_2) and Ru–CO complexes, as observed by in-situ IR spectroscopy. On the other hand, electrolysis at -1.55 V vs Fc/Fc^+ in DMF/0.1 M Me_4NBF_4 selectively produced CO (current efficiency of 35%) with a small amount of HCO_2H (2%) at room temperature.

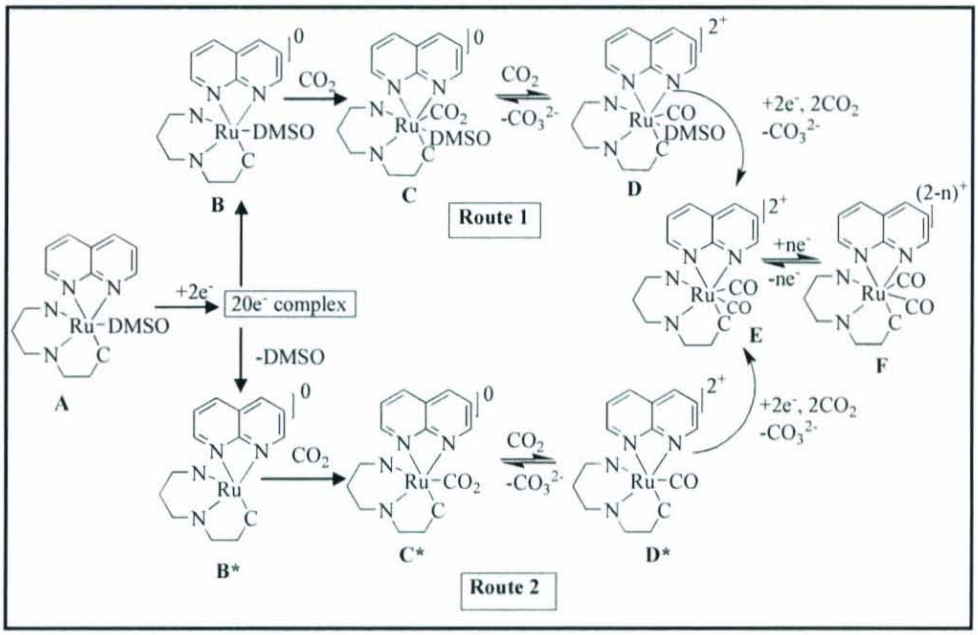

Scheme 1.8: Possible mechanism for formation of Ru-(η^1–CO_2) and Ru–CO complexes by [RuL-(**napy-κ^2N,N''**)(dmso)]$(PF_6)_2$ in CO_2-saturated solution. Reproduced with permission from *J. Organomet. Chem.* 2005, 690, 4272 [79]. Copyright © 2005 published by Elsevier Science B.V.

According to the report, upon controlled potential electrolysis at -1.44 V (vs Fc/Fc^+), this complex produced two important IR bands at 1873 and 1942 cm^{-1} mainly due to ν(C≡O) for the formation of a Ru–CO complex (see Figure 1.6). These bands were found to be shifted to 1956 and 2027 cm^{-1} respectively upon reoxidation at -0.95 V vs Fc/Fc^+ which would indicate that species **E** or **F** (see Scheme 1.8) were generated at a potential of -1.44 V. Two possible routes for the formation of **E** and **F** are shown in

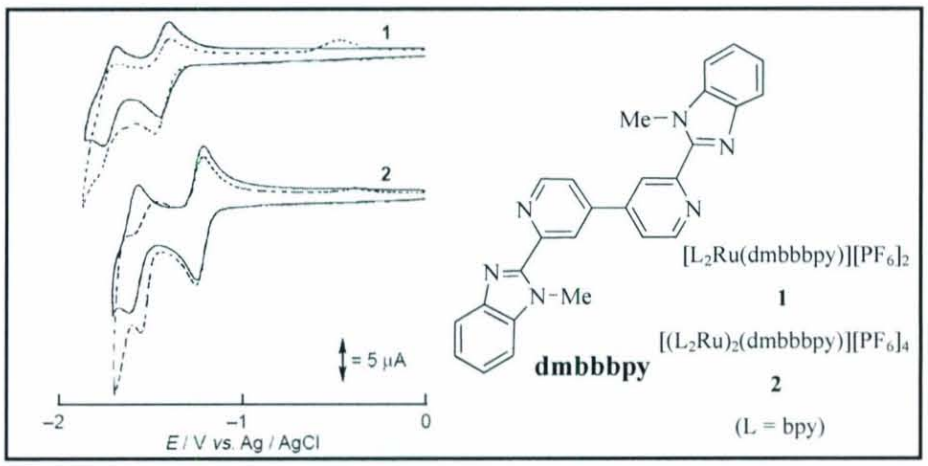

Figure 1.7: Structures and cyclic voltammograms of $[(bpy)_2Ru(\mathbf{dmbbbpy})][PF_6]_2$ and $[\{(bpy)_2Ru\}_2(\mathbf{dmbbbpy})][PF_6]_4$ (0.3 mM) in 0.1 M Bu_4NBF_4/MeCN at a glassy carbon electrode, under N_2 (——) and CO_2 (------) (scan rate = 50 mV/s). Reproduced with permission from *Chem. Commun.* 1998, 249 [77]. Copyright © 1998 Royal Society of Chemistry.

Scheme 1.8. However, two reversible ligand-based redox couples at -2.0 V for this complex confirms an intact DMSO ligand with the Ru centre and it was concluded that the dechelation of **napy** would be the favorable pathway for the formation of these complexes (**E** or **F**).

Tanaka et al. [77] reported that electrochemical CO_2 reduction by $[(bpy)_2Ru(\mathbf{dmbbbpy})][PF_6]_2$ and $[\{(bpy)_2Ru\}_2(\mathbf{dmbbbpy})][PF_6]_4$ [see Figure 1.7] (dmbbbpy = 2,2′-bis(1-methylbenzimidazol-2-yl)-4,4′-bipyridine) can selectively produce formate and oxalate as the main products as well as a negligible amount of CO.

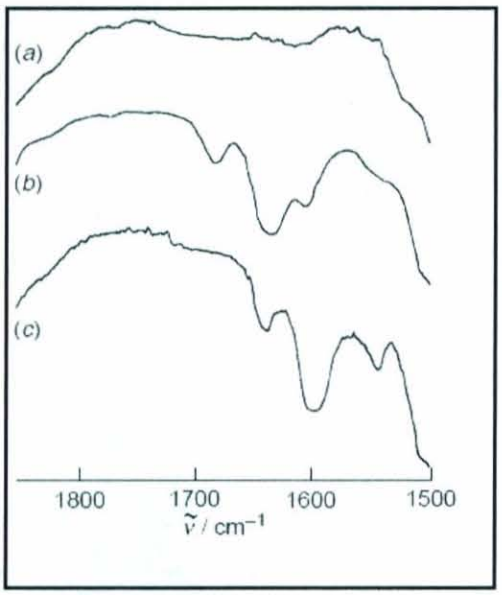

Figure 1.8: IR spectra of $[(bpy)_2Ru(\mathbf{dmbbbpy})][PF_6]_2$ (0.8 mM) during thin-cell bulk electrolysis in CD_3CN with $LiBF_4$ (*a*) starting scans, (*b*) using $^{12}CO_2$, (*c*) using $^{13}CO_2$. Reproduced with permission from *Chem. Commun.* 1998, 249 [77]. Copyright © 1998 Royal Society of Chemistry.

The faradaic efficiency for the formation of formate for the monometallic complex was reported to be around 89% (electrolysis potential at -1.65 V vs Ag/AgCl) with a trace amount of CO (2–3%) under aqueous conditions. On the other hand, oxalate was produced with a faradaic efficiency of up to 64% under "dry" conditions. Whereas, for the bimetallic ruthenium complex, formate was produced with a faradaic efficiency of up to 90% (electrolysis potential at -1.55 V vs Ag/AgCl) under aqueous conditions and oxalate was produced with a faradaic efficiency of up to 70% under "dry" conditions.

The reactions described above were monitored by in-situ IR spectroscopy [see

Figure 1.8] in order to reveal the electrocatalytic pathways of formation of products. The reductive electrolysis of $[(bpy)_2Ru(\mathbf{dmbbbpy})][PF_6]_2$ at -1.65 V vs Ag/AgCl produced three bands at 1684, 1633 and 1603 cm^{-1} [see Figure 1.8 (*b*)] in CO_2-saturated CD_3CN solution. The 1633 cm^{-1} band was assigned to $C_2O_4^{2-}$ which remained unchanged upon reoxidation at -0.70 V and under similar electrolysis conditions using $^{13}CO_2$ [see Figure 1.8 (*c*)]. Thus, the authors proposed that dechelation of **dmbbbpy** ligand was a possible way to generate oxalate rather than by dimerization of free $CO_2^{\bullet-}$ [77]. In the process of two-electron reduction of both complexes, a five-coordinate Ru centre could be formed and create reaction sites for CO_2 to attack at the Ru centre. The monodentate **dmbbbpy**$^-$ could then possibly provide two binding sites for an attack of CO_2 and allow a coupling reaction of CO_2 to oxalate. However, the faradaic efficiencies for the formation of $C_2O_4^{2-}$ and HCO_2^- by both complexes depend upon the presence and absence of water in acetonitrile.

1.4 Ruthenium chemistry

The chemistry of ruthenium complexes has received continuous attention for many decades due to its excellent electron transfer properties. It has an extensive range of oxidation states (-2 to +8), which are electrochemically accessible and thus offer their use as redox active reagents in various chemical reactions [80]. Ruthenium complexes with polypyridyl ligands have been frequently used in electron and energy-transfer reactions, especially electrochemical energy conversion to fuels (e.g., through CO_2 electroreduction), in various molecular electronic device applications (e.g., charge

separation devices for photochemical solar energy conversion), and information storage devices [81]. Considering these important applications, species (e.g., ligands) that control photophysical properties and redox behaviour are of particular interest to the materials chemists. That is why a rational design of ligands that would impart desired properties such as absorption energies and redox potentials to the complexes is very important.

Transition metal complexes with multiple metal centres are important to facilitate multi-electron transfer that would essentially produce highly reduced species [82]. The special interest in ruthenium polypyridyl based complexes, including bimetallic complexes here is that some of these complexes are able to effectively catalyze the electrochemical CO_2 reduction [77-78]. It is very interesting to use bimetallic complexes to attempt to produce HCOOH or CO via concerted two-electron processes. In order to better understand the mechanisms of the CO_2 electoreduction catalyzed by bimetallic ruthenium polypyridyl complexes, it is important here to discuss the effect of ligands and electronic interactions between the metal centres.

1.4.1 Bimetallic Ru complexes and superexchange

Mixed-valent metal complexes with various bridging ligands have been of special interest for various molecular designs (e.g., molecular electronic devices) since the early 1990s. Bridging ligands within polymetallic Ru complexes have important effects in mediating the electronic communication and delocalization between metal centers.

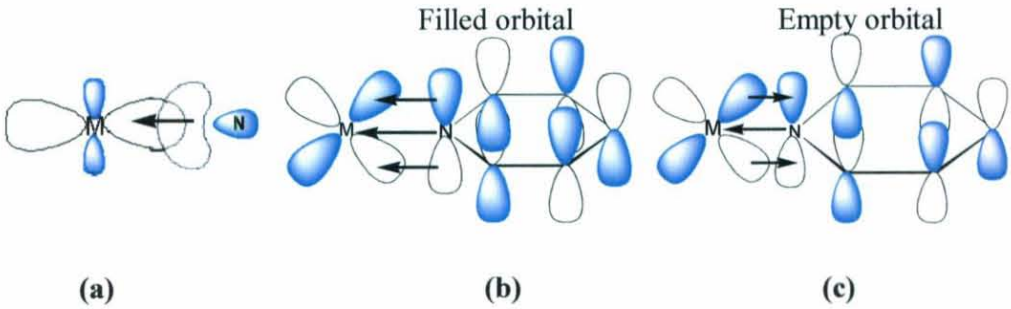

(a) **(b)** **(c)**

Figure 1.9: Overlap between: (a) a σ-donor bond of a ligand and the d_z^2 or $d_{x^2-y^2}$ orbital of a metal and (b) π-donation from a ligand's π orbital to a d_{xy}, d_{xz} or d_{yz} orbital of the metal (c) back donation or back bonding from a metal to a ligand via overlap of a metal based d_{xy}, d_{xz} or d_{yz} orbital and a ligand π* orbital. Reproduced with permission from *Coord. Chem. Rev.* 2006, 250, 1653 [85]. Copyright © 2006 published by Elsevier Science B.V.

In the case of a π-acceptor ligand, it has filled π and empty π* orbitals. Bonding with metals (t_{2g}) for this type of ligand is usually "synergic", that is, upon σ-donation to the metal, electron density on the metal increased [see Figure 1.9], which allows increased π-back donation from metal to the ligand [83]. On the other hand, electron density on the metal decreases upon π-back donation and permits more σ-donation from the ligand to the metal (increased electron density on metal). In addition to this, a π-donor ligand has a filled orbital with π symmetry and lies in lower energy level than the partially filled metal's d orbital. Pyridine, pyrazine, and pyrimidines are the example of some known π-acceptor ligands for their low-lying π* LUMO orbitals, whereas imidazole ligands are better π-donors and poor π-acceptors [84]. The importance of these

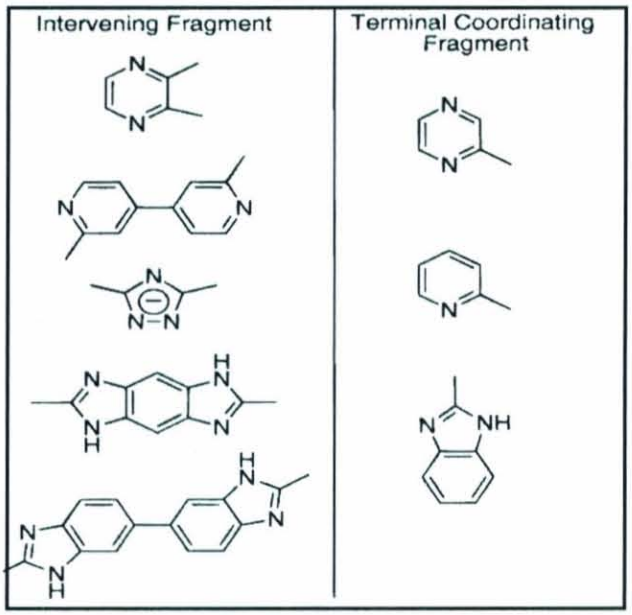

Figure 1.10: Terminal coordinating and intervening fragments for bimetallic ruthenium complexes. Reproduced with permission from *Inorg. Chem.* 1996, 35, 3335 [84]. Copyright © 1996 American Chemical Society.

ligands is that the appropriate combination (see Figure 1.10) of them could control the metal-metal distance and/or the donor/acceptor properties of the bridging ligands in bimetallic/polymetallic metal complexes.

There are some important factors required for the formation of mixed-valence bimetallic complexes, such as electronic interaction between mixed-valence states, the electron transport processes between metal centers, and the stability of the mixed-valence state. Haga et al. [84] reported that electronic coupling between acceptor-donor metal centers, solvent polarities and the free energy of the reaction are important parameters

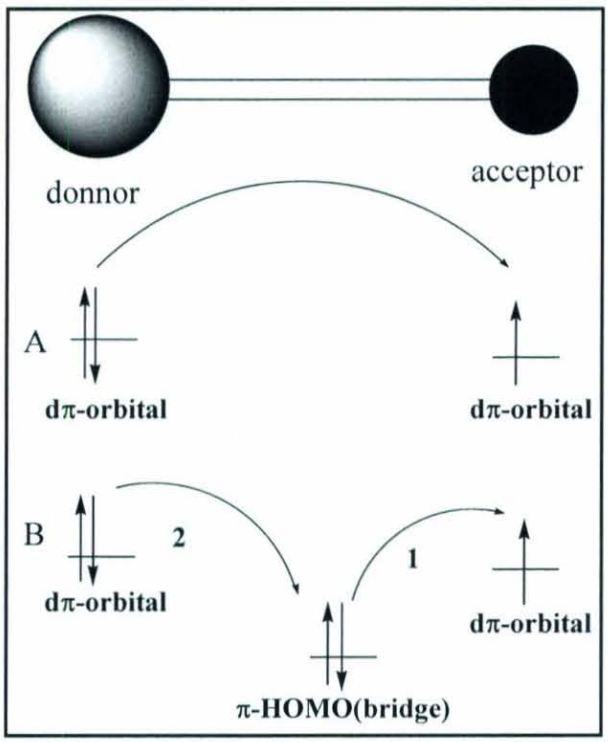

Figure 1.11: Mechanisms for electron transfer between metal sites in bimetallic complexes. Reproduced with permission from *J. Organomet. Chem.* 2008, 693, 793 [86]. Copyright © 2008 published by Elsevier Science B.V.

which can influence the intramolecular electron transfer in mixed-valence metal complexes. Figure 1.11 describes two types of possible electronic interactions between metal centres in bimetallic metal complexes. For example, during the intramolecular electron transport processes, the first pathway [path **A**] the dπ-dπ interaction between two metal centers is by an outersphere electron transfer processes. On the other hand, the second pathway [path **B**], where the electron transfer occurs through the bridging ligand,

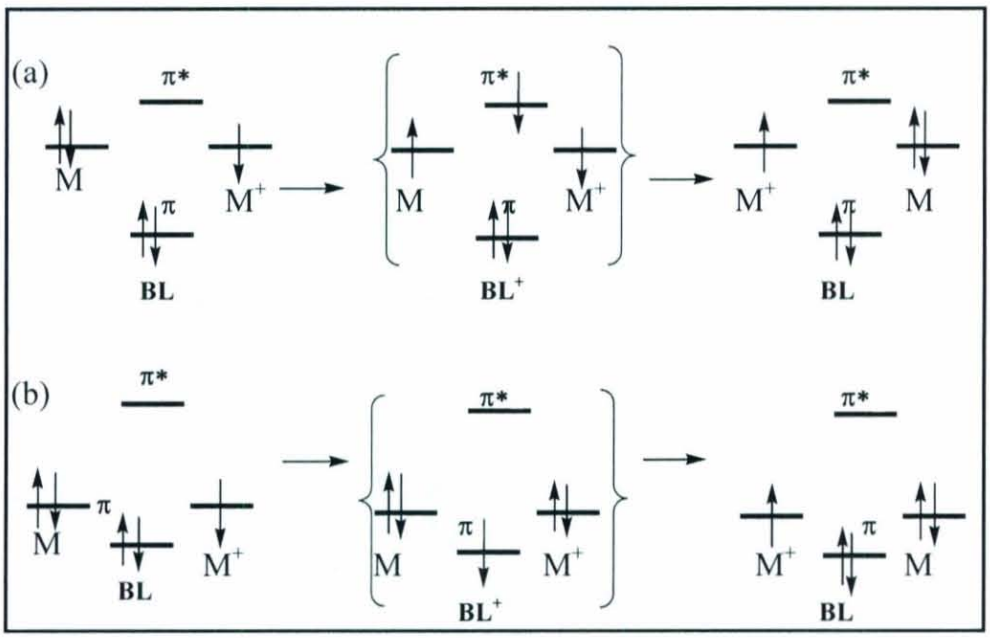

Figure 1.12: (a) LUMO and (b) HOMO bridging ligand assisted superexchange. Reproduced with permission from *Coord. Chem. Rev.* 2006, 250, 1653 [85]. Copyright © 2006 Published by Elsevier Science B.V.

is known as a superexchange pathway. According to Pickup et al. [87], during the superexchange processes, both relative energy levels (metal dπ's and ligands π/π* orbitals) and the absolute energy gap between the metal and the bridging ligands orbitals are important factors that influence the leading pathway of a superexchange process. Figure 1.12 represents HOMO and LUMO type superexchange processes. In the electron type superexchange mechanism, the electron transfer occurs via the LUMO π* orbital (low energy) of the bridging ligand to Ru dπ orbitals. On the other hand, for the hole type

superexchange, the positive charge (hole) is transfered through the HOMO π orbital (higher energy) of the bridging ligand to Ru dπ orbitals. Thus, increasing the bridging ligand's HOMO energy usually favors the hole type superexchange by creating a stronger interaction with the Ru dπ orbitals than for the LUMO π* orbital [88]. Ruzic et al. [89] have proposed a general theory for this type of multistep charge transfer at electrodes.

The stability of the intervalence state of the bimetallic complex might be affected by electron delocalization and superexchange interactions (both electron and hole) [90] and could be determined from the comproportionation constant (K_c) [Equations 7-10]. A bimetallic complex with equivalent redox sites and $\Delta E^{\circ}_{ox} = 0$, the value of K_c should be ca. 4 and usually indicates an unstable intervalence state [90-91]. A different scenario occurs when two metal centers interact electrostatically and/or through delocalization: the value of K_c increases and a stable intervalence state emerges. K_c can be related to the thermodynamic parameters and its value can be calculated from electrochemical data as shown in equations 9 and 10.

$$Ru^{II}Ru^{II} + Ru^{III}Ru^{III} \underset{K_c}{\leftrightarrow} 2Ru^{II}Ru^{III} \quad \text{.....(7)}$$

$$\underset{\text{Red}}{M^n\text{-L-}M^n} \overset{-e^-}{\underset{(E_1)}{\leftrightarrow}} \underset{\text{Int}}{M^n\text{-L-}M^{n+1}} \overset{-e^-}{\underset{(E_2)}{\leftrightarrow}} \underset{\text{Ox}}{M^{n+1}\text{-L-}M^{n+1}} \quad \text{.....(8)}$$

$$K_c = \frac{[\text{Int}]^2}{[\text{Red}][\text{Ox}]} \quad \text{.....(9)}$$

$$K_c = \exp[(\Delta E_{ox}/\text{mV})/25.69] \quad \text{.....(10)} \quad (\text{at } 298 \text{ K}; \Delta E_{ox} = E^{\circ}_2 - E^{\circ}_1)$$

1.4.2 Review of a number of bimetallic Ru complexes

Since a number of ruthenium based polypyridyl bimetallic complexes were studied in this thesis work (as electrocatalysts), it is important and relevant here to discuss the mechanism of electron transport system proposed for each system. The first series of bimetallic complexes used here is composed of pyrazine–bridged systems. In 1969, the first pyrazine-bridged mixed-valence complex, $[\{(NH_3)_5Ru\}_2(pz)]^{5+}$, known as the "Creutz–Taube" ion (CT ion) was reported [see Figure 1.13]. In fact, this is a well studied model bimetallic complex for the investigation of electron transfer processes and metal-metal interactions [92].

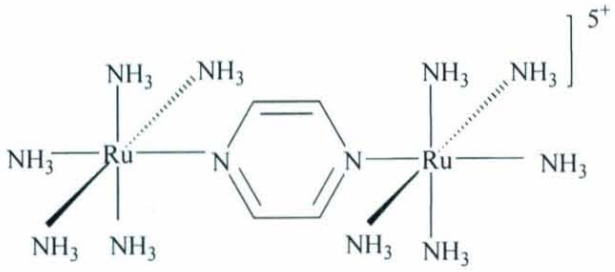

Figure 1.13: The Creutz–Taube ion [91].

The CT ion has the general properties of a large separation between the two oxidation states (ΔE° = 360 mV) with $K_c \approx 10^7$, and an intervalence charge transfer state absorption band at around 1570 nm [85]. Due to the large value of ΔE° and low lying π^* LUMO energy for the pyrazine-bridge system, the electronic interaction between the two

metal centers follows a LUMO type superexchange pathway. Changing the peripheral ligands has an effect on the metal-metal interaction (by perturbation of internuclear interaction in the Ru(II) Ru(III) state). For example, if one of the NH_3 ligands of the CT ion is replaced by H_2O there is a small shift in the IT band (1530 nm), while replacement of NH_3 by Cl^- (1450 nm) or a pyrazine ligand (1160 nm) causes a significant shift of the IT band to the higher energy region. A shift of the IT band to even higher energy is caused if the substitution of monodentate "NH_3" groups occurs with Cl^- (960 nm), NO_2^- (790 nm) and CH_3CN (750 nm) [93]. Another CT ion analogue, $[\{(bpy)_2ClM\}_2(\mu\text{-pyrazine})]^{2+}$ (M = Ru, Os) was reported by Meyer and coworkers [94]. The degree of electron delocalization for this metal complex was smaller with a value of $\Delta E° = 120$ mV and the IT band was at 1300 nm. Both of the complexes show poor stability of the fully oxidized species with decomposition [95]. The similar $[\{(bpy)_2ClRu\}_2(pyrimidine)]^{2+}$, which exhibited $\Delta E° = 120$ mV with the IT band at about 1360 nm, also shows instability of the fully oxidized species followed by decomposition [96].

When the bridging pyrazine unit of the CT ion was modified by 2,3- or 2,5-substituents of the pyrazine-bridging units, the groud state properties of the CT ion were found to change. For example, $[\{(bpy)_2Ru\}_2(2,3\text{-dpp})]^{4+}$ and $[\{(bpy)_2Ru\}_2(2,5\text{-dpp})]^{4+}$ [dpp = bis(2-pyridyl)pyrazine] are two important derivatives of pyrazine type ligands and have been studied extensively for intercomponent interactions of the redox states of the bridging ligand. Both 2,3-dpp and 2,5-dpp bridging ligands produce strong π-acceptor ligand characteristics [97]. A LUMO based superexchange mechanism is proposed for

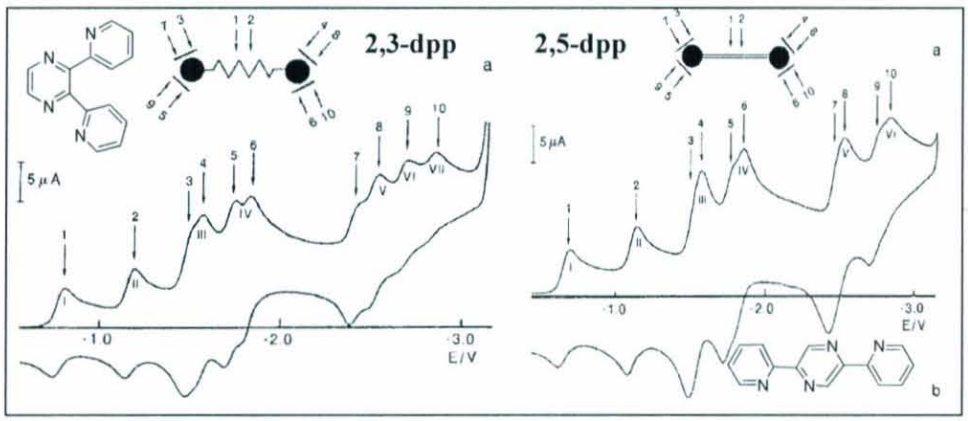

Figure 1.14: Cyclic voltammograms for a 0.5 mM $[\{(bpy)_2Ru\}_2(2,3\text{-dpp})]^{4+}$ and $[\{(bpy)_2Ru\}_2(2,5\text{-dpp})]^{4+}$, 0.05 M Et_4NBF_4/DMF solutions. Working electrode Pt; T = -54 °C; scan rate 0.1 V/s. Reproduced with permission from *J. Am. Chem. Soc.* 1999, 121, 10081 [97]. Copyright ©1999 American Chemical Society.

these pyrazine-bridged, ruthenium-based polypyridyl complexes, similar to the Creutz–Taube ion [98]. Figure 1.14 illustrates the cyclic voltammetry for $[\{(bpy)_2Ru\}_2(2,3\text{-dpp})]^{4+}$ and $[\{(bpy)_2Ru\}_2(2,5\text{-dpp})]^{4+}$. It was suggested that the first two reduction peaks are due to the LUMO of the bridging ligand and the 3rd and 4th peaks are due to the sequential reduction of two bpy ligands of each metal center.

Another series of bimetallic and polymetallic ruthenium complexes bridged by imidazole/benzimidazole ligands have received considerable attention due to the possibility of using them in molecular electronic devices, electrocatalysts, etc. Numerous studies have been conducted in this field by Haga et al. [77, 81, 84, 99] [see Figure 1.15]. As imidazole/benzimidazole containing ligands are poor π-acceptors and good π-donors,

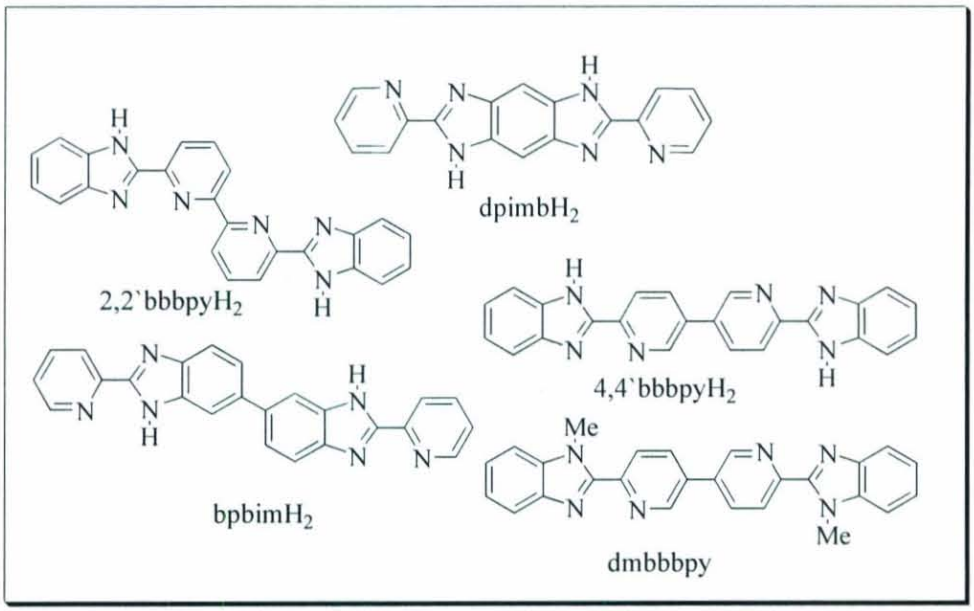

Figure 1.15: Examples of some imidazole/benzimidazole based ligands for bimetallic ruthenium complexes from Haga's papers [77, 81].

because of having imino N-H proton, they have the ability to control orbital energies by proton transfer. When a benzimidazole unit is coordinated to a metal ion, the imino N-H proton of the imidazole ring becomes more acidic and can be easily removed. Usually deprotonation of the intervening groups in the Ru bimetallic complex causes an increase in the Ru–Ru interaction for the mixed-valence Ru^{II}–Ru^{III} state (see Figure 1.16). Upon protonation/deprotonation of these complexes, large changes of molecular orbital energies occur, particularly for the HOMO and LUMO energies.

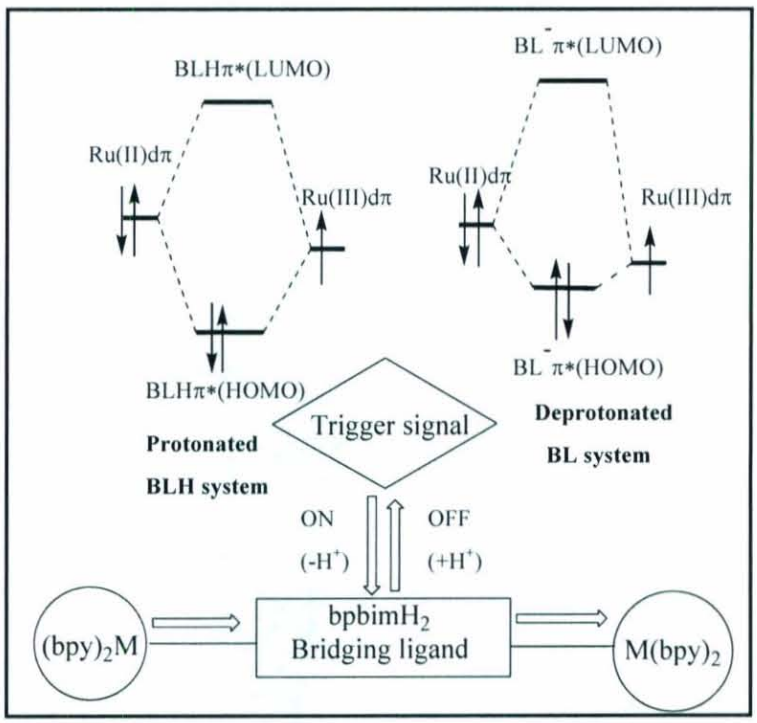

Figure 1.16: A molecular switching device: proton transfer acts as a trigger signal Reproduced with permission from *Inorg. Chem.* 1991, 30, 3843 [81]. Copyright ©1991 American Chemical Society.

1.5 Objectives of the thesis work

The main aim of this PhD research was the development of a novel catalytic system that can effectively reduce CO_2 and produce important chemicals that could be eventually used as fuels for alternative energy sources or non-fossil chemicals. Benzimidazole and benzothiazole-based monometallic and bimetallic ruthenium complexes were employed here to explore ligand effects on electrochemical CO_2 reduction. The effects of the extended π conjugation, different substituents (S, Me, H) on the

benzimidazole/benzothiazole ligands and the donor or acceptor (σ, π) properties of the ligands were also investigated for effective CO_2 reduction under electrochemical conditions.

The long term goal of this work is the development of an effective electrocatalyst that can reduce CO_2 at low positive potentials such as at -1.0 V vs SCE or even better that could generate useful fuels/chemicals such as, MeOH and HCOOH. Direct methanol fuel cells have already been well developed and direct formic acid fuel cells are currently under development in Canada by Tekion. Electrochemical CO_2 reduction has huge potential benefits for the production of liquid fuels, and more importantly by consumption of a greenhouse gas. In short the use of ruthenium polypyridyl complexes as catalysts for electrochemical CO_2 reduction have several advantages:

1. Ruthenium polypyridyl complexes of benzothiazole and benzimidazole ligands (**L**) exhibit reversible electrochemistry under N_2, which in the presence of CO_2 might change (e.g., in cyclic voltammetry) and could provide valuable information on CO_2 activation processes.
2. Use of different substituents on the ligands with the same metal (Ru) centres and observation of different activities for electrochemical CO_2 reduction will help in determining the mechanistic pathways of the electrocatalytic processes.
3. Ruthenium polypyridyl complexes are well-known electrocatalysts for the effective formation of formic acid and methanol, along with a number of other products, during electrochemical CO_2 reduction [10].
4. Among the different types of Ru based polypyridyl complexes, very few

$[Ru(L)(bpy)_2]^{2+}/[\{(bpy)_2Ru\}_2(L)]^{4+}$ type molecular catalysts have been studied as electrocatalysts for CO_2 reductions. So studying the structure-activity-relationships (S-A-R) of these types of complexes with a variety of organic ligands could pave the way for a so-called "magic" electrocatalyst for CO_2 reduction.

Organic ketones have also been exploited to reduce CO_2. For this purpose fluorene-9-one has been chosen as one of the model compounds in this study. The main aims of this part of the project were -

a) To investigate the electrochemical reduction of **Fl** in the presence of CO_2.

b) To indentify products and elucidate subsequent mechanisms.

c) To investigate and quantify (faradaic efficiency) the products formed in the electrolysis of **Fl** under CO_2.

d) To investigate the effect of water on product distributions.

An overview and introduction of the electrochemical reduction of CO_2 by aliphatic and aromatic ketones is given in detail in Chapter 5.

Chapter 2

Synthesis and characterization of some monometallic and bimetallic ruthenium polypyridyl complexes

2.1 Instrumentation and starting materials

Benzothiazole and benzimidazole-based monometallic and bimetallic ruthenium polypyridyl complexes have been designed and synthesized to be used as electrocatalysts for CO_2 reduction. The ligands were synthesized by a general acid-catalyzed condensation reaction between a series of phenylenediamine derivatives and pyridine/pyrazine carboxylic acids. Finally, the metal complexes were synthesized by refuxing the ligands with the $Ru(bpy)_2Cl_2$ in aqueous ethanol/ethylene glycol. All the ligands and metal complexes were characterized by spectroscopic techniques including FTIR and ^1H NMR. Some of the structures of metal complexes were also confirmed by X-ray crystallography and are discussed in section 2.4.

Infrared spectra were obtained on a Bruker TENSOR 27 infrared spectrometer. This instrument has a spectral range of 7500 to 370 cm^{-1}. Infrared quality KBr (The Harshaw Chemical Co. Cleveland, Ohio) was used for making KBr disks for all of the compounds reported in this chapter. Spectra are reported as wavenumber (cm^{-1}) and appearence (br = broad, s= strong, vs = very strong, w = weak).

Mass spectra were obtained with an Agilent 1100 series LC/MSD chromatographic system equipped with an Atmospheric Pressure Ionization-Mass Spectrometer (API-MS). The MS can perform either electrospray (ESI) or atmospheric pressure chemical ionization (APCI) and positive or negative ions can be acquired. Both ESI-MS and APCI-MS analyses were performed with HPLC grade acetonitrile (Aldrich). Molecular ions and fragment ions are reported as *m/z* (molecular ion peak) at a

fragmentation voltage of 70 eV. MALDI TOF MS analyses were carried out at the Genomics and Proteomics (GaP) Facility, Memorial University. As a matrix, α-cyano-4-hydroxycinnamic acid (10 mg/mL) in H_2O was used together with each metal complex (1 mg/mL) in CH_3CN.

^1H NMR spectra were obtained using a Bruker Avance 500 instrument equiped with an inverse detect ion gradient probe at 500 MHz and a Tecmag Apolo 300 MHz instrument. Acetonitrile-d_3 (Aldrich, 99.99 atom % D) and trifluoroacetic acid-*d* (Aldrich, 99.50 atom % D) were used as NMR solvents. Chemical shifts were reported in ppm relative to TMS, calculated by using the solvent peak for both CD_3CN (δ = 1.93 ppm) and TFA-*d* (δ = 11.5 ppm) as internal standards. For all spectra, peaks are reported as chemical shift, δ (ppm), multiplicity (s = singlet, d = doublet, dd = doublet of doublets, ddd = doublet of doublet of doublets, dt = doublet of triplets, t = triplet, m = multiplet) and relative integration ratio. Coupling constants are reported in Hz. Data processing was accomplished with the MestReNova software package.

Elemental analyses for the complexes were performed by Canadian Microanalytical Services, 207-8116 Alexander Road, RR # 7, Delta, BC, V4G 1G7.

X-Ray crystal structure determination and data workup for metal complexes was performed by Dr. Louise N. Dawe, C-CART, Memorial University.

Starting materials, such as polyphosphoric acid (PPA), 2,5-pyrazinedicaboxylic acid (for ligands) and $Ru(bpy)_2Cl_2 \cdot 2H_2O$ (for metal complexes) were prepared according

to the methods reported by Dr. Colin Cameron [100]. For purification of metal complexes, size exclusion chromatography was performed using Sephadex™ LH-20 (Sigma Aldrich).

2.2 Preparation of ligands

2.2.1 1-Methyl-2-(pyridin-2-yl)-1H-benzo[d]imidazole [Me-pybim]

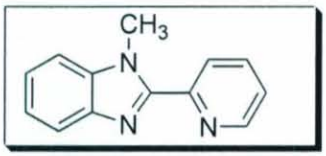

Picolinic acid (0.61 g, 5.0 mmol), N-methyl-1,2-phenylenediamine (0.61 g, 5.0 mmol) and PPA (7.0 g) were heated and stirred together under N_2 at 160 °C for 8 h. The resulting viscous, reddish solution was cooled and poured into 200 mL deionized water and stirred. The purple solution was then neutralized by adding Na_2CO_3 and the product was extracted into diethyl ether. The organic phase was dried with anhydrous $MgSO_4$ and evaporation of the solvent gave dark brown crystals (1.09 g, 95%) of 1-methyl-2-(pyridin-2-yl)-1H-benzo[d]imidazole. FTIR (KBr cm^{-1}): 3443 (br), 3047 (s), 2947 (w), 1891 (s), 1613 (s), 1590 (s), 1565 (s), 1471 (s), 1447 (s), 1424 (s), 1383 (s), 1278 (w), 1090 (w), 1068 (w), 796 (vs), 742 (vs). ^{1}H NMR (500 MHz, CD_3CN) δ 8.74 (d, J = 4.0 Hz, 1H), 8.35 (d, J = 8.0 Hz, 1H), 7.95 (t, J = 6.9 Hz, 1H), 7.75 (d, J = 7.9 Hz, 1H), 7.57

(d, J = 8.1 Hz, 1H), 7.50 – 7.43 (m, 1H), 7.38 (t, J = 7.6 Hz, 1H), 7.32 (t, J = 7.6 Hz, 1H), 4.27 (s, 3H). APCI-MS (positive mode) *m/z* calculated for $C_{13}H_{11}N_3$, 209.2; found, 210.1 $(M+1)^+$.

2.2.2 2,5-Bis(1-methyl-1H-benzo[d]imidazol-2-yl)pyrazine [Me_2-pzbbim]

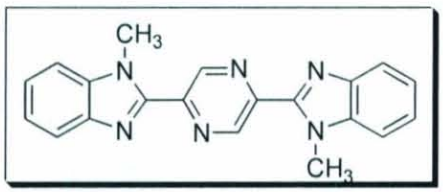

2,5-Pyrazinedicaboxylic acid (1.04 g, 6.20 mmol) and N-methyl-1,2-phenylenediamine (1.56 g, 12.8 mmol) were added to 28.0 g PPA at room temperature. The reaction was then warmed to 115 °C under N_2 and stirred for 24 h. P_2O_5 (3.4 g, 2.0 mmol) was added and the reaction was stirred at 140 °C for a further 72 h. Dilution of the resulting red solution with 150 mL of deionzed water produced a large quantity of green solid. The product 2,5-bis(1-methyl-1H-benzo[d]imidazol-2-yl)pyrazine was collected as a green powder by suction filtration and dried under vacuum (1.63 g, 110%). FTIR (KBr cm^{-1}): 3442 (br), 3064 (w), 2952 (w), 1723 (m), 1614 (m), 1587 (s), 1535 (s), 1476 (s), 1446 (s), 1425 (s), 1408 (m), 1384 (m), 1357 (s), 1335 (m), 1284 (s), 1255 (s), 1179 (s), 1006 (s), 930 (m), 902 (m), 816 (s), 742 (vs). ^{1}H NMR (500 MHz, TFA-*d*) δ 9.84 (s, 2H), 8.02 (d, J

= 8.3 Hz, 2H), 7.98 (d, J = 6.7 Hz, 2H), 7.94 – 7.87 (m, 4H), 4.60 (s, 6H). APCI-MS (positive mode) *m/z* calculated for $C_{20}H_{16}N_6$, 240.38; found, 241.20 $(M+1)^+$.

2.2.3 3,3′-dimethyl-2,2′-di(pyridin-2-yl)-5,6′-bi(3H-benzo[*d*] imidazole) [Me_2-py_2bbim]

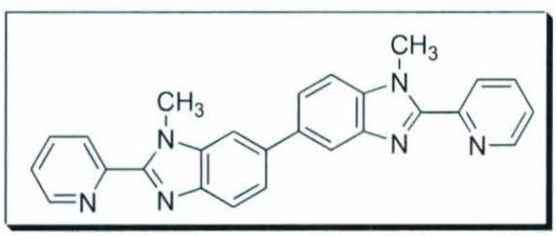

Picolinic acid (2.5 g, 2.0 mmol) and 3,3′-diaminobenzidine (2.1 g, 1.0 mmol) were added to 28 g PPA and stirred under N_2 at 175 °C for 7 h. The reaction mixture was then poured into 700 mL of H_2O and stirred vigorously for 1 h which produced a yellow powder that was filtered and washed with 100 mL of dilute aqueous $NaHCO_3$. The solid was recrystallized from methanol/water to give 2,2′-di(pyridin-2-yl)-5,6′-bi(3H-benzo[d]-imidazole as yellow crystals [83] (1.52 g, 40%). ^{1}H NMR (300 MHz, TFA-d)) δ 9.25 (d, J = 5.4 Hz, 2H), 9.03 (d, J = 8.0 Hz, 2H), 8.94 (t, J = 8.0 Hz, 2H), 8.45 – 8.37 (m, 2H), 8.32 (s, 2H), 8.20 (s, 4H). APCI-MS (positive mode) *m/z* calculated for $C_{24}H_{16}N_6$, 388.4; found, 389.2 $(M+1)^+$.

For methylation [101, 102] of 2,2′-di(pyridin-2-yl)-5,6′-bi(3H-benzo[d]imidazole,

CH_3I (0.71 g, 5.0 mmol) and NaOH (0.20 g, 5.0 mmol) in water (1.0 mL) were added dropwise and simultaneously to a stirred ice-cold solution of 2,2′-di(pyridin-2-yl)-5,6′-bi(3H-benzo[d]imidazole (0.97 g 2.5 mmol) in MeOH (6.0 mL). The solution was refluxed for 30 min and cooled to room temperature. A portion of 25 mL deionized water was added to the reaction mixture and the product was extracted into $CHCl_3$. The solution was dried over $MgSO_4$ and filtered. $CHCl_3$ was removed under reduced pressure to produce a yellow residue. The residue was re-dissolved in boiling petroleum ether (60-80 °C), treated with activated charcoal, filtered and then the petroleum ether was removed under reduced pressure. Concentrated HCl (10 M, 3.0 mL) was then added and the required product, 3,3′-dimethyl-2,2′-di(pyridin-2-yl)-5,6′-bi(3H-benzo[d]imidazole), was obtained as pale yellow crystals (0.24 g, 32%) following neutralization with NaOH and extraction into diethyl ether. FTIR (KBr cm^{-1}): 3444 (br), 2925 (w), 2853 (w), 1719 (m), 1620 (m), 1590 (s), 1542 (s), 1471 (s), 1446 (s), 1424 (s), 1408 (m), 1384 (s), 1284 (w), 1072 (w), 1042 (w), 794 (s). ^1H NMR (500 MHz, CD_3CN) δ 8.79 – 8.71 (m, 2H), 8.42 – 8.37 (m, 2H), 8.1 – 8.07 (m, 1H), 8.0 – 7.95 (m, 2H), 7.93 – 7.90 (m, 1H), 7.83 (t, J = 8.0 Hz, 1H), 7.80 – 7.74 (m, 1H), 7.74 – 7.69 (m, 1H), 7.69 – 7.63 (m, 1H), 7.51 – 7.45 (m, 2H), 4.36 (d, J = 6.3 Hz, 3H), 4.32 (d, J = 1.9 Hz, 3H). APCI-MS (positive mode) *m/z* calculated for $C_{26}H_{20}N_6$, 416.2; found, 417.2 $(M+1)^+$.

2.2.4 2-(Pyridin-2-yl)benzo[*d*]thiazole [pybtz]

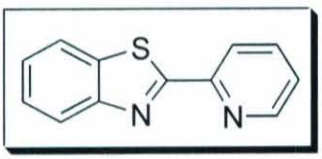

This preparation is based on Colin Cameron's PhD thesis [100] with some modifications. Picolinic acid (0.66 g, 5.4 mmol) and 2-aminothiophenol (0.66 g, 5.3 mmol) were added together to PPA (18 g) at 120 °C. The reaction was stirred under N_2 for 20 h at 160 °C. The mixture was cooled, added to water (400 mL) and neutralized slowly with NaOH, resulting as a pale yellow colored solid. The solid was recrystallized from MeOH to yield 2-(pyridin-2-yl)benzo[d]thiazole as pale yellow crystals (1.0 g, 90%). FTIR (KBr cm^{-1}): 3405 (s), 1725 (s), 1661 (s), 1584 (s), 1565 (s), 1510 (s), 1456 (s), 1433 (s), 1316 (s), 1293 (w), 1088 (w), 1042 (w), 783 (s), 740.^{1}H NMR (500 MHz, CD_3CN) δ 8.69 (d, J = 4.8 Hz, 1H), 8.38 – 8.33 (m, 1H), 8.07 (t, J = 8.0 Hz, 2H), 7.97 (td, J = 7.7, 1.7 Hz, 1H), 7.59 – 7.55 (m, 1H), 7.54 – 7.47 (m, 2H). APCI-MS (positive mode) *m/z* calculated for $C_{12}H_8N_2S$, 212.3; found, 213.1 $(M+1)^+$.

2.2.5 2,6′-Bis(2-pyridyl)-2,2′:6,2″-thiazolo[4,5-d]-benzothiazole [py_2tbtz] [103]

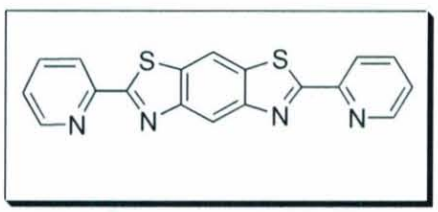

2,5-Diamino-1,4-benzenedithiol dihydrochloride (1.28 g, 5.30 mmol) was degassed at 130 °C under a stream of N_2 to effect dehydrochlorination which was completed through repeated cycles of evacuating the flask and flushing it with N_2. Picolinic acid (1.38 g, 11.2 mmol) was added at 120 °C and heated at 160 °C for 24 h. The solid was poured into 200 mL H_2O and the resulting yellow precipitate was collected. The precipitate was neutralized with dilute aq. $NaHCO_3$ and the resulting tan product was collected by suction filtration and then dried under vacuum (1.92 g, 106%). FTIR (KBr cm^{-1}/N_2): 3444 (br), 3050 (s), 2959 (w), 2927 (w), 1732 (m), 1684 (m), 1650 (s), 1584 (s), 1529 (s), 1456 (s), 1436 (s), 1399 (s), 1384 (s), 1317 (s), 1290 (s), 1275 (s), 1246 (s), 1092 (w), 997 (s), 980 (s), 884 (vs). ^1H NMR (500 MHz, TFA-*d*) δ 9.10 (d, J = 5.6 Hz, 2H), 9.05 (s, 2H), 8.91 (t, J = 7.9 Hz, 2H), 8.69 (d, J = 8.0 Hz, 2H), 8.34 – 8.28 (m, 2H). APCI-MS (positive mode) *m/z* calculated for $C_{18}H_{10}N_4S_2$, 346.4; found, 347.1 $(M+1)^+$.

2.2.6 2,5-Di(benzo[*d*]thiazol-2-yl)pyrazine [pzbbtz]

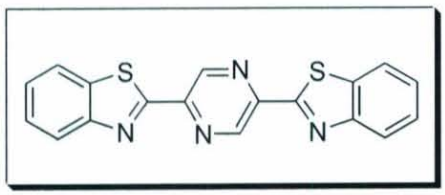

2-Aminothiophenol (2.90 g, 23.2 mmol) and 2,5-pyrazinedicarboxylic acid (1.81 g, 10.8 mmol) were stirred in PPA (28 g) under N_2 for 72 h at 165 °C. A further 6.1 g of P_2O_5 was added to the reaction mixture during this time to compensate for water of condensation. The dark green slurry was cooled and poured into 400 mL H_2O, and the resulting yellow precipitate was collected, stirred vigorously in methanol and again with dilute aqueous NaOH (during the course of which the precipitate became green). A large quantity of green solid was collected by suction filtration to give 2,5-di(benzo[*d*]thiazol-2-yl)pyrazine which was finally dried under vacuum (4.03 g, 108%). FTIR (KBr cm^{-1}): 3444 (br), 3058 (w), 1717 (m), 1617 (m), 1553 (s), 1523 (s), 1492 (s), 1451 (s), 1384 (s), 1359 (w), 1310 (s), 1250 (s), 1198 (s), 1176 (s), 1074 (s), 1030 (s), 979 (vs), 765 (vs). ^{1}H NMR (500 MHz, TFA-*d*) δ 9.88 (s, 2H), 8.44-8.39 (m, 4H), 8.11 (t, J = 7.8 Hz, 2H), 8.04 (t, J = 7.7 Hz, 2H). APCI-MS (positive mode) *m/z* calculated for $C_{18}H_{10}N_4S_2$, 346.4; found, 347.1 $(M+1)^+$.

2.2.7 2,5-Bis(1-methyl-1*H*-benzo[*d*]imidazol-2-yl)pyridine [Me_2-pybbim]

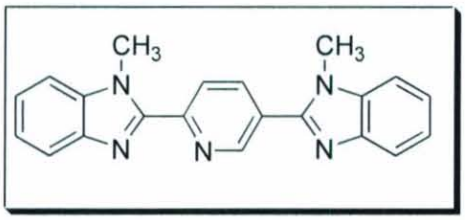

N-Methyl-1,2-phenylenediamine (0.61 g, 5.0 mmol) was added to 32 g PPA at 120 °C under N_2. The temperature was raised to 175 °C and 2,5-pyridinedicarboxylic acid (0.43 g 2.5 mmol) was added slowly over 5 d. When approximately one-half of the reagent had been added, more P_2O_5 (1.4 g, 10 mmol) was added to compensate for the water of condensation. Following addition of all the diacid, the reaction was allowed to stir for a further 2 d. The reaction mixture was then poured into 150 mL H_2O and stirred for 8 h giving a fine yellow solid, which was collected by suction filtration. This was stirred overnight in 200 mL of NaOH (0.5 M), and then filtered again to give a yellow solid. Finally the product was recrystallyzed from $CHCl_3$ as yellow crystals (0.39 g, 45%). FTIR (KBr cm^{-1}): 3444 (br), 3060 (w), 2929 (w), 1717 (m), 1620 (m), 1598 (m), 1593 (m), 1458 (s), 1429 (s), 1384 (s), 1326 (vs), 1279 (s), 1072 (w), 743 (vs). ^{1}H NMR (500 MHz, CD_3CN) δ 9.23 – 9.10 (m, 1H), 8.53 (t, J = 8.1 Hz, 1H), 8.37 (ddd, J = 8.0, 4.7, 2.1 Hz, 1H), 7.82 – 7.76 (m, 2H), 7.64 – 7.57 (m, 2H), 7.40 (ddd, J = 7.3, 3.3, 1.4 Hz, 2H), 7.35 (t, J = 7.1 Hz, 2H), 4.35 (s, 3H), 3.98 (s, 3H). APCI-MS (positive mode) *m/z*

calculated for $C_{21}H_{17}N_5$, 339.39; found, 340.1 $(M+1)^+$.

2.3 Preparation of complexes

2.3.1 [Ru(**Me-pybim**)(bpy)$_2$](ClO$_4$)$_2$

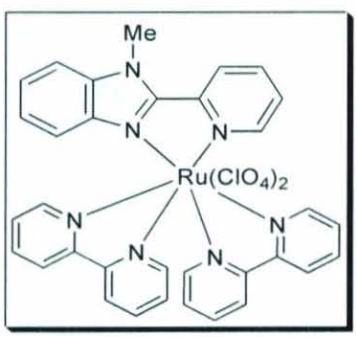

1-Methyl-2-(pyridin-2-yl)-1H-benzo[d]imidazole (Me-pybim) (0.0196 g, 0.0938 mmol) and $Ru(bpy)_2Cl_2 \cdot 2H_2O$ (0.0572 g, 0.109 mmol) were refluxed in 80% ethanol (50 mL) for 24 h. After 24 h, the red solution was cooled and evaporated in a rotary evaporator until dry. The red solid was then dissolved in deionized water (10 mL). A concentrated solution of $NaClO_4$ was added dropwise, resulting in a red precipitate. The precipitate was collected and dried under vacuum. The complex was purified by size-exclusion chromatography using Sephadex^{TM} LH-20 (1:1 acetonitrile: methanol) and eluted as a single band (0.064 g, 84%). FTIR (KBr cm^{-1}): 3420 (br), 3069 (w), 1972 (s), 1699 (m), 1651 (s), 1091 (vs), 765 (vs), 625 (vs). ^{1}H NMR (500 MHz, CD_3CN) δ 8.59 (d, J = 8.2 Hz, 1H), 8.54 – 8.48 (m, 3H), 8.42 (d, J = 8.1 Hz, 1H), 8.14 – 8.06 (m, 2H), 8.06 – 8.00

(m, 2H), 7.97 (td, J = 8.1, 1.3 Hz, 1H), 7.91 (d, J = 5.6 Hz, 1H), 7.81 (t, J = 4.7 Hz, 2H), 7.78 – 7.71 (m, 3H), 7.47 – 7.35 (m, 5H) 7.34 – 7.30 (m, 1H), 7.05 (t, J = 8.1 Hz, 1H), 5.79 (d, J = 8.4 Hz, 1H), 4.36 (s, 3H). ^{13}C NMR (126 MHz, CD_3CN) δ 157.56, 157.34, 156.76, 156.66, 152.72, 152.16, 151.97, 151.84, 151.53, 150.90, 149.05, 140.04, 137.45, 137.38, 137.25, 137.13, 136.91, 136.66, 127.27, 127.21, 127.07, 126.90, 126.84, 125.63, 125.17, 124.62, 124.00, 123.84, 123.75, 123.43, 115.30, 111.89, 32.85. Anal. Calcd for $C_{33}H_{27}N_7O_8Cl_2Ru{\cdot}3H_2O$: C 45.27%; H 3.80%; N 11.20%. Found: C 45.50%; H 3.60%; N 10.85%. ESI-MS (positive mode) *m/z* calculated for $C_{33}H_{27}N_7O_8Cl_2Ru$, 821.6; found, 722.0 $(M\text{-}ClO_4)^+$.

2.3.2 Ru(**pybtz**)(bpy)$_2$](ClO$_4$)$_2$

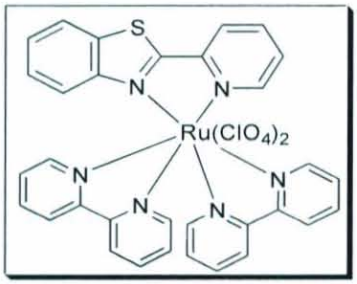

2-(Pyridin-2-yl)benzo[*d*]thiazole (pybtz) (0.0199 g, 0.0938 mmol) and $Ru(bpy)_2Cl_2{\cdot}2H_2O$ (0.0572 g, 0.108 mmol) were refluxed in 80% ethanol (50 mL) for 24 h. The red solution was then cooled to room temperature and filtered. The filtered solution was then evaporated in a rotary evaporator until dry. The red solid was diluted

with deionized water and filtered. A saturated solution of $NaClO_4$ was added drop-wise to the filtrate, resulting in a red precipitate. The precipitate was collected and dried under vacuum. The complex was purified by size exclusion chromatography using Sephadex™ LH-20 (1:1) acetonitrile:methanol. From the two bands, the dark orange fraction was separated and used for further studies (0.35 g, 96%). FTIR (KBr cm^{-1}): 3424 (br), 3074 (w), 2009 (s), 1603 (m), 1563 (s), 1464 (s), 1444 (s), 1423 (s), 1325 (s), 1243 (s), 1091 (vs), 764 (vs), 729 (vs), 623 (vs). ^1H NMR (500 MHz, CD_3CN) δ 8.59 – 8.54 (m, 4H), 8.48 (d, J = 8.1 Hz, 1H), 8.23 (d, J = 8.2 Hz, 1H), 8.20 – 8.16 (m, 1H), 8.16 – 8.13 (m, 1H), 8.10 (ddd, J = 9.4, 6.0, 1.3 Hz, 2H), 8.04 (td, J = 8.0, 1.3 Hz, 1H), 7.95 (d, J = 5.6 Hz, 1H), 7.87 (d, J = 5.6 Hz, 1H), 7.77 (d, J = 5.6 Hz, 1H), 7.72 (dd, J = 8.5, 5.6 Hz, 2H), 7.63 – 7.58 (m, 1H), 7.51 (dtd, J = 6.8, 5.6, 1.2 Hz, 2H), 7.43 (dtd, J = 6.9, 5.6, 1.1 Hz, 2H), 7.41 – 7.36 (m, 1H), 7.30 (ddd, J = 8.4, 7.4, 1.0 Hz, 1H), 6.34 (d, J = 8.5 Hz, 1H).^{13}C NMR (126 MHz, CD_3CN) δ 167.24, 158.07, 157.85, 157.36, 157.33, 153.72, 153.43, 152.83, 152.59, 152.47, 152.30, 151.81, 138.72, 138.59, 138.37, 138.26, 134.61, 129.09, 128.80, 128.67, 128.25, 128.21, 128.19, 128.15, 127.03, 124.92, 124.90, 124.85, 124.58, 124.48, 120.28. MALDI TOF MS *m/z* calculated for $C_{32}N_6H_{24}SCl_2O_8Ru$, 824.6; found, 625.08 $(M\text{-}2ClO_4)^+$.

2.3.3 [Ru(**Me_2-pybbim**)$(bpy)_2$]$(ClO_4)_2$

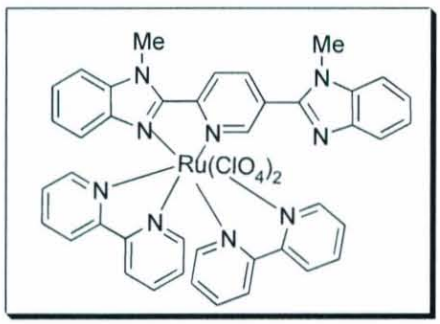

2,5-Bis(1-methyl-1*H*-benzo[*d*]imidazol-2-yl)pyridine (Me_2-pybbim) (0.0318 g, 0.0938 mmol) and $Ru(bpy)_2Cl_2 \cdot 2H_2O$ (0.0572 g, 0.108 mmol) were refluxed together in 80% ethanol (50 mL) for 24 h. The red solution was cooled to room temperature, filtered and evaporated in a rotary evaporator until dry. The red precipitate was diluted with deionized water (10 mL) and filtered again. $NaClO_4$ was added dropwise to the filtrate resulting in a reddish orange precipitate. The red solid was collected and dried under vacuum and used directly without further purification (0.071 g, 80%). FTIR (KBr cm^{-1}): 3385 (br), 3060 (w), 2926 (w), 1968 (s), 1602 (m), 1463 (s), 1384 (s), 1145 (s), 1116 (vs), 1088 (vs), 767 (vs), 625 (s). ^1H NMR (500 MHz, CD_3CN) δ 8.76 (d, J = 8.6 Hz, 1H), 8.59 – 8.51 (m, 4H), 8.47 (d, J = 8.1 Hz, 1H), 8.23 (d, J = 1.4 Hz, 1H), 8.19 – 8.14 (m, 1H), 8.09 (td, J = 9.1, 1.3 Hz, 2H), 8.05 – 8.00 (m, 1H), 7.96 (d, J = 5.5 Hz, 2H), 7.89 (d, J = 5.4 Hz, 1H), 7.84 (d, J = 5.2 Hz, 1H), 7.80 (d, J = 8.4 Hz, 1H), 7.68 (d, J = 8.0 Hz, 1H), 7.54 – 7.47 (m, 3H), 7.47 – 7.42 (m, 2H), 7.42 – 7.37 (m, 2H), 7.36 – 7.30 (m, 1H), 7.12 (t, J = 7.7

Hz, 1H), 5.87 (d, J = 8.4 Hz, 1H), 4.45 (s, 3H), 3.64 (s, 3H). ^{13}C NMR (126 MHz, CD_3CN) δ157.43, 156.70, 156.64, 152.34, 152.08, 152.02, 151.69, 149.14, 140.22, 137.64, 137.50, 137.35, 137.09, 136.86, 136.62, 127.43, 127.30, 126.99, 124.73, 124.09, 123.61, 123.50, 122.68, 119.18, 115.44, 112.02, 110.37, 32.91, 31.29. Anal. Calcd for $C_{41}H_{33}N_9O_8Cl_2Ru{\cdot}2H_2O$: C 49.85%; H 3.78%; N 12.76%. Found: C 49.75%; H 3.74%; N 12.37%. MALDI TOF MS *m/z* calculated for $C_{41}H_{33}N_9O_8Cl_2Ru$, 951.74; found, 752.19 $(M\text{-}2ClO_4)^+$.

2.3.4 $[\{(bpy)_2Ru\}_2(\mathbf{Me_2\text{-}pzbbim})](ClO_4)_4$

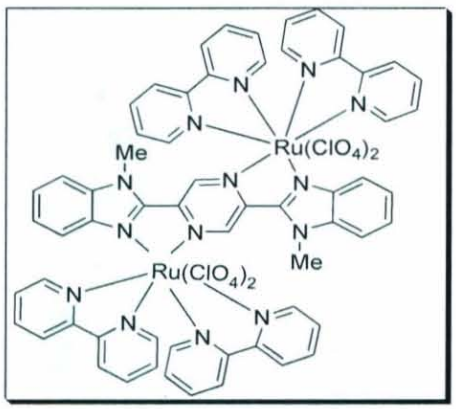

2,5-Bis(1-methyl-1H-benzo[d]imidazol-2-yl)pyrazine (Me_2-pzbbim) (0.0615 g, 0.181 mmol) and $Ru(bpy)_2Cl_2{\cdot}2H_2O$ (0.1908 g, 0.366 mmol) were refluxed in ethylene glycol (30 mL) at 250 °C for 24 h. The resulting solution turned green during this time. This was then poured into 150 mL deionized water and an excess of $NaClO_4$ was added to give a

green precipitate. This was collected by suction filtration and washed well with deionized water and dried under vacuum. The monometallic (red) and bimetallic (green) complexes were separated by size exclusion chromatography (Sephadex^{TM} LH-20) using (1:1) methanol:acetonitrile (0.26 g, 65%). FTIR (KBr cm^{-1}): 3415 (br), 3072 (w), 2002 (s), 1602 (m), 1559 (s), 1515 (s), 1465 (s), 1445 (s), 1422 (s), 1087 (vs), 762 (vs), 727 (vs), 622 (vs). ^{1}H NMR (500 MHz, CD_3CN) δ 8.65 (dd, J = 8.8, 4.6 Hz, 3H), 8.61 – 8.56 (m, 3H), 8.53 (s, 1H), 8.48 (t, J = 3.7 Hz, 2H), 8.44 (d, J = 8.2 Hz, 1H), 8.38 (d, J = 5.3 Hz, 1H), 8.21 (t, J = 7.2 Hz, 5H), 8.11 – 8.06 (m, 2H), 7.99 (t, J = 6.0 Hz, 2H), 7.92 – 7.83 (m, 4H), 7.80 (d, J = 5.5 Hz, 1H), 7.70 – 7.61 (m, 4H), 7.60 – 7.49 (m, 7H), 7.32 – 7.28 (m, 1H), 7.27 – 7.23 (m, 1H), 7.13 (t, J = 7.8 Hz, 2H), 5.93 (d, J = 8.5 Hz, 1H), 5.91 – 5.88 (m, 1H), 3.75 (s, 6H). ^{13}C NMR (126 MHz, CD_3CN) δ 157.59, 157.47, 156.91, 156.84, 156.54, 156.46, 155.89, 155.74, 153.74, 153.23, 153.12, 152.68, 152.52, 152.38, 151.53, 151.42, 148.48, 148.41, 146.81, 146.75, 145.97, 140.14, 138.38, 138.17, 138.15, 137.99, 137.97, 137.94, 137.68, 136.84, 136.82, 127.83, 127.81, 127.60, 127.56, 127.53, 126.77, 126.75, 125.41, 124.69, 124.57, 124.44, 124.29, 123.93, 123.47, 115.51, 112.00, 31.84, 31.80. Anal. Calcd for $C_{60}H_{48}N_{14}O_{16}Cl_4Ru_2 \cdot 3H_2O$: C 44.51%; H 3.36%; N 12.11%. Found: C 44.49%; H 3.46%; N 12.01%. MALDI TOF MS *m/z* calculated for $C_{60}H_{48}N_{14}O_{16}Cl_4Ru_2$, 1565.07; found, 1465.06 $(M\text{-}ClO_4)^+$; 1365.11 $(M\text{-}2ClO_4+H)^+$; 1265.12 $(M\text{-}3ClO_4+ H)^+$; 1166.21 $(M\text{-}4ClO_4+H)^+$.

2.3.5 $[\{(bpy)_2Ru\}_2(\mathbf{pzbbtz})](ClO_4)_4$

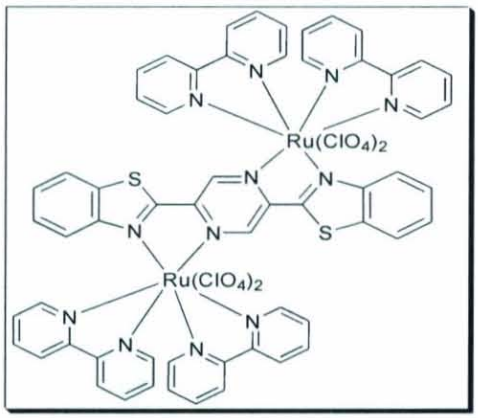

2,5-Di(benzo[*d*]thiazol-2-yl)pyrazine (pzbbtz) (0.031 g, 0.090 mmol) and $Ru(bpy)_2Cl_2 \cdot 2H_2O$ (0.097 g, 0.19 mmol) were refluxed in ethylene glycol (30 mL) at 250 °C for 24 h. The resulting solution turned green during this time, which was poured into 150 mL deionized water and then filtered. Addition of an excess of $NaClO_4$ resulted in a green precipitate, which was collected by suction filtration, washed well with deionized water and dried under vacuum. This complex produced two bands during the chromatographic separations (size exclusion) with Sephadex™ LH-20 using (1:1) methanol:acetonitrile. The monometallic (red) and bimetallic (green) complexes were separated and the bimetallic fraction was used for further study (0.091 g, 65%). FTIR (KBr cm^{-1}): 3419 (br), 3072 (w), 1734 (m), 1699 (s), 1651 (s),1603 (s) ,1504 (s) 1145 (s), 1116 (vs),1088 (vs), 763 (vs),623 (vs). ^1H NMR (500 MHz, CD_3CN) δ 8.67 (d, J = 7.9 Hz, 3H), 8.60 (t, J = 9.3 Hz, 3H), 8.50 (d, J = 8.0 Hz, 1H), 8.46 (d, J = 7.9 Hz, 2H), 8.31

– 8.17 (m, 8H), 8.13 (t, J = 7.8 Hz, 2H), 8.09 (d, J = 5.3 Hz, 2H), 8.05 – 8.01 (m, 2H), 7.91 (d, J = 5.0 Hz, 1H), 7.83 – 7.78 (m, 4H), 7.71 (s, 2H), 7.62 – 7.54 (m, 6H), 7.53 (d, J = 5.8 Hz, 2H), 7.33 (s, 3H), 7.23 (d, J = 6.6 Hz, 1H). ^{13}C NMR (126 MHz, CD_3CN) δ 162.82, 162.68, 157.22, 156.97, 156.64, 156.56, 155.83, 155.72, 153.40, 153.25, 153.19, 152.85, 152.55, 152.25, 151.37, 151.17, 150.50, 150.45, 147.90, 147.78, 138.91, 138.72, 138.60, 138.53, 138.31, 138.18, 135.14, 135.08, 128.88, 128.84, 127.89, 127.84, 127.77, 127.67, 127.62, 127.43, 124.76, 124.71, 124.57, 124.49, 124.35, 123.89, 123.83, 119.79. Anal. Calcd for $C_{58}H_{42}N_{12}S_2Cl_4O_{16}Ru_2 \cdot 2H_2O$: C 43.35%; H 2.88%; N 10.46%. Found: C 43.46%; H 2.91%; N 10.47%. MALDI TOF MS *m/z* calculated for $C_{58}H_{42}N_{12}S_2Cl_4O_{16}Ru_2$, 1571.11; found, 1371.01 $(M\text{-}2ClO_4)^+$; 1272.06 $(M\text{-}3ClO_4)^+$; 1172.10 $(M\text{-}4ClO_4)^+$.

2.3.6 [{(bpy)$_2$Ru}$_2$(**py$_2$tbtz**)](ClO$_4$)$_4$ [103]

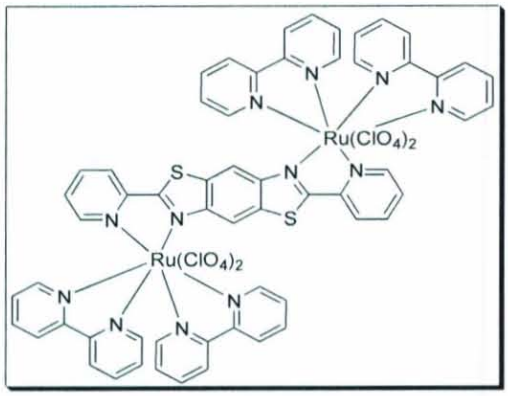

This complex was synthesized following the method of Haga et al. [103]. 2,6′-Bis(2-pyridyl)-2,2′:6,2′′-thiazolo[4,5-d]-benzothiazole (py_2tbtz) (0.0352 g, 0.102 mmol) and $Ru(bpy)_2Cl_2 \cdot 2H_2O$ (0.0973 g, 0.187 mmol) were refluxed in glycerol (30 mL) for 24 h. The red solution was then poured into 150 mL deionized water and an excess of $NaClO_4$ was added producing a red precipitate, which was collected by suction filtration and washed well with deionized water and dried under vacuum. This complex produced several bands in the size exclusion chromatography using Sephadex™ LH-20 (1:1) acetonitrile:methanol, from which a dark red fraction (bimetallic) was collected for further studies (0.11 g, 70%). FTIR (KBr cm^{-1}): 3406 (br), 3070 (w), 1968 (s) 1601 (m), 1463 (s), 1384 (s), 1341 (s), 1244 (s), 1145 (s), 1116 (vs), 1088 (vs), 767 (vs), 730 (s), 624 (s). ^1H NMR (500 MHz, CD_3CN) δ 8.63 (d, J = 8.2 Hz, 1H), 8.60 – 8.50 (m, 8H), 8.43 (d, J = 8.1 Hz, 1H), 8.28 – 8.21 (m, 2H), 8.18 – 8.10 (m, 6H), 8.09 – 8.04 (m, 2H), 8.04 – 8.01 (m, 1H), 8.00 – 7.96 (m, 3H), 7.83 (d, J = 5.1 Hz, 1H), 7.79 (t, J = 5.3 Hz, 2H), 7.68 (d, J = 4.6 Hz, 2H), 7.65 – 7.61 (m, 2H), 7.60 – 7.57 (m, 1H), 7.56 – 7.52 (m, 2H), 7.46 – 7.42 (m, 4H), 7.40 (d, J = 7.1 Hz, 1H), 7.34 – 7.30 (m, 1H), 6.94 (d, J = 4.2 Hz, 2H). ^{13}C NMR (126 MHz, CD_3CN) δ 169.41, 169.19, 157.34, 157.08, 156.67, 156.59, 156.51, 156.49, 153.26, 152.99, 152.45, 152.40, 152.39, 152.27, 152.20, 151.70, 151.64, 150.09, 149.96, 138.02, 137.91, 137.80, 137.75, 137.69, 137.59, 134.44, 134.40, 128.77, 128.72, 127.74, 127.58, 127.39, 124.53, 124.42, 124.26, 124.24, 124.18, 124.11, 123.89, 114.95, 114.88, 99.27. MALDI TOF MS *m/z* calculated for $C_{58}H_{42}N_{12}S_2O_{16}Cl_4Ru_2$, 1571.12; found, 1172.10 $(M\text{-}4ClO_4\text{-}H)^+$.

2.3.7 $[\{(bpy)_2Ru\}_2(\mathbf{Me_2\text{-}py_2bbim})](ClO_4)_4$ [101]

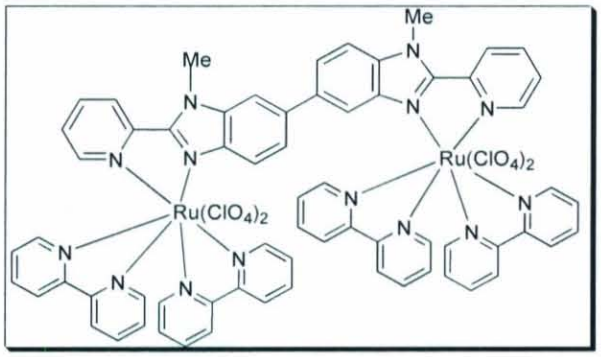

This complex was synthesized following the method of Nozaki and Ohno [101]. 3,3′-Dimethyl-2,2′-di(pyridin-2-yl)-5,6′-bi(3H-benzo[d]imidazole) (Me_2-py_2bbim) (0.0424 g, 0.102 mmol) and $Ru(bpy)_2Cl_2{\cdot}2H_2O$ (0.0973 g, 0.187 mmol) were refluxed in ethylene glycol (50 mL) for 24 h. The red solution was then poured into 150 mL deionized water and an excess of $NaClO_4$ was added to that solution resulting in a red precipitate. The red precipitate was then collected by suction filtration and washed well with deionized water and dried under vacuum. The complex was purified by size exclusion chromatography using of Sephadex^{TM} LH-20 (1:1) acetonitrile:methanol. A dark red fraction was collected for further analysis (0.063 g, 38%). FTIR (KBr cm^{-1}): 3392 (br), 3069 (w), 1972 (s), 1602 (m), 1515 (s), 1481 (s), 1444 (s), 1463 (s), 1089 (vs), 764 (vs), 729 (vs), 622 (vs). ^{1}H NMR (500 MHz, CD_3CN) δ 8.66 – 8.61 (m, 2H), 8.57 – 8.52 (m, 5H), 8.51 – 8.46 (m, 3H), 8.12 – 8.06 (m, 3H), 8.04 – 7.95 (m, 5H), 7.90 – 7.84 (m, 6H), 7.81 (t, J = 6.9 Hz, 4H), 7.78 (t, J = 5.4 Hz, 4H), 7.62 – 7.53 (m, 2H), 7.50 –

7.43 (m, 2H), 7.40 – 7.35 (m, 7H), 5.88 (t, J = 8.7 Hz, 3H), 4.43 (m, 6H). ^{13}C NMR (126 MHz, CD_3CN) δ 157.33, 156.75, 156.69, 156.63, 156.51, 155.14, 152.76, 152.26, 152.19, 151.94, 151.86, 151.74, 151.55, 148.93, 148.88, 140.75, 139.82, 137.41, 137.31, 137.20, 136.46, 136.05, 127.36, 127.28, 127.08, 126.99, 126.91, 125.30, 124.02, 123.83, 123.45, 112.51, 109.87, 62.84, 33.10, 33.04, 32.97. Anal. Calcd for $C_{66}H_{52}N_{14}O_{16}Cl_4Ru_2 \cdot 3H_2O$: C 46.76%; H 3.45%; N 11.57%. Found: C 46.82%; H 3.68%; N 11.05%. ESI-MS (positive mode) *m/z* calculated for $C_{66}H_{52}N_{14}Cl_4O_{16}Ru_2$, 1641.17; found, 1541.7 $(M\text{-}ClO_4)^+$.

2.4 X-ray crystallographic studies of the ruthenium polypyridyl complexes

Some of the synthsized monometallic and bimetallic ruthenium polypyridyl complexes were able to be crystallized. Their crystal structures were determined as part of further verification of molecular structures. It was found that mixed solvent systems were effective for the crystallization of perchlorate salts of the benzothiazole and benzimidazole complexes. Slow evaporation of acetonitrile from chloroform or methanol solution resulted in well-shaped crystals of three benzothiazole complexes and one benzimidazole complex. Although similar conditions were applied to crystallize other complexes, crystals were so small that they did not diffract at the desired angle (55°). Table 2.1 and 2.2 summarizes crystallographic data for the four complexes.

2.5 X-ray diffraction studies

The following text was taken from reports prepared by Dr. Lousie N. Dawe, who collected the data and solved the crystal structures described below. All measurements were made on a Rigaku Saturn CCD area detector equipped with a Rigaku SHINE optic, with Mo-Kα radiation. The structure was solved by direct methods [104] and expanded by using Fourier transform techniques [105]. The non-hydrogen atoms were refined anisotropically. Hydrogen atoms were introduced in calculated positions with isotropic thermal parameters set 25% greater than those of their bonding partners. They were refined on the riding model. Neutral atom scattering factors were taken from Cromer and Waber's "International Tables for X-ray Crystallography" [106]. Anomalous dispersion effects were included in Fcalc [107]; the values for Δf' and Δf'' were those of Creagh and McAuley [108]. The values for the mass attenuation coefficients are those of Creagh and Hubbell [109]. All calculations were performed using the CrystalStructure [110-111] crystallographic software package except for refinement, which was performed using SHELXL-97 [104].

Table 2.1: Summary of crystallographic data for $[Ru(\mathbf{pybtz})(bpy)_2]^{2+}$, $[Ru(\mathbf{Me_2pybbim})(bpy)_2]^{2+}$, $[\{(bpy)_2Ru\}_2(\mathbf{pzbbtz})]^{4+}$

Chemical Formula (Experimental)	$[Ru(\mathbf{pybtz})(bpy)_2]^{2+}$	$[Ru(\mathbf{Me_2pybbim})(bpy)_2]^{2+}$	$[\{(bpy)_2Ru\}_2(\mathbf{pzbbtz})]^{4+}$
	$C_{35}H_{28}Cl_5N_7O_8RuS$	$C_{41}H_{43}Cl_2N_9O_{13}Ru$	$C_{66}H_{54}Cl_4N_{16}O_{16}Ru_2S_2$
M	985.04	1041.82	1735.32
T(K)	153(2)	153(2)	153(2)
Crystal System	monoclinic	triclinic	triclinic
Space Group	$P2_1/n$ (#14)	P-1 (#2)	P-1 (#2)
a (Å)	19.432(3)	9.313(6)	13.599(4)
b (Å)	8.8126(14)	14.766(10)	16.050(5)
c (Å)	24.654(4)	17.970(12)	17.237(6)
α (°)	90.00	103.50(2)	88.874(19)
β (°)	111.760(3)	104.18(3)	86.357(19)
γ (°)	90.00	104.12(4)	70.514(13)
V (Å^3)	3921.1(12)	2208(3)	3539.6(19)
Z	4	2	2
D_{calc} (g/cm^3)	1.668	1.567	1.628
μ(MoKα) (cm^{-1})	8.54	5.52	7.17
Reflections Total	72920	18276	32634
Reflections Unique ($I>2.00\sigma(I)$)	8054 (7322)	9011 (7997)	14466 (12802)
R_{int}	0.0469	0.0387	0.0717
R_1 ($I>2.00\sigma(I)$)	0.0712	0.1180	0.0850
wR_2 (All reflections)	0.1869	0.3055	0.2470
Goodness-of-Fit	1.106	1.058	1.048

Table 2.2: Summary of crystallographic data for $[\{(bpy)_2Ru\}_2(\mathbf{py_2tbtz})]^{4+}$.

Chemical Formula (Experimental)	$[\{(bpy)_2Ru\}_2(\mathbf{py_2tbtz})]^{4+}$ $C_{58}H_{54}Cl_4N_{12}O_{22}Ru_2S_2$
M	1679.20
T(K)	153(2)
Crystal System	triclinic
Space Group	P-1 (#2)
a (Å)	12.0249 (11)
b (Å)	12.75010 (10)
c (Å)	13.9516 (14)
α (°)	93.388 (18)
β (°)	112.8809 (13)
γ (°)	117.909 (18)
V ($Å^3$)	1663.4 (2)
Z	1
D_{calc} (g/cm^3)	1.676
μ(MoKα) (cm^{-1})	7.64
Reflections Total	6116 (5467)
Reflections Unique ($I>2.00\sigma(I)$)	8054 (7322)
R_{int}	0.0356
R_1 ($I>2.00\sigma(I)$)	0.0855
wR_2 (All reflections)	0.2475
Goodness-of-Fit	1.072

2.5.1 Crystal structure for Ru(**pybtz**)$(bpy)_2(ClO_4)_2$

The ORTEP structure shown in Figure 2.1 confirms the proposed structure for $[Ru(\mathbf{pybtz})(bpy)_2]^{2+}$. This complex was co-crystallized with two perchlorate ions and two lattice solvent molecules of $CHCl_3$ and CH_3CN (1:9) were present for each monometallic ruthenium complex. A red chip crystal of $[Ru(\mathbf{pybtz})(bpy)_2]^{2+}$ having approximate dimensions of 0.33 x 0.20 x 0.20 mm was mounted on a low temperature diffraction loop. Selected bond lengths and bond angles are listed in Table 2.3.

The crystal structure in Figure 2.1 confirms that the **pybtz** ligand is coordinated to Ru(1) via the N1 and N2 atoms. The Ru–N(1)(**btz**) distance [2.078(4) Å] is slightly shorter than that of the Ru–N(2)(py) distance [2.084(4)Å]. The bite angle for the N(1)–Ru(1)–N(2) is 78.43(15)° and is comparable to that for [Ru(2-(2-pyridyl)benzimidazole)-$(bpy)_2]ClO_4$ (deprotonated), 78.37(8)° [113]. The bite angles for the bpys of 78.67(15)° and 78.73(14)° and Ru–N distances of 2.055(4)–2.065(4) Å are comparable to those found in other complexes [113-116]. The comparatively higher Ru(1)–N(1) and Ru(1)–N(2) bond lengths {2.078(4) Å and 2.084(4) Å} are comparable to Ru–N(bpy) bonds and are due to the partial π-backbonding to the electron rich bridging ligand from the metal centre [113]. The bond angles around Ru(1) are: N(1)–Ru(1)–N(5): 171.06(14)°; N(2)–Ru(1)–N(4): 175.98(16)°; N(3)–Ru(1)–N(6): 173.21(12)°. This deviation from the octahedral geometry may be due to the acute bite angles of both the 2,2′-bpy and the **pybtz** ligands.

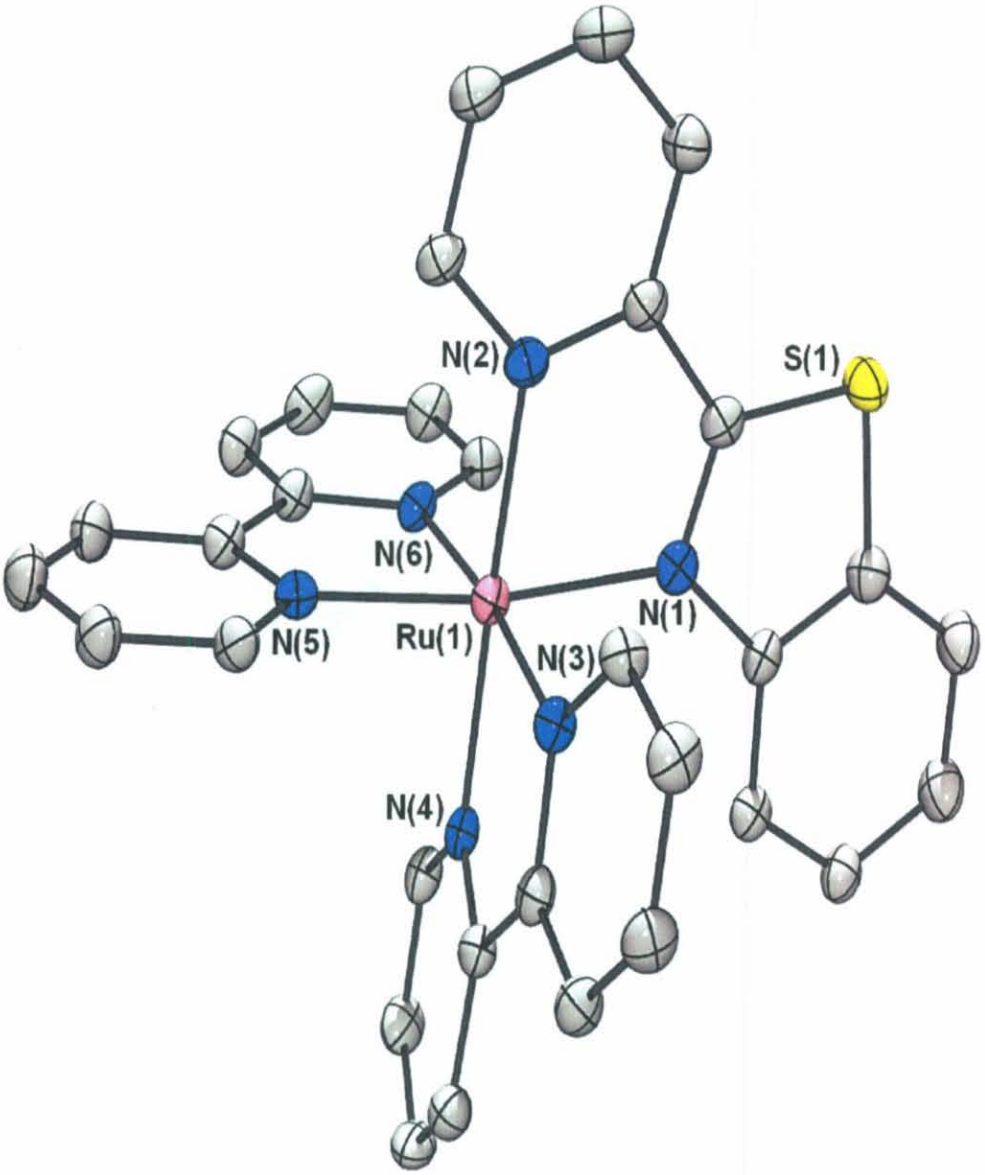

Figure 2.1: X-ray crystal structure for $[Ru(\mathbf{pybtz})(bpy)_2]^{2+}$. 30% probability ellipsoids; anions and hydrogen atoms omitted for clarity.

Table 2.3: Selected bond distances (Å) and angles (°) of $[Ru(\mathbf{pybtz})(bpy)_2]^{2+}$

Ru(1)-N(5)	2.055(4)	Ru(1)-N(1)	2.078(4)
Ru(1)-N(6)	2.065(4)	Ru(1)-N(3)	2.060(4)
Ru(1)-N(4)	2.058(4)	Ru(1)-N(2)	2.084(4)
N(1)-Ru(1)-N(2)	78.44(15)	N(1)-Ru(1)-N(3)	88.94(15)
N(1)-Ru(1)-N(4)	100.85(15)	N(1)-Ru(1)-N(5)	171.06(14)
N(1)-Ru(1)-N(6)	95.35(15)	N(2)-Ru(1)-N(3)	97.34(14)
N(2)-Ru(1)-N(4)	175.98(16)	N(2)-Ru(1)-N(5)	94.62(15)
N(3)-Ru(1)-N(5)	97.60(15)	N(3)-Ru(1)-N(6)	173.21(12)
N(4)-Ru(1)-N(5)	86.46(15)	N(4)-Ru(1)-N(6)	95.32(14)
N(5)-Ru(1)-N(6)	78.73(15)		

2.5.2 Crystal structure for $Ru(\mathbf{Me_2\text{-}pybbim})(bpy)_2(ClO_4)_2$

Figure 2.2 shows the ORTEP structure for $[Ru(\mathbf{Me_2\text{-}pybbim})(bpy)_2]^{2+}$ and confirms the predicted structure. A red prism crystal of $C_{41}H_{43}C_{12}N_9O_{13}Ru$ having approximate dimensions of 0.26 x 0.19 x 0.04 mm was grown from a variety of solvents, however, all diffracted weakly in this case. The Platon [117] squeeze procedure was applied to recover 104 electrons per unit cell in one void (total volume 369 $Å^3$); that is 52 electrons per formula unit (~5 H_2O). The crystal selected for full data collection was grown from a slow evaporation of acetonitrile from methanol (1:1) solvent. This complex was co-crystallized with two perchlorate ions, which were present for each monometallic

ruthenium complex. Selected bond lengths and bond angles are listed in Table 2.4.

The crystal structure for $[Ru(\mathbf{Me_2\text{-}pybbim})(bpy)_2]^{2+}$ (see Figure 2.2) confirms that the **Me_2-pybbim** ligand is coordinated to Ru(1) via the N(3) and N(5) atoms. The Ru–N(5)(benzimidazole) distance [2.056(8) Å] is slightly shorter than the Ru–N(3)(pyridyl) distance [2.068 (8) Å]. The bite angle for the N(3)–Ru(1)–N(5) of 78.10 (3)° is comparable to that for $[Ru(2\text{-}(2\text{-pyridyl})benzimidazole)(bpy)_2](ClO_4)_2$ (deprotonated), 78.37(8)° [84]. The bite angles for the bpy's of 78.70(3)° and 79.20(3)° and Ru–N distance 2.040(8)–2.062(7) Å are comparable to those found in other complexes [113-116]. The bond angles around Ru(1) are: N(7)–Ru(1)–N(5): 168.9(3)°; N(8)–Ru(1)–N(6): 173.7(3)°; N(9)–Ru(1)–N(3): 172.0(3)°. This deviation from the octahedral geometry may be related to the acute bite angles of both the 2,2′-bpy and the **Me_2-pybbim** ligands.

Table 2.4: Selected bond distances (Å) and angles (°) for $[Ru(\mathbf{Me_2\text{-}pybbim})(bpy)_2]^{2+}$.

Ru(1)-N(9)	2.040(8)		Ru(1)-N(5)	2.056(8)	
Ru(1)-N(8)	2.046(7)		Ru(1)-N(6)	2.062(7)	
Ru(1)-N(7)	2.053(8)		Ru(1)-N(3)	2.068(8)	
N(9)-Ru(1)-N(8)	78.7(3)	N(9)-Ru(1)-N(7)	92.7(3)	N(8)-Ru(1)-N(7)	97.7(3)
N(9)-Ru(1)-N(5)	96.2(3)	N(8)-Ru(1)-N(5)	90.6(3)	N(7)-Ru(1)-N(5)	168.9(3)
N(9)-Ru(1)-N(6)	95.8(3)	N(8)-Ru(1)-N(6)	173.7(3)	N(7)-Ru(1)-N(6)	79.2(3)
N(5)-Ru(1)-N(6)	93.2(3)	N(9)-Ru(1)-N(3)	172.0(3)	N(8)-Ru(1)-N(3)	95.5(3)
N(7)-Ru(1)-N(3)	93.6(3)	N(5)-Ru(1)-N(3)	78.1(3)	N(6)-Ru(1)-N(3)	90.2(3)

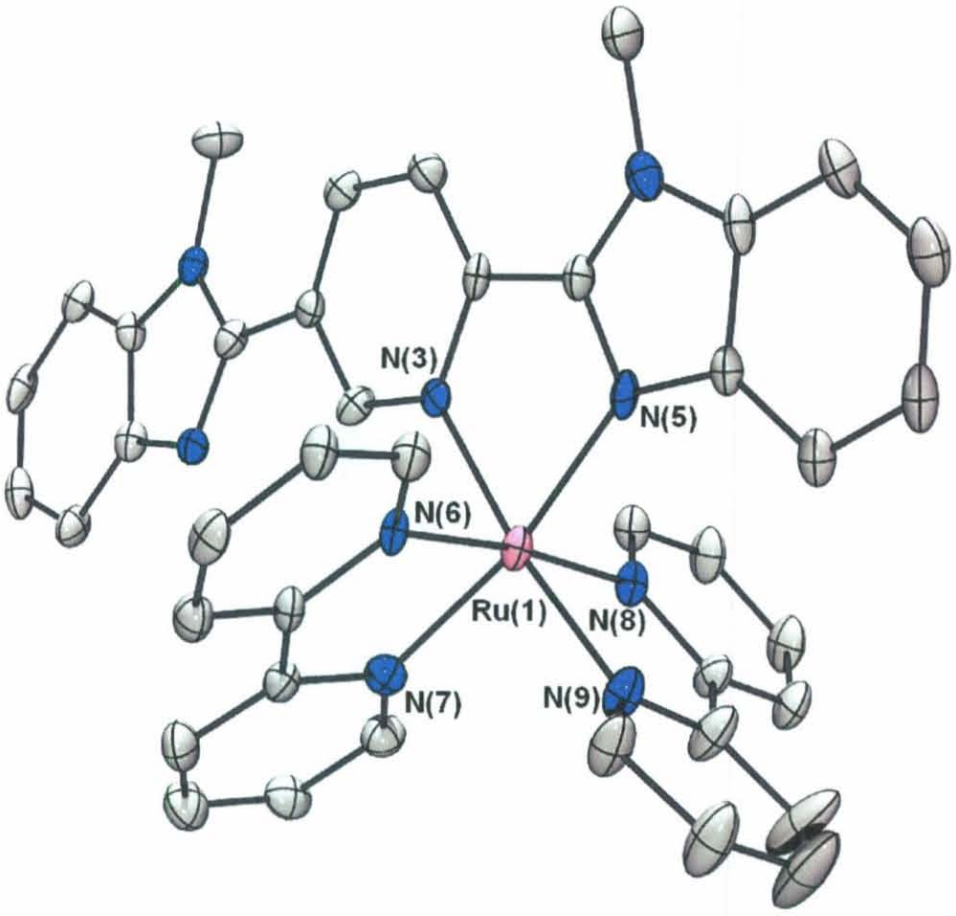

Figure 2.2: X-ray crystal structure for $[Ru(\mathbf{Me_2.pybbim})(bpy)_2]^{2+}$. 30% probability ellipsoids; anions and hydrogen atoms omitted for clarity.

2.5.3 Crystal structure for $[\{(bpy)_2Ru\}_2(\mathbf{pzbbtz})](ClO_4)_4$

The ORTEP structure shown in the Figure 2.3 confirms the expected structure for $[\{(bpy)_2Ru\}_2(\mathbf{pzbbtz})]^{4+}$. A black prismatic crystal of $[\{(bpy)_2Ru\}_2(\mathbf{pzbbtz})]^{4+}$ having approximate dimensions of 0.34 x 0.28 x 0.15 mm was treated in a similar way to that of

Ru(**pybtz**)$(bpy)_2^{2+}$. One acetonitrile lattice solvent molecule was refined isotropically, while all other non-hydrogen atoms were refined anisotropically. The crystal selected for full data collection was grown from a mixture of acetonitrile and methanol (1:1) solvents. This complex was co-crystallized with four perchlorate ions and three molecules of acetonitrile were present for each bimetallic ruthenium complex. Selected bond lengths and bond angles for this complex are listed in Table 2.5.

The structure consists of two hexa-coordinated ruthenium(II) centres (see Figure 2.3) in which the two $Ru(bpy)_2$ units are bridged by the N(2) and N(3) nitrogen atoms of the pyrazine moiety of **pzbbtz**, while the remaining sixth coordination sites are occupied by N(4) and N(1) benzothizole nitrogen atoms. The Ru–N(**btz**) distance [2.084(4) Å] is slightly longer than the Ru–N(**pz**) distance [2.048(4) Å]. The decrease in the Ru–N(pz) bond length is a clear evidence of π-back donation between Ru and the pyrazine ring. The bite angle for the N(1)–Ru(1)–N(2) is 78.17(15)° and that of N(3)–Ru(2)–N(4) is 77.75(15)°, which are comparable to the bite angles of $[\{(bpy)_2Ru\}_2(\mathbf{pzbzth})]^{3+}$ [78.4(4)° and 78.80(4)°, respectively] [118]. The bite angles for bpys 78.51(17)° to 79.94(16)° and the Ru-N distance 2.045(4) Å to 2.084(4) Å are comparable to those found in other complexes having similar structures [113-116]. The shorter Ru(1)–N(2)(pz) and Ru(2)–N(3)(pz) bond lengths [2.052(4) Å and 2.048(4) Å] are comparable to those of $[(bpy)_2Ru(\mathbf{dpp})]^{2+}$ [2.033 (12) (Å)] [119] and are responsible for the shorter metal-metal distance of 6.89 (Å) between the two ruthenium centres. This assumption is consistent with the cyclic voltammograms (redox potentials) and especially the high comproportionation constant, K_c value (see Chapter 3, page 90). Additionally, from the

electronic emission spectrum (see Chapter 3, page 108), the shifting of the MLCT band to the lower energy (near-IR) for this bimetallic metal complex is consistent with strong metal-metal interaction. The bond angles around Ru(1) are: N(2)–Ru(1)–N(7): 174.16(16)°; N(6)–Ru(1)–N(8): 173.45(16)°; N(5)–Ru(1)–N(1): 171.01(15)°, while those for Ru(2) atom are: N(12)–Ru(2)–N(9): 171.46(15)°; N(3)–Ru(2)–N(11): 175.48(15)°; N(10)–Ru(2)–N(4): 171.44(15)°. This deviation from octahedral geometry is due to the acute bite angles of both the bpy and the **pzbbtz** ligands.

Table 2.5: Selected bond distances (Å) and angles (°) for $[\{(bpy)_2Ru\}_2(\mathbf{pzbbtz})]^{4+}$.

Ru(1)-N(5)	2.045(4)	Ru(2)-N(10)	2.041(4)	Ru(1)-N(2)	2.052(4)
Ru(2)-N(3)	2.048(4)	Ru(1)-N(6)	2.065(4)	Ru(2)-N(12)	2.062(4)
Ru(1)-N(7)	2.069(4)	Ru(2)-N(9)	2.065(4)	Ru(1)-N(8)	2.074(4)
Ru(2)-N(11)	2.069(4)	Ru(1)-N(1)	2.082(4)	Ru(2)-N(4)	2.084(4)
N(5)-Ru(1)-N(2)	93.29(16)	N(5)-Ru(1)-N(6)	78.51(17)		
N(2)-Ru(1)-N(6)	90.33(15)	N(5)-Ru(1)-N(7)	88.12(16)		
N(2)-Ru(1)-N(7)	174.16(16)	N(6)-Ru(1)-N(7)	95.50(17)		
N(5)-Ru(1)-N(8)	98.07(16)	N(2)-Ru(1)-N(8)	95.46(16)		
N(6)-Ru(1)-N(8)	173.45(16)	N(7)-Ru(1)-N(8)	78.72(17)		
N(5)-Ru(1)-N(1)	171.01(15)	N(2)-Ru(1)-N(1)	78.17(15)		
N(6)-Ru(1)-N(1)	98.53(16)	N(7)-Ru(1)-N(1)	100.66(15)		

Continued.....

Table 2.5: Selected bond distances (Å) and angles (°) for $[\{(bpy)_2Ru\}_2(\mathbf{pzbbtz})]^{4+}$.

N(8)-Ru(1)-N(1)	85.67(15)	N(10)-Ru(2)-N(3)	93.86(15)
N(10)-Ru(2)-N(12)	96.97(16)	N(3)-Ru(2)-N(12)	97.00(16)
N(10)-Ru(2)-N(9)	78.94(16)	N(3)-Ru(2)-N(9)	90.79(16)
N(12)-Ru(2)-N(9)	171.46(15)	N(10)-Ru(2)-N(11)	87.94(15)
N(3)-Ru(2)-N(11)	175.48(15)	N(12)-Ru(2)-N(11)	78.65(16)
N(9)-Ru(2)-N(11)	93.63(15)	N(10)-Ru(2)-N(4)	171.44(15)
N(3)-Ru(2)-N(4)	77.75(15)	N(12)-Ru(2)-N(4)	85.92(15)
N(11)-Ru(2)-N(4)	100.54(14)		

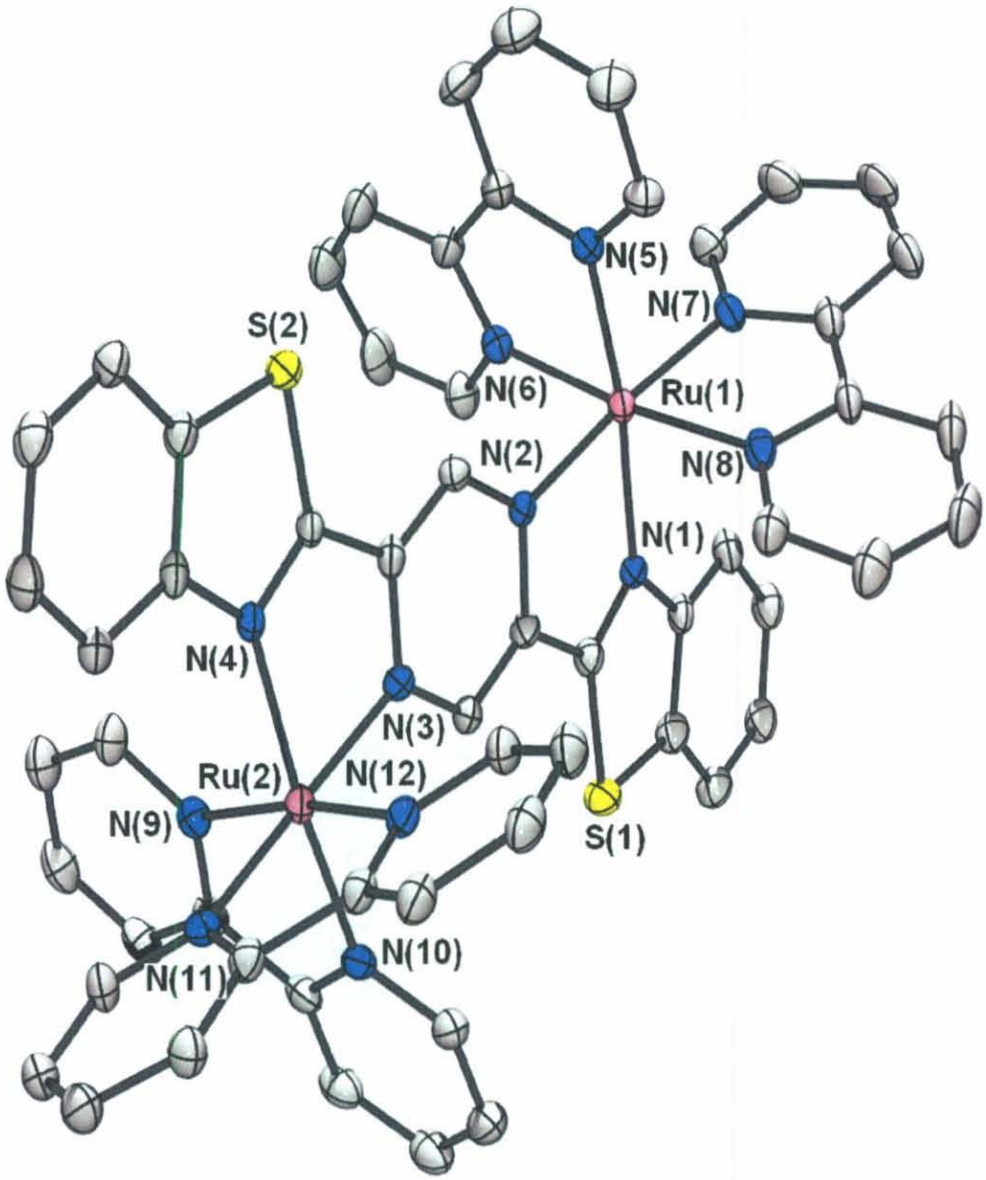

Figure 2.3: X-ray crystal structure for $[\{(bpy)_2Ru\}_2(\mathbf{pzbbtz})]^{4+}$. 30% probability ellipsoids; anions and hydrogen atoms omitted for clarity.

2.5.4 Crystal structure for $[\{(bpy)_2Ru\}_2(\mathbf{py_2tbtz})](ClO_4)_4$

The ORTEP structure shown in the Figure 2.4 confirms the expected structure for the $[\{(bpy)_2Ru\}_2(\mathbf{py_2tbtz})]^{4+}$. A red prism crystal of $C_{58}H_{54}Cl_4O_{22}Ru_2S_2$ having approximate dimensions of 0.28 x 0.27 x 0.18 mm was mounted on a low temperature diffraction loop. The crystal selected for full data collection was grown in a NMR tube by slow evaporation of acetonitrile from methanol (1:1). Selected bond lengths and bond angles are listed in the Table 2.6.

From Figure 2.4, it is confirmed that the structure consists of two hexa-coordinated ruthenium(II) centers in which the two $Ru(bpy)_2$ units are bridged by the N(2) nitrogen atoms of the benzothiazole moiety of **py$_2$tbtz** ligand, while the remaining sixth coordination sites are occupied by the pyridyl N(1) nitrogen atoms. Also, the crystal structure clarifies that ligand **py$_2$tbtz** is coordinated to Ru(1) via the N(1) and N(2). The Ru–N(**btz**) distance [2.096(4) Å] is slightly longer than the Ru–N(py) distance [2.054(4) Å] of the bridging ligand. The bite angle for the N(1)–Ru(1)–N(2) (78.3(2)°) is comparable to that for $[\{(bpy)_2Ru\}_2$(2,5-di(2-pyridyl)thiazolo[5,4-*d*]thiazole$]^{4+}$ (77.93°) [120]. The bite angles for bpy units are 79.9(2)° to 79.2(2)° and the Ru-N distances of 2.047(6) to 2.096(4) Å are comparable to those found in other complexes [113-116]. The metal-metal distance (9.13 Å) between Ru(1)–Ru(2) indicates a weaker electronic interaction between metal centers and is consistent with the cyclic voltammograms (redox potentials) having low K_c values (see chapter 3, page 92) and from the electronic emission spectroscopy data with a very weak emission band at 735 nm (see chapter 3, page 110). The large metal-metal distance indicates that electron density at the

coordinating centers is relatively small because of LUMO delocalization within the ligand. The bond angles around Ru(1) are: N(1)–Ru(1)–N(4): 173.6(2)°; N(2)–Ru(1)–N(5): 175.9(3)°; N(3)–Ru(1)–N(6): 173.0(2)°. This deviation from the octahedral geometry may be related to the acute bite angles of both the bpy and the **py_2tbtz** ligands.

Table 2.6: Bond lengths (Å) and bond angles (°) for $[\{(bpy)_2Ru\}_2(\mathbf{py_2tbtz})]^{4+}$.

Ru(1)-N(1)	2.054(6)		Ru(1)-N(2)	2.096(4)	
Ru(1)-N(3)	2.056(7)		Ru(1)-N(4)	2.047(6)	
Ru(1)-N(5)	2.053(5)		Ru(1)-N(6)	2.056(8)	
N(1)-Ru(1)-N(2)	78.3(2)	N(1)-Ru(1)-N(3)	96.4(2)	N(1)-Ru(1)-N(4)	175.9(3)
N(1)-Ru(1)-N(5)	96.0(2)	N(1)-Ru(1)-N(6)	89.0(2)	N(2)-Ru(1)-N(3)	88.0(2)
N(2)-Ru(1)-N(4)	99.8(2)	N(2)-Ru(1)-N(5)	173.6(2)	N(2)-Ru(1)-N(6)	97.5(2)
N(3)-Ru(1)-N(4)	79.9(2)	N(3)-Ru(1)-N(5)	95.7(2)	N(3)-Ru(1)-N(6)	173.0(2)
N(4)-Ru(1)-N(5)	86.1(2)	N(4)-Ru(1)-N(6)	94.9(2)	N(5)-Ru(1)-N(6)	79.3(2)

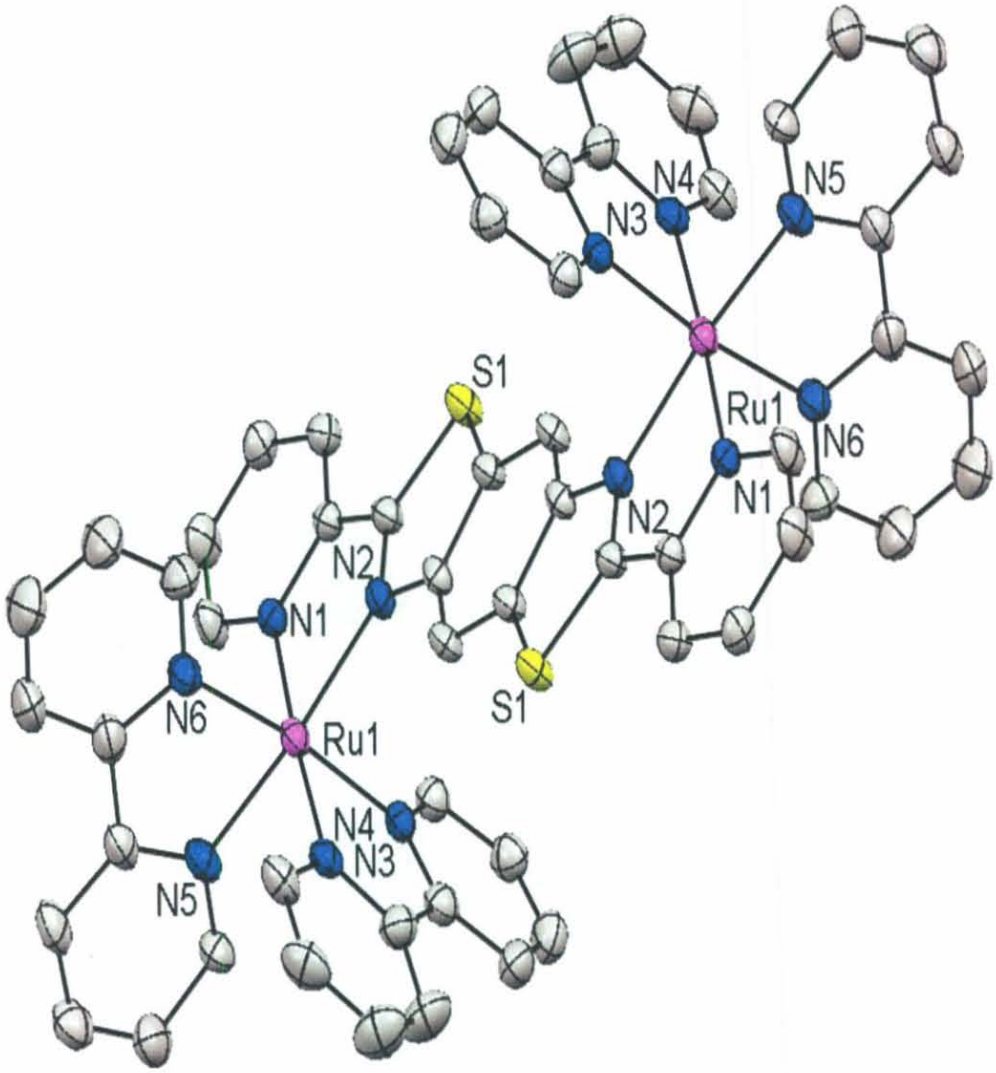

Figure 2.4: X-ray crystal structure for $[\{(\mathbf{bpy})_2Ru\}_2(\mathbf{py_2tbtz})]^{4+}$. 30% probability ellipsoids; anions and hydrogen atoms omitted for clarity.

Chapter 3

Electrochemical and photophysical properties of the synthesized Ru polypyridyl complexes

3.1 Introduction

This chapter describes the cyclic voltammetry (CV) and differential pulse voltammetry (DPV) under N_2 of all the synthesized complexes designed for this project. The monometallic and bimetallic ruthenium polypyridyl benzimidazole and benzothiazole complexes showed reversible redox waves, which were compared to those for $Ru(bpy)_3^{2+}$, to investigate the effects of ligand structure and donor-acceptor properties. The metal-metal interactions for the bimetallic complexes are revealed by their oxidation waves.

3.2 Electrochemical measurements

Electrochemical experiments were performed with a Pine Instrument AFCBP1 biopotentiostat, except for differential pulse voltammetry which was performed with an Epslon EC-2000 XP instrument. Acetonitrile (Sigma-Aldrich, anhydrous, 99.8%) and Tetraethyl ammonium tetrafluoroborate (Bu_4NBF_4) (Alfa Aesar, 99.0%) were used as received. Et_4NClO_4 was prepared from Et_4NBr and $HClO_4$ and purified by recrystallization six times from hot water and finally dried overnight under vacuum at 40 °C. An Ag/AgCl/KCl (saturated, aqueous) reference electrode was used with a Pt wire counter electrode and glassy carbon (0.20 cm^2) or pt disk working electrode. The working electrodes were cleaned by using alumina polishing solution (0.30 micron) followed by washing with water and finally acetone. A three chambered glass cell, with a luggin capillary for the reference electrode, was used for electrochemical measurements.

Cyclic and differential pulse voltammetry of the metal complexes were carried out in CH_3CN/Bu_4NBF_6 (0.1 M) solutions unless otherwise indicated. The solutions were purged with N_2 (5-10 min) prior to electrochemical measurements. The formal potentials (E^o) for cyclic voltammetry were calculated by using the equation $(E_{p,a} + E_{p,c})/2$ vs Ag/AgCl. Both anodic ($E_{p,a}$) and cathodic ($E_{p,c}$) peak potentials were found to be independent of scan rates. The number of electrons (n) was determined from the equation of peak separation as $\Delta E_p = E_{p,a} - E_{p,c} = 59/n$ mV. Generally, for all complexes the cyclic voltammetric data showed metal based oxidation processes, whereas, the reduction processes (follows EEE reaction mechanism) are associated with the $\pi*$ LUMO energy of ligands, similar to those for other reported ruthenium polypyridyl complexes [121-125].

3.3 Electrochemistry under N_2

3.3.1 Monometallic complexes

3.3.1.1 $Ru(bpy)_3^{2+}$

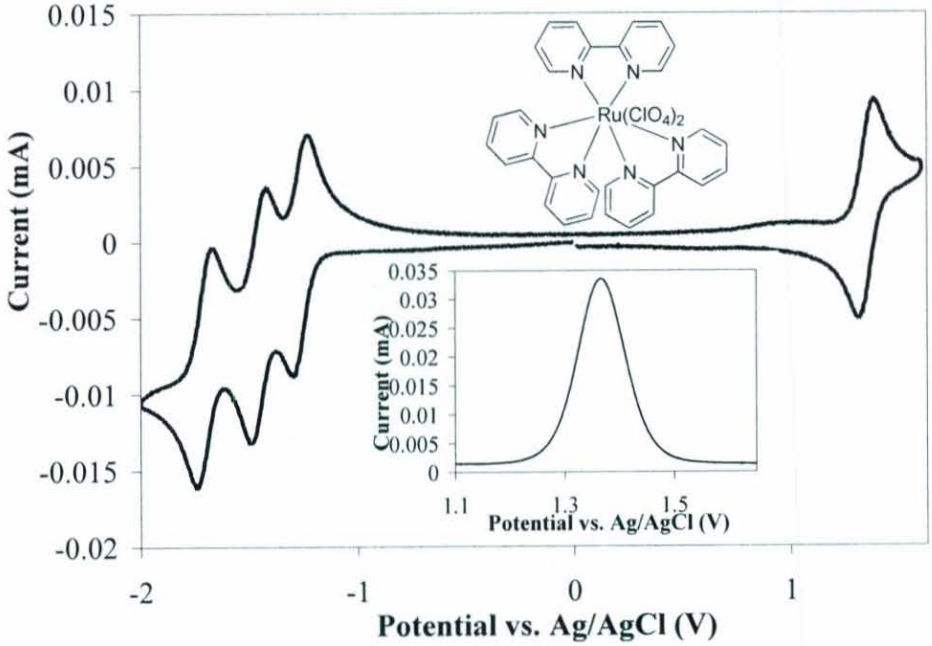

Figure 3.1: Cyclic voltammogram of 1 mM $Ru(bpy)_3^{2+}$ in CH_3CN/0.1 M Bu_4NBF_4 under N_2 at a glassy carbon electrode (at ν = 50 mV/s). (Inset: differential pulse voltammogram under N_2 at a glassy carbon electrode).

Figure 3.1 shows a cyclic voltammogram of $Ru(bpy)_3^{2+}$ in acetonitrile. There are four reversible one-electron waves. The $Ru^{3+/2+}$ process is noted at a formal potential of +1.34 V, and three peaks with formal potential values of -1.24 V, -1.46 V, and -1.70 V, correspond to bipyridine-based reductions [121].

3.3.1.2 $[Ru(\textbf{Me-pybim})(bpy)_2]^{2+}$

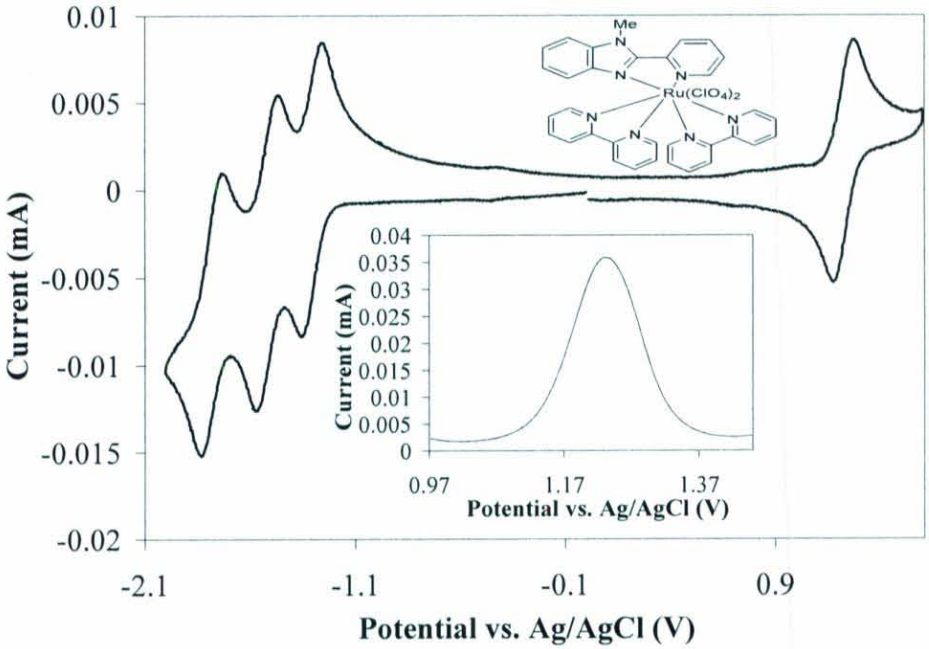

Figure 3.2: Cyclic voltammogram of 1 mM $[Ru(\textbf{Me-pybim})(bpy)_2]^{2+}$ in CH_3CN/0.1 M Bu_4NBF_4 under N_2 at a glassy carbon electrode (at v = 50 mV/s). (Inset: differential pulse voltammogram under N_2 at a glassy carbon electrode).

Cyclic voltammetry of $[Ru(\textbf{Me-pybim})(bpy)_2]^{2+}$ (see Figure 3.2) is very similar to that of $Ru(bpy)_3^{2+}$. It shows a one-electron reversible $Ru^{3+/2+}$ wave with a formal potential of +1.23 V. The formal potential for the oxidation wave is about 110 mV less positive than that for $Ru(bpy)_3^{2+}$, and could be explained as the stabilization of the Ru^{3+} state by the **Me-pybim** ligand relative to bpy in $Ru(bpy)_3^{2+}$. In the reduction processes, this complex showed three one-electron reversible waves with formal potentials of -1.31 V, -1.52 V,

and -1.79 V, which are very close to those of $Ru(bpy)_3^{2+}$. So it can be concluded that replacing one bpy with a **Me-pybim** ligand does not necessarily cause any significant change on the π^* LUMO energy.

3.3.1.3 $[Ru(\mathbf{pybtz})(bpy)_2]^{2+}$

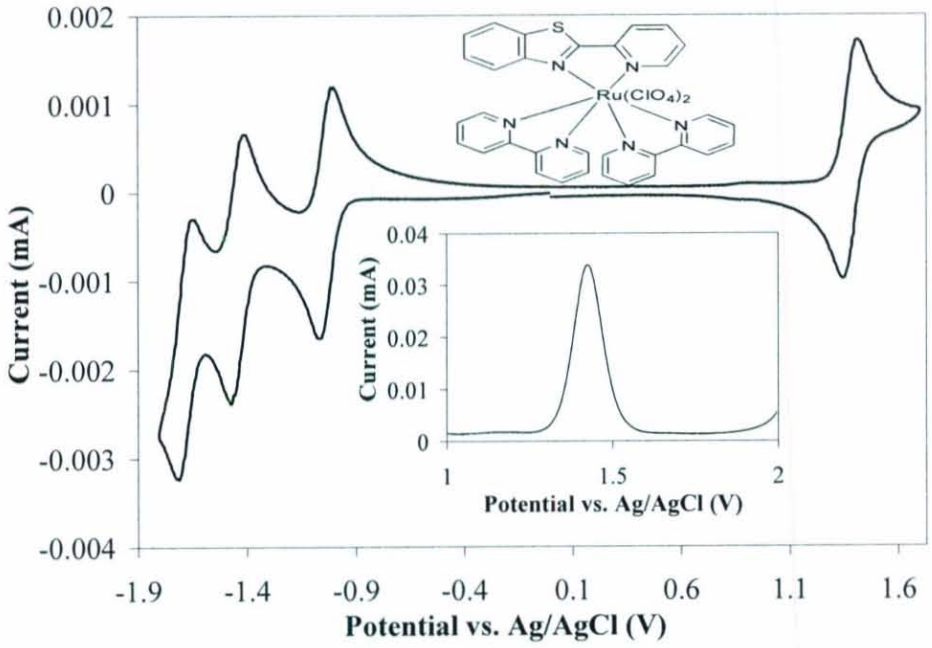

Figure 3.3: Cyclic voltammogram of 1 mM $[Ru(\mathbf{pybtz})(bpy)_2]^{2+}$ in CH_3CN/0.1M Bu_4NBF_4 under N_2 at a platinum electrode (at ν = 100 mV/s). (Inset: differential pulse voltammogram under N_2 at a glassy carbon electrode).

Figure 3.3 shows a cyclic voltammogram of $[Ru(\mathbf{pybtz})(bpy)_2]^{2+}$, with four reversible one-electron waves within the scanned potential region. The formal potential for the

$Ru^{3+/2+}$ wave is seen at about +1.42 V, which is about 80 mV more positive region than that for $Ru(bpy)_3^{2+}$. The shifting of the potential indicates a more stable Ru^{3+} state relative to that in $Ru(bpy)_3^{2+}$. Also, the formal potential for the $Ru^{3+/2+}$ couple with the **pybtz** ligand is higher by 0.19 V relative to the **Me-pybim** ligand.

$[Ru(\mathbf{pybtz})(bpy)_2]^{2+}$ shows three reduction waves. The first wave (-1.03 V) is assigned to the **pybtz** reduction, because the first reduction wave for $Ru(bpy)_3^{2+}$ does not appear until -1.24 V. The first reduction wave for the **pybtz** ligand is 0.30 V more positive than for the **Me-pybim** ligand, suggesting that the **pybtz** is a better π-acceptor ligand. The other two waves, due the reduction of bpy fragments, appear at -1.44 V and -1.68 V, whereas in $Ru(bpy)_3^{2+}$, these reductions take place of -1.46 V and -1.70 V respectively (see Figure 3.1).

3.3.1.4 $[Ru(\mathbf{Me_2\text{-}pybbim})(bpy)_2]^{2+}$

The cyclic voltammetry of $[Ru(\mathbf{Me_2\text{-}pybbim})(bpy)_2]^{2+}$ (see Figure 3.4) shows four reversible waves. The one-electron $Ru^{3+/2+}$ peak appears at a formal potential of +1.27 V. Three one-electron reduction waves appear with formal potentials of -1.10 V, -1.40 V, and -1.64 V, respectively. The formal potential for the reduction of the **Me_2-pybbim** ligand is 200 mV more positive than for the **Me-pybim** ligand, due to the effect of the extended π-conjugation. The last two reduction peaks (-1.40 V and -1.64 V) are due to the reduction of bpy and occurred at similar potentials to those for $Ru(bpy)_3^{2+}$.

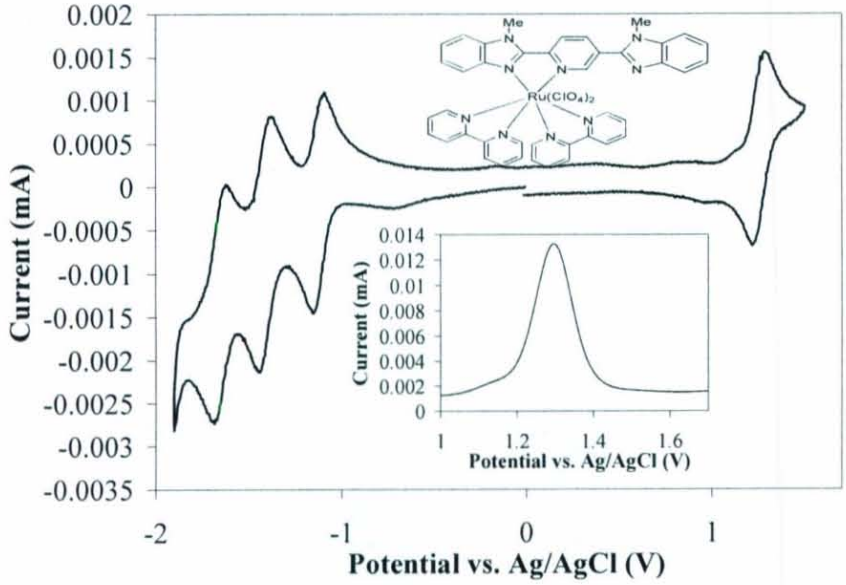

Figure 3.4: The cyclic voltammogram of 1 mM $[Ru(\mathbf{Me_2\text{-}pybbim})(bpy)_2]^{2+}$ in CH_3CN/0.1 M Bu_4NBF_4 under N_2 at a platinum electrode (at v = 100 mV/s). (Inset: differential pulse voltammogram under N_2 at a glassy carbon electrode).

3.3.2 Bimetallic complexes

3.3.2.1 $[\{(bpy)_2Ru\}_2(\mathbf{Me_2\text{-}pzbbim})]^{4+}$

Figure 3.5 shows a cyclic voltammogram of $[\{(bpy)_2Ru\}_2(\mathbf{Me_2\text{-}pzbbim})]^{4+}$. This complex shows five reversible redox waves. Acoording to the literature [126-128], for similar complexes, the first two one-electron waves for the Ru^{2+}-Ru^{2+} $\leftrightarrow$ Ru^{3+}-Ru^{2+} and Ru^{3+}-Ru^{2+} $\leftrightarrow$ Ru^{3+}-Ru^{3+} processes, are observed at formal potentials of +1.37 V and +1.55 V, respectively. The difference between these formal potentials ($\Delta E°$) is about 180 mV, which indicates that there is a strong electronic interaction between the two

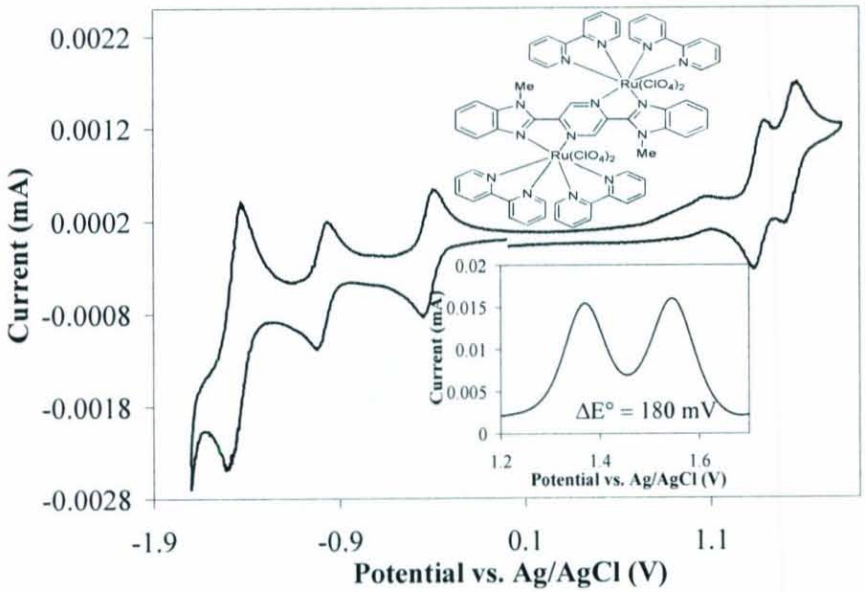

Figure 3.5: The cyclic voltammogram of 1 mM $[\{(bpy)_2Ru\}_2(\mathbf{Me_2\text{-}pzbbim})]^{4+}$ in CH_3CN/0.1 M Bu_4NBF_4 under N_2 at a platinum electrode (at ν = 100 mV/s). (Inset differential pulse voltammogram under N_2 at a glassy carbon electrode.)

ruthenium centers. This electronic interaction is assumed to occur via the LUMO of the bridging ligand, by a superexchange process, which is the proposed mechanism for a similar 2,5-dipyridyl-pyrazine (2,5-dpp) based ruthenium bimetallic complex [98]. The stability of the mixed-valence state is related to the thermodynamic equilibrium constant K_c and can be shown as [92, 129]:

$$[\text{Ru(II)}\mathbf{Me_2\text{-}pzbbim}\text{Ru(II)}]^{4+} + [\text{Ru(III)}\mathbf{Me_2\text{-}pzbbim}\text{Ru(III)}]^{6+} \leftrightarrow$$

$$2\,[\text{Ru(III)}\mathbf{Me_2\text{-}pzbbim}\text{Ru(II)}]^{5+}$$

The value of K_c is at around 1104, indicating the stability of the mixed-valence state (Ru^{3+}-Ru^{2+}) for **Me_2-pzbbim**. Of the three other reversible waves, the two one-electron reduction waves with formal potentials of -0.42 V and -1.06 V are assigned to reduction of the **Me_2-pzbbim** ligand (low lying π^* LUMO orbitals) because of the fact that the first reduction does not appear until -1.24 V for $Ru(bpy)_3^{2+}$. This reveals the electron-deficient nature of the pyrazine based ligand [130] relative to those for bpy in $Ru(bpy)_3^{2+}$. The third reduction wave (two-electron) at about -1.46 V must be due to the simultaneous reduction of two bpy ligands [85].

3.3.2.2 $[\{(bpy)_2Ru\}_2$**(pzbbtz)**$]^{4+}$

$[\{(bpy)_2Ru\}_2$**(pzbbtz)**$]^{4+}$ shows very similar cyclic voltammetry (see Figure 3.6) to that of $[\{(bpy)_2Ru\}_2$**(Me_2-pzbbim)**$]^{4+}$. There are two one-electron reversible peaks for Ru^{2+}-Ru^{2+} $\leftrightarrow$ Ru^{3+}-Ru^{2+} and Ru^{3+}-Ru^{2+} $\leftrightarrow$ Ru^{3+}-Ru^{3+} processes with formal potentials at about +1.54 V and +1.73 V. The difference between these formal potentials ($\Delta E°$) is about 190 mV, indicating a strong electronic interaction between the two ruthenium centers. This interaction presumably occurs via the LUMO of the bridging ligand **(pzbbtz)** by a superexchange process. The value of K_c is calculated to be about 1629 (from $\Delta E°$), which indicates a stable mixed-valence state and can be shown as:

$$[Ru(II)\textbf{pzbbtz}Ru(II)]^{4+} + [Ru(III)\textbf{pzbbtz}Ru(III)]^{6+} \leftrightarrow 2\,[Ru(III)\textbf{pzbbtz}Ru(II)]^{5+}$$

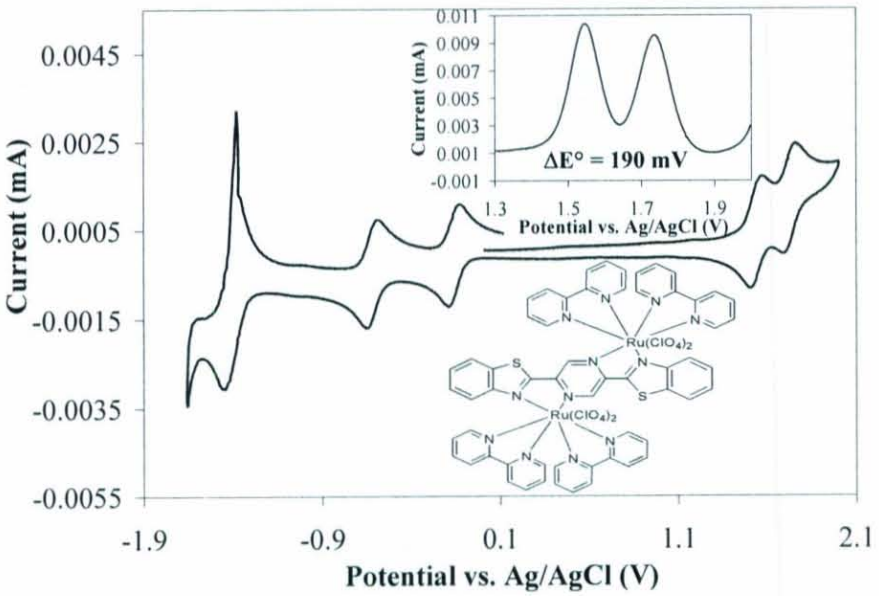

Figure 3.6: The cyclic voltammogram of 1 mM $[\{(bpy)_2Ru\}_2(\mathbf{pzbbtz})]^{4+}$ in CH_3CN/0.1 M Bu_4NBF_4 under N_2 at a platinum electrode (at v = 100 mV/s). (Inset: differential pulse voltammogram under N_2 at a glassy carbon electrode).

A large value of K_c may often be an indication of a short metal-metal distance [131] (which was found to be 6.89 Å for this complex from X-ray crystallography). It is found that the formal potentials for the two oxidation peaks for $[\{(bpy)_2Ru\}_2(\mathbf{pzbbtz})]^{4+}$ are shifted to more positive potentials by about 180 mV and 190 mV respectively relative to those for the $[\{(bpy)_2Ru\}_2(\mathbf{Me_2\text{-}pzbbim})]^{4+}$. Also, compared to the value of K_c it is seen that the mixed-valence state (Ru^{3+}-Ru^{2+}) is more stable for $[\{(bpy)_2Ru\}_2(\mathbf{pzbbtz})]^{4+}$ than for $[\{(bpy)_2Ru\}_2(\mathbf{Me_2\text{-}pzbbim})]^{4+}$.

The formal potentials for the first two reduction peaks are found at about -0.17 V

and -0.61 V, which are due to the lower lying π* LUMO orbital of the **pzbbtz** bridging ligand. It is interesting that first two reduction peaks are much more positively shifted and appeared at about 250 mV and 450 mV respectively more positive potentials than those for $[\{(bpy)_2Ru\}_2(\mathbf{Me_2\text{-}pzbbim})]^{4+}$, which may indicate that the **pzbbtz** ligand has more π-acceptor characteristics than **Me_2-pzbbim**. The last two-electron reversible wave at about -1.42 V is due to the simultaneous reduction of two bpy ligands.

3.3.2.3 $[\{(bpy)_2Ru\}_2(\mathbf{py_2tbtz})]^{4+}$

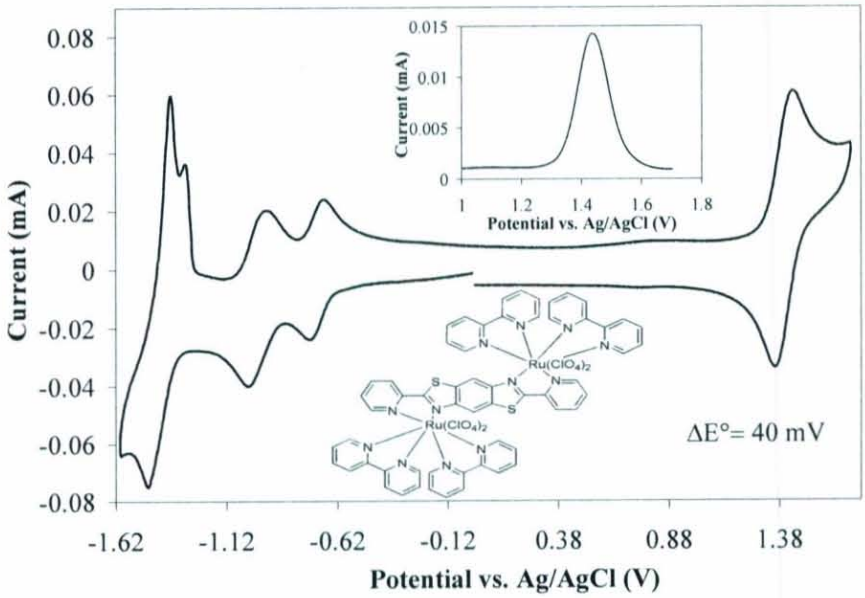

Figure 3.7: The cyclic voltammogram of 1 mM $[\{(bpy)_2Ru\}_2(\mathbf{py_2tbtz})]^{4+}$ in CH_3CN/0.1 M Et_4NClO_4 under N_2 at a glassy carbon electrode (at ν = 50 mV/s). (Inset: differential pulse voltammogram under N_2 at a glassy carbon electrode).

Figure 3.7 shows a cyclic voltammogram of $[\{(bpy)_2Ru\}_2(\mathbf{py_2tbtz})]^{4+}$ in acetonitrile. It shows a two-electron reversible peak for Ru^{2+}-Ru^{2+} ↔ Ru^{3+}-Ru^{2+} and Ru^{3+}-Ru^{2+} ↔ Ru^{3+}-Ru^{3+} processes with a $\Delta E°$ value of 40 mV as determined by Haga et al. [103]. Oxidative formal potentials were calculated by using the Richardson and Taube method [132], and were found at around +1.42 V and +1.46 V respectively. The lower value of $\Delta E°$ relative to the other two bimetallic complexes [see Section 3.3.2.1 and 3.3.2.2] is an indication of a lower stability of the mixed-valence state with the **py$_2$tbtz** bridging ligand. The stability of the mixed-valence state can be shown from the comproportionation constant (K_c):

$$[Ru(II)\mathbf{py_2tbtz}Ru(II)]^{4+} + [Ru(III)\mathbf{py_2tbtz}Ru(III)]^{6+} \leftrightarrow 2\,[Ru(III)\mathbf{py_2tbtz}Ru(II)]^{5+}$$

The value of K_c can be calculated from the formal potentials of the oxidative waves and was found to be approximately 4.7. The lower value of K_c relative to the other two bimetallic complexes is an indication of a weak electronic interaction between the metal centers for this complex. The lower value of K_c can be explained by the longer metal-metal distance [131], which is 9.13 Å for this complex relative to $[\{(bpy)_2Ru\}_2(\mathbf{pzbbtz})]^{4+}$ (from X-ray crystallography). According to Haga et al. [104], the electronic interacton for this complex is via the HOMO of the bridging ligand (**py$_2$tbtz**) by a "hole-type superexchange process". The first two reversible one-electron reduction peaks of this complex with formal potentials at about -0.70 V and -0.98 V are assumed to be due to the **py$_2$tbtz** ligand. The third (two-electron) wave is due to the

simultaneous reduction of two bpy ligands at a formal potential of -1.41 V, which is similar to that for the second reduction of $Ru(bpy)_3^{2+}$ at -1.46 V.

3.3.2.3 $[\{(bpy)_2Ru\}_2(\mathbf{Me_2\text{-}py_2bbim})]^{4+}$

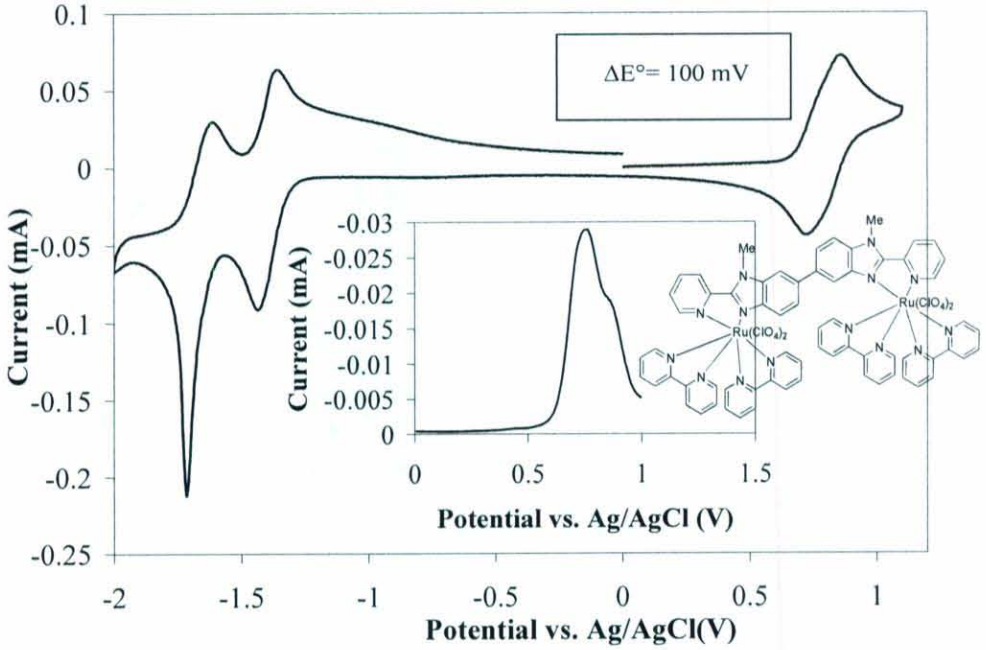

Figure 3.8: Cyclic voltammogram of 1 mM $[\{(bpy)_2Ru\}_2(\mathbf{Me_2\text{-}py_2bbim})]^{4+}$ in CH_3CN/0.1 M Bu_4NBF_4 under N_2 at a glassy carbon electrode (at ν = 100 mV/s). (Inset: differential pulse voltammogram under N_2 at a glassy carbon electrode).

Cyclic voltammetry of $[\{(bpy)_2Ru\}_2(\mathbf{Me_2\text{-}py_2bbim})]^{4+}$ (see Figure 3.8) shows three reversible redox waves. The oxidation wave of this complex clearly indicates that the oxidation involves two closely spaced, one-electron processes, due to Ru^{2+}-$Ru^{2+} \leftrightarrow Ru^{3+}$-

Ru^{2+} and Ru^{3+}-Ru^{2+} ↔ Ru^{3+}-Ru^{3+} processes and is composed of two clearly spaced one-electron with formal potentials of +0.77 V and +0.87 V (determined from the differential pulse voltammetry), and with a ΔE° value of about 100 mV. The mixed-valence state for this complex could be expressed as follows:

$$[\text{Ru(II)}\mathbf{Me_2\text{-}py_2bbim}\text{Ru(II)}]^{4+} + [\text{Ru(III)}\mathbf{Me_2\text{-}py_2bbim}\text{Ru(III)}]^{6+} \leftrightarrow 2\,[\text{Ru(III)}\mathbf{Me_2\text{-}py_2bbim}\text{Ru(II)}]^{5+}$$

The lower value of ΔE° is an indication of a lower stability of the mixed-valence state with the **Me_2-py_2bbim** bridging ligand for this complex. From the value of K_c (49), it is estimated that there is a weak electronic interaction between metal centers with the **Me_2-py_2bbim** ligand i.e. a long-distance mixed-valence electron transfer for long π-bridging ligand. In the literature, a similar interpretation is given for similar complexes [131, 133]. The other two waves are two-electron reversible reduction peaks with formal potentials of -1.40 V and -1.67 V. The first reduction wave is due to the simultaneous reduction of two bpy ligands. The other two-electron wave might be due to the reduction of the **Me_2-py_2bbim** ligand. The reduction of the bpy ligands for this complex are found shifted towards more negative potentials relative to the bpy ligands (-1.24 V) in $Ru(bpy)_3^{2+}$ and it could be due to the electron donating nature of the **Me_2-py_2bbim** ligand.

3.4 Summary of electrochemical characterization of Ru complexes

Table 3.1 illustrates the formal potentials of all of the complexes. The redox potentials of the monometallic complexes varied with the different types of ligand used. The incorporation of **Me-pybim, pybtz,** and **Me_2-pybbim** ligand in the ruthenium polypyridyl

Table 3.1: Formal potentials vs Ag/AgCl of all the complexes in the presence of 0.1 M Bu_4NBF_4/CH_3CN.

Complexes	E° (V)	
	Oxidation	Reduction
$Ru(bpy)_3^{2+}$	1.34(1e)	-1.24(1e), -1.46(1e), -1.70(1e)
$[Ru(\mathbf{Me\text{-}pybim})(bpy)_2]^{2+}$	1.23(1e)	-1.31(1e), -1.52(1e), -1.79(1e)
$[Ru(\mathbf{pybtz})(bpy)_2]^{2+}$	1.42(1e)	-1.01(1e), -1.48(1e), -1.73(1e)
$[Ru(\mathbf{Me_2\text{-}pybbim})(bpy)_2]^{2+}$	1.27(1e)	-1.10(1e), -1.40(1e), -1.64(1e)
$[\{(bpy)_2Ru\}_2(\mathbf{pzbbtz})]^{4+}$	1.37(1e), 1.55(1e)	-0.42(1e), -1.06(1e), -1.46(2e)
$[\{(bpy)_2Ru\}_2(\mathbf{Me_2\text{-}pzbbim})]^{4+}$	1.54(1e), 1.73(1e)	-0.17(1e), -0.61(1e), -1.42(2e)
$[\{(bpy)_2Ru\}_2(\mathbf{py_2tbtz})]^{4+}$	1.42(1e),1.46(1e)	-0.70(1e), -0.98(1e), -1.41(2e)
$[\{(bpy)_2Ru\}_2(\mathbf{Me_2\text{-}py_2bbim})]^{4+}$	0.77(1e), 0.87(1e)	-1.40(2e), -1.67(2e)

complexes caused the redox potentials to vary according to the π or σ donor-acceptor properties of the ligand. It was found that for the complexes with **pybtz** and **Me_2-pybbim** ligands, the reduction potential were shifted to the more positive potentials relative to **Me-pybim** ligand due to π-acceptor characteristics of **pybtz** ligand and the extended π delocalization characteristics for **Me_2-pybbim** ligand.

For bimetallic ruthenium complexes it was found that intramolecular electron

Table 3.2: Separation between oxidation formal potentials, ΔE° (mV), and the corresponding comproportionation constant, K_c (eqn. 10, Chapter 1, page 36), for all bimetallic complexes.

Complexes	ΔE° (mV)	K_c
$[\{(bpy)_2Ru\}_2(\mathbf{pzbbtz})]^{4+}$	190	1629
$[\{(bpy)_2Ru\}_2(\mathbf{Me_2pzbbim})]^{4+}$	180	1104
$[\{(bpy)_2Ru\}_2(\mathbf{Me_2py_2bbim})^{4+}$	100	49
$[\{(bpy)_2Ru\}_2(\mathbf{py_2tbtz})]^{4+}$	40	4.7

transfer is strongly dependent on the nature of ligand used (see Table 3.2). For example, with the **Me_2-pzbbim** ligand, the bimetallic complex shows lower values of K_c and ΔE° relative to that of **pzbbtz**, that has a similar pyrazinyl ligand moiety. This difference is likely to be related to the coordination environment of the metals which is varied here by using benzimidazole/benzothiazole moiety. Thus changes in the LUMO energy of the bridging ligand resulted in energy differences and caused variations in the bridging ligand-mediated Ru(II)/Ru(III) electronic coupling (superexchange). Usually, bimetallic complexes involving pyrazine-based bridges (better π-acceptors than pyridines) have low lying π^* LUMO orbitals. This feature endows these complexes with higher (more positive) [134-139] first reduction potentials than the other bimetallic complexes considered in this work. On the other hand, with the **pzbbtz** ligand, the bimetallic complex showed higher values of K_c and ΔE° relative to **py_2tbtz** ligand. This variation

can be explained by the fact that, compared to **pzbbtz** ligand, **py_2tbtz** has a larger π-bridging system, where the LUMO is located primarily within the **py_2tbtz** ligand and coordinating metal centers have low electron density [131]. For another bimetallic complex with **Me_2-py_2bbim** ligand, the value of K_c was found to be only 49, which is indicative of a long range mixed-valence electron transfer with a weak electronic interaction between the metal centers through a long bridging ligand (π delocalized system) [133].

3.5 Photophysical properties

This section describes the electronic absorption and emission spectra of the synthesized complexes to get supportive information for the results found in cyclic voltammetry. In order to reveal the σ-donor/π-acceptor properties of each ligand, UV-Vis absorption and emission spectra were compared to those of known complexes having similar structural features.

Electronic absorption and emission spectroscopy for the d^6 complex systems can simply be explained by the Franck-Condon principle [140]. When light is absorbed, an excited species is created with redistributed electron density within the molecule. As the movement of the electron is faster than the adjusting nuclei of the absorbing species, a new electronic field is generated by excitation. Figure 3.9 illustrates the potential wells of the ground and excited states of a molecule. For absorption of light, the electronic transition is from the ground vibrational energy state of the ground electronic state to an

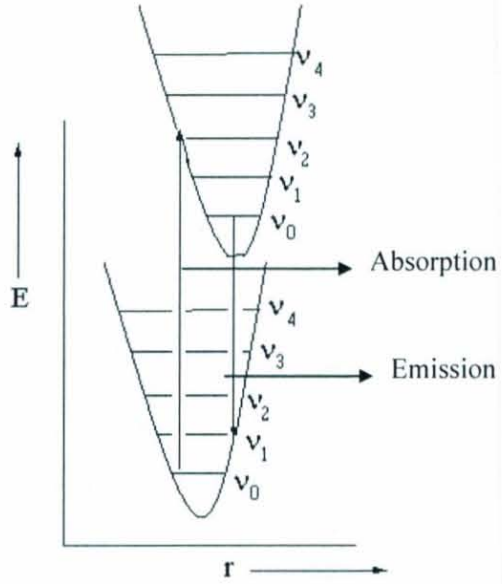

Figure 3.9: Potential energy wells for a ground state and an excited state [140].

excited vibrational energy state of the excited electronic state (upper). For the case of emission of light, the electronic transition is from the excited vibrational energy state of the lower excited electronic state to the ground vibrational energy state of the ground electronic state. The transitions are depicted in the Figure 3.9 by the vertical arrows for both absorption and emission.

3.5.1 Monometallic complexes

Figure 3.10 represents the absorption spectra of all monometallic ruthenium polypyridyl complexes synthesized for this study. As seen in this figure the absorption region around 260-320 nm is for the π-π^* transitions for all bpy ligands, while the 311-410 nm region

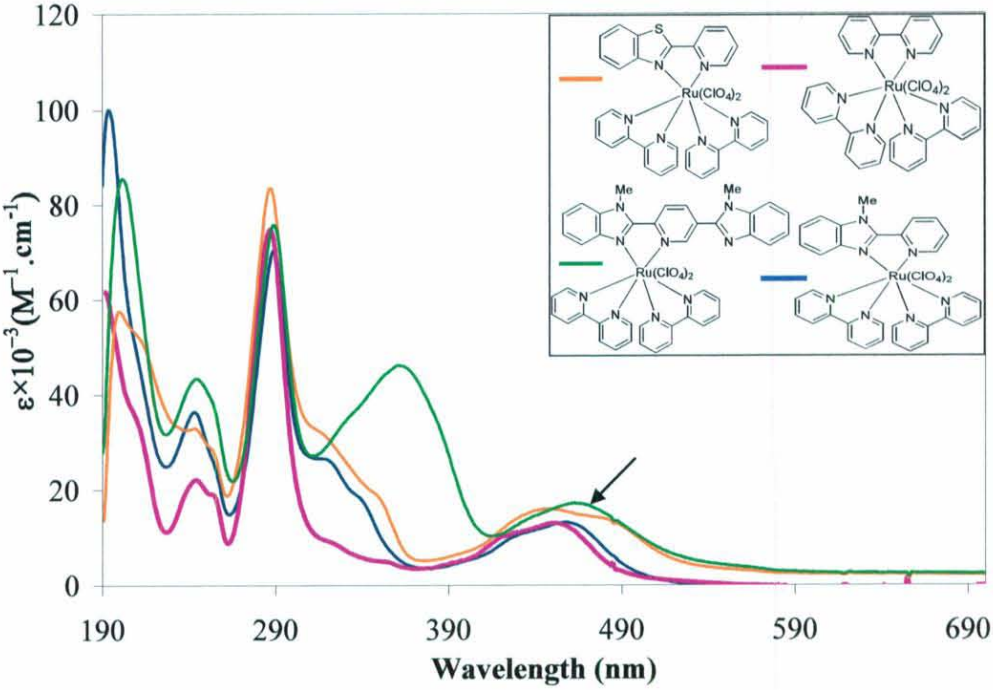

Figure 3.10: Electronic absorption spectra of $[Ru(\mathbf{Me\text{-}pybim})(bpy)_2]^{2+}$, $[Ru(\mathbf{pybtz})(bpy)_2]^{2+}$, $[Ru(\mathbf{Me_2\text{-}pybbim})(bpy)_2]^{2+}$, and $Ru(bpy)_3^{2+}$ (ca. 7.5×10^{-6} M) in CH_3CN at ambient temperature.

corresponds to the π-π* transitions for the benzimidazole and benzothiazole ligands, and the 390-520 nm region is due to MLCT bands for the dπ-π* transitions. It is evident that all the monometallic complexes show similar MLCT bands except, for the $[Ru(\mathbf{pybtz})(bpy)_2]^{2+}$ complex, whose MLCT absorption band was shifted slightly towards the lower energy region. This shifting of absorption maxima for $[Ru(\mathbf{pybtz})(bpy)_2]^{2+}$ might be related to the **pybtz** ligand's π-acceptor strength (metal to **pybtz** ligands π-backbonding) which is indicated by the redox potentials from the cyclic voltammetry

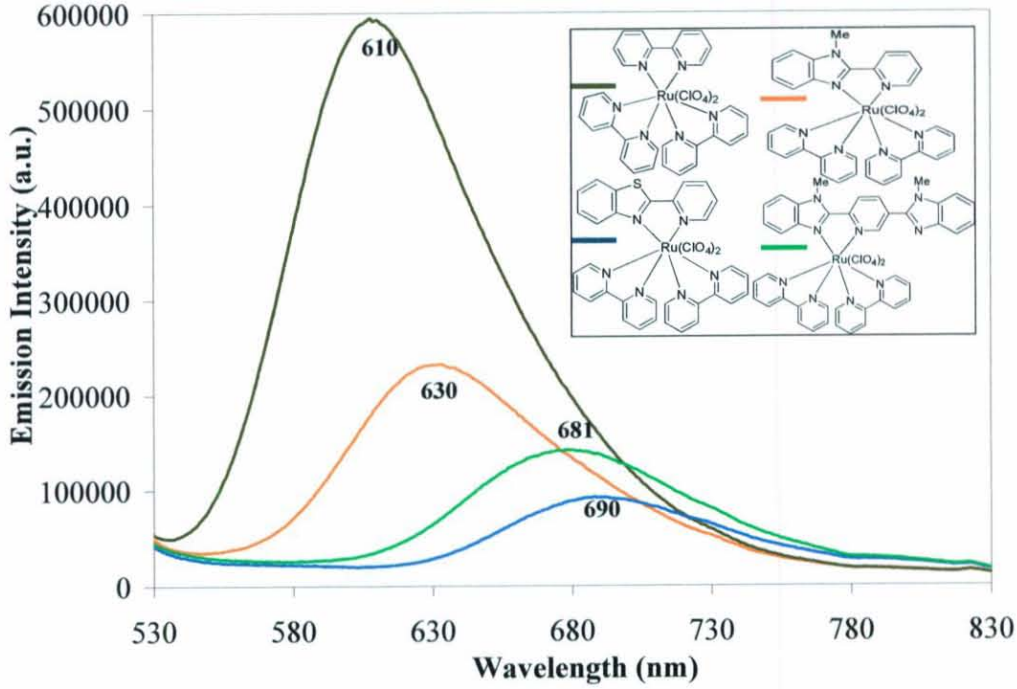

Figure 3.11: Electronic emission spectra of $[Ru(\mathbf{Me\text{-}pybim})(bpy)_2]^{2+}$, $[Ru(\mathbf{pybtz})(bpy)_2]^{2+}$, $[Ru(\mathbf{Me_2\text{-}pybbim})(bpy)_2]^{2+}$, and $Ru(bpy)_3^{2+}$ (ca. 7.5×10^{-6} M) in CH_3CN at ambient temperature.

relative to those for $[Ru(\mathbf{Me_2\text{-}pybbim})(bpy)_2]^{2+}$. On the other hand for $[Ru(\mathbf{Me_2\text{-}pybbim})(bpy)_2]^{2+}$, the lower energy of the π-π^* transition for the **Me_2-pybbim** ligand can be attributed to the extended π conjugation relative to **Me-pybim** and **pybtz**.

Emission spectra of the monometallic complexes are shown in Figure 3.11. It can be seen that the emission bands for the benzimidazole and benzothiazole complexes are quenched and shifted to lower energies relative to $Ru(bpy)_3^{2+}$. The emission bands at 681 and 690 nm for $[Ru(\mathbf{pybtz})(bpy)_2]^{2+}$ and $[Ru(\mathbf{Me_2\text{-}pybbim})(bpy)_2]^{2+}$ are at lower

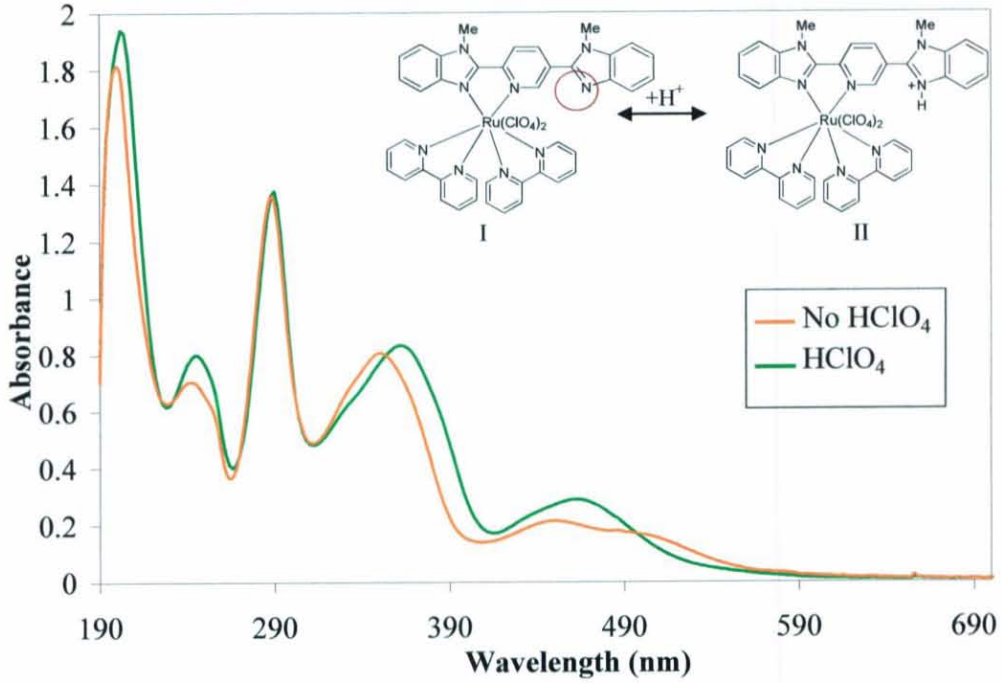

Figure 3.12: Electronic absorption spectrum of $[Ru(\mathbf{Me_2\text{-}pybbim})(bpy)_2]^{2+}$ in acetonitrile under N_2 and in the absence and presence of $HClO_4$ at ambient temperature.

energies than that of $[Ru(\mathbf{Me\text{-}pybim})(bpy)_2]^{2+}$ (630 nm). This red shift for $[Ru(\mathbf{pybtz})(bpy)_2]^{2+}$ can be explained by the π-acceptor strength of the **pybtz** ligand that enhances π-back donation from the metal to ligand [Ru(dπ) to pybtz (π*)] causing a more stable ^{3}MLCT state compared to that of $[Ru(\mathbf{Me\text{-}pybim})(bpy)_2]^{2+}$. For $[Ru(\mathbf{Me_2\text{-}pybbim})(bpy)_2]^{2+}$, the shift of the MLCT band to the lower energy is related to the **Me_2-pybbim** ligand's extended π conjugation, which allows better delocalization of the MLCT excited state, that is associated with a decrease in non-radiative decay relative to

$[Ru(\mathbf{Me\text{-}pybim})(bpy)_2]^{2+}$ [141]. This is also supported by the redox potentials from CV relative to those of $[Ru(\mathbf{Me\text{-}pybim})(bpy)_2]^{2+}$. Figure 3.11 shows that quenching of the excited states of the monometallic ruthenium polypyridyl complexes follow the order of **Me-pybim <Me_2-pybbim <pybtz,** which may arise due to the difference in the energy gaps between ^{3}MLCT-^{3}MC states.

The **Me_2-pybbim** ligand has one uncoordinated -N- and is obviously susceptible to protonation. Figure 3.12 shows the effect of acid on the absorption spectrum of $[Ru(\mathbf{Me_2\text{-}pybbim})(bpy)_2]^{2+}$. In the presence of just a drop of $HClO_4$ (11.0 M) added to a solution of the complex in acetonitrile, the solution color changes from orange to an orange-red color. In the absorption spectrum, the absorption due to ligand's π-π^* is shifted by 10 nm to lower energy (red shift). Also, the broad MLCT band at 464 nm is split into two peaks. The highest energy of the MLCT is blue shifted to 450 nm and the lowest energy one is red shifted to 510 nm. It could be assumed that upon protonation the ligand's LUMO $\pi*$ energy might have been lowered, that might cause this splitting and shifting of the MLCT band to lower energy.

Table 3.3: Absorption and emission maxima data for the monometallic and bimetallic complexes in acetonitrile at ambient temperature.

Complexes	λ_{max} (L) (nm)	λ_{max} (MLCT) (nm)	Emission max (nm) [excitation at 460 nm]
$[Ru(bpy)_3]^{2+}$	288	422, 457	610
$[Ru(\mathbf{Me\text{-}pybim})(bpy)_2]^{2+}$	323, 341	428, 463	630
$[Ru(\mathbf{pybtz})(bpy)_2]^{2+}$	325, 350	442, 485	690
$[Ru(\mathbf{Me_2\text{-}pybbim})(bpy)_2]^{2+}$	365	466	681
$[\{(bpy)_2Ru\}_2(\mathbf{Me_2\text{-}pzbbim})]^{4+}$	410, 430	630	
$[\{(bpy)_2Ru\}_2(\mathbf{Me_2\text{-}py_2bbim})]^{4+}$	363	441, 463	640
$[\{(bpy)_2Ru\}_2(\mathbf{py_2tbtz})]^{4+}$	365, 385	440, 525	735
$[\{(bpy)_2Ru\}_2(\mathbf{pzbbtz})]^{4+}$	411, 431	660	

Table 3.4: Absorption, emission maxima, excitation wavelength and HOMO-LUMO energy gap of some monometallic complexes.

Complexes	Excitation at	E_{ab} (eV)	E_{em} (eV)	HOMO-LUMO energy gap (eV)*
$[Ru(\mathbf{Me\text{-}pybim})(bpy)_2]^{2+}$	460 nm	2.70	1.89	2.30
$[Ru(\mathbf{pybtz})(bpy)_2]^{2+}$		2.56	1.89	2.23
$[Ru(\mathbf{Me_2\text{-}pybbim})(bpy)_2]^{2+}$		2.67	1.77	2.22
$[Ru(bpy)_3]^{2+}$		2.70	2.01	2.35

*$(E_{ab} + E_{em})/2 = \Delta E_{oo}$

Table 3.5: Excitation wavelength, emission intensity, absorbance, and emission quantum yields of some monometallic complexes in CH_3CN at room temperature.

Complexes	Excitation at	Integrated emission intensity	Absorbance at 460 nm	Quantum yield Φ [a]
$[Ru(\mathbf{Me\text{-}pybim})(bpy)_2]^{2+}$	460 nm	2.5267×10^7	0.11	0.022
$[Ru(\mathbf{pybtz})(bpy)_2]^{2+}$		1.0239×10^7	0.11	0.0089
$[Ru(\mathbf{Me_2\text{-}pybbim})(bpy)_2]^{2+}$		1.6258×10^7	0.12	0.013
$Ru(bpy)_3(ClO_4)_2$		5.8233×10^7	0.097	0.062*

* For $Ru(bpy)_3^{2+}$ in acetonitrile at room temperature [142]

a: $\varphi_{em} = \varphi_s \times \int/\int_{std} \times A_s/A \times \eta^2/\eta_s^2$, $\int$ = the integrated emission intensities of the sample, φ_s = quantum yield of the std. $Ru(bpy)_3^{2+}$, $\int_{std}$ = the integrated emission intensities of the std. $Ru(bpy)_3^{2+}$, η^2/η_s^2 = refractive index of the media. A_s = Absorbance of the sample, A = absorbance of the std. $Ru(bpy)_3^{2+}$.

Table 3.3 summarizes absorption and emission maxima for the monometallic and bimetallic complexes studied. Tables 3.4 and 3.5 report HOMO-LUMO energy gaps and the quantum yields of all monometallic complexes relative to $Ru(bpy)_3^{2+}$ in the same solvent mixture as the standard [143]. It was found that quantum yield and HOMO-LUMO energy gap for $[Ru(\mathbf{pybtz})(bpy)_2]^{2+}$ is lower relative to $[Ru(\mathbf{Me\text{-}pybim})(bpy)_2]^{2+}$; due to the **pybtz** ligand's π-acceptor properties relative to the **Me-pybim** ligand. It is interesting that the quantum yield for $[Ru(\mathbf{pybtz})(bpy)_2]^{2+}$ was found to be similar to that of the -S- containing $Ru(\mathbf{bth})_3^{2+}$ (**bth** = 2,2'-bithiazole) [144]. Whereas, $[Ru(\mathbf{Me_2}$-

pybbim)$(bpy)_2]^{2+}$ also shows a lower quantum yield and HOMO-LUMO energy gap relative to $[Ru(\textbf{Mepybbim})(bpy)_2]^{2+}$ and could be related to **Me_2-pybbim** ligand's extended π conjugation (electron delocalization) relative to **Me-pybim** ligand. The energy difference in ^{3}MLCT-^{3}MC states for different ligands in the corresponding complexes could be responsible for the low quantum yields and possibly for the low HOMO-LUMO energy gap also.

3.5.2 Bimetallic complexes

3.5.2.1 $[\{(bpy)_2Ru\}_2(\textbf{Me}_2\textbf{-pzbbim})]^{4+}$ and $[\{(bpy)_2Ru\}_2(\textbf{pzbbtz})]^{4+}$

Figure 3.13 illustrates absorption spectra for two pyrazine based bimetallic complexes, for comparison between $[\{(bpy)_2Ru\}_2(\textbf{Me}_2\textbf{-pzbbim})]^{4+}$ and $[\{(bpy)_2Ru\}_2(\textbf{pzbbtz})]^{4+}$. It can be noted that for bimetallic complexes, the absorptions (extinction coefficient values) are higher and the BL's π-π*, and MLCT bands are shifted to lower energy relative to $Ru(bpy)_3^{2+}$. The region from 360 nm to 490 nm shows the characteristic bands for pyrazine systems. It is also found that, the absorption spectra for both bimetallic complexes are very similar to each other except that the lowest energy MLCT band at 630 nm for $[\{(bpy)_2Ru\}_2(\textbf{Me}_2\textbf{-pzbbim})]^{4+}$ is slightly blue shifted (30 nm) compared to the corresponding 660 nm transition for $[\{(bpy)_2Ru\}_2(\textbf{pzbbtz})]^{4+}$, which is in agreement with the electrochemical properties (redox potentials).

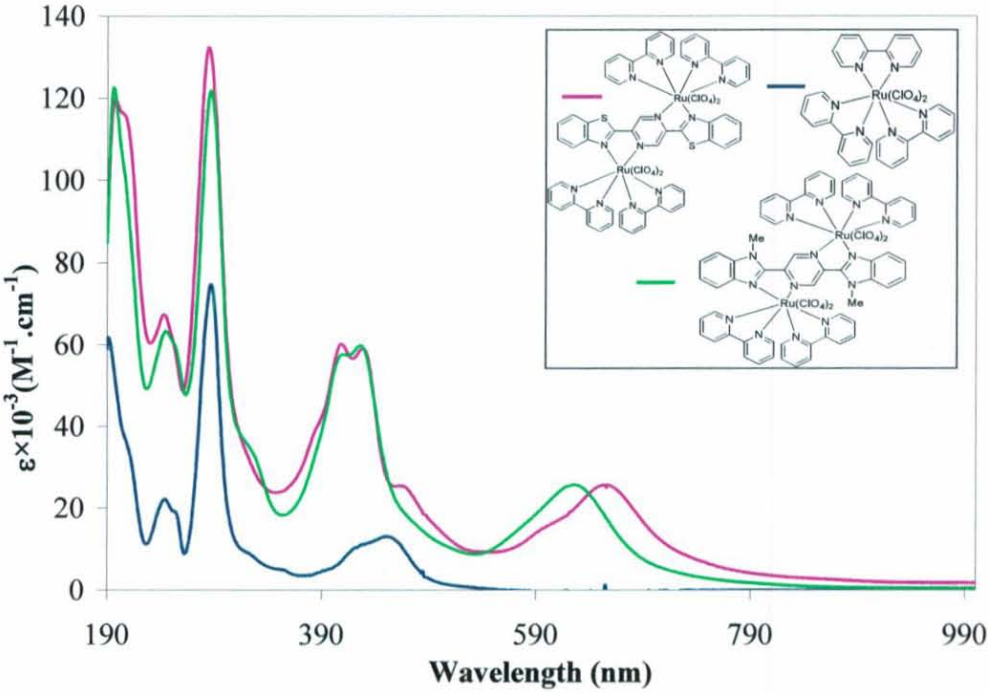

Figure 3.13: Electronic absorption spectra of $[\{(bpy)_2Ru\}_2(\mathbf{Me_2\text{-}pzbbim})]^{4+}$, $[\{(bpy)_2Ru\}_2(\mathbf{pzbbtz})]^{4+}$, and $Ru(bpy)_3^{2+}$ in CH_3CN at ambient temperature.

Figure 3.14 shows emission spectra of $[\{(bpy)_2Ru\}_2(\mathbf{pzbbtz})]^{4+}$, and $[\{(bpy)_2Ru\}_2(\mathbf{Me_2\text{-}pzbbim})]^{4+}$ and provide the excited state properties of both complexes. Compared to the emission spectrum of $Ru(bpy)_3^{2+}$, neither of the complexes show significant emission over the scanned wavelength region. The emission band could be possibly shifted out of the scanned range and/or quenched. A shifting of the emission band can be explained by the fact that, for bimetallic metal complexes with strong electronic interactions between the two metal centers, their MLCT bands move to lower energy as the metal–metal separation decreases [145]. However, both spectra were scanned up to 1000 nm and still

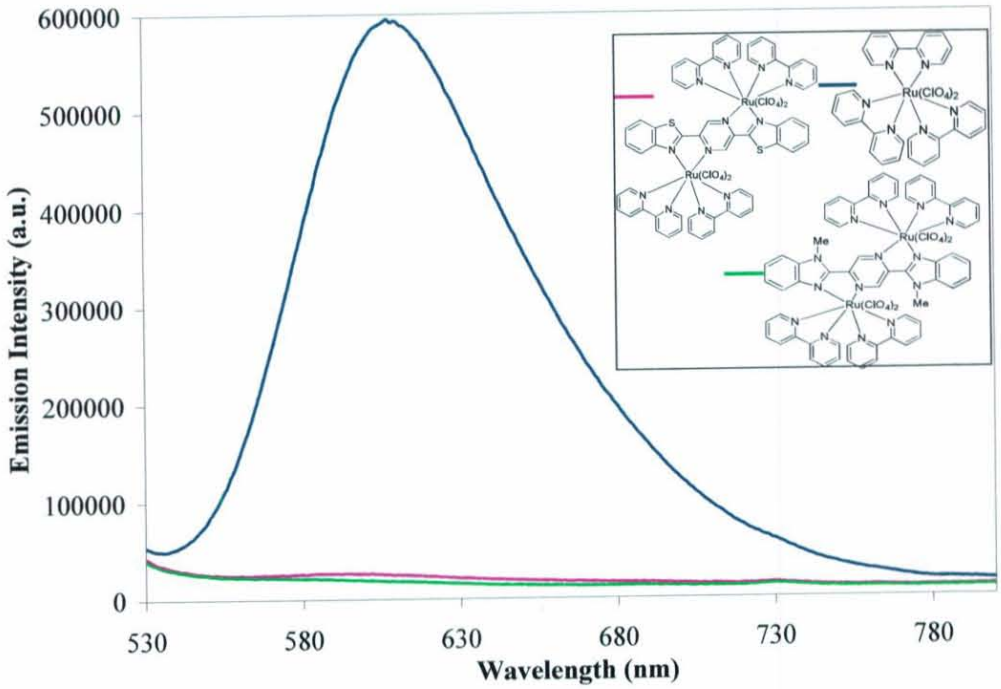

Figure 3.14: Electronic emission spectrums of $[\{(bpy)_2Ru\}_2(\mathbf{pzbbtz})]^{4+}$, $[\{(bpy)_2Ru\}_2(\mathbf{Me_2\text{-}pzbbim})]^{4+}$ and $Ru(bpy)_3^{2+}$ in CH_3CN at ambient temperature.

no emission was observed. From this observation, it can be assumed that both of the emission bands are quenched. The possible mechanism for this quenching could be related to the intermolecular electronic energy transfer from the upper lying ^{3}MLCT levels of the various components, which is a common phenomenon and has been reported for the similar pyrazinyl ligand based complex $[(bpy)_2Ru(\mathbf{dpp})](PF_6)_2$ [146-147].

3.5.2.2 $[\{(bpy)_2Ru\}_2(\mathbf{py_2tbtz})]^{4+}$ and $[\{(bpy)_2Ru\}_2(\mathbf{pzbbtz})]^{4+}$

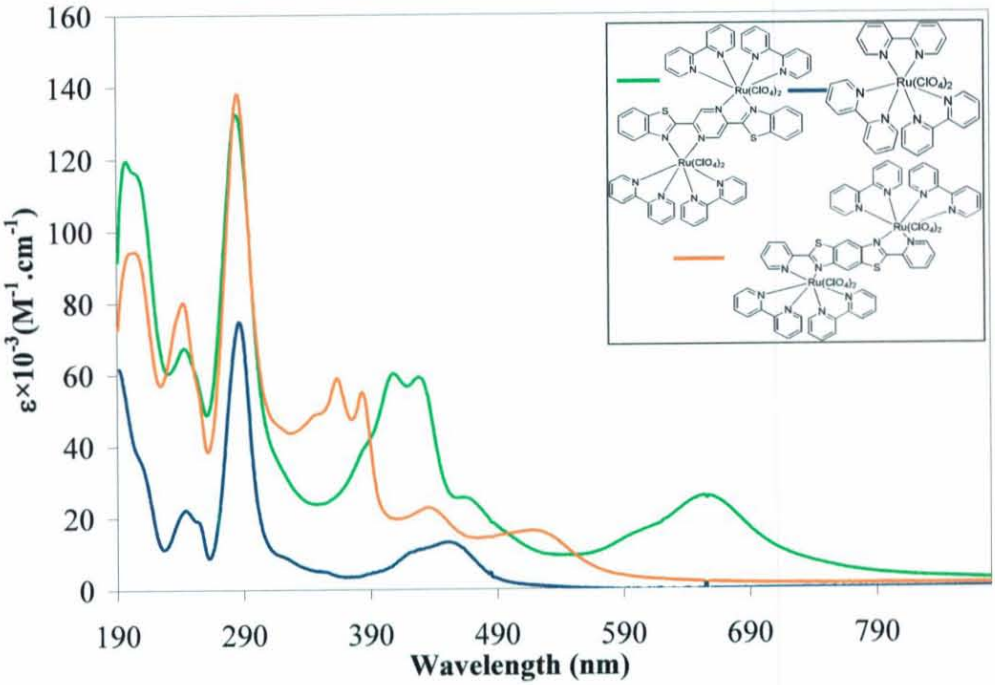

Figure 3.15: Electronic absorption spectra of $Ru(bpy)_3^{2+}$, $[\{(bpy)_2Ru\}_2(\mathbf{py_2tbtz})]^{4+}$, and $[\{(bpy)_2Ru\}_2(\mathbf{pzbbtz})]^{4+}$ in CH_3CN at ambient temperature.

The absorption spectrum of $[\{(bpy)_2Ru\}_2(\mathbf{py_2tbtz})]^{4+}$ is compared with that of $[\{(bpy)_2Ru\}_2(\mathbf{pzbbtz})]^{4+}$ in Figure 3.15. It can be seen that the MLCT band for $[\{(bpy)_2Ru\}_2(\mathbf{py_2tbtz})]^{4+}$ is splited into two peaks. Since the electrochemical studies indicate that the first two reductions are associated with the **py₂tbtz** ligand, the lower energy MLCT absorption band is assigned to the Mdπ $\rightarrow$BL's π^* transition and the higher energy MLCT absorption band is attributed to the Mdπ $\rightarrow$ bpy π^* transition. It can

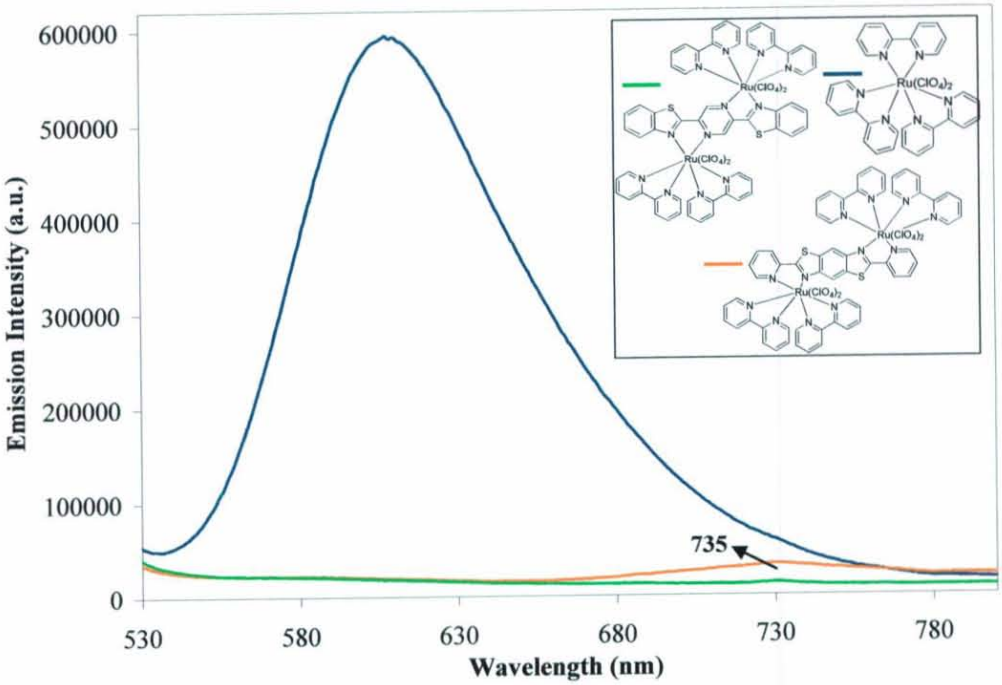

Figure 3.16: Electronic emission spectra of $Ru(bpy)_3^{2+}$, $[\{(bpy)_2Ru\}_2(\mathbf{py_2tbtz})]^{4+}$ and $[\{(bpy)_2Ru\}_2(\mathbf{pzbbtz})]^{4+}$ in CH_3CN at ambient temperature.

be noted that compared to $[\{(bpy)_2Ru\}_2(\mathbf{pzbbtz})]^{4+}$, the MLCT band for $[\{(bpy)_2Ru\}_2(\mathbf{py_2tbtz})]^{4+}$ is shifted to higher energy. This is consistent with the redox potentials for the complexes. From X-ray crystallography data it was found that the Ru-Ru distance for $[\{(bpy)_2Ru\}_2(\mathbf{pzbbtz})]^{4+}$ is 6.89 Å, but 9.13 Å for $[\{(bpy)_2Ru\}_2$-$(\mathbf{py_2tbtz})]^{4+}$. Possibly a weak electronic interaction between the metal centers for $[\{(bpy)_2Ru\}_2(\mathbf{py_2tbtz})]^{4+}$ could shift the MLCT band to higher energy.

Emission spectra (see Figure 3.16) for the complexes $[\{(bpy)_2Ru\}_2(\mathbf{py_2tbtz})]^{4+}$ and $[\{(bpy)_2Ru\}_2(\mathbf{pzbbtz})]^{4+}$ explained their excitation properties. The emission bands

for the bimetallic complexes clearly showed how the metal-metal distances can influence the MLCT band. For example, the complex $[\{(bpy)_2Ru\}_2(\mathbf{py_2tbtz})]^{4+}$ showed a very weak emission band at 735 nm, whereas $[\{(bpy)_2Ru\}_2(\mathbf{pzbbtz})]^{4+}$ did not have any emission band in the scanned wavelength region. This result might be due to the strong electronic interaction between the two metal centers in $[\{(bpy)_2Ru\}_2(\mathbf{pzbbtz})]^{4+}$ due to a lower metal-metal distance in the **pzbbtz** ligand relative to the **py$_2$tbtz** ligand.

3.5.2.3 $[\{(bpy)_2Ru\}_2(\mathbf{Me_2\text{-}py_2bbim})]^{4+}$

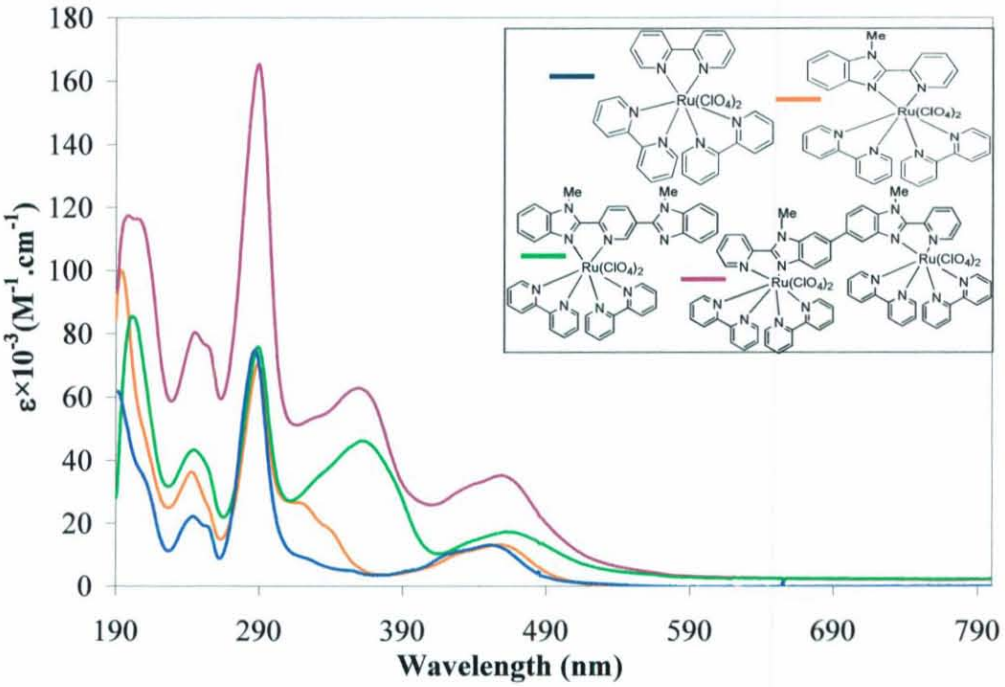

Figure 3.17: Electronic absorption spectra of $Ru(bpy)_3^{2+}$, $[Ru(\mathbf{Me\text{-}pybim})(bpy)_2]^{2+}$, $[Ru(\mathbf{Me_2\text{-}pybbim})(bpy)_2]^{2+}$, and $[\{(bpy)_2Ru\}_2(\mathbf{Me_2\text{-}py_2bbim})]^{4+}$ in CH_3CN at ambient temperature.

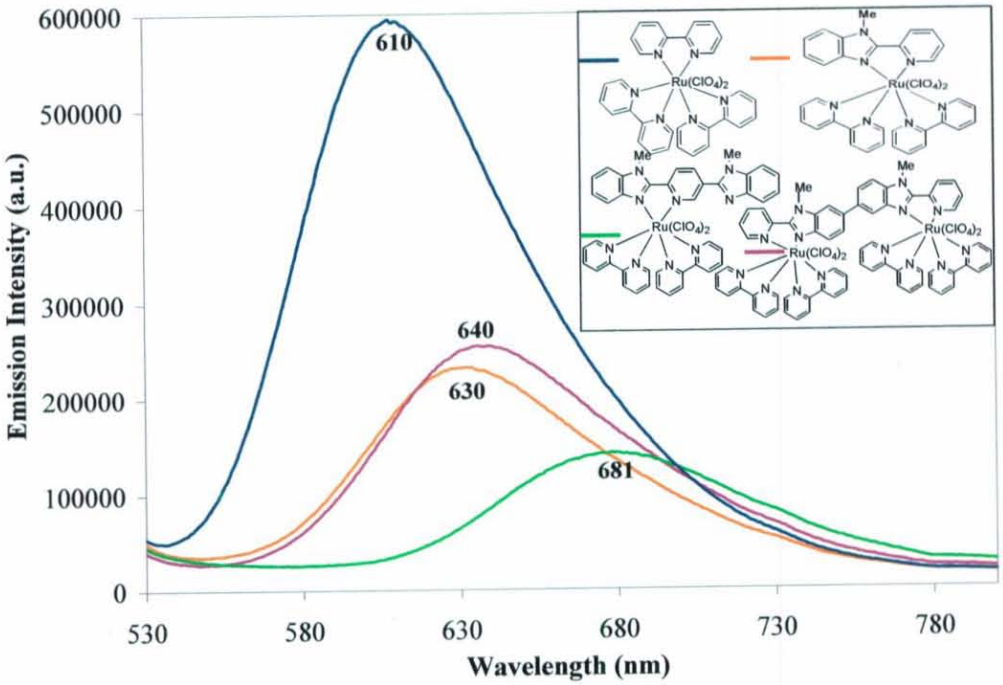

Figure 3.18: Electronic emission spectra of $Ru(bpy)_3^{2+}$, $[Ru(\mathbf{Me\text{-}pybim})(bpy)_2]^{2+}$, $[Ru(\mathbf{Me_2\text{-}pybbim})(bpy)_2]^{2+}$, and $[\{(bpy)_2Ru\}_2(\mathbf{Me_2\text{-}py_2bbim})]^{4+}$ in CH_3CN at ambient temperature.

The absorption spectrum of bimetallic $[\{(bpy)_2Ru\}_2(\mathbf{Me_2\text{-}py_2bbim})]^{4+}$ is compared to spectra of the related monometallic complexes, $[Ru(\mathbf{Me\text{-}pybim})(bpy)_2]^{2+}$ and $[Ru(\mathbf{Me_2\text{-}pybbim})(bpy)_2]^{2+}$ in Figure 3.17. It can be seen that $[\{(bpy)_2Ru\}_2(\mathbf{Me_2\text{-}py_2bbim})]^{4+}$ shows a **MLCT** band at a wavelength similar to the two monometallic complexes, but with a higher extinction coefficient value. The higher extinction coefficient for $[\{(bpy)_2Ru\}_2(\mathbf{Me_2\text{-}py_2bbim})]^{4+}$ might be related to its bimetallic nature relative to the other two monometallic complexes. The reason for having similar MLCT bands may be

related to the fact that each of the parts behave independently like a single complex $[Ru(\mathbf{Me\text{-}pybim})(bpy)_2]^{2+}$.

Figure 3.18 shows emission spectra of two monometallic complexes $[Ru(\mathbf{Me\text{-}pybim})(bpy)_2]^{2+}$ and $[Ru(\mathbf{Me_2\text{-}pybbim})(bpy)_2]^{2+}$ and a bimetallic ruthenium complex, $[\{(bpy)_2Ru\}_2(\mathbf{Me_2\text{-}py_2bbim})]^{4+}$. It can be noted that the emission maximum for $[\{(bpy)_2Ru\}_2(\mathbf{Me_2\text{-}py_2bbim})]^{4+}$ appears at 640 nm, which is only 10 nm red shifted relative to $[Ru(\mathbf{Me\text{-}pybim})(bpy)_2]^{2+}$ (630 nm). The reason for this small shift of the **MLCT** band for the bimetallic complex can be explained by the fact that in $[\{(bpy)_2Ru\}_2(\mathbf{Me_2\text{-}py_2bbim})]^{4+}$ the two benzimidazoles are joined together by a sigma bond, along which two chromophores can rotate and behave like the simple monometallic

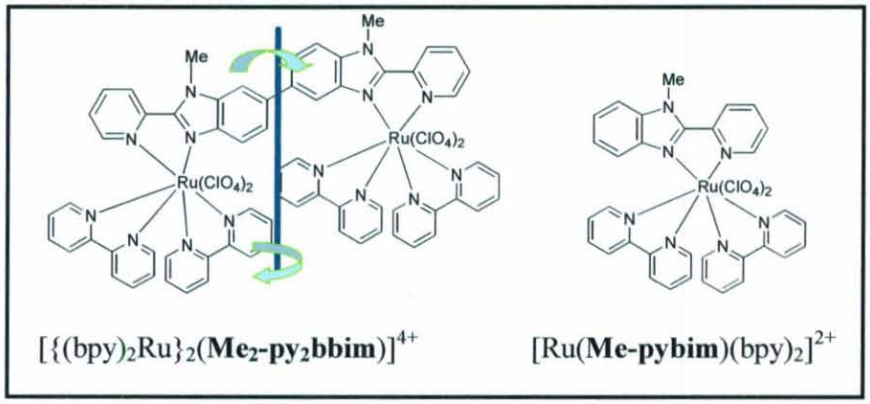

Figure 3.19: Structures of $[\{(bpy)_2Ru\}_2(\mathbf{Me_2\text{-}py_2bbim})]^{4+}$ and $[Ru(\mathbf{Me\text{-}pybim})(bpy)_2]^{2+}$.

complex $[Ru(\mathbf{Me\text{-}pybim})(bpy)_2]^{2+}$ (see Figure 3.19). The quantum yield and HOMO-LUMO energy gap were calculated for this complex. The quantum yield of 0.011 is

smaller relative to that for the monometallic $[Ru(\mathbf{Me\text{-}pybim})(bpy)_2]^{2+}$ complex (0.022). Also, the HOMO-LUMO energy gap for $[\{(bpy)_2Ru\}_2(\mathbf{Me_2\text{-}py_2bbim})]^{4+}$ (2.28 eV) is very close to that for $[Ru(\mathbf{Me\text{-}pybim})(bpy)_2]^{2+}$ (2.30 eV). Both of these factors may be related to its almost similar behavior with the complex $[Ru(\mathbf{Me\text{-}pybim})(bpy)_2]^{2+}$ shown in both emission and absorption spectra.

3.6 Conclusions

Monometallic complexes of ruthenium with **Me-pybim**, **Me_2-pybbim**, and **pybtz** ligands showed different MLCT bands in their emission spectra and similar MLCT bands in their absorption spectra for $d\pi-\pi^*$ interactions. The variation of the MLCT bands mainly arises from the differences in the t_{2g}-π^* transitions. For complexes with **pybtz** and **Me_2-pybbim** ligands, the MLCT bands are red shifted and quenched relative to the **Me-pybim** complex. This could be due to stronger back donation, $d\pi$-π^* with **pybtz** and extended π conjugation with **Me_2-pybbim**. These differences are also reflected in their quantum yields and HOMO-LUMO energy gaps. For bimetallic ruthenium complexes with **pzbbtz** and **Me_2-pzbbim** ligands, it was found that the MLCT bands are nonemissive. Usually for bimetallic complexes with strong metal-metal interactions, their MLCT bands are red shifted because of the intramolecular electronic energy transfer from upper lying ^{3}MLCT levels to the various components. However, for the bimetallic ruthenium complex with the **py_2tbtz** ligand, the emission band was found at 735 nm and for absorption the MLCT bands appeared at higher energy relative to the **pzbbtz** and **Me_2-pzbbim** ligand containing metal complexes. A weak electronic interaction between the metal centers for

$[\{(bpy)_2Ru\}_2(\mathbf{py_2tbtz})]^{4+}$ bimetallic complex could possibly be the reason that the MLCT bands were not shifted to higher wavelengths.

Chapter 4

Electrochemical CO_2 reduction by metal complexes and product analyses

4.1 Introduction

This chapter describes the effect of the synthesized ruthenium monometallic and bimetallic complexes on CO_2 reduction under electrochemical conditions. The cyclic voltammograms under N_2 (described in Chapter 3) were compared with those under CO_2 to observe the effect of the different ligands in the complexes for electrocatalytic activities of CO_2 reduction. Cyclic voltammetry is generally considered as one of the most convenient and informative techniques for the evaluation of electrocatalysts. An active catalyst can be identified and evaluated by monitoring changes in its cyclic voltammogram in the presence of CO_2; for example, an increase in the cathodic current, change of the shapes of the CV, growth of new peaks, and/or shift of potentials can give evidence of catalytic activities. The reverse peak of the cyclic voltammogram might become small [11] (if the product is chemically removed from the vicinity of the electrode) or could disappear (if the product is converted to another product by a fast forward chemical reaction). Thus to elucidate the reaction pathways and to provide chemical information about reaction intermediates, cyclic voltammetry could play an important rule. Also, the technique can yield kinetic information such as rate laws and constants. Other information may be obtained from electrolysis experiments under CO_2, and product analyses. By calculating the faradaic yield of each of the products, the catalytic performances of the electrocalysts can be revealed.

4.2 Electrochemical measurements under CO_2

All electrochemical measurements under CO_2 were carried out using a Pine Instruments AFCBP1 bipotentiostat in CH_3CN/0.1 M Et_4NClO_4, unless otherwise mentioned. A three-chambered gas tight glass electrochemical cell was used with a gas inlet and outlet, and with a flat bottom having a Pt wire connection for an Hg pool electrode. The counter electrode chamber was separated from that of the working electrode by a porous glass frit. An O_2-free environment was maintained by purging the cell with N_2 prior to electrochemical experiments (~10 min) and then the cell was purged with CO_2 [Air Liquide, 99.8% (bone dry grade)].

4.2.1 Monometallic complexes

4.2.1.1 $Ru(bpy)_3^{2+}$

Figure 4.1 shows cyclic voltammetry of $Ru(bpy)_3^{2+}$ in the presence of N_2 and CO_2. The CV with three one electron reversible reduction peaks under N_2 shows significantly different features from that under CO_2. The first reduction peak remains reversible with no increase in current. The second peak becomes quasi reversible with a very small increase in current. The third one is completely irreversible with a large increase in current, which is an indication of catalytic behavior.

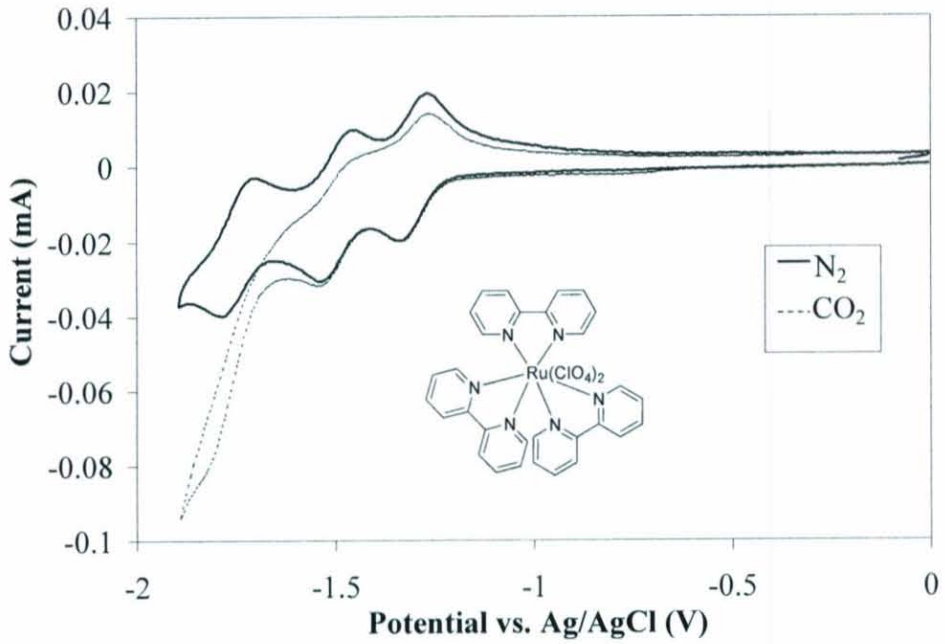

Figure 4.1: Cyclic voltammograms of 1 mM $Ru(bpy)_3(ClO_4)_2$ in CH_3CN/0.1 M Et_4NClO_4 containing 1% water under N_2 and CO_2 at a glassy carbon electrode (at ν = 100 mV/s).

4.2.1.2 $[Ru(\textbf{Me-pybim})(bpy)_2]^{2+}$

Cyclic voltammetry for the reduction waves of $[Ru(\textbf{Me-pybim})(bpy)_2]^{2+}$ [see Figure 4.2] show that, in the presence of CO_2 all three peaks are smaller with no significant shifts in potentials. So this complex can be considered as an inactive catalyst for electrochemical CO_2 reduction. It should be mentioned here that similar results were reported by Tanaka et al. [77] for a complex with a similar stucture.

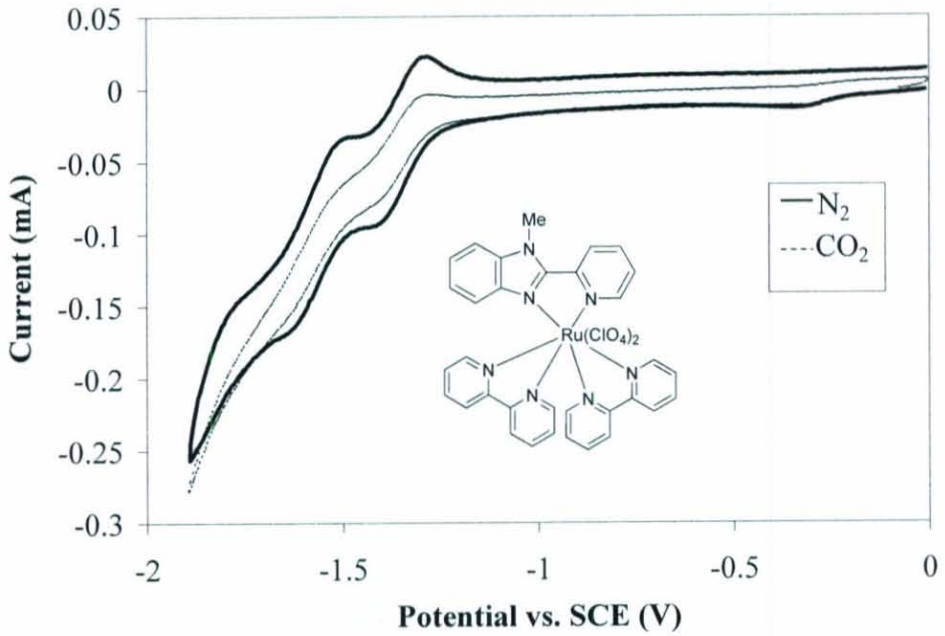

Figure 4.2: Cyclic voltammograms of 1 mM [Ru(**Me-pybim**)$(bpy)_2]^{2+}$ in CH_3CN/0.1 M Et_4NClO_4 containing 1% water under N_2 and CO_2 at a glassy carbon electrode (at ν = 100 mV/s).

4.2.1.3 [Ru(**Me_2-pybbim**)$(bpy)_2]^{2+}$

Figure 4.3 shows significant changes in the cyclic voltammetry for all the reduction waves of [Ru(**Me_2-pybbim**)$(bpy)_2]^{2+}$ in the presence CO_2. This complex shows three reversible reduction peaks under N_2. In the presence of CO_2 the first peaks become irreversible with a slightly increased cathodic current and the cathodic peak potential is shifted in the negative region by 20 mV. The second peak also becomes irreversible with a large increase in the cathodic current (almost two times that under N_2) and the cathodic

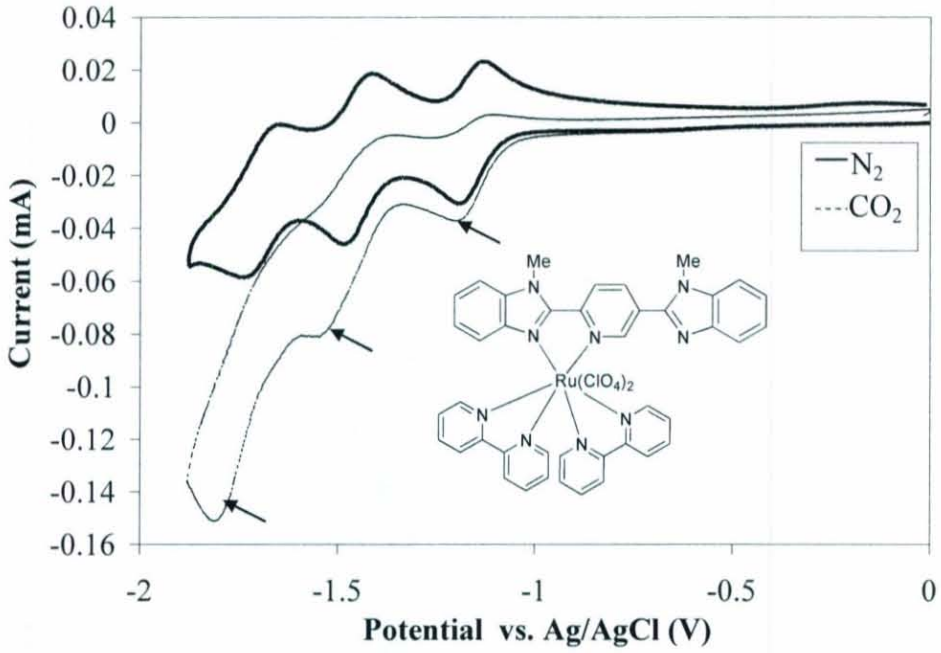

Figure 4.3: Cyclic voltammograms of 1 mM $[Ru(\mathbf{Me_2\text{-}pybbim})(bpy)_2]^{2+}$ in CH_3CN/0.1 M Et_4NClO_4 containing 1% water under N_2 and CO_2 at a glassy carbon electrode (at ν = 100 mV/s).

potential is also shifted negatively by ca. 60 mV. The third peak exhibits an even larger increase in cathodic current. It can be deduced that this complex has good catalytic activity in the presence of CO_2. It was suggested that, the asymmetric nature of the ligand could be the reason for the high activity of this type of complex, which would have possibly provided a coordination site for CO_2 by dechelation [77].

The benzimidazole complex $[Ru(\mathbf{pybbim})(bpy)_2]^{2+}$ shows different behavior (see Figure 4.4) from that of the methyl-benzimidazole complex $[Ru(\mathbf{Me_2\text{-}pybbim})(bpy)_2]^{2+}$.

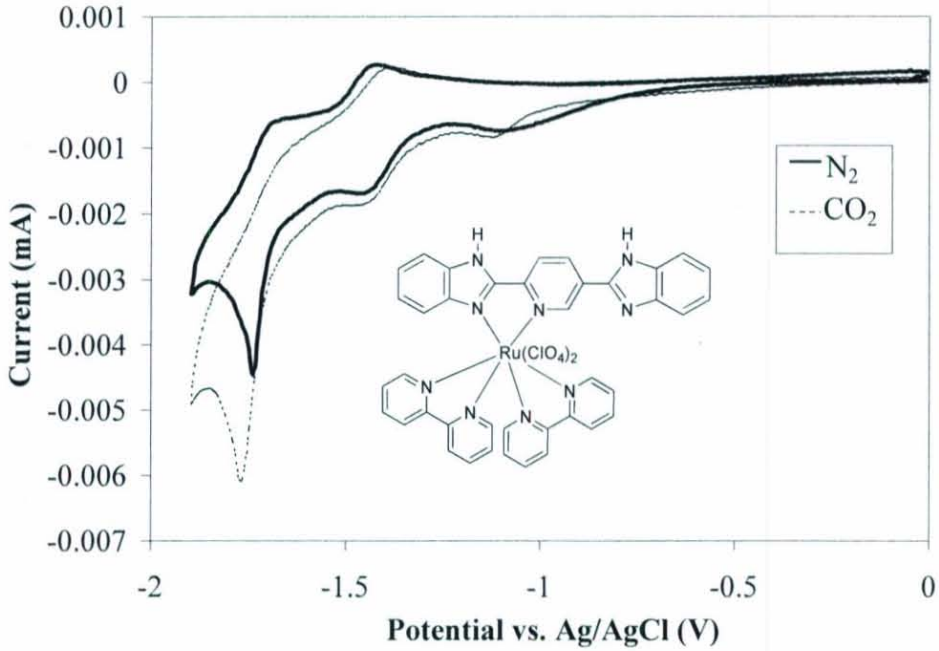

Figure 4.4: Cyclic voltammograms of 1 mM $[Ru(\textbf{pybbim})(bpy)_2]^{2+}$ in CH_3CN/0.05 M Et_4NClO_4 containing 1% water under N_2 and CO_2 at a platinum electrode (at v = 100 mV/s).

The **pybbim**-containing complex actually showed a lower catalytic effect on electrochemical CO_2 reduction than that of the **Me_2-pybbim** containing complex. The first peak becomes irreversible under N_2, which in the presence of CO_2 still maintained its irreversibility with a shift to cathodic potentials by ca. 50 mV. The second peak remained reversible with a slight increase in current and a positive shift of the formal potential by ca. 10 mV. The third peak also remained irreversible with an increase in current. In the presence of CO_2 it seems that this complex behaved similarly to $Ru(bpy)_3^{2+}$.

4.2.1.4 $[Ru(\mathbf{pybtz})(bpy)_2]^{2+}$

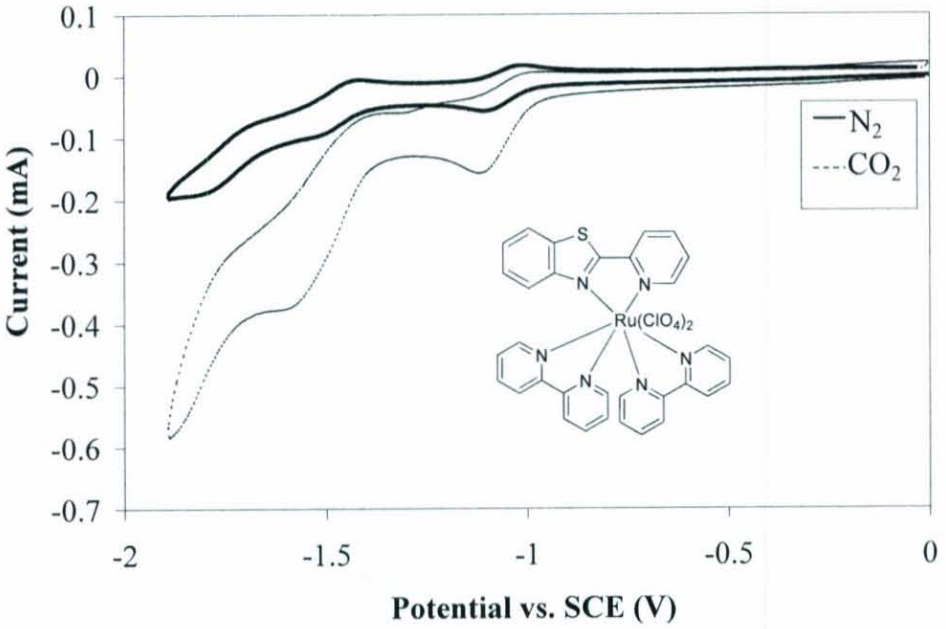

Figure 4.5: Cyclic voltammograms of 1 mM $[Ru(\mathbf{pybtz})(bpy)_2]^{2+}$ in CH_3CN/0.1 M Et_4NClO_4 containing 1% water under N_2 and CO_2 at a glassy carbon electrode (at ν = 100 mV/s).

$[Ru(\mathbf{pybtz})(bpy)_2]^{2+}$ showed a profound electrocatalytic effect on CO_2 reduction relative to that of the similar **Me-pybim** complex [see Figure 4.5]. It can be observed from Figure 4.5 that all three reversible one electron peaks under N_2 became irreversible under CO_2. For the first peak, the current found increased by almost a factor of two with a slight (ca. 10 mV) negative shift in potential. It is definitely an indication of an electrocatalytic process. For the second peak, the current increases to almost four times as high as that

under N_2 with a shift in the cathodic potential by ca. 90 mV. The third peak is also shifted under the scanned potential region with an increase in current. It is interesting to mention here that the electrocatalytic effect of CO_2 on the first wave was found to be variable when this experiment was repeated, a little electrocatalytic activity was observed for the first wave in most experiments.

4.2.2 Bimetallic complexes

4.2.2.1 $[\{(bpy)_2Ru\}_2(\mathbf{Me_2\text{-}py_2bbim})]^{4+}$

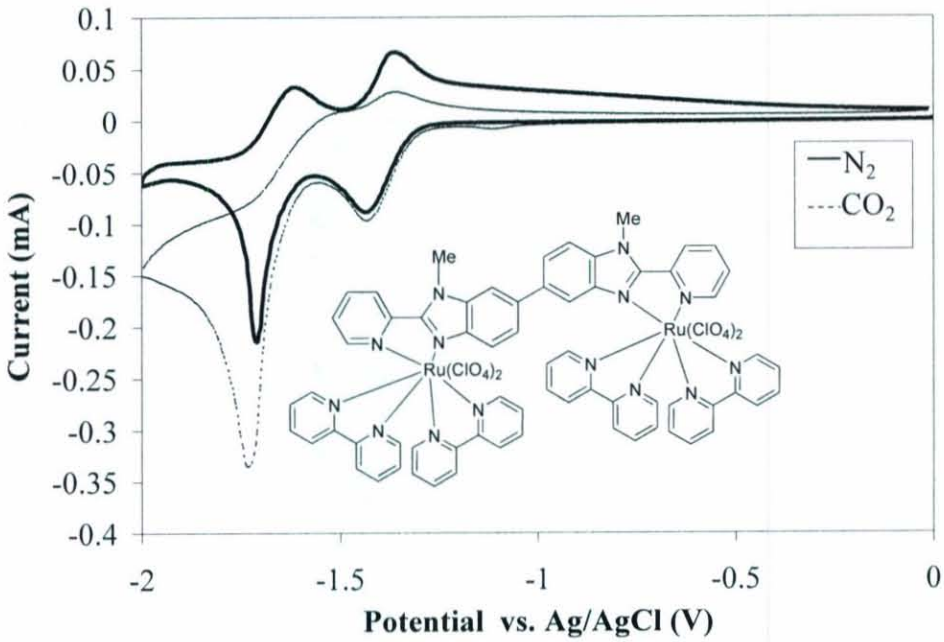

Figure 4.6: Cyclic voltammograms of 1 mM $[\{(bpy)_2Ru\}_2(\mathbf{Me_2\text{-}py_2bbim})]^{4+}$ in CH_3CN/0.1 M Bu_4NBF_4 containing 1% water under N_2 and CO_2 at a glassy carbon electrode (at ν = 100 mV/s).

Cyclic voltammograms of $[\{(bpy)_2Ru\}_2(\mathbf{Me_2\text{-}py_2bbim})]^{4+}$ in the presence and absence of CO_2 show the activities towards CO_2 reduction (see Figure 4.6). Under CO_2, the first peak became quasi-reversible to irreversible, with a slightly enhanced cathodic current. The second peak became irreversible and the cathodic potential was shifted by 30 mV to lower potentials with an enhancement in the cathodic current. All of these things indicated that this complex is active for CO_2 reduction. The mechanism for this kind of activity might be related to the asymmetric nature of the ligand as was also reported by Tanaka et al. [77] for similar complexes [see Figure 4.7].

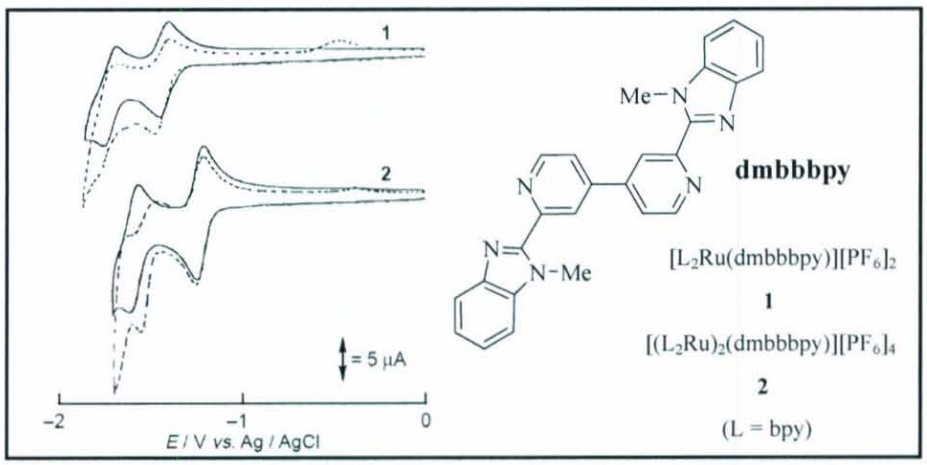

Figure 4.7: Structures and cyclic voltammograms of 0.3 mM **1** or **2** in 0.1 M Bu_4NBF_4/MeCN at a glassy carbon electrode (3.0 mm) under N_2 (—) and CO_2 (----) atmospheres. Scan rate = 50 mV/s. Reproduced with permission from *Chem. Commun.* 1998, 249 [77]. Copyright ©1998 Royal Society of Chemistry.

The formal potentials for this complex are an indication that the **Me_2-py_2bbim** ligand has strong π-electron donating properties. The possible activation of CO_2 by this complex can be explained by the reduced form of the ruthenium center having high enough electron density to dechelate either **Me_2-py_2bbim** (similar to Tanaka's catalyst [77]) or the **bpy** ligand to provide a coordination site on Ru for CO_2 activation.

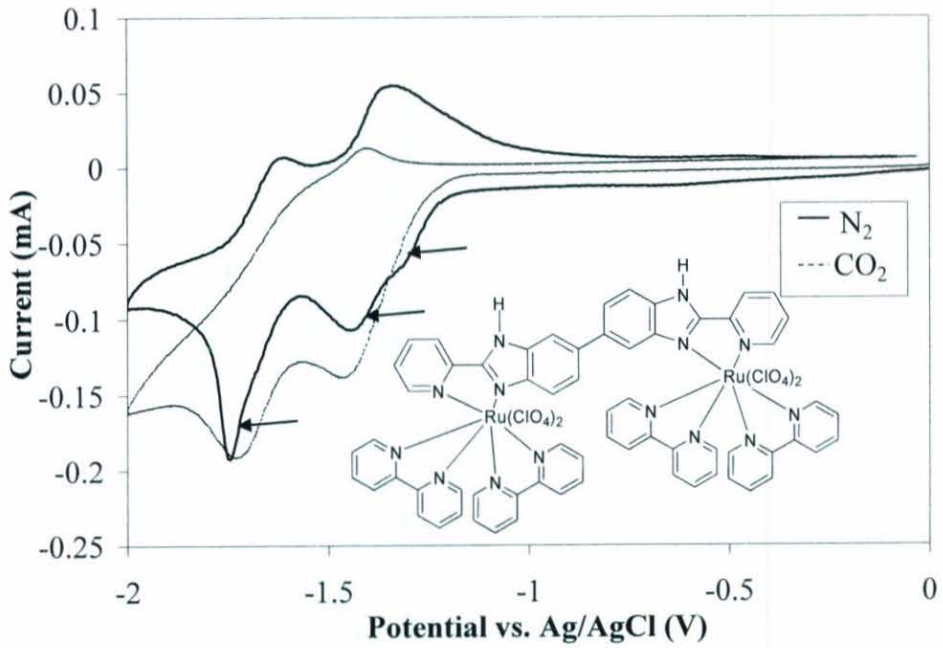

Figure 4.8: Cyclic voltammograms of 1 mM $[\{(bpy)_2Ru\}_2(\mathbf{py_2bbim})]^{4+}$ in CH_3CN/0.1 M Bu_4NBF_4 containing 1% water under N_2 and CO_2 at a glassy carbon electrode (at ν = 100 mV/s).

The benzimidazole complex $[\{(bpy)_2Ru\}_2(\mathbf{py_2bbim})]^{4+}$ showed different behavior

from that of the methyl-benzimidazole complex $[\{(bpy)_2Ru\}_2(\mathbf{Me_2\text{-}py_2bbim})]^{4+}$, as described in the Figure 4.8. In the presence of N_2 this complex showed three reduction waves [similar to what was mentioned by Haga et al. [99 (a)]. In the presence of CO_2 the first two peaks were both shifted to more negative potentials and became coincident. The second peak became quasi-reversible with a negative shift in the formal potential by ca. 50 mV and an increase in current. The second peak showed irreversiblity with no subsequent increase in the cathodic current.

4.2.2.2 $[\{(bpy)_2Ru\}_2(\mathbf{py_2tbtz})]^{4+}$

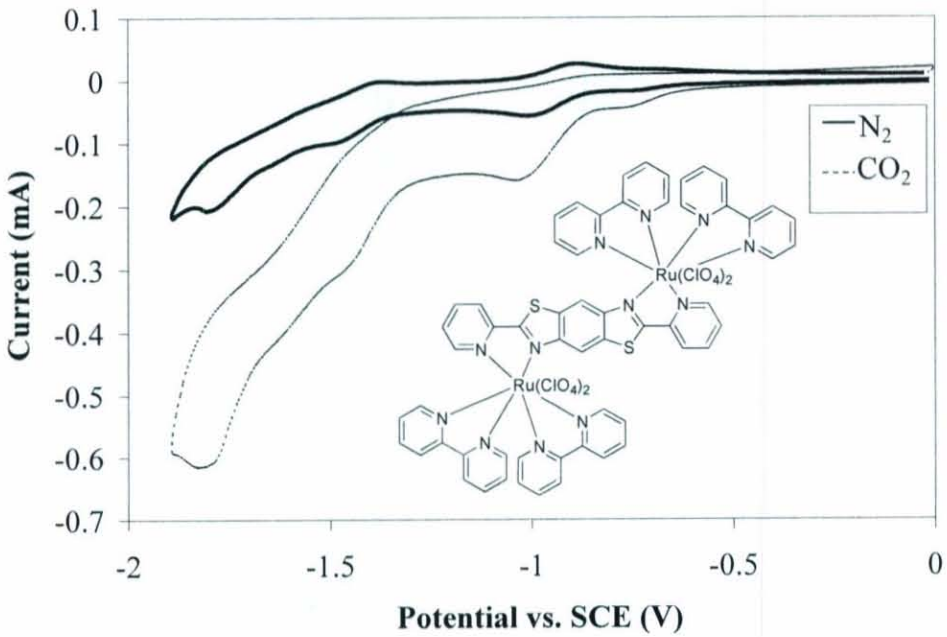

Figure 4.9: Cyclic voltammograms of 1 mM $[\{(bpy)_2Ru\}_2(\mathbf{py_2tbtz})]^{4+}$ in CH_3CN/0.1 M Et_4NClO_4 (1% water) under N_2 and CO_2 at a glassy carbon electrode (at ν = 100 mV/s).

Figure 4.9 shows cyclic voltammograms of the complex $[\{(bpy)_2Ru\}_2(\mathbf{py_2tbtz})]^{4+}$ in the presence of CO_2 and N_2. Under CO_2 the first peak became irreversible with a substantial increase in current (almost two times that under N_2) and the potential is shifted negatively by 10 mV. This shift in potential and increase in current are an indication of an electrocatalytic process. The second peak was found to be irreversible with an increase in catalytic current almost three times as high as that under N_2. On the other hand the third peak demonstrated a large increase in the cathodic current. This is obviously very good electrocatalytic behavior.

The profound electrocatalytic effect shown by this complex could be explained by the fact that there is a weak electronic interaction (from $\Delta E°$ of CV) between the metal centers and the **py_2tbtz** ligand acts essentially individually with each of the ruthenium centres, which results in similar behavior to that of the monometallic complex $[Ru(\mathbf{pybtz})(bpy)_2]^{2+}$. It is interesting that during the reduction under N_2 electron density seems not to be delocalized over the **py_2tbtz** ligand (which would have shown two reduction waves instead of one).

4.2.2.3 $[\{(bpy)_2Ru\}_2(\mathbf{Me_2\text{-}pzbbim})]^{4+}$

A different scenario is shown for $[\{(bpy)_2Ru\}_2(\mathbf{Me_2\text{-}pzbbim})]^{4+}$ in the presence of CO_2 from those of the two other bimetallic complexes [see Section 4.2.2.1 and 4.2.2.2]. Figure 4.10 shows the cyclic voltammograms (under N_2 and CO_2) where the first two reversible peaks become irreversible under CO_2 with a slightly shift in the cathodic potential to the negative region. But when these peaks were scanned individually, both of them showed

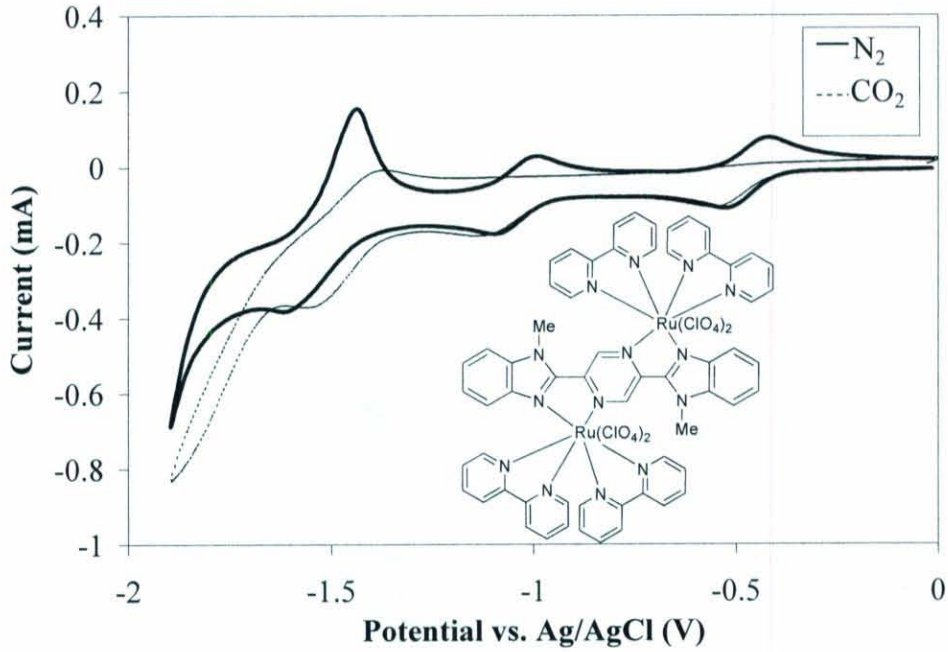

Figure 4.10: Cyclic voltammograms of 1 mM $[\{(bpy)_2Ru\}_2(\mathbf{Me_2\text{-}pzbbim})]^{4+}$ in CH_3CN/0.1 M Et_4NClO_4 containing 1% water under N_2 and CO_2 at a glassy carbon electrode (at ν = 100 mV/s).

reversible behavior. On the other hand, the third peak maintained its reversibility with a shifting in cathodic potentials to the positive (ca. 60 mV) direction with subsequently no increase in the cathodic current. The **Me_2-pzbbim** ligand of this complex is highly π-accepting in nature and the stronger π-back donation should have made the Ru centre less electron rich which in turn could support preservation of the ligand and would reasonably inhibit binding of CO_2 to the Ru centre. All these combined effects might be expected to result in the inactivity of the complex towards electrocatalytic reduction of CO_2.

4.2.2.4 $[\{(bpy)_2Ru\}_2(\mathbf{pzbbtz})]^{4+}$

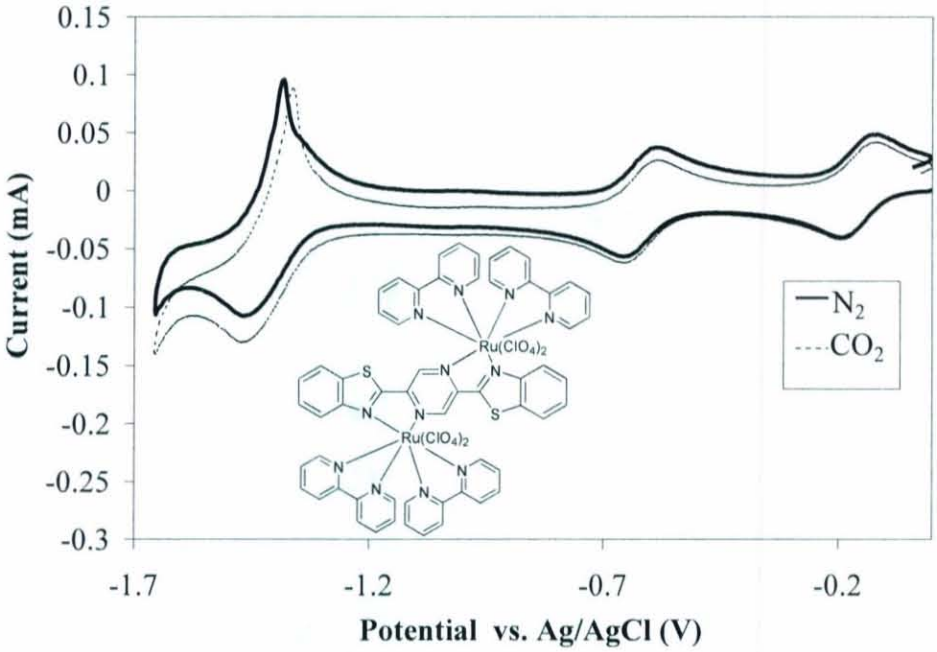

Figure 4.11: Cyclic voltammograms of 1 mM $[\{(bpy)_2Ru\}_2(\mathbf{pzbbtz})]^{4+}$ in CH_3CN/0.1 M Bu_4NBF_4 containing 1% water under N_2 and CO_2 at a glassy carbon electrode (at ν = 100 mV/s).

The cyclic voltammograms in the Figure 4.11 for $[\{(bpy)_2Ru\}_2(\mathbf{pzbbtz})]^{4+}$ under N_2 and CO_2 show similar behavior to that of $[\{(bpy)_2Ru\}_2(\mathbf{Me_2\text{-}pzbbim})]^{4+}$. Under CO_2, all three reduction peaks maintained their reversibility with no increase in current or shift in potentials. The **pzbbtz** ligand has good π-acceptor characteristics creating low electron density on each Ru centre that inhibits bonding with CO_2. This complex is therefore not an effective catalyst for CO_2 reduction.

4.3 Discussion

Complexes with the benzothiazole moiety e.g., $[Ru(\mathbf{pybtz})(bpy)_2]^{2+}$ and $[\{(bpy)_2Ru\}_2(\mathbf{py_2tbtz})]^{4+}$ showed profound activities (in the CV) on CO_2 reductions relative to benzimidazole complexes e.g., $[Ru(\mathbf{Me_2\text{-}pybbim})(bpy)_2]^{2+}$ and $[\{(bpy)_2Ru\}_2(\mathbf{Me_2\text{-}pzbbim})]^{4+}$. Compared to the bimetallic complexes, the monometallic complexes showed higher current in the first reduction waves under CO_2, which was similar to Tanaka's catalysts [77].

The profound electrocatalytic effect for $[Ru(\mathbf{pybtz})(bpy)_2]^{2+}$ under CO_2 could be due to reaction of CO_2 at the benzothiazole moiety or promotion of ligand loss. After the first reduction, the electron would be largely localized on the thiazole ring, so possibly CO_2 could then react at the benzothiazole moiety. However, computational studies [148] did not show any strong evidence for interaction between CO_2 and the reduced benzothiazole ligand to support this hypothesis. Alternatively, electron localization on the thiazole ring after the first reduction could lead the dechelation of one of the bpy's (see arrow on the structure of the $[Ru(\mathbf{pybtz})(bpy)_2]^{2+}$), resulting in activation for CO_2 reduction.

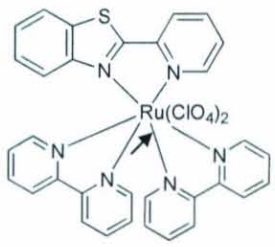

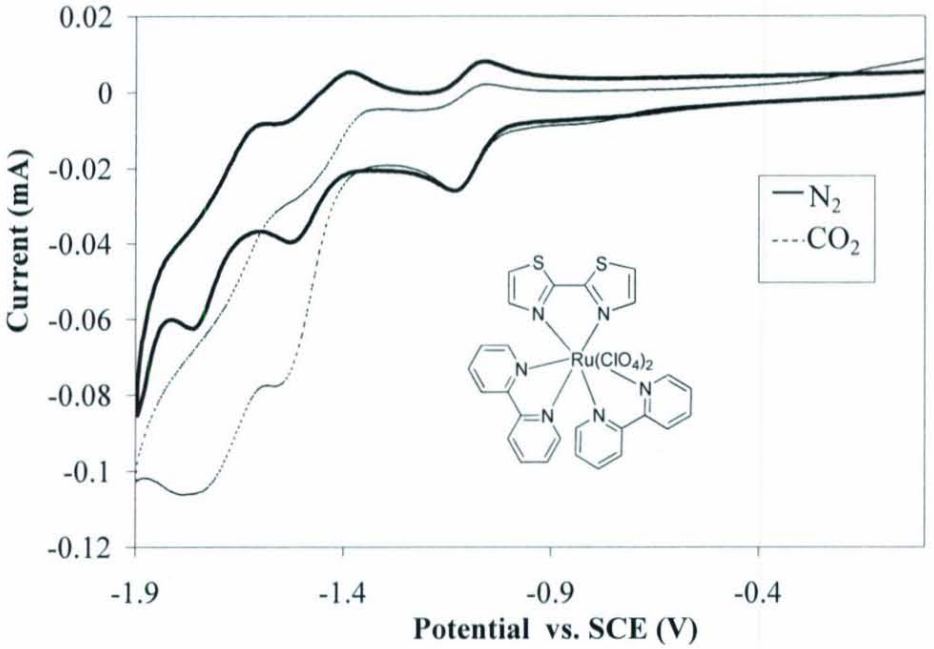

Figure 4.12: Cyclic voltammograms of 1 mM $[(bpy)_2Ru(\mathbf{tz})]^{2+}$ in CH_3CN/0.1 M Et_4NClO_4 containing 1% water under N_2 and CO_2 at a glassy carbon electrode (at ν = 100 mV/s).

In order to further investigate the activity of bithiazole containing complexes for CO_2 reduction, the use of $[(bpy)_2Ru(\mathbf{tz})]^{2+}$ (**tz** = 2,2′-bithiazole) ligand could provide further evidence [149]. Figure 4.12 presents cyclic voltammograms for $[(bpy)_2Ru(\mathbf{tz})]^{2+}$ in the absence and presence of CO_2. For the first reduction wave, the one-electron reduction of $[(bpy)_2Ru(\mathbf{tz})]^{2+}$ did not produce any catalytic current for CO_2 reduction. This could be due to the fact that the electron density is now shared by two thiazole fragments. The resulting lower electron density on each thiazole fragment might not be

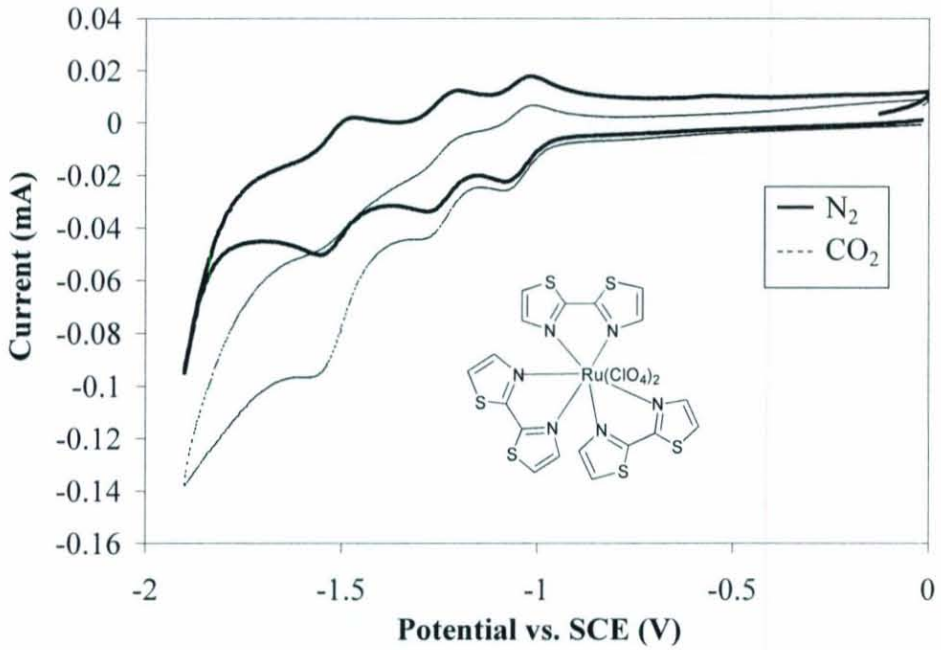

Figure 4.13: Cyclic voltammograms of 1 mM $[Ru(\mathbf{tz})_3]^{2+}$ in CH_3CN/0.1 M Et_4NClO_4 containing 1% water under N_2 and CO_2 at a glassy carbon electrode (at ν = 100 mV/s).

sufficient to dechelate one of bpy ligands. After the second reduction, the electron would be largely localized on bpy ligands, but could also add to the electron density on the bithiazole. This additional electron density is obviously responsible for CO_2 activation at the ruthenium center. It might promote dissociation of one of the bpy bonds on Ru, so that CO_2 can coordinate to the Ru centre.

Cyclic voltammetry for $[Ru(\mathbf{tz})_3]^{2+}$ in the absence and presence of CO_2 is presented in Figure 4.13. It could provide further evidence of the binding of CO_2 to the ruthenium centre. In this case, high activity for CO_2 reduction was only observed on the

third reduction wave. Since this complex contains six thiazole rings, any added electrons will be delocalized over the three bithiazole ligands, resulting in less electron density on each ligand for the first two reductions. Thus, addition of a third electron is required for CO_2 activation.

4.4 Electrolysis and product analysis of complexes under CO_2

To evaluate the electrocatalytic activities for each of the complexes, electrolysis (at a fixed potential) was performed and the electrolyzed products were analyzed to evaluate the mechanistic pathways to the formation of those products. The electrolyses were performed at an Hg pool electrode with anhydrous grade acetonitrile (99.8%, Sigma-Alrich) as the solvent. Most of the complexes were electrolyzed under CO_2, however only $[\{(bpy)_2Ru\}_2(\mathbf{py_2tbtz})]^{4+}$ yielded electrocatalytic products with satisfactory and reproducible results.

4.4.1 Electrolysis of $[\{(bpy)_2Ru\}_2(\mathbf{py_2tbtz})]^{4+}$ under CO_2

A three-chambered gas tight glass electrochemical cell was used with a gas inlet and outlet. The cell consisted of a flat bottom having a Pt wire connection for an Hg pool electrode (W.E.) (distilled three times). The counter electrode chamber was separated from that of the working electrode by a porous glass frit. The outlet portion of the cell was connected to a "V-shaped" glass tube which contained [$PdCl_2$ in HCl (12.0 M) (1 mL) + $Al_2(SO_4)_3$ (10%, 10 μL)] solution. The gas from the outlet was bubbled through

this solution in order to detect and measure the amount of CO produced by a spectrophotometric method [150]. An O_2-free environment was maintained by purging the cell with N_2 prior to electrochemical experiments (~10 min) and then the cell was purged with CO_2. Electrolysis of $[\{(bpy)_2Ru\}_2(\mathbf{py_2tbtz})]^{4+}$ was performed under potentiostatic control at -1.46 V vs Ag/AgCl, at a current of 10 mA. A total charge of 14.5 C was passed during the electrolysis process. The electrolysis was carried out for ~2 h; the current dropped slightly during the first 6 min and remained constant throughout the rest of the experiment. The electrolysis was performed at room temperature (~25 °C) with 1 mM of $[\{(bpy)_2Ru\}_2(\mathbf{py_2tbtz})]^{4+}$ in 0.1 M Bu_4NBF_4/CH_3CN solution (17 mL) in the presence of 2.5% water (as addition of 2.5% water shows highest increased current). However, addition of more water did not enhance the current significantly. This observation indicates that the presence of a proton donor influences the electrocatalytic reduction of CO_2. A CO_2 flow rate of ca. 60 mL/min was maintained throughout the whole electrolysis. During the electrolysis the complex changed its color from dark purple to faint red and some precipitation was observed. A slow evolution of tiny bubbles was seen from the surface of the Hg electrode which was very fast at the beginning of the reaction. After the electrolysis, a few drops of NH_3 solution were added in order to make the solution basic. The mercury was removed and the solvent of the reaction mixture was distilled by rotary evaporation and the residue was suspended in 3 mL water and the remaining material (electrolyte + complex) was removed with a Chromspec Syringe Filter (13 MM PTFE 0.2 μm). Oxalic and formic acid were determined in the aqueous phase.

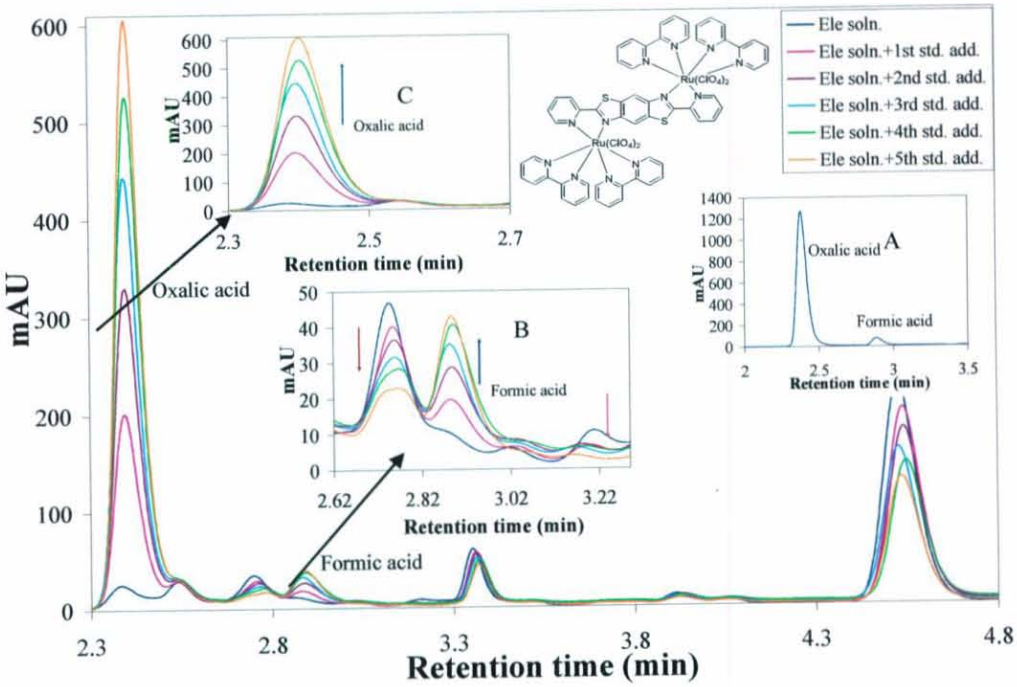

Figure 4.14: HPLC chromatograms for separation of: A) standards; B) formic acid, and C) oxalic acid from an electrolyzed solution of $[\{(bpy)_2Ru\}_2(\mathbf{py_2tbtz})]^{4+}$ (1 mM) in CO_2 saturated CH_3CN/0.1 M Bu_4NBF_4, under wet conditions at an Hg pool electrode.

Separation and quantification were performed by HPLC with an Agilent 1100 series Eclipse instrument with an XDBC-18 (5 μm and 4.6× 250 mm) reverse phase column and coupled to an Agilent 1100 series G13158 Photodiode Array Detector with UV detection at 210 and 214 nm for formic and oxalic acid, respectively. Acetonitrile (5 %) was employed together with phosphate buffer [KH_2PO_4 (50 mM) + H_3PO_4] at pH = 2.45 as an isocratic eluent. A flow rate of ca. 0.9 mL/min and pressure of 150 bar were used.

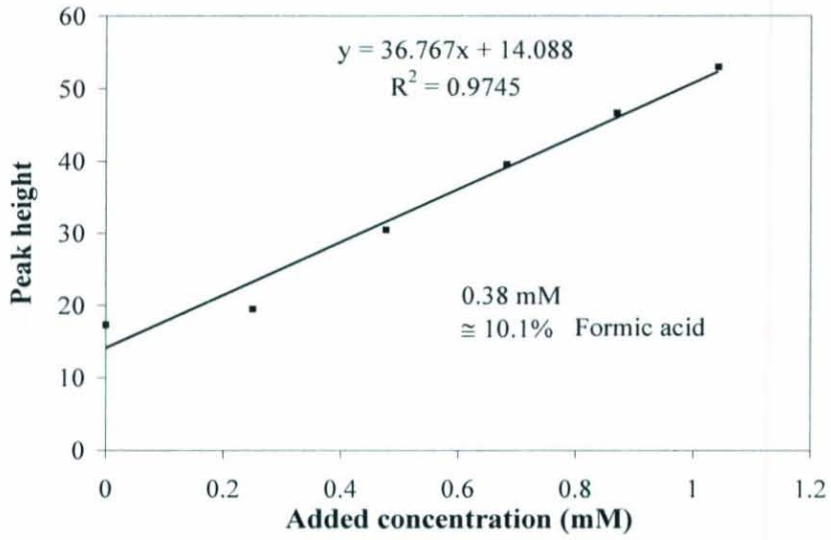

Figure 4.15: Standard addition plot for the quantification of formic acid in the electro-lyzed solution of $[\{(bpy)_2Ru\}_2(\mathbf{py_2tbtz})]^{4+}$.

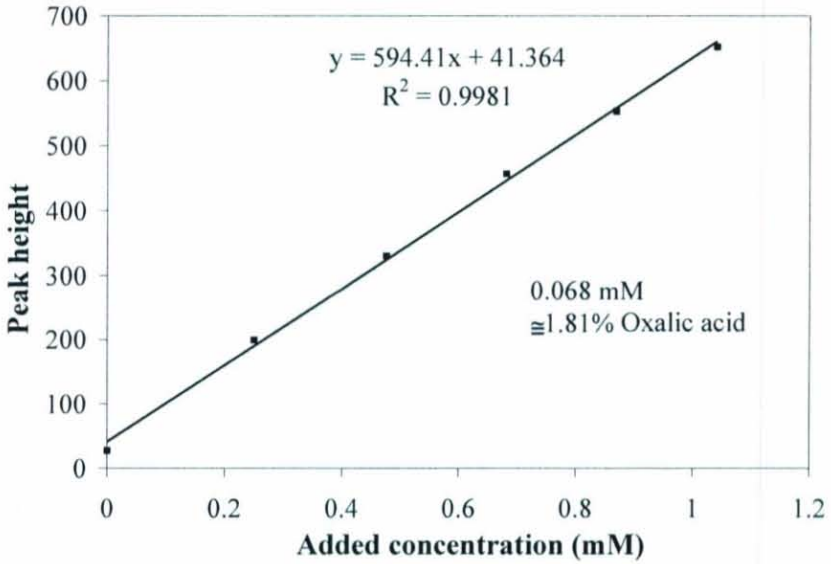

Figure 4.16: Standard addition plot for the quantification of oxalic acid in the electro-lyzed solution of $[\{(bpy)_2Ru\}_2(\mathbf{py_2tbtz})]^{4+}$.

Figure 4.14 shows HPLC chromatograms of the electrolyzed solution of $[\{(bpy)_2Ru\}_2(\mathbf{py_2tbtz})]^{4+}$. The retention times of the electrolyzed solution were compared with those of the standards. It can be seen that addition of standards to the electrolyzed solution gave a continuous increase in absorption peaks having similar retention times to those of the sample peaks, indicating the presence of formic and oxalic acid in the electrolyzed solution. Figure 4.15 and 4.16 represents the standard addition plot for quantifications of formic acid and oxalic acid. Faradaic efficiency for the formation of formic acid (calculated from the ratio between the charge necessary to produce the measured quantities of formic and oxalic acid {two-electrons/mol = 100 %} and the total charge passed during the electrolysis process) was found to be ca. 10% and that for oxalic acid was ca. 2%. No CO was detected in the exhaust gas. The presence of other gaseous products (e.g., H_2) was not investigated.

4.4.2 Discussion

$[\{(bpy)_2Ru\}_2(\mathbf{py_2tbtz})]^{4+}$ showed moderate activity for CO_2 reduction. The required proton sources for the productions of formic and oxalic acid could be from the added water [37, 46, 75, 151]. It was anticipated that during the electrochemical reduction of CO_2 by metal complexes, the initial step might be the formation of M–CO_2 adducts (key intermediate) [152-153], which in the presence of a proton source produces a stable M–CO bond via the formation of a [M–C(O)OH] intermediate [44, 67-68(a), 152-154]. According to Meyer et al. [44] metal complexes with polypyridyl ligands might provide the site for the initial reduction. Formation of this stable M–CO bond was thought to be a

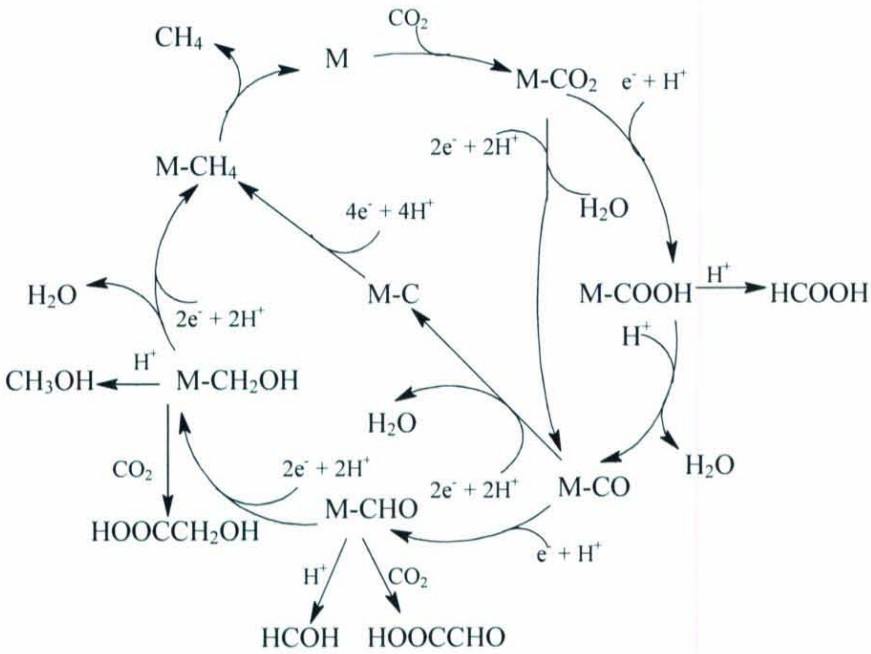

Scheme 4.1: General cycle for the production of various products during electrochemical CO_2 reduction by metal complexes with acyclic ligands as electrocatalysts. Reproduced with permission from *Coord. Chem. Rev.* 1996, 148, 221 [152]. Copyright © 1996 published by Elsevier Science B.V.

possible route for the CO expulsion to multiple-electron reduction products [79]. For $[\{(bpy)_2Ru\}_2(\mathbf{py_2tbtz})]^{4+}$, oxalate could be formed by the development of five-coordinate Ru by the dechelation of the **py_2tbtz/bpy** ligand, similar to the mechanism reported by Tanaka et al. [77] for their bimetallic Ru complexes. The five-coordinate Ru complex could provide binding sites for CO_2 to attack, followed by coupling of two anion radicals of CO_2 to oxalate. It was found that oxalate formation with other bimetallic metal

complexes followed the same mechanism [19], whereas in the presence of a proton source, formate can be produced.

Faradaic efficiencies for the oxalate and formate formation by $[\{(bpy)_2Ru\}_2(\mathbf{py_2tbtz})]^{4+}$ were found to be low relative to Tanaka's catalysts [77]. There could have several explanations for low faradaic yields such as:

i) There must be some other products formed during the electrolysis according to the Scheme 4.1, as there are multiple ways to the formation of other products.

iii) H_2 may be produced during the electrolysis as some bubbles were seen to be coming out from the surface of the Hg pool electrode (in the first few minutes).

iv) Decomposition of the complex might have lowered the faradaic efficiencies for formic or oxalic acid (as some precipitation were observed and the color of the electrolyzed solution was found to be changed after the electrolysis).

v) If the decomposition occurred, there is the possibility of formation of ligand carboxylated products.

vi) CO_2 can itself bind onto the Ru centre and form a stable Ru–CO_2 complex.

vii) The formation of a less stable intermediate state during the reaction between the CO_2 and the $[\{(bpy)_2Ru\}_2(\mathbf{py_2tbtz})]^{4+}$ as the ruthenium centre has low electron donating capability due to the ligand **py$_2$tbtz**'s π-acceptor nature [153(d)].

4.5 Conclusions

Benzothiazole complexes of Ru exhibited remarkable electrocatalytic activity for CO_2

reduction (from the CV's). It was found that structural variations influence this activity but all benzothiazole complexes exhibit much higher activities than the corresponding benzimidazole complexes. On the other hand, pyrazine ligand based benzothiazole/ benzimidazole bimetallic complexes did not show any appreciable activity for CO_2 reduction, whereas pyridine ligand based benzimidazole/benzothiazole complexes showed high activities. It was observed that the variation of substituents on the benzimidazole ring has an effect on electrochemical CO_2 reduction. For example, Me-substituted benzimidazole complex showed more activities for CO_2 reduction than the corresponding benzimidazole complexes (in the CV). This could be related to the electron-donating nature of the -Me- group [78].

Electrolysis of $[\{(bpy)_2Ru\}_2(\mathbf{py_2tbtz})]^{4+}$ was performed in the presence of CO_2. Oxalic and formic acids produced in catalytic products. No other products were detected from the electrolyzed solution. The characteristic features of the cyclic voltammograms under N_2 and CO_2, the recovery of the original CV after purging the CO_2 saturated solution with N_2 and the formation of electrocatalytic products upon electrolysis, are indications of an EC_{cat} process. Interestingly, this is the first benzothiazole based bimetallic complex that showed the electrocatalytic activities towards CO_2 reduction to the best of our knowledge. The reported system opens a path for benzothiazole based transition metal catalysts for CO_2 reduction, although faradaic efficiencies were found to be low. Additionally benzothiazole complexes of Ru exhibit electrocatalytic activity for CO_2 reduction at a moderately low cathodic overpotential.

Chapter 5

Electrochemical reduction of CO_2 by fluorene-9-one

5.1 Overview of electrochemical reduction of CO_2 by aliphatic and aromatic ketones

The electrochemical reduction of CO_2 has been a field of paramount interest for more than fifty years, not only for producing alternative energy sources, but also for the inexpensive production of carboxylated products for industrial applications. CO_2 is a widely available and thermodynamically stable molecule that can be used as a reactant in the electrochemical reduction of aromatic and aliphatic ketones. A significant amount of work has been done (and patented) in order to produce fine chemicals from the intermediate α-hydroxyacids of aromatic ketones [155-156]. For example, the widely known nonsteroidal anti-inflammatory drugs (NSAIDs) 2-arylpropanoic acids (e.g., ibuprofen and fenoprofen) [40] are produced during the electrocarboxylation of aromatic ketones [155]. Wawzonek and Gunderson [157] pioneered the electrochemical reduction of CO_2 by aromatic ketones. Unlike some other methods, the electrochemical route presents the advantage of not using phosgene and cyanides [155, 39] for the preparation of these carboxylic acids.

5.2 Proposed mechanisms for electrochemical reduction pathways of CO_2 by aromatic and aliphatic ketones

The electrochemical reduction of CO_2 by various aromatic and aliphatic ketones can lead either to carboxylation or electrocatalytic reduction pathway, or sometimes both paths. Some of these pathways and mechanisms are discussed below.

5.2.1 Electrocarboxylation

Electrochemical carboxylation of several aromatic and aliphatic ketones, such as acetophenones, benzophenones, quinones, anthraquinones, benzoquinones, benzil, esters and some nitriles have been investigated and reported during the last fifty years [155, 158-159]. According to the literature reports, the products are mainly hydroxycarboxylic acids, alcohols and pinacols that are produced from carbanions, radical anions and dianions of aromatic/aliphatic ketones during the electrochemical carboxylation by coupling, polymerization, displacement, and carboxylation reactions [160-161]. Halogen [158] and methyl [162] substituted forms of these compounds have also been investigated and it has been reported that compounds with electron-donating groups usually decrease the yield of carboxylated products [163].

Some work on electrocarboxylation is patented [164, 165] for the synthesis of compounds with specific applications, such as herbicides [166], fungicides [167] and bactericides [168]. Electrochemical carboxylation has usually been performed using sacrificial anodes, such as, Mg, Al, Zn and Fe [168–172] and cathodes such as Pt, Au, Ni and graphite [170] in order to get higher yields of hydroxycarboxylic acids and lower the rates of dimerization to pinacols. Although the use of sacrificial anodes improves the product yields, selectivity and easy isolation, the dissolved metal on the remaining aqueous solutions may yield a severe impact on the environment in the form of metal pollution [156]. Use of a Hg pool electrode as a cathode can increase the selectivity for formation of carboxylic acid derivatives, [173] but due to its high toxicity this electrode material is often replaced by compact graphite [168] or stainless steel [174].

Furthermore, it has been reported that an unexpected ring carboxylation may also occur during the electrocarboxylation of aromatic ketones in anhydrous media [175]. The yield of this product is very low, but can hinder the separation of carboxyl products.

Aromatic radical anions are chemically stable in aprotic solvents and can act either as homogeneous electron transfer species or neucleophiles or both. When a radical anion acts as a nucleophile, the reaction can follow an **ECE** (steps 1, 2, 3 in Scheme 5.1) [176] type mechanism:

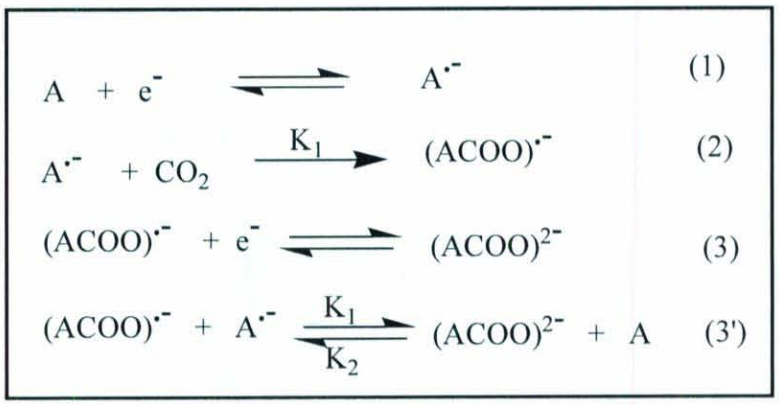

Scheme 5.1: General mechanisms for the electrochemical carboxylation of aromatic ketones by CO_2 in non-aqueous solution. Reproduced from *J. Braz. Chem. Soc.* 1998, 9(2), 157 [176]. DOI:10.1590/S0103-50531998000200007.

In this reaction scheme the overall electrode process is composed of successive electrochemical, chemical and electrochemical steps. This mechanism is common for

most electrochemical carboxylation reactions of aromatic ketones. In addition to **ECE** mechanisms, some others described **ECE-DISP** (steps 1, 2, 3' in Scheme 5.1) mechanisms, where the starting material is regenerated in addition to other products being formed. Other mechanisms, like **EEC, ECEC, ECCE, DISP1** [176], and **DISP2** have also been proposed for the electrochemical carboxylation of aromatic and aliphatic ketones.

5.2.2 Homogeneous catalysis

As was mentioned previously, an efficient electrocatalyst has the capability to both accelerate and participate in an electron transfer reaction. Redox potentials, current efficiencies, electron transfer rates and chemical kinetics are the parameters that determine the effectiveness of an electrocatalyst [11]. The function of an electrocatalyst (in homogeneous media) was discussed in detail in Chapter 1 and this section is limited to discussions of a number of organocatalysts and their functions as electrocatalysts.

According to Genero et al. [177], anion radicals of aromatic nitriles, esters and diketones [178] are good candidates for the formation of oxalate and insignificant amounts of carboxylated products. These are known homogeneous redox catalysts for the reduction of CO_2 in aprotic media and oxalate might be formed by coupling of two anion radicals of CO_2. In addition, Savéant [10] reported that an inner-sphere electron transfer between CO_2 and these organic molecules could be responsible for the formation of an

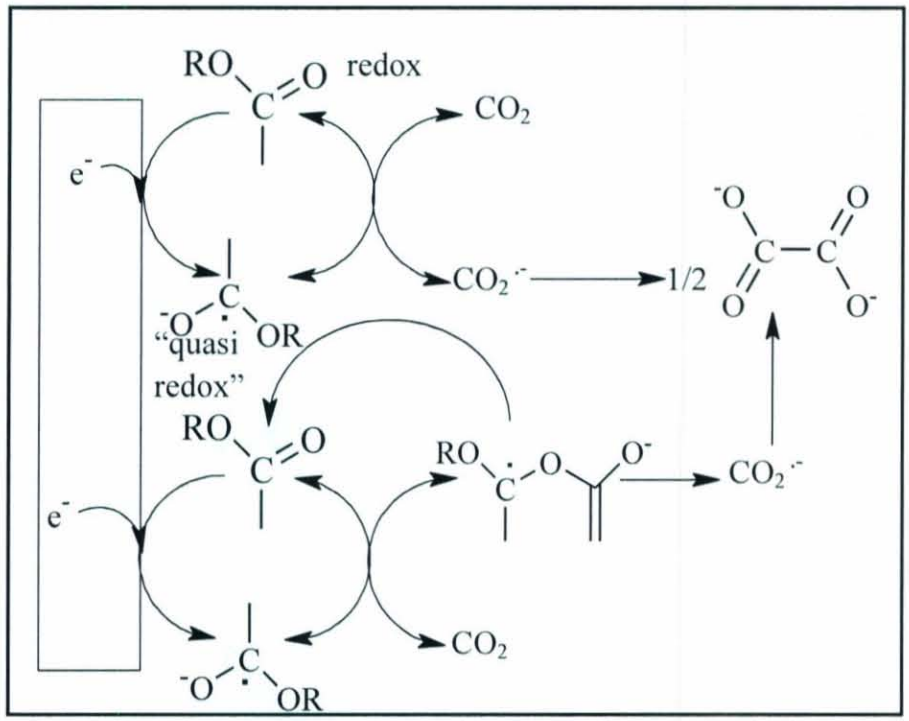

Scheme 5.2: Redox catalysis and quasi-redox catalysis processes for electrochemical CO_2 reduction by esters [10]. Reproduced with permission from *Chem. Rev.* 2008, 108, 2348. Copyright © 2008 American Chemical Society.

intermediate to the anion radical of CO_2 [see Scheme 5.2]. The author concluded that in the case of nitriles and esters, the electrocatalytic activity is by a "quasi-redox" process, where the intermediate product is an adduct between the anion radical of the organic molecule (produced in the first step by transfer of an electron from the electrode surface) and CO_2. This adducts readily breaks down to produce the anion radical of CO_2, which would eventually dimerize to give oxalate.

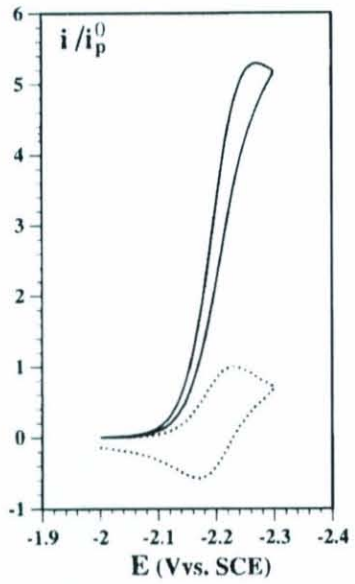

Figure 5.1: Cyclic voltammogram of methyl benzoate (2.6 mM) in DMF/0.1 M n-Bu_4NClO_4 in the absence (dotted line) and presence (solid line) of CO_2 (26 mM). The current scale is normalized relative to the cathodic peak current in the absence of CO_2, i_p°. Scan rate 1 V/s. Temperature 25 °C. Reproduced with permission from *J. Am. Chem. Soc.* 1996, 118 (30), 7190 [177]. Copyright ©1996 American Chemical Society.

For anion radicals of ketones/esters behaving as electrocatalysts in carboxylation reactions, it is a general observation that currents in cyclic voltammograms are found to be enhanced beyond the expected one-electron/molecule stoichiometry, when occured under a CO_2 atmosphere. Figure 5.1 shows a cyclic voltammogram, which depicts this behavior, for an organocatalyst- methyl benzoate [177] under N_2 and CO_2.

5.3 Goals

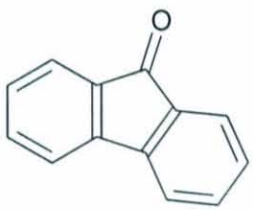

Fluorene-9-one (**Fl**)

Fluorene-9-one (**Fl**) has been chosen as a model organoelectrocatalyst for this part of the project. This structure has already been reported in such applications as a polymer unit for organic light emitting diodes [179], unit for forming a conjugated oligomer with dithiophene [180] etc. Immobilized nitro-fluorenone [181] and its derivatives [182] can act as electrocatalysts for NADH oxidation. However, the electrocatalytic activity of **Fl** for CO_2 reduction has not been reported so far. The main aims of this part of the project were to investigate electrochemical CO_2 reducton by **Fl**, characterizing the products of the electrocatalytic processes, and elucidating reaction mechanisms.

5.4 Electrochemical studies of fluorene-9-one

5.4.1 Under N_2

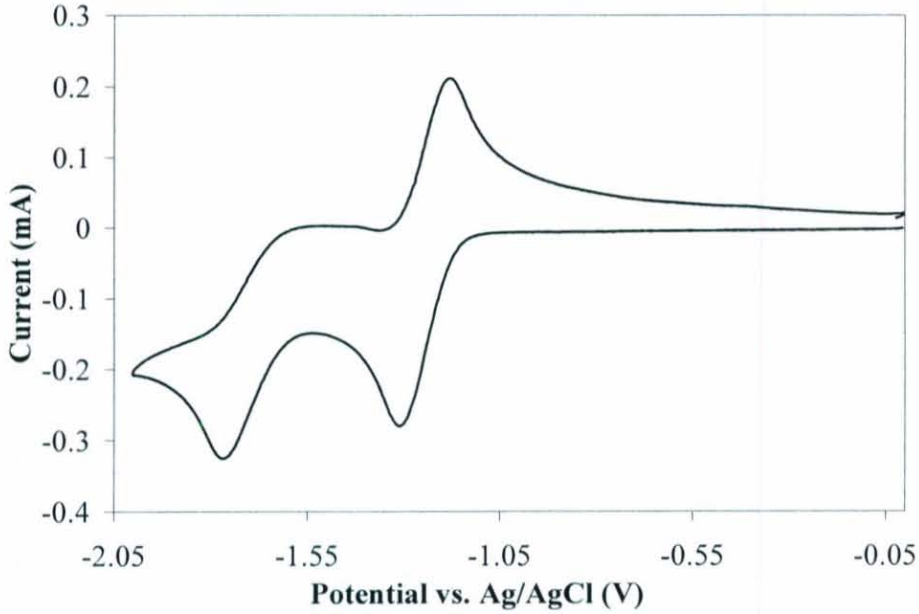

Figure 5.2: Cyclic voltammogram of **Fl** (5 mM) in CH_3CN/0.1 M Et_4NBF_4, under N_2 at a glassy carbon electrode, (ν = 50 mV/s). Ag/AgCl (RE), Pt (CE).

Figure 5.2 shows the cyclic voltammogram of **Fl** under N_2. The electrochemical reduction of this compound occurs as two one-electron processes (peaks). According to Elving et al. [183], electrochemical reduction mechanism for this kind of ketone follows two successive steps. The initial one-electron reduction represents the reversible reduction of **Fl** to the free radical anion $\mathbf{Fl}^{\cdot-}$ (reaction 1). A further one-electron reduction of the radical anion ($\mathbf{Fl}^{\cdot-}$) results in the formation of the dianion ($\mathbf{Fl}^{2-}$) (reaction 2), which

is chemically irreversible (no reverse peak). Similar behaviour was seen for benzophenone under N_2 by Tsierkezos [184] and for quinones and anthraquinones by Lehmann et al. [185]. The second step of this process may involve a chemical reaction between the solvent and $\mathbf{Fl^{2-}}$.

$$\mathbf{Fl} + e^- \rightleftharpoons \mathbf{Fl^{\cdot-}} \quad \text{.....(1)}$$

$$\mathbf{Fl^{\cdot-}} + e^- \longrightarrow \mathbf{Fl^{2-}} \quad \text{..... (2)}$$

The electrochemical reduction of **Fl** under N_2 thus may be expressed as an **EEC** process, where the first two steps are electrochemical and the third step, a chemical process. Table 5.1 summarizes the anodic peak potential (E_{pa}), cathodic peak potential (E_{pc}), anodic and cathodic peak current ratio (i_{pa}/i_{pc}), and half-wave potential ($E_{1/2}$) of the $\mathbf{Fl/Fl^{\cdot-}}$ couple and the cathodic peak potential (E_{pc}), and cathodic peak current (i_{pc}) for $\mathbf{Fl^{\cdot-}/Fl^{2-}}$ couple.

Table 5.1: Potentials and currents for the first two reduction peaks of **Fl** (5 mM) in CH_3CN/0.1 M Et_4NBF_4 at $\nu = 0.05$ V/s in N_2-saturated solution.

Peak-1				Peak-2	
$\mathbf{Fl/Fl^{\cdot-}}$ couple				$\mathbf{Fl^{\cdot-}/Fl^{2-}}$ couple	
E_{pa} (V)	E_{pc} (V)	i_{pa}/i_{pc}	$E_{1/2}$ (V)	E_{pc} (V)	i_{pc} (A)
-1.17	-1.31	0.97	- 1.24	-1.78	-3.25×10^{-4}

5.4.2 Under CO_2

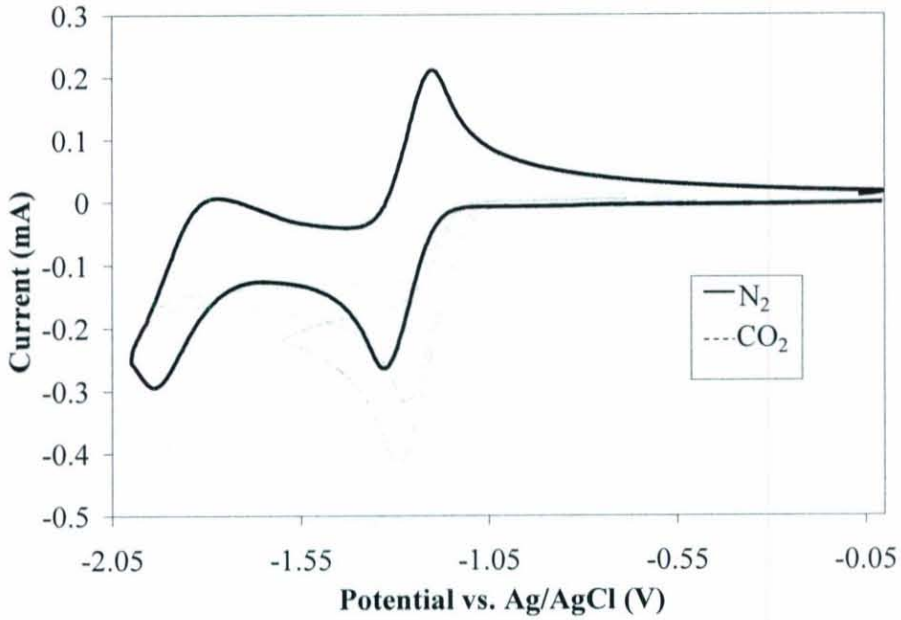

Figure 5.3: Cyclic voltammograms of **Fl** (5 mM) in CH_3CN/0.1 M Et_4NBF_4 under CO_2 (----) and N_2 (—) at a glassy carbon electrode, (ν = 50 mV/s), Ag/AgCl (RE), Pt (CE) (shows both peak).

Electrochemical reduction of **Fl** in the presence of CO_2 shows significant changes in the cyclic voltammogram, relative to that under N_2. Before passing CO_2 through the cell, the solution was purged thoroughly with N_2 for 5-10 min in order to remove O_2. Figures 5.3 and 5.4 show cyclic voltammograms of **Fl** before and after saturation of the solution with CO_2 respectively. Under CO_2, a diffusion-limited current peak at -1.3 V is enhanced to twice the current observed in the N_2-purged solution. This increased current suggests that

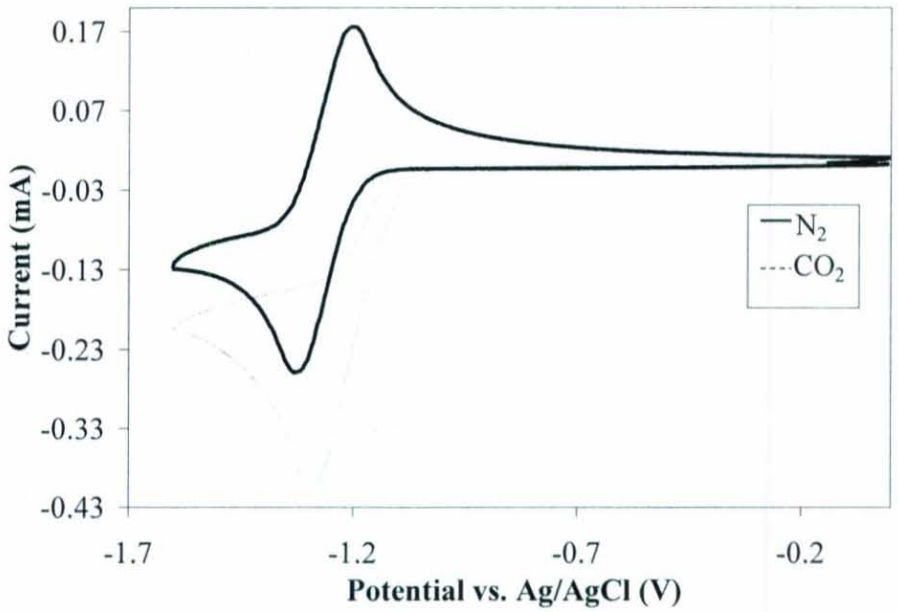

Figure 5.4: Cyclic voltammograms of **Fl** (5 mM) in CH_3CN/0.1 M Et_4NBF_4, under CO_2 (----) and N_2 (—) at glassy carbon electrode (0.20 cm^2) at the scan rate of 50 mV/s (first peak).

(the initial reduction of **Fl** changes from a one-electron under N_2), to a two-electron process in the presence of CO_2. The first reduction peak is irreversible, even at a scan speed of 1V/s, whereas the second peak is absent (see Figure 5.3). Some specific points were noticed on the electrochemical reduction of **Fl** in the presence of CO_2:

1) The first peak appeared at a potential 40 mV more positive than under N_2.
2) The first peak became irreversible, and the second peak disappeared or was shifted beyond the range employed.

3) Quenching of the first anodic peak indicated that the rate-determining step of the overall process was fast compared to diffusion and that the consumption of the substrate in the diffusion–reaction layer was negligible [186].

4) The peak current for the first cathodic peak was almost twice the peak current under N_2. The enhancement of the one-electron wave suggested that the anion radical of **Fl** reacted with CO_2 to give a new species ($\mathbf{FlCO_2^{\cdot-}}$) that was electroactive under the reaction conditions.

The mechanism for the electrochemical reduction of CO_2 by **Fl** can tentatively be assigned as following either ECE, ECE_{cat}, ECEC, or $ECEC_{cat}$ pathways. Catalytic options are included here because of products observed in this work and other reports for similar systems [185]. For the elucidation of electrocatalytic processes and the mechanism of the formation of products during the electrochemical reduction of **Fl** under CO_2, the following studies could be undertaken:

i) Performing preparative scale electrolysis for determination of faradaic yields of each of the products, or

ii) Cyclic voltammetry at various scan rates, and

iii) Rotating disk voltammetry experiments at various rotation speeds.

5.5 Electrolysis of fluorene-9-one under CO_2

Electrolyses of **Fl** were performed under potentiostatic control at -1.2 V vs Ag/AgCl. A mercury pool electrode was used as a working electrode with a Pt wire counter electrode (CE) and a saturated Ag/AgCl reference electrode. The CE was separated from the catholyte by a glass frit. All the experiments were performed at room temperature (~25 °C) with 5 mM of **Fl** in 20 mM Et_4NBF_4/CH_3CN solution. A CO_2 flow of ca. 70 mL/min was used throughout all electrolysis processes as well as continuous stirring with a magnetic stirrer bar. All reaction conditions were the same for all electrolyses, unless otherwise mentioned.

5.5.1 Current and charge during the electrolyses

Current vs time responses obtained during an electrolysis of **Fl** under CO_2 are illustrated in Figure 5.5. The electrolysis was performed under anhydrous conditions. During the electrolysis process, 11.12 C of charge was passed. It can be noted from the figure that the current changed only slightly with time during the whole electrolysis. Also, during the first few seconds the current was found to decrease but soon stabilized. This is probably due to a balance being reached between depletion at the electrode and slow diffusion, before a steady state is achieved. The observation of a steady state implies that **Fl** is regenerated in a catalytic process. This reveals the catalytic behavior of the **Fl**, which was also supported by recovery of a significant amount of unreacted **Fl** after the electrolysis.

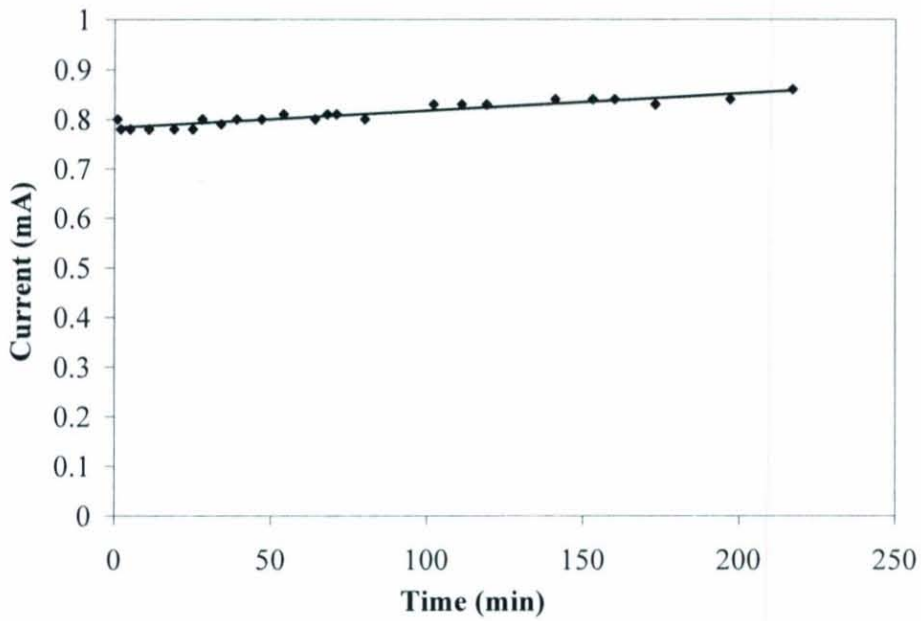

Figure 5.5: Current vs time response during the electrolysis of 5 mM **Fl** in CH_3CN/20 mM Et_4NBF_4 (anhydrous), under CO_2, at -1.2 V vs Ag/AgCl at a Hg pool electrode (11.12 C passed).

Figure 5.6 represents the amount of charge passed with time during the electrolysis of **Fl** under CO_2 for anhydrous and hydrous (1% v/v water) CH_3CN conditions. As mentioned, under anhydrous conditions, 11.12 C of charge was passed. The Q vs t plot was slightly nonlinear with $R^2 = 0.9878$ (see Figure 5.6 A); with 1% water, 11.06 C of charge was passed ($R^2 = 1.000$, for Q vs t plot) (see Figure 5.6 B).

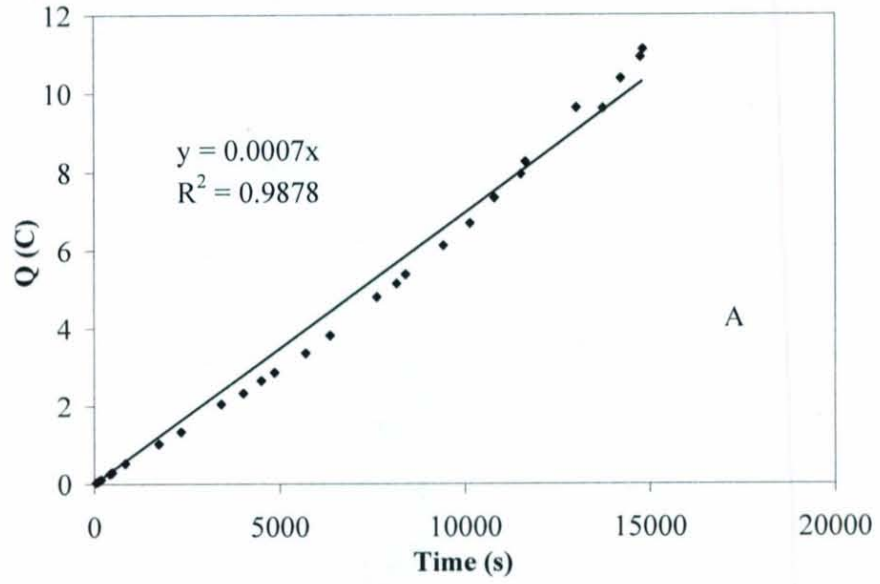

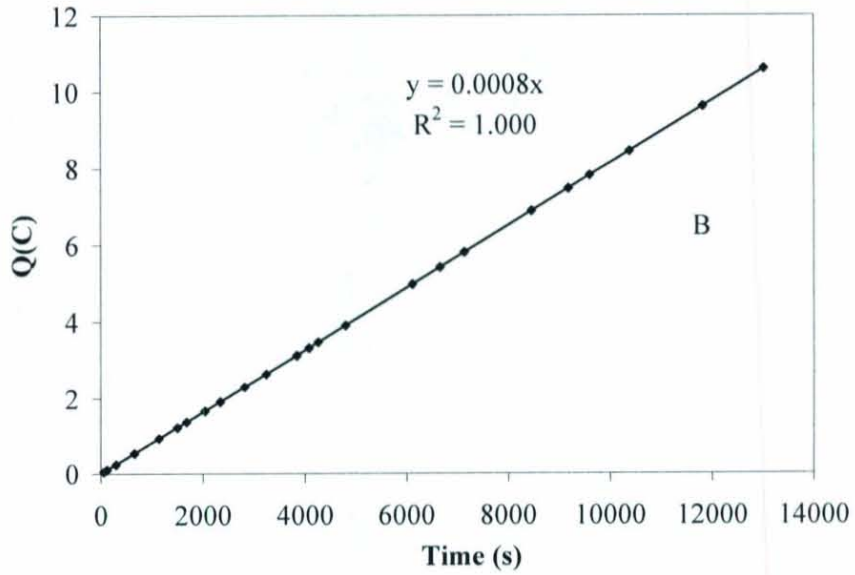

Figure 5.6: Q vs t response during the electrolysis of 5 mM **Fl** in CH_3CN/20 mM Et_4NBF_4, under CO_2, at -1.2 V vs Ag/AgCl at a Hg pool electrode A) anhydrous (11.12 C passed), B) 1% v/v water (11.06 C passed).

5.5.2 Cyclic voltammetry of electrolysis solutions

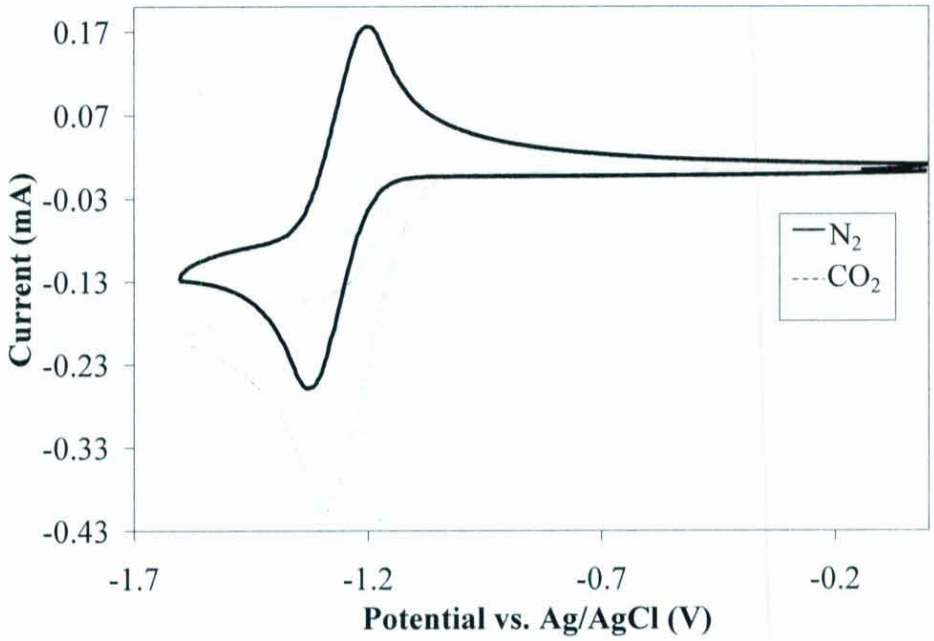

Figure 5.7: Cyclic voltammograms of 5 mM of **Fl** in CH_3CN/0.1 M Et_4NBF_4 at a glassy carbon electrode (0.20 cm^2), scan rate of 50 mV/s (before electrolysis) under N_2 and CO_2.

Figures 5.7 and 5.8 show cyclic voltammograms of 5 mM of **Fl** in 0.1 M Et_4NBF_4/CH_3CN under N_2 and CO_2-saturated solutions, before and after the electrolysis. In the N_2-saturated solution (see Figure 5.8), the reduction is reversible, with a slight change in the formal potential (~24 mV) compared to the non-electrolyzed solution (see Figure 5.7). As some of the solution evaporated (~2 mL) during the electrolysis, i_{pc} seems increased. The reversible behavior of **Fl** in the electrolyzed solution suggests catalytic

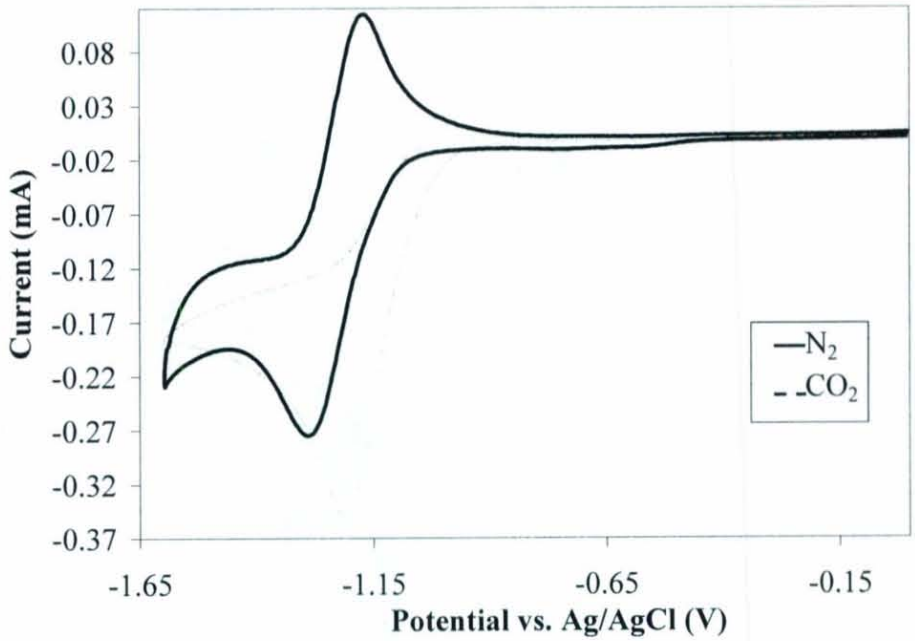

Figure 5.8: Cyclic voltammograms of 5 mM of **Fl** in CH_3CN/0.1 M Et_4NBF_4 at a glassy carbon electrode (0.20 cm^2), scan rate of 50 mV/s after electrolysis at a Hg pool electrode, at -1.2 V vs Ag/AgCl (12.8 C passed) under N_2 and CO_2.

behavior, as a significant amount of **Fl** was recovered. Whereas, in CO_2-saturated solutions, the reverse peak is quenched before and after the electrolysis, and the cathodic peak current was increased almost two-fold relative to that observed under N_2.

Figure 5.9 shows a cyclic voltammogram of an electrolyzed solution of **Fl** under CO_2. A new irreversible peak is seen in the positive potential region (~ +1.1 V) with enhanced current for this process (~202 μA) compared to the cyclic voltammogram collected under a N_2 atmosphere. According to Mizen et al. [187], the electrochemical

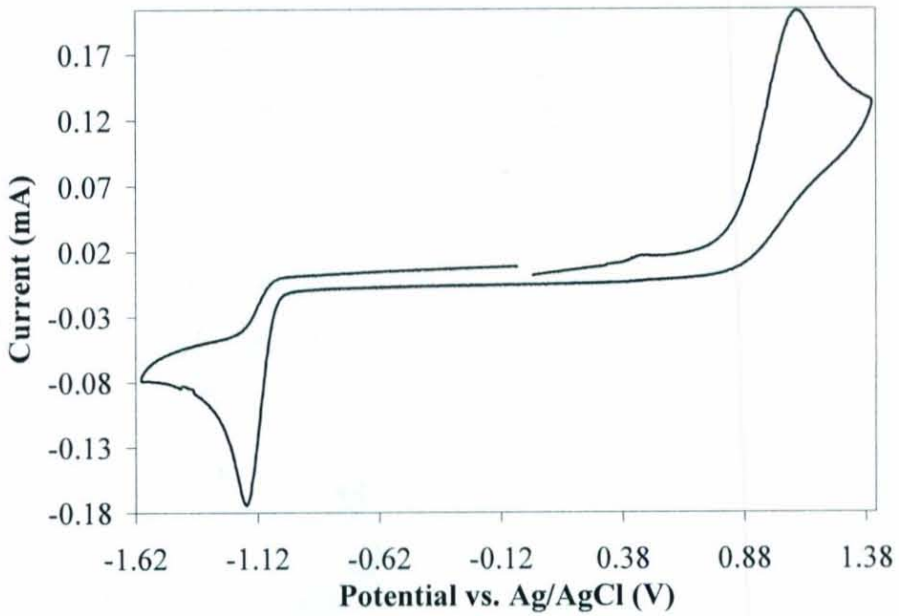

Figure 5.9: Cyclic voltammogram of an electrolyzed solution of 5 mM **Fl** in CH_3CN/0.1 M Et_4NBF_4 at a glassy carbon electrode (0.20 cm^2), scan rate of 50 mV/s after electrolysis under CO_2 at a Hg pool electrode at -1.2 V vs Ag/AgCl (12.8 C passed).

reduction of 9,10-phenanthrenequinone under CO_2 can form an adduct between the anion radical of the ketone and CO_2 that can be oxidized at positive potentials. So the new peak at + 1.1 V may be due to the formation of an adduct between the dianion of **Fl** and CO_2. The reduction wave still appeared as an irreversible wave, even after passing 12.8 C of charge. The cathodic peak current was quenched (ca. 230 μA) and the cathodic potential shifted slightly (ca. 14 mV) to positive potentials, relative to the non-electrolyzed solution (see Figure 5.7). The irreversible reduction wave also revealed the presence of a significant amount of **Fl** in the electrolyzed solution.

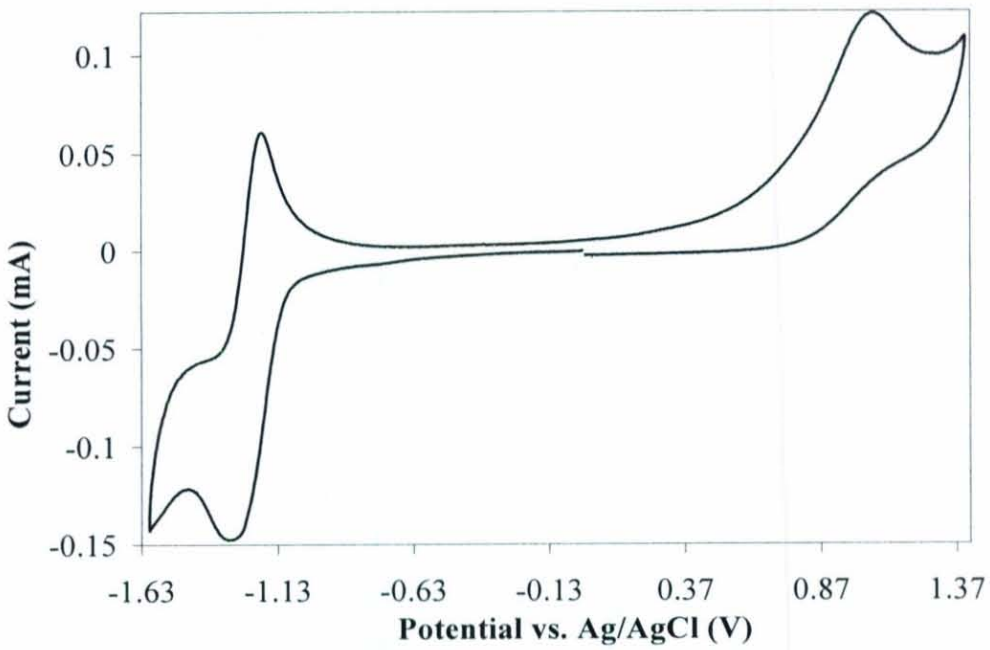

Figure 5.10: Cyclic voltammogram of an electrolyzed solution (12.8 C) of 5 mM **Fl**, in CH_3CN/0.1 M Et_4NBF_4 at -1.2 V vs Ag/AgCl at a glassy carbon electrode (0.20 cm^2), scan rate of 50 mV/s after flushing with N_2 (ca. 2 h.).

Figure 5.10 shows a cyclic voltammogram of an electrolyzed solution, following a thorough purge with N_2. The process that appeared as an irreversible wave near -1.3 V (see Figure 5.9), displayed reversible behavior when the CO_2 atmosphere was flushed with N_2. The irreversible reduction wave returned to being reversible with a small enhancement of the anodic peak. The current for the irreversible oxidation at +1.1 V deceased (by ca. ~90 μA) relative to the original electrolyzed solution (see Figure 5.10). Recovery of the reversible behavior for the reduction at ~ -1.3 V wave and quenching of

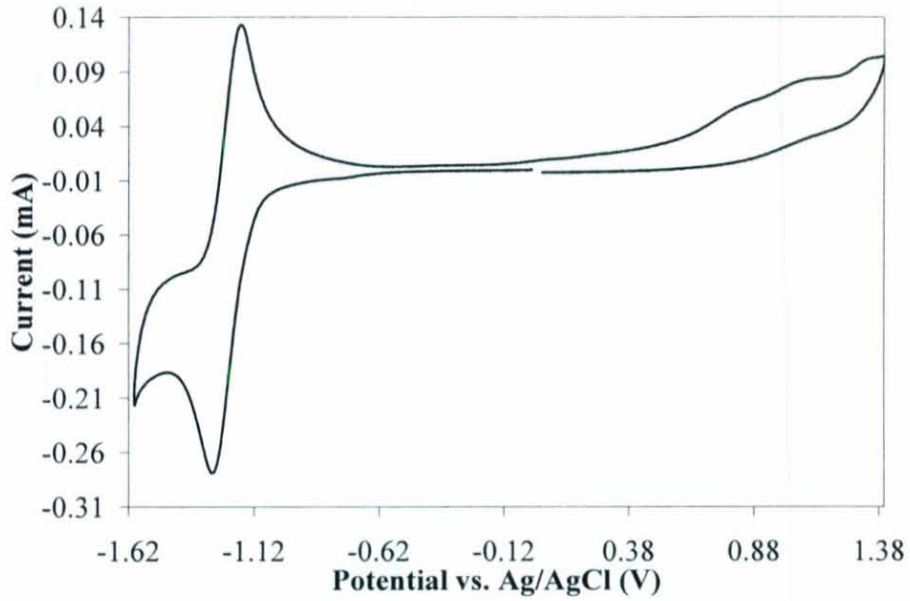

Figure 5.11: Cyclic voltammogram of an electrolyzed solution (12.8 C) of 5 mM **Fl**, in CH_3CN/0.1 M Et_4NBF_4 at -1.2 V vs Ag/AgCl at a glassy carbon electrode (0.20 cm^2), scan rate of 50 mV/s after exposure to air for several hours and then flushing with N_2.

the oxidation wave (at +1.1 V) upon flushing the electrolyzed solution with N_2 suggested that the adduct decomposed back to **Fl**, as was reported for 9,10-phenanthrenequinone by Mizen et al. [187].

The electrolyzed solution was then kept open to the air for several hours to promote oxidation of any oxidizable products and intermediates, and then flushed with N_2. The resulting CV, shown in Figure 5.11, reveals that most of the **Fl** is recovered, as the reduction wave returned to the initial, reversible shape and the oxidation peak was greatly decreased. This shape of the CV is a characteristic of **Fl** under N_2. The current for

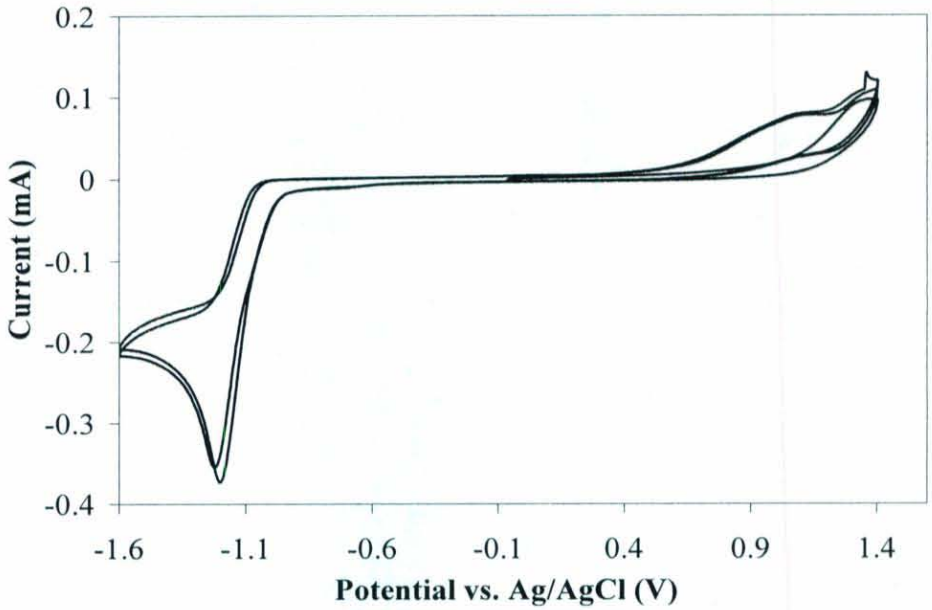

Figure 5.12: Cyclic voltammogram of an electrolyzed solution (12.8 C) of 5 mM **Fl**, in CH_3CN/0.1 M Et_4NBF_4 at -1.2 V vs Ag/AgCl at a glassy carbon electrode (0.20 cm^2), scan rate of 50 mV/s after exposure to air for several hours, flushing with N_2 and then with CO_2.

the reduction wave increased (i_{pc} ca. 300 μA) and the peak-to-peak separation decreased. This could be due to evaporation of solvent during (CO_2 flow) and after the electrolysis (open to air).

Figure 5.12 shows cyclic voltammograms collected for the same solution described by Figure 5.11, but then flushed with N_2 and then with CO_2. An irreversible peak was again observed at ~ -1.3 V with a slight shift in the peak potential, in the positive direction. The cyclic voltammogram indicates that the recovered **Fl** readily reacts

again with CO_2, retaining its electrocatalytic properties.

5.5.3 Product analysis by ^{1}H NMR and GC-EIMS

The solvent was removed from the electrolyzed solution (8.4 C, anhydrous conditions) and the residue was separated by column chromatography (silica) using an ethyl acetate and hexanes (5:95) solvent system. TLC indicated that the first fraction contained the electrolyte, followed by an unidentified fraction, and unreacted **Fl**. A ^{1}H NMR (MeOD as solvent) spectrum of the middle fraction is shown in Figure 5.13, contains a structure whose chemical shifts and integration of the resonances match with those of 9-hydroxyfluorene. ^{1}H NMR (MeOD) δ 7.69 (d, J = 7.5 Hz, 2H), 7.60 (d, J = 7.4 Hz, 2H), 7.37 (t, J = 7.4 Hz, 2H), 7.30 (t, J = 7.4 Hz, 2H), 5.53 (s, 1H).

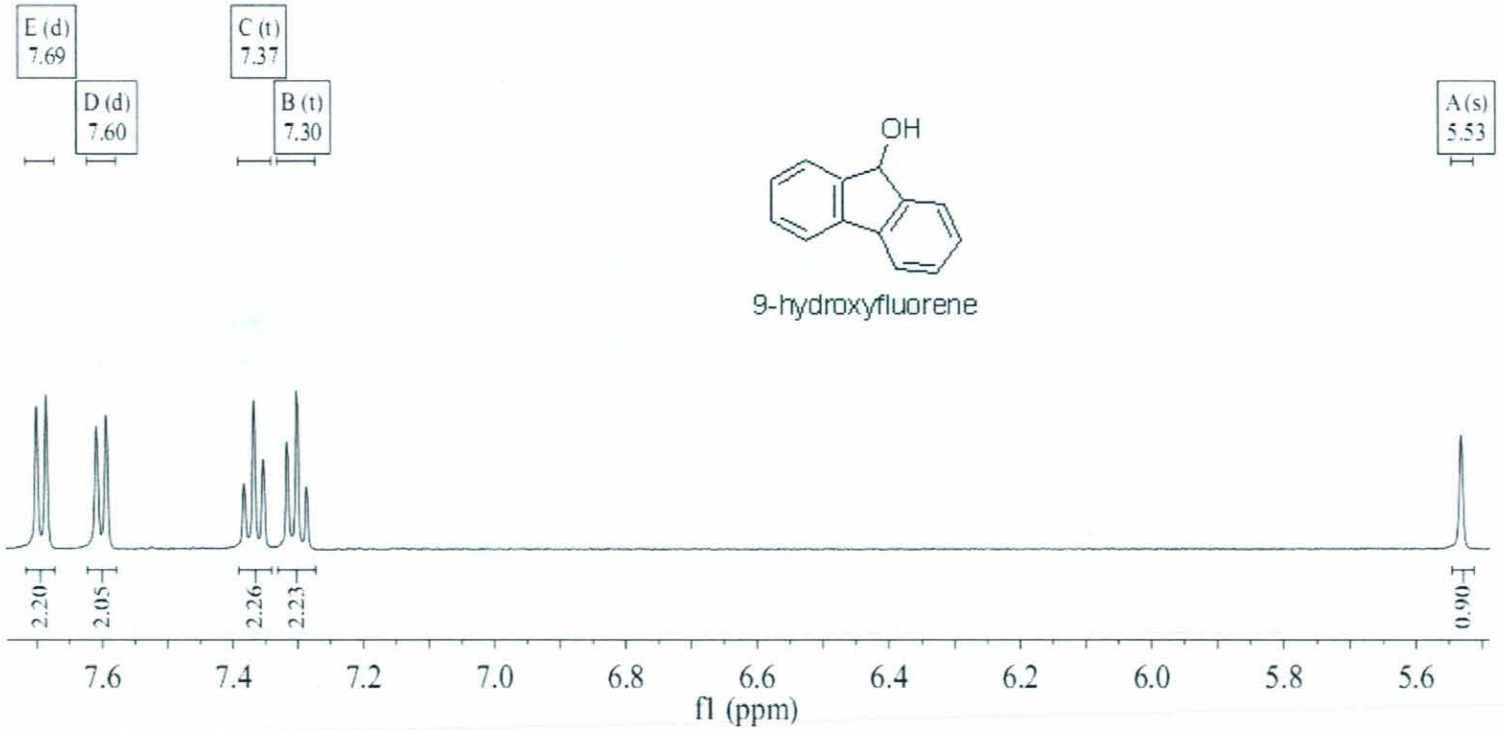

Figure 5.13: ^{1}H NMR spectrum (MeOH-d) of the middle chromatographic band from the electrolysis of **F1** under anhydrous conditions.

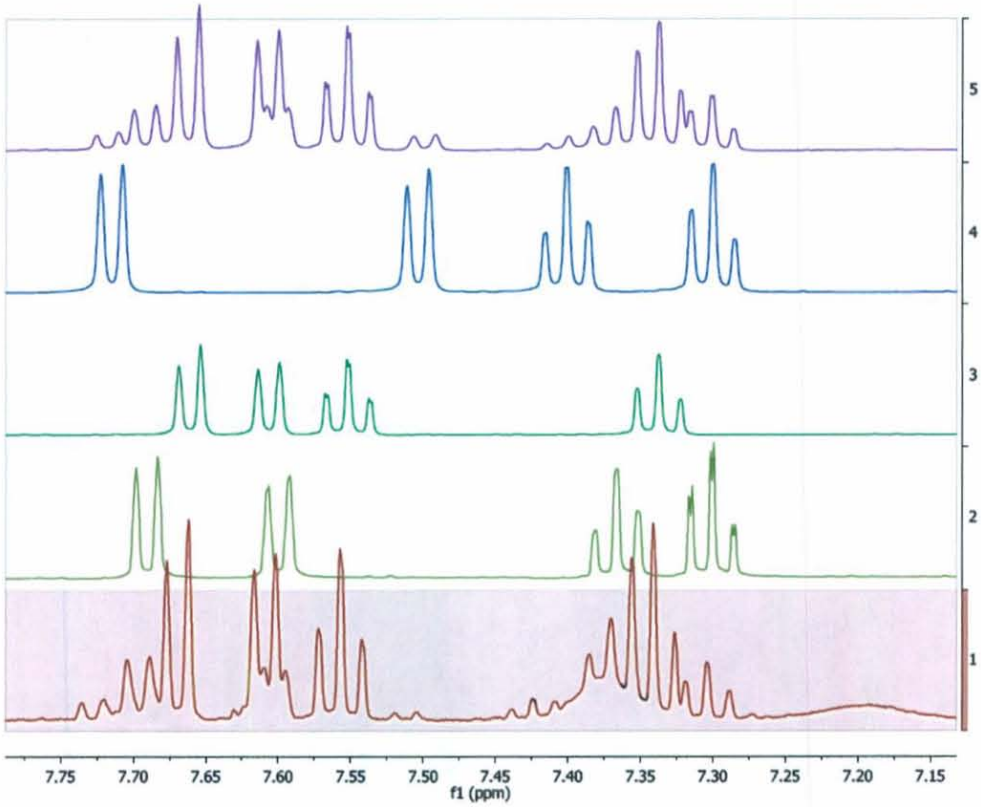

Figure 5.14: ^{1}H NMR spectra in MeOD of: 1) the solid residue from a **Fl/CO$_2$** electrolysis solution (1% water, 11.06 C passed); 2) 9-hydroxyfluorene; 3) **Fl**; 4) 9-hydroxyfluorene-9-carboxylic acid; 5) a standard mixture (2 drops from each 5 mM solution) of **Fl**, 9-hydroxyfluorene, and 9-hydroxyfluorene-9-carboxylic acid.

For the electrolysis of **Fl** in 1% water and acetonitrile (11.06 C), the solvent was removed from an electrolyzed solution (some portion) by distillation. The extracted, solid residue was checked by TLC, which indicated four spots, including a new unidentified fraction near the baseline, followed by electrolyte (second fraction), 9-hydroxyfluorene (third fraction), and unreacted **Fl**. Attempts to separate the unidentified fraction failed due

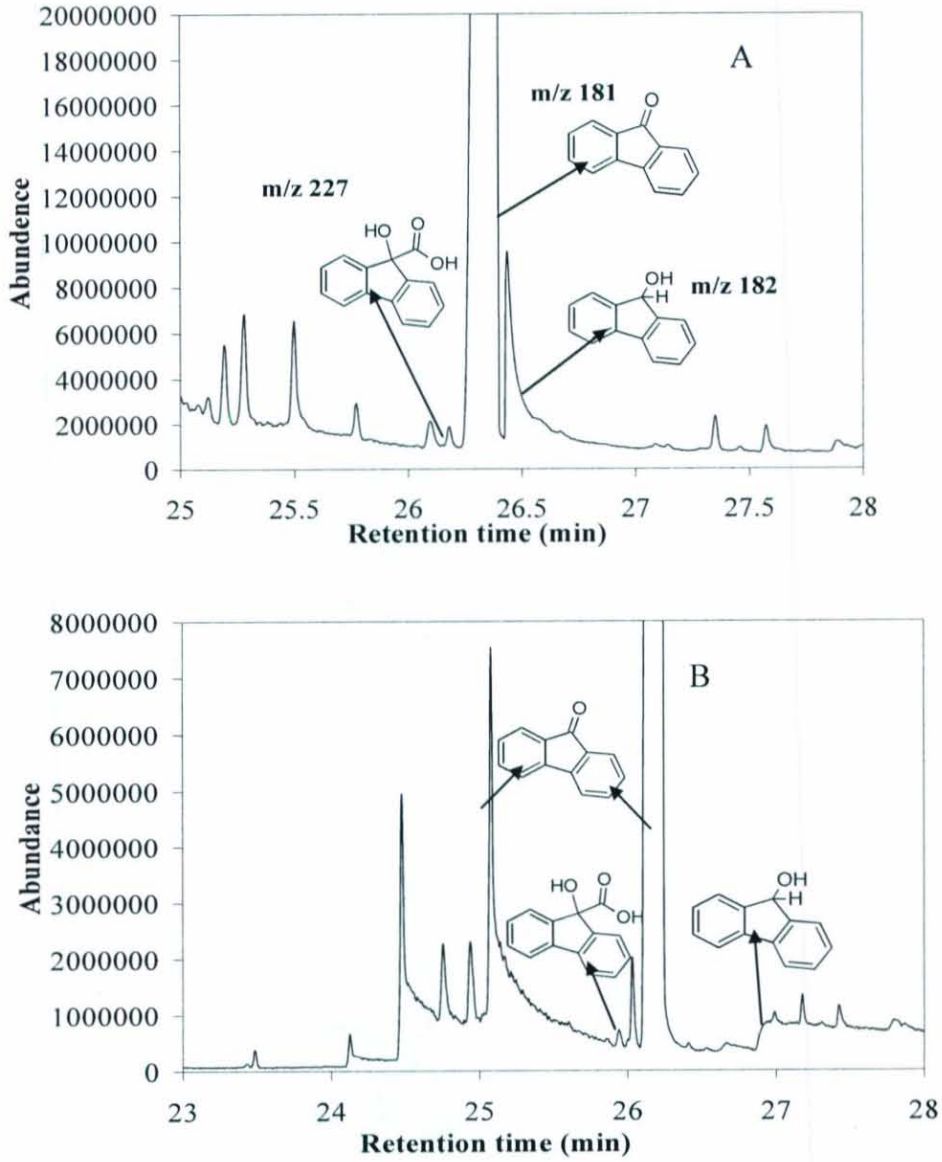

Figure 5.15: GC-EIMS separation of electrolyzed solutions of: A) 11.5 C passed, hydrous systems; B) 12.7 C passed, anhydrous system for 5 mM **Fl**, 20 mM of Et_4NBF_4 under CO_2. 9-Hydroxyfluorene-9-carboxylic acid, 9-hydroxyfluorene and **Fl** were identified as products.

to its low yield, so a small portion of the electrolyzed solution was used directly for ^{1}H NMR analyses (MeOD). For identification of the unknown fraction, the ^{1}H NMR spectrum of the electrolysis mixture was compared with the ^{1}H NMR spectra (in MeOD) of standards (5 mM) 9-hydroxyfluorene-9-carboxylic acid, 9-hydroxyfluorene and **Fl** and a mixture (1:1:1) of these compounds, as illustrated in Figure 5.14. By comparing the chemical shifts of the standards and the mixture, 9-hydroxyfluorene-9-carboxylic acid was identified.

Also, GC-EIMS (see Figure 5.15) was performed for the detection of 9-hydroxyfluorene-9-carboxylic acid and 9-hydroxyfluorene. Solutions electrolyzed both "wet" (1% water, 11.5 C) and anhydrous (12.7 C) acetonitile were used directly for analysis. From the peak at m/z = 182 $M^{+\cdot}$, it was confirmed that one product was 9-hydroxyfluorene, and from the molecular ion peak at m/z = 227 $(M+1)^+$, it was confirmed that another product was 9-hydroxyfluorene-9-carboxylic acid.

5.5.4 Separation and quantification of 9-hydroxyfluorene and 9-hydroxyfluorene-9-carboxylic acid by HPLC

The electrolysis products were determined and quantified by HPLC using an Agilent 1100 series Eclipse with an XDBC-18 (5 μm and 4.6 × 250 mm) reverse phase column and coupled with an Agilent 1100 series G13158 Photodiode Array Detector at 254 nm. A short guard column was also set up with the analytical column. For the mobile phase, HPLC grade water and acetonitrile were used. Gradient elution was employed, with 80 mM aqueous acetic acid at (pH = 2.45) and acetonitrile with a flow rate of 0.90 mL/min.

Table 5.2 illustrates the gradients with time, stop time, and post time that were used for the separation of 9-hydroxyfluorene and 9-hydroxyfluorene-9-carboxylic acid in the electrolyzed solutions of **Fl** (5 mM) under CO_2. The initial pressure was set at 400 bar and a sample volume of 5 μL was injected. A standard addition method was used for the quantification of each of the products.

Table 5.2: HPLC gradients used for the separation and quantification of 9-hydroxyfluorene and 9-hydroxyfluorene-9-carboxylic acid in the electrolyzed solutions of **Fl** (5 mM) under CO_2.

Initial time (min)	80 mM aquous acetic acid (%)	Acetonitrile (%)	Stop time (min)	Post time (min)
0	30	70	15.0	5.00
2	28	72		
3	28	72		
5	20	80		
8	10	90		
12	0	100		

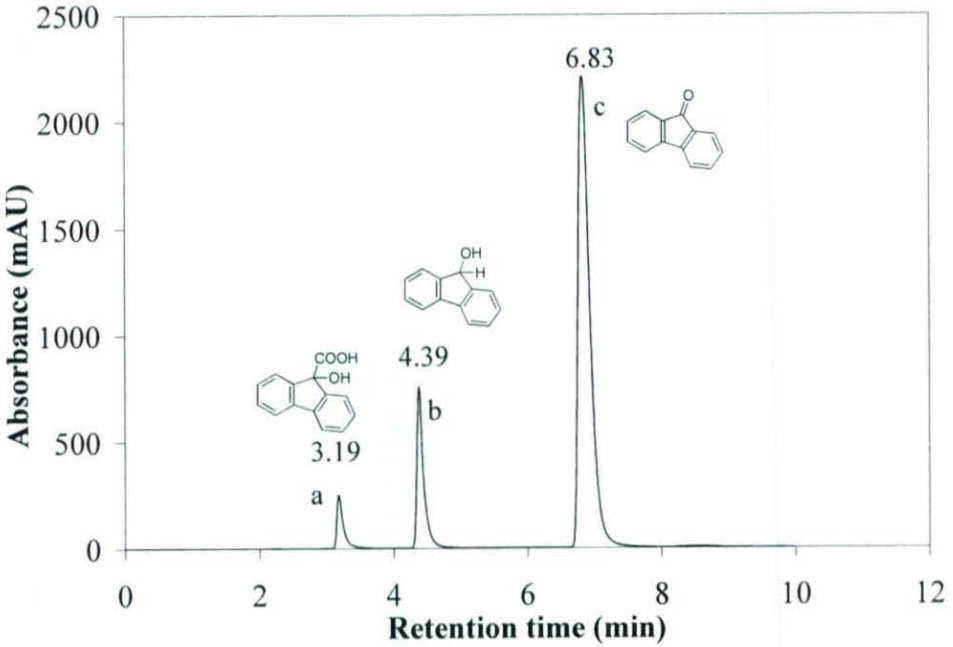

Figure 5.16: Chromatographic separation of three standards (5 mM): a) 9-hydroxyfluorene-9-carboxylic acid; b) 9-hydroxyfluorene; c) **Fl** using CH_3CN/80 mM aqueous CH_3COOH eluent.

Figure 5.16 shows the separation of a standard mixture of 9-hydroxyfluorene-9-carboxylic acid, 9-hydroxyfluorene and **Fl** (5 mM). The corresponding elution time of each of the standard compounds was used for identification and quantification of the products in the electrolyzed solutions. Figure 5.17 shows the chromatogram of a non-electrolyzed solution of **Fl** (5 mM) in CH_3CN/20 mM Et_4NBF_4, where the peak at 4.12 min is for the electrolyte Et_4NBF_4 and the peak at a retention time of around 7.0 min is for **Fl** itself.

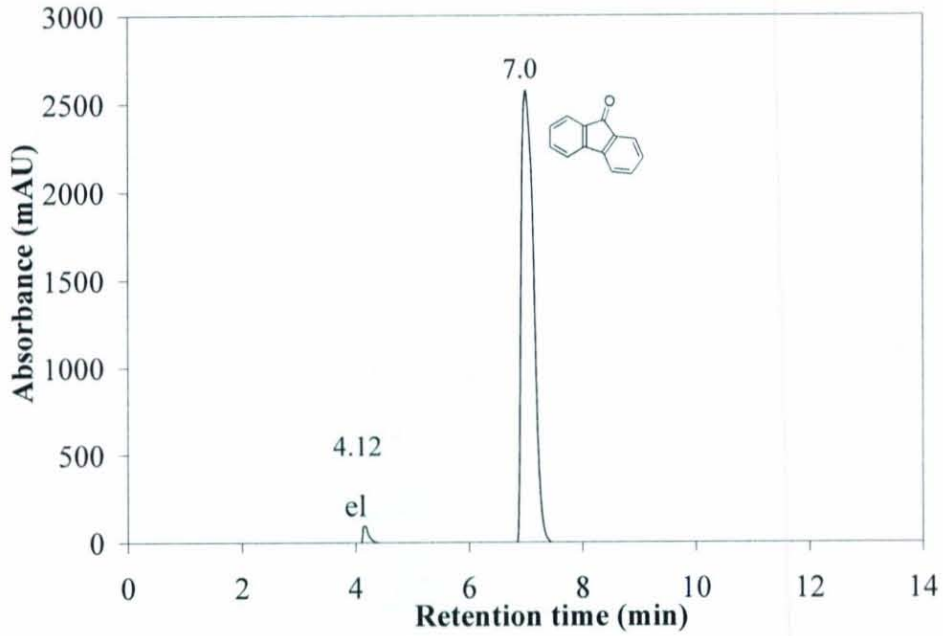

Figure 5.17: Chromatographic separation of a non-electrolyzed solution of **Fl** (5 mM) in acetonitrile and 20 mM of Et_4NBF_4 using CH_3CN/80 mM aqueous CH_3COOH as an eluent.

Figure 5.18 shows chromatograms of electrolyzed solutions of both hydrous (8.6 C) and anhydrous systems (12.7 C) of **Fl** in the presence of CO_2. The charge passed in both of the electrolyses corresponds to one-electron per **Fl** molecule. It is clear from these chromatograms that a large amount of **Fl** (ca. 80%) was recovered unchanged. 9-Hydroxyfluorene and 9-hydroxyfluorene-9-carboxylic acid were also identified together with the electrolyte.

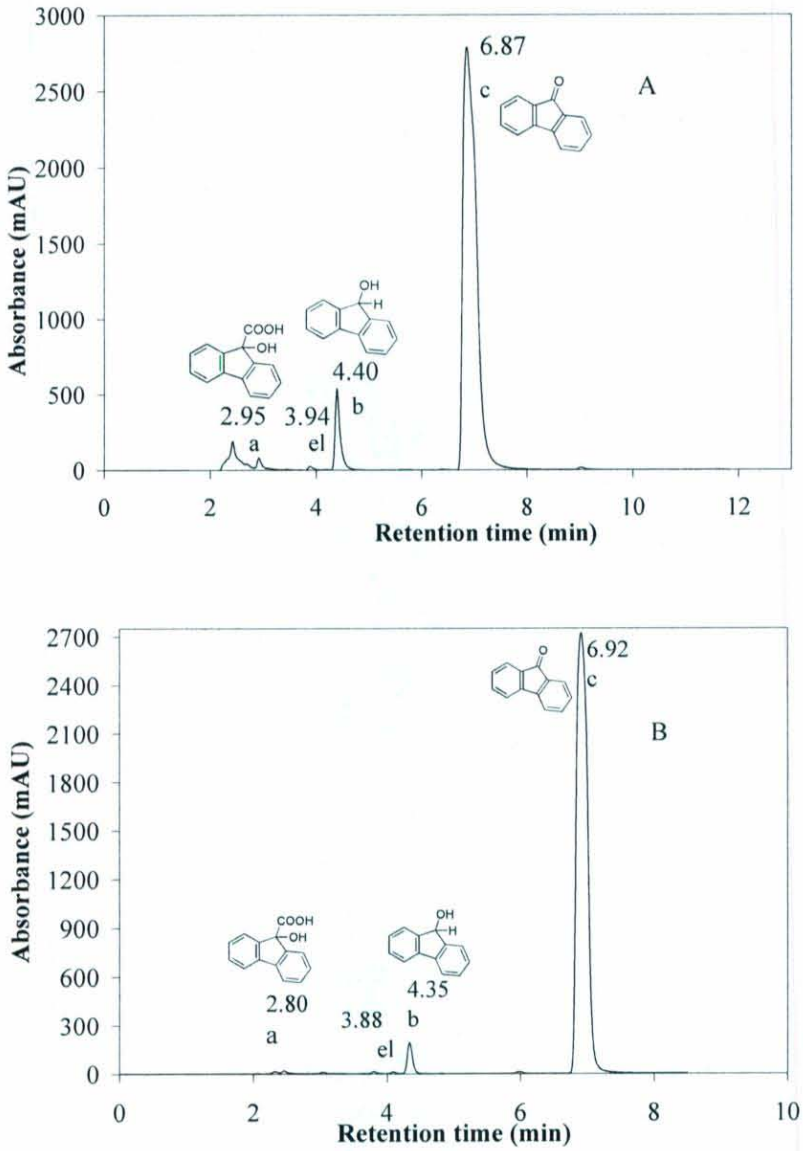

Figure 5.18: Chromatographic separation of electrolyzed solutions of: (A) 8.6 C passed, hydrous system; and (B) 12.7 C passed, anhydrous system, of 5 mM **Fl**, 20 mM of Et_4NBF_4 in CH_3CN/80 mM aqueous CH_3COOH as an eluent. a) 9-hydroxyfluorene-9-carboxylic acid, b) 9-hydroxyfluorene, and c) **Fl**.

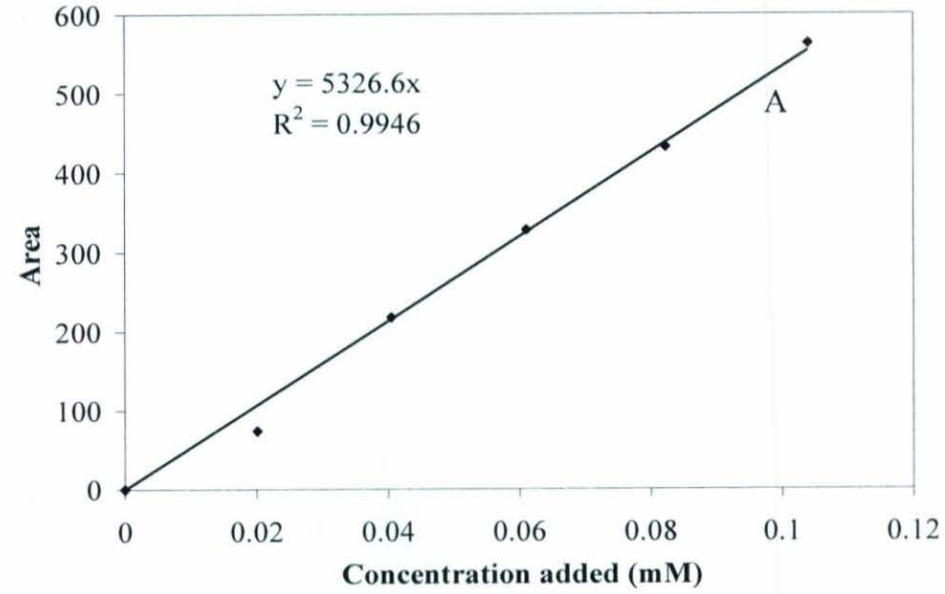

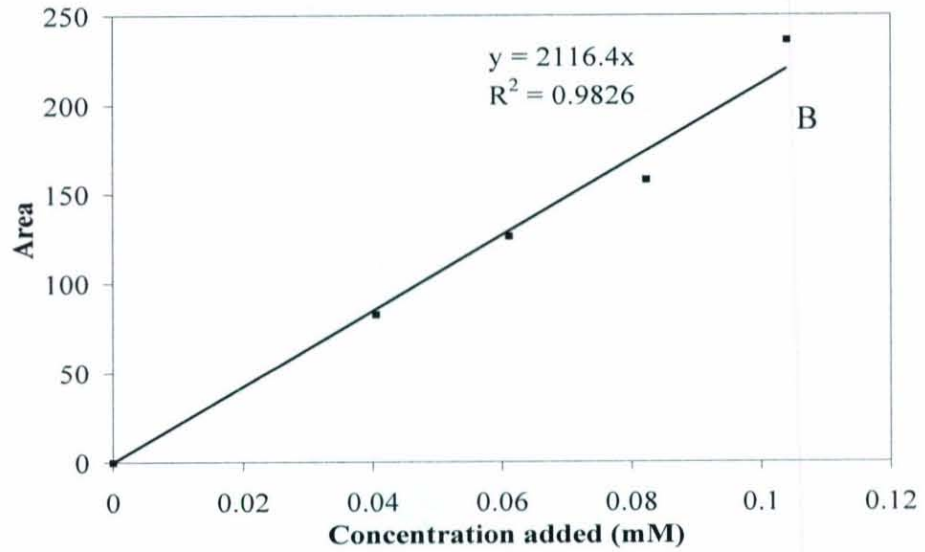

Figure 5.19: Calibration plots for A) 9-hydroxyfluorene, and B) 9-hydroxyfluorene-9-carboxylic acid obtained by using acetonitrile and aqueous 80 mM of acetic acid as gradient eluent.

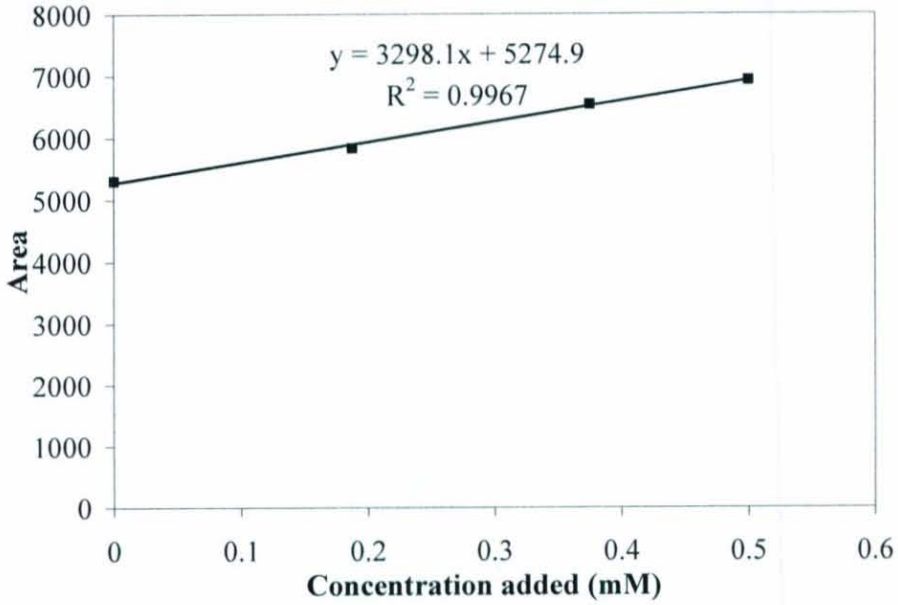

Figure 5.20: Standard addition plot for the quantification of 9-hydroxyfluorene for the electrolysis (8.06 C) solution of **Fl** (5 mM) in 20 mM of Et_4NBF_4 (anhydrous conditions), by using acetonitrile and aqueous 80 mM of acetic acid as gradient eluent.

Standard addition was used for the quantification of each of 9-hydroxyfluorene and 9-hydroxyfluorene-9-carboxylic acid that were produced during the electrolysis, as well as to determine the amount of **Fl** remaining. Figure 5.19 shows calibration plots for both of the standards, and Figure 5.20 shows a standard addition plot for 9-hydroxyfluorene for the electrolysis solution (8.06 C) of **Fl** (5 mM) in 20 mM of Et_4NBF_4 (anhydrous conditions) under CO_2, which is linear, with R^2 = 0.9967. The 9-hydroxyfluorene concentration was determined to be 22% of the initial amount of **Fl** (mol) with a RSD = 4.6%. For 1% water, 9-hydroxyfluorene was determined to be 31%

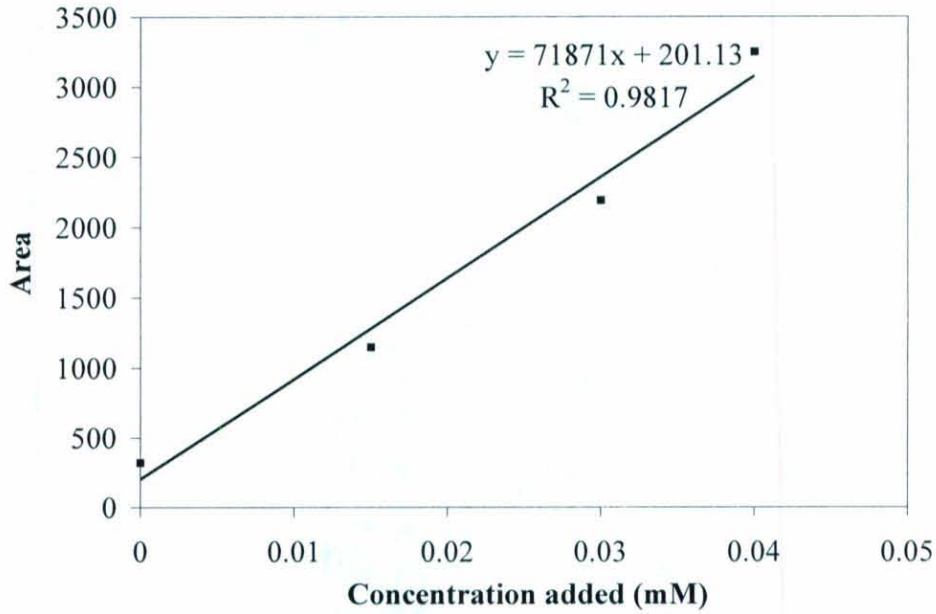

Figure 5.21: Standard addition plot for the quantification of 9-hydroxyfluorene-9-carboxylic acid for the electrolysis (8.6 C) solution of **Fl** (5 mM) in CH_3CN/20 mM Et_4NBF_4 (hydrous conditions), by using acetonitrile and aqueous 80 mM of acetic acid as gradient eluent.

of the initial **Fl** (mol) with a RSD = 7.6%.

Figure 5.21 shows a standard addition plot for 9-hydroxyfluorene-9-carboxylic acid, under aqueous (1% water) and anhydrous conditions. It was quantified by HPLC to be only 4.4% and 2.1%, respectively, to the initial concentration (mol) of **Fl** used for the electrolysis with $R^2 = 0.9990$ and $R^2 = 0.9817$ (Figure 5.21). Table 5.3 summarizes the results for HPLC analyses of **Fl** solution electrolyzed under CO_2. Faradaic efficiencies were calculated from the ratio between the charge necessary to produce the measured

quantities of 9-hydroxyfluorene-9-carboxylic acid or 9-hydroxyfluorene (two-electrons/mol = 100 %) and the total charge passed during the electrolysis process.

Table 5.3: HPLC quantification of products from the electrolysis of 5 mM **Fl** in CH_3CN/20 mM Et_4NBF_4 in CO_2 saturated solution. The charge passed in these electrolyses corresponds to one-electron per **Fl** molecule.

Electrolysis conditions	Product (% conversion) [faradaic efficiency]	Product (% conversion) [faradaic efficiency]
Anhydrous (8.06 C charge passed)	9-hydroxyfluorene (22%) [43%] RSD = 4.6%	9-hydroxyfluorene-9-carboxylic acid (4.4%) [8.8%] RSD = 16%
1% v/v water (8.6 C charge passed)	9-hydroxyfluorene (31%) [61%] RSD = 7.6%	9-hydroxyfluorene-9-carboxylic acid (2.1%) [4.2%]

5.5.5 HPLC separation and quantification of oxalic and formic acid

For the determination of oxalic acid/formic acid, many attempts were made to identify and quantify these products. Initially, GC-FID (see Figure 5.22) was used to characterize these acids by derivatization to their corresponding esters (by use of TMS diazomethane and at an initial column temperature of 10 °C). Although this method worked to some

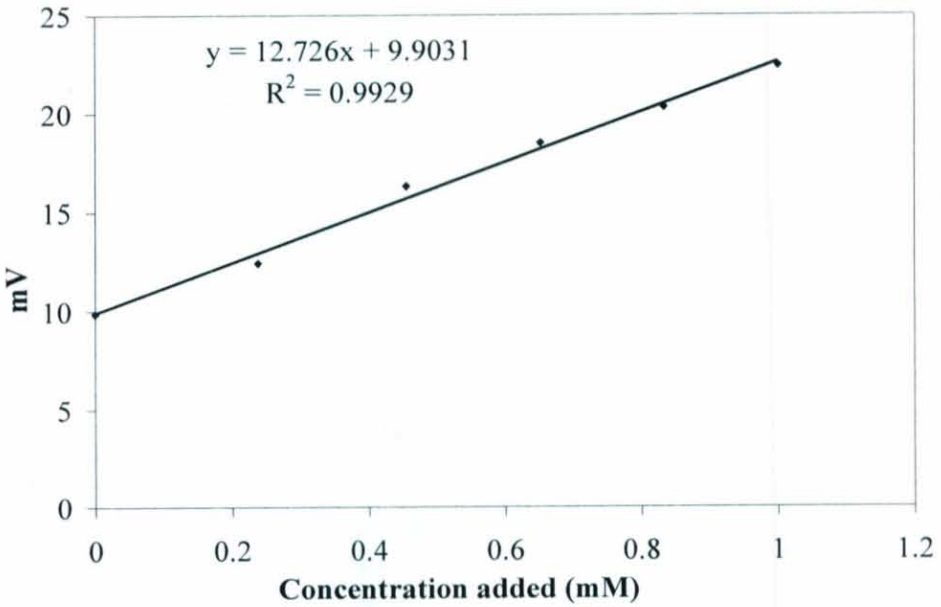

Figure 5.22: Standard addition plot for quantification of formic acid by GC-FID method in an electrolyzed solution (11.0 C passed, 1% water) of 5 mM **Fl**, 20 mM of Et_4NBF_4.

extent for formic acid (faradaic yield ~28%) determination but did not work for oxalic acid. Even for formic acid, the high concentration of electrolyte in the electrolysis solution resulted in poor reproducibility.

HPLC was found to be much more suitable. For separation and quantification of oxalic and formic acid, the HPLC and detector described in section 5.5.4 was used with UV detection at 210 and 214 nm for formic and oxalic acid, respectively. Phosphate buffer (KH_2PO_4 (50 mM) + H_3PO_4) at pH = 2.45 was used as the eluent. Acetonitrile (5%) was added to this buffer in order to decrease the back pressure of the column. Thus the buffer and acetonitrile (95:5) mixture was used as an isocratic eluent at a flow rate of

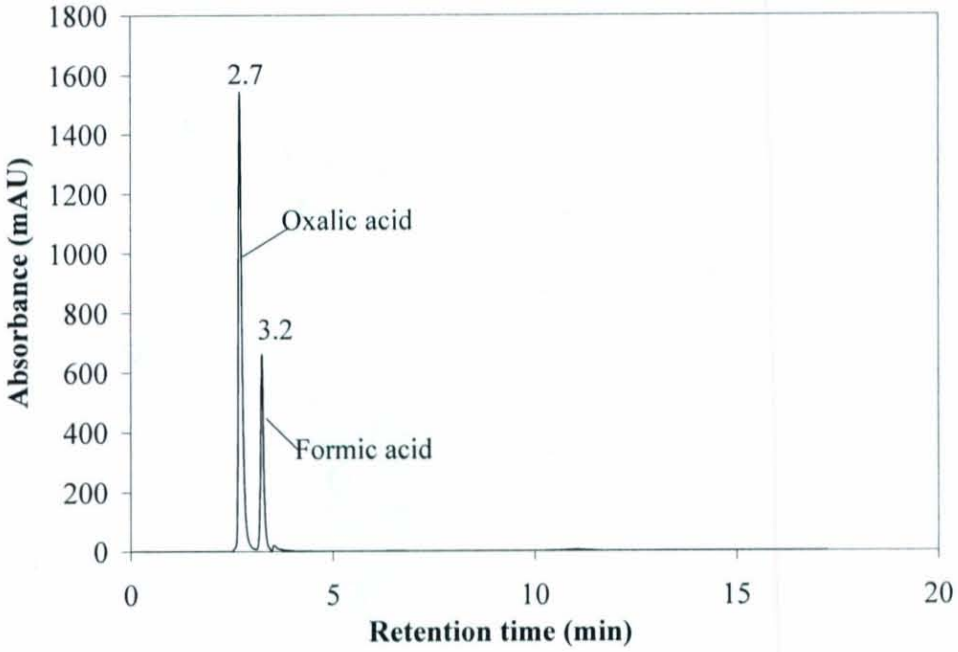

Figure 5.23: Chromatogram of a standard mixture of 5 mM oxalic acid and 5 mM formic acid using 50 mM KH_2PO_4/H_3PO_4 at pH = 2.45 and acetonitrile (95:5) as the eluent.

ca. 0.90 mL/min. The pressure was set at 150 bar maximum during the separations. A sample volume of 20.0 μL was introduced through an injection loop.

Figure 5.23 shows the separation of a standard mixture of oxalic acid and formic acid, while Figure 5.24 shows a chromatogram of an electrolyzed solution (8.06 C, anhydrous system) of 5 mM **FI** in CH_3CN containing 20 mM Et_4NBF_4 and saturated with CO_2. The separations of the different components produced during the electrolysis process are illustrated in Figure 5.24.

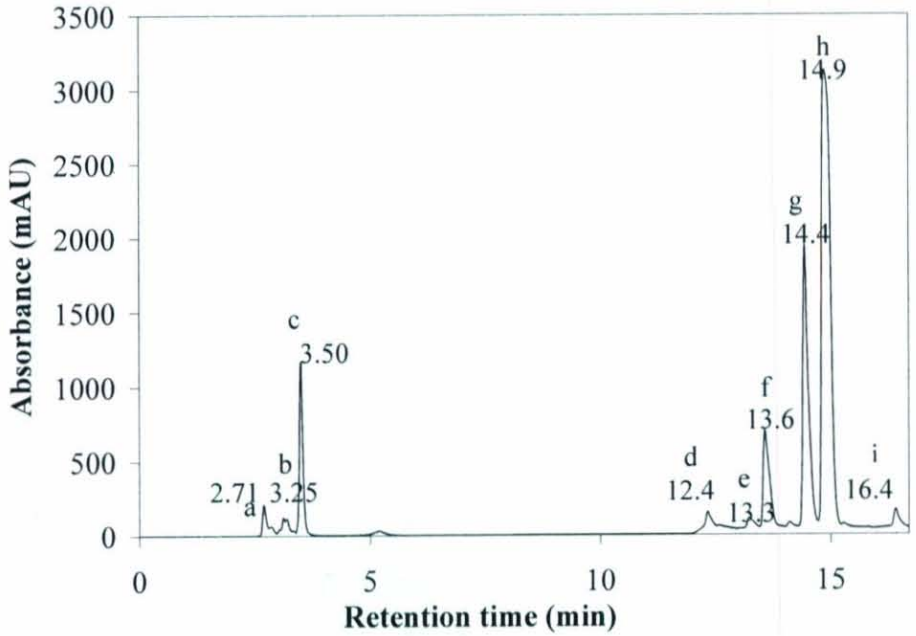

Figure 5.24: HPLC chromatogram of an electrolyzed solution (8.06 C, anhydrous system) of 5 mM **Fl** in CH_3CN containing 20 mM Et_4NBF_4. The isocratic eluent was KH_2PO_4/H_3PO_4 at pH = 2.45 and acetonitrile (95:5). Peaks are tentatively identified as: a) oxalic acid; b) not identified; c) not identified; d) not identified; e) 9-hydroxyfluorene-9-carboxylic acid; f) Et_4NBF_4 (electrolyte); g) 9-hydroxyfluorene; h) **Fl** and i) not identified.

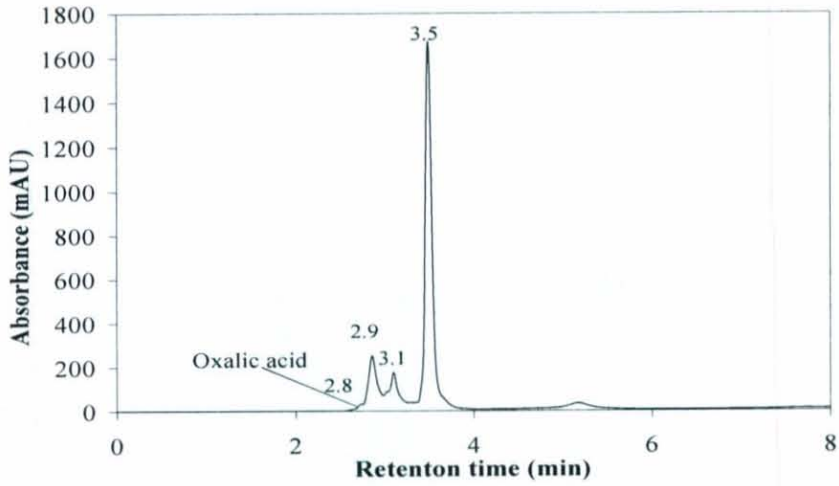

Figure 5.25: HPLC chromatogram of an electrolyzed solution (8.06 C, anhydrous system) of 5 mM of **Fl** in CH_3CN containing, 20 mM of Et_4NBF_4. The eluent was KH_2PO_4/H_3PO_4 at pH = 2.45 and acetonitrile (95:5) as isocratic eluent.

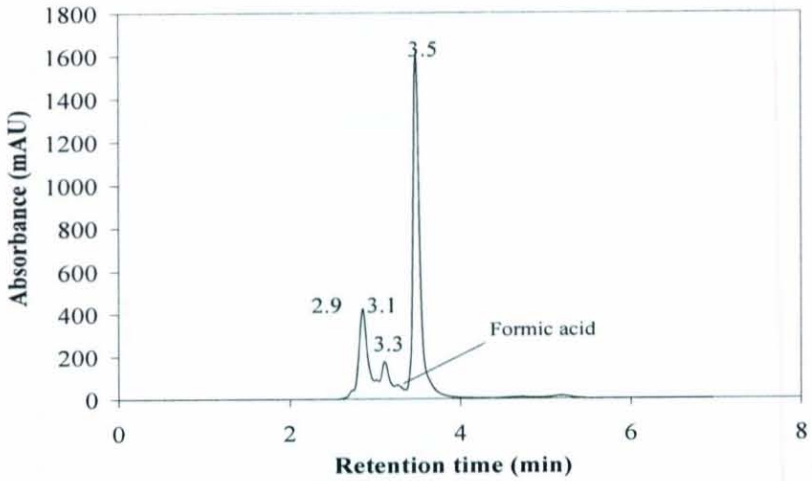

Figure 5.26: HPLC chromatogram of an electrolyzed solution (11.06 C, hydrous system) of 5 mM **Fl** in CH_3CN containing, 20 mM of Et_4NBF_4. The eluent was KH_2PO_4/H_3PO_4 at pH = 2.45 and acetonitrile (95:5) as an isocratic eluent.

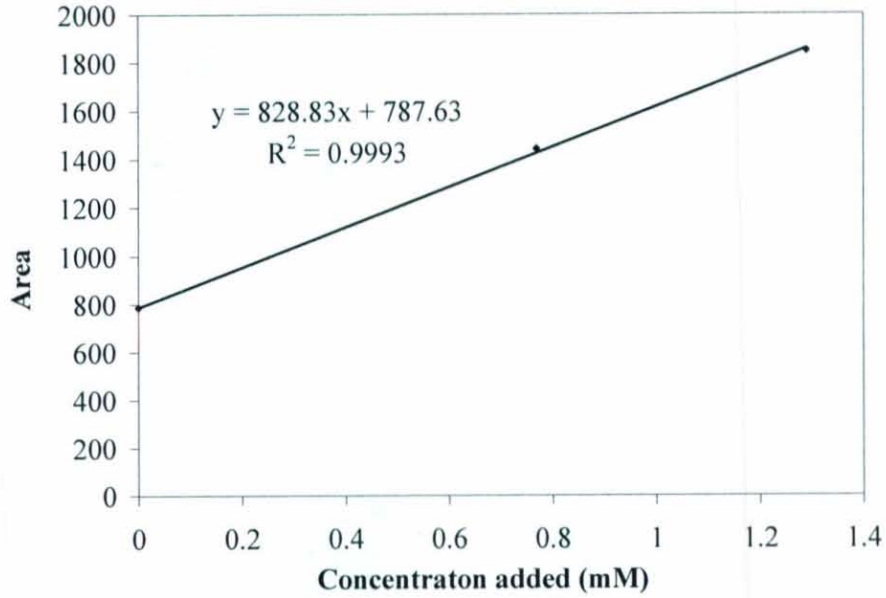

Figure 5.27: Standard addition plot for the quantification of formic acid for the electrolysis (11.06 C) solution of **Fl** (5 mM) in CH_3CN/20 mM of Et_4NBF_4 (hydrous conditions), by using 50 mM of KH_2PO_4/H_3PO_4 buffer (pH = 2.45) and acetonitrile (95:5) as an isocratic eluent.

Figures 5.25 and 5.26 show expansions of the initial parts of chromatograms of 5 mM of **Fl** electrolyzed in CO_2 saturated anhydrous and hydrous (1% water) solutions, respectively. Small peaks corresponding to oxalic and formic acid were identified by standard addition with HPLC chromatographic separation. Figure 5.27 shows a standard addition plot for quantification of formic acid from an electrolyzed solution of **Fl** (5 mM) in acetonitrile containing 20 mM of Et_4NBF_4 (11.06 C, hydrous conditions). The linear plot ($R^2 = 0.9993$) gave a formic acid concentration of 0.950 mM which corresponded to

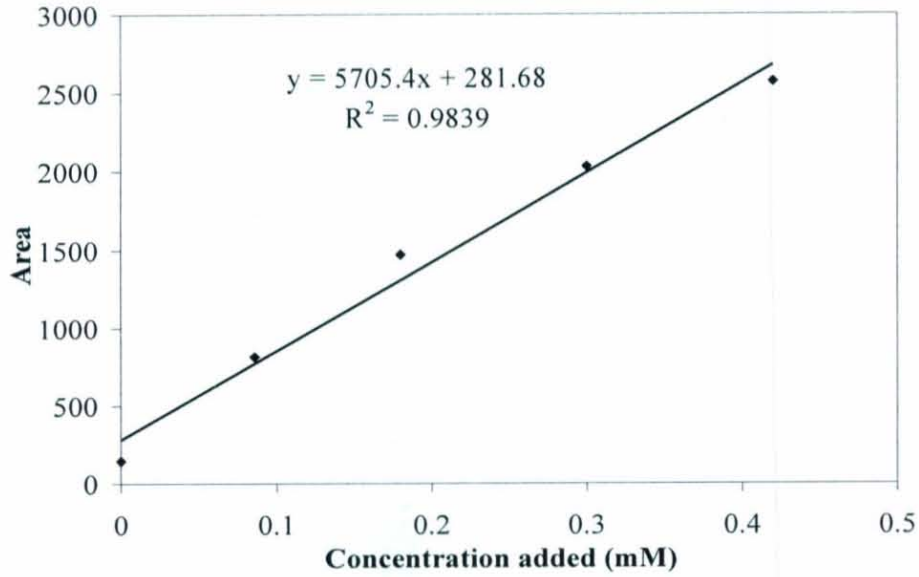

Figure 5.28: Standard addition plot for the quantification of oxalic acid for the electrolysis (8.06 C) solution of **FI** (5 mM) in CH_3CN/20 mM Et_4NBF_4 (anhydrous conditions), by using 50 mM of KH_2PO_4/H_3PO_4 buffer (pH = 2.45) and acetonitrile (95:5) as an isocratic eluent.

a faradaic yield of 28%. This result is also consistent with the GC-FID result (see Figure 5.22).

Figure 5.28 shows a standard addition plot for quantification of oxalic acid from an electrolysis solution of **FI** (5 mM) in acetonitrile containing 20 mM of Et_4NBF_4 on both anhydrous and aqueous (1% water) conditions. The standard addition plot (R^2 = 0.9839) gave a oxalic acid concentration of 0.024 mM in the anhydrous system (8.06 C) which corresponded to a faradaic yield of 2.0%. For the hydrous system (11.06 C) it gave oxalic acid concentrations of 0.289 mM that corresponded to a faradaic yield of 11.0%

with a high RSD values that indicated oxalic acid is detectable but not quantitiable.

Table 5.4 summarizes the type of electrolysis, amount of charge passed, faradaic efficiency, and products formed during the electrolysis of **Fl** under CO_2. Faradaic efficiency was calculated from the ratio between the charge necessary to produce the oxalic acid or formic acid (two-electrons/mol = 100%) and the total charge passed during electrolysis.

Table 5.4: HPLC quantification of products from the electrolysis of 5 mM **Fl** in CO_2-saturated CH_3CN/20 mM Et_4NBF_4 solution. The charge passed in these electrolyses corresponds to one-electron per **Fl** molecule.

Electrolysis conditions (total charge passed)	Oxalic acid	Formic acid
Anhydrous (8.06 C)	~2%	Not detected
1% v/v of water (11.06 C)	~11%	28%

5.5.6 Discussion

Scheme 5.3 and Figure 5.29 show the results for the electrolysis of **Fl** at −1.2 V vs Ag/AgCl in the presence of CO_2 at the Hg pool electrode in CH_3CN/20 mM Et_4NBF_4 solution under both anhydrous and 1% aqueous conditions. The amount of charge passed (one-electron per **Fl** molecule) and the percentage that goes into each pathway are

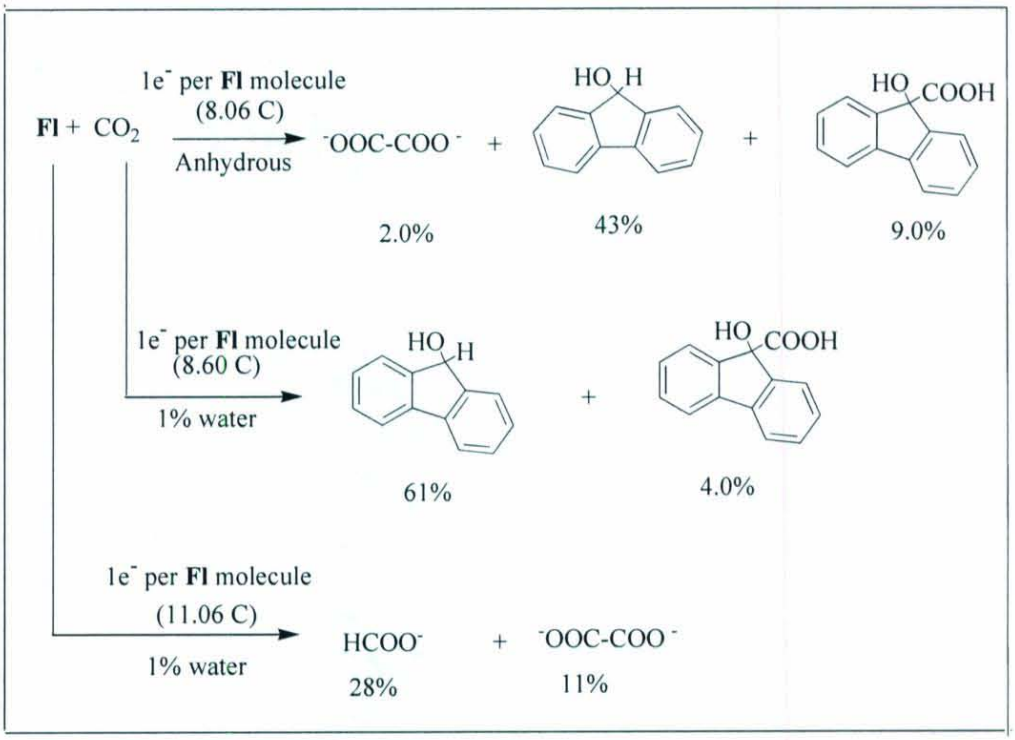

Scheme 5.3: Multiple competing pathways of product formation during the electrolysis of **Fl** in CO_2-saturated acetonitrile under both anhydrous and 1% water conditions. Percentage of charge was calculated based on the initial amount of charge passed and faradaic efficiency for each of the products.

summarized in Scheme 5.3. The reduction of CO_2 by **Fl** takes place via both electrocatalytic and carboxylation pathways. According to the literature [77], the electrocatalytic reduction of CO_2 should result in formic acid in the presence of water and oxalic acid under anhydrous conditions. Our results presented in Table 5.4 are not consistent with this. The electrocatalytic reduction of CO_2 by fluorene-9-one, produced

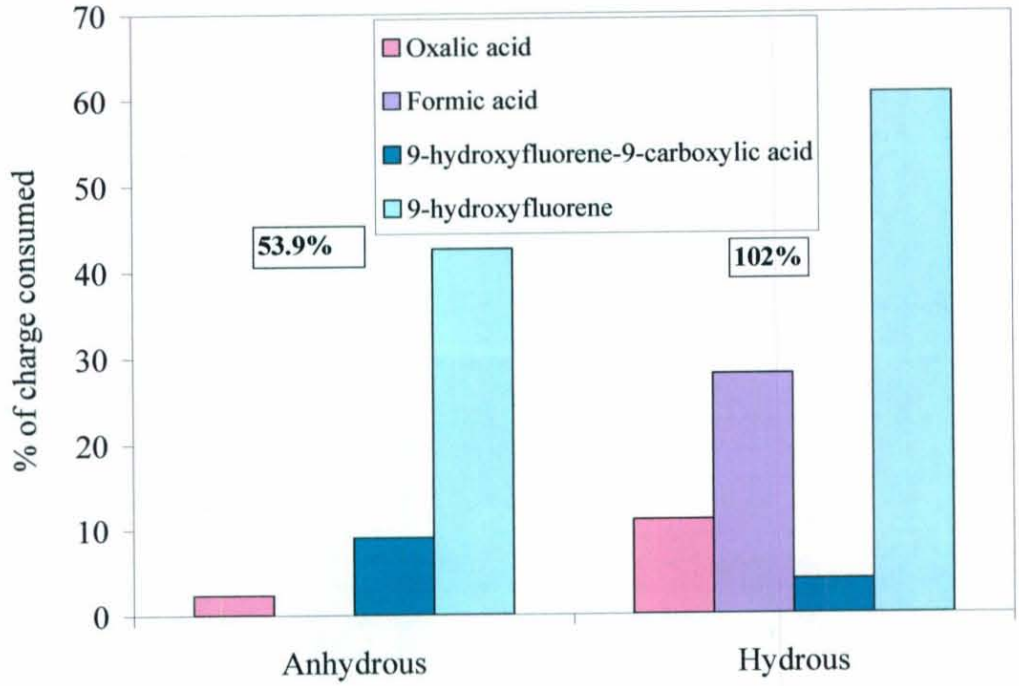

Figure 5.29: Plot of percentage of charge consumed for each of the products relative to the total amount of charge passed for the electrolysis of **Fl** (5 mM) in CO_2-saturated acetonitrile and 20 mM of Et_4NBF_4 solutions under anhydrous and 1% water conditions at a Hg pool electrode at -1.2 V vs Ag/AgCl.

only a trace of oxalic acid under anhydrous conditions but formic acid was formed predominantly (28%) under hydrous conditions.

It can be noted from Figure 5.29 that the total percentage of charge consumed during the aqueous condition of electrolysis was around ~100%, which is the expected result. Under anhydrous conditions, the percentage of charge accounted for was only 54%. The rest of the charge consumed under anhydrous conditions can be explained by

the build-up of a **FlCO$_2$** complex with CO_2 similar to the reductive addition of CO_2 to 9,10-phenanthrenequinone, as was also reported by Mizen et al. [187]. This **FlCO$_2$** complex would reoxidize back to **Fl** when the solution was opened to air.

Formation of carboxylated **Fl** products is mainly from carboxylation reactions. 9-Hydroxyfluorene-9-carboxylic acid is produced in both electrolyzed systems. The mechanism of the formation of this product may be due to the ECECC pathway, as was proposed by Pletcher et al. [188]. 9-Hydroxyfluorene-9-carboxylic acid was formed in 9.0% (anhydrous) to 4.0% (1% water) yield. Formation of higher yields of alcohol products is explained in the literature [155-156, 189-190] by the presence of proton donors in the solvent (like water traces). In this case, protonation of the anion radical of **Fl** (**Fl**$^{\cdot-}$) can lead to the formation of 9-hydroxyfluorene. Thus in the anhydrous system, the yield of 9-hydroxyfluorene is only around 43%, while in presence of 1% v/v of water, the yield becomes 61%.

Figure 5.30 illustrates the formation of carboxylation products (%) relative to the faradaic yields during the electrolysis of **Fl** for both anhydrous and 1% aqueous conditions. It is evident from the figure that under anhydrous conditions ca. 50% and for 1% aqueous conditions ca. 30% **Fl** should be recovered based on the initial amounts of **Fl** (mol) used for electrolysis. The starting material **Fl** was recovered ca. 67% for the anhydrous system and about 77% was for hydrous system. However, the recovery of large amount of **Fl** after the electrolysis suggests the formations of oxalate, formate are due to the electrocatalytic activities of **Fl**. Thus **Fl** can act as an effective agent for electrocatalytic reduction of CO_2 at sufficiently low cathodic potentials. Although for the

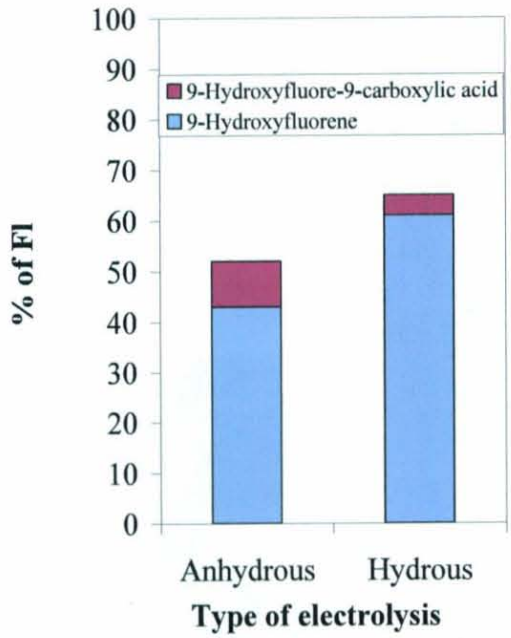

Figure 5.30: Plot of the percentage of carboxylated products formed relative to faradaic yields of **Fl** (5 mM) at -1.2 V vs Ag/AgCl in CO_2-saturated acetonitrile and 20 mM of Et_4NBF_4 solutions under anhydrous and 1% water conditions at a Hg pool electrode.

electrocatalytic products faradic efficiency was found to be low in all the cases, it could be possibly from the competitive formation of carboxylation products.

Chapter 6

Summary

The unifying idea of the thesis work is the development of efficient electrocatalytic systems that can effectively reduce CO_2 to produce useful products, such as fuels, and chemicals which is currently one of the most challenging research areas for chemists. Ruthenium polypyridyl complexes were reported to be good catalysts for the selective production of formic acid. So metal complexes with $[Ru(bpy)_2(L)]^{2+}$ and $[\{Ru(bpy)_2\}_2(L)]^{4+}$ systems (where L = benzimidazole/benzothiazole), have been of particular interest in this PhD research. The nature of a ligand (π-donor/π-acceptor) has an effect on the metal centres, so different types of benzimidazole and benzimidazole ligands were used in this work to see their effect on CO_2 reductions. In addition to that, it is feasible to use bimetallic (two-electron systems) over monometallic complexes in order to get highly reduced species and facilitate the formation of two-electron products like HCOOH and/or CO.

It was found that the benzothiazole complexes of Ru exhibited remarkable electrocatalytic activities for CO_2 reductions, especially $[Ru(\mathbf{pybtz})(bpy)_2](ClO_4)_2$ and $[\{(bpy)_2Ru\}_2(\mathbf{py_2tbtz})](ClO_4)_4$ [where, **pybtz** = 2-(pyridin-2-yl)benzo[*d*]thiazole] and **py$_2$tbtz** = 2,6′-bis(2-pyridyl)-2,2′:6,2″-thiazolo[4,5-d]benzothiazole]. Although structural variations influence the activity, but all benzothiazole complexes exhibited much higher activities than those of the corresponding benzimidazole complexes (in the CV's). The difference between the remarkable activities of the benzothiazole and benzimidazole analogues together with the requirement of multiple reductions for CO_2 activation would represent interesting chemistry, and obviously it represents an unprecedented result for CO_2 activation. It was also found that benzimidazole e.g., $[Ru(\mathbf{pybbim})(bpy)_2](ClO_4)_2$

(**pybbim** = 2,2′-(pyridine-2,5-diyl)bis(1H-benzo[d]imidazole) complexes showed lower activities against CO_2 reductions than that of the corresponding Me-benzimidazole complex (e.g., [Ru(**Me_2-pybbim**)$(bpy)_2$]$(ClO_4)_2$ (where, **Me_2-pybbim** = 2,5-bis(1-methyl-1*H*-benzo[*d*]imidazole-2-yl)pyridine). This might be related to the electron donating nature of the Me-groups [79]. Among the benzimidazole complexes, monometallic [Ru(**Me_2-pybbim**)$(bpy)_2$]$(ClO_4)_2$ showed higher activities towards CO_2 reduction relative to their bimetallic counterparts, [{$(bpy)_2Ru$}$_2$(**Me_2-py_2bbim**)]$(ClO_4)_4$ (where, **Me_2-py_2bbim** = 3,3′-dimethyl-2,2′-di(pyridin-2-yl)-5,6′-bi(3H-benzo[d]-imidazole). These results are also supported by similar findings in the literature [78, 191]. It was also interesting to report that formate and oxalate were produced and detected at a moderate low cathodic overpotential for bimetallic [{$(bpy)_2Ru$}$_2$(**py_2tbtz**)]$(ClO_4)_4$ complexes.

All the products were separated and identified and quantified by HPLC and UV-Vis spectroscopy. It was anticipated that the electrocatalytic process here is by EC_{cat} pathways. Although faradic efficiencies were found low, it can be stated that this result for CO_2 activation towards electrocatalytic reduction of CO_2 by Ru benzothiazole complexes is unprecedented and our findings would allow opening a new window for benzothiazole based transition metal electrocatalysts in CO_2 reduction.

The same idea of electrocatalytic reduction of CO_2 has been studied using an organic ketone, fluorene-9-one. The products from these experiments were identified as 9-hydroxyfluorene and 9-hydroxyfluorene-9-carboxylic acid which are the predicted electrocarboxylation products from previous literature reports. On the other hand, formic

and oxalic acid were the products from electrocatalytic pathways. Faradic efficiencies were found low for formic and oxalic acids. These might be due to the competitive formation of carboxylation products. Additionally **Fl** was recovered under both anhydrous (67%) and hydrous (77%) electrolytic conditions. All those results conclude that **Fl** can also be used as organocatalyst and can effectively catalyze electrochemical reduction of CO_2.

Future work could involve the development of even better electrocatalytic systems that can effectively reduce CO_2 to produce HCOOH and MeOH as fuels. Instead of homogeneous catalytic systems, the use of heterogeneous catalytic systems might be feasible in the sense that it might allow for higher efficiencies for the formation of products by enabling better diffusion of CO_2 to the electrode surface. For example, high surface area gas diffusion electrodes (e.g., molecular catalyst on a carbon black support) might be used to increase the yield of the catalytic products. Immobilized complexes have been of special interest and multimetallic complexes could potentially be attached through highly stable linkages to the carbon surface. Additionally, conjugated metallopolymers might allow the study of the effects of extended conjugation on electrocatalytic activities towards CO_2 reductions. The importance of using a delocalized π-orbital network is that this system allows faster charge transfer processes between metal centres relative to monometallic complexes and could act as an active electrocatalyst for CO_2 reduction.

References

[1] Gattrell, M.; Gupta, N.; Co, A. *Energy Conversion and Management*, **2007**, *48*, 1255.

[2] Proceedings of the High Level Conference on World Food Security: "The Challenges of Climate Change and Bioenergy. Soaring Food Prices: Facts, Perspectives, Impacts and Actions Required" (HLC/08/INF/1); Conference organized by the Food and Agricultural Organization of the United Nations, Rome, 3-5 June, **2008**.

[3] Searchinger, T.; Heimlich, R.; Houghton, R. A.; Fengxia, D.; Elobeid, A.; Fabiosa, J.; Tokgoz, S.; Hayes, D.; Yu, T.-H. *Science* **2008**, *319*, 1238.

[4] Fargione, J.; Hill, J.; Tilman, D. S. P.; Hawthorne, P. *Science* **2008**, *319*, 1235.

[5] "Climate Change 2007: Synthesis Report; International Panel on Climate Change". Cambridge University Press: Cambridge, UK, **2007**.

[6] Olah, G. A.; Goeppert, A.; Surya Prakash, G. K. *J. Org. Chem.* **2009**, *74*, 487.

[7] Federsel, C.; Jackstell, R.; Beller, M. *Angew. Chem. Int. Ed.* **2010**, *49*, 6254.

[8] Song, C. *Catalysis Today* **2006**, *115*, 2.

[9] Campbell, C. J. "The Coming Oil Crisis". In Multi-science Publishing: Brentwood, England, **1988**.

[10] Savéant, J.-M. *Chem. Rev.* **2008**, *108*, 2348.

[11] Benson, E. E.; Kubiak, C. P.; Sathrum, A. J.; Smieja, J. M. *Chem. Soc. Rev.* **2009**, *38*, 89.

[12] Bard, A. J.; Faulkner, L. R. "Electrochemical Methods: Fundamentals and Applications". Wiley-VCH: New York, **2004**; chapter 12, 501.

[13] Andrieux, C. P.; Dumas-Bouchiat, J.-M.; Savéant, J.-M. *J. Electroanal. Chem.* **1978**, *87*, 39.

[14] Merz, A. *Top. Curr. Chem.* **1990**, *152*, 49.

[15] Deronzier, A.; Moutet, J.-C. *Coord. Chem. Rev.* **1996**, *147*, 339.

[16] Cheung, K.-C.; Guo, P.; So, M.-H.; Lee, L.;Y. S.; Ho , K.-P.; Wong, W.-L.; Lee, K.-H.; Wong, W.-T.; Zhou, Z.-Y.; Wong, K.-Y. *J. Organomet. Chem.***2009**, *694,* 2842.

[17] Jitaru, M. "Electrochemical carbon dioxide reduction- fundamental and applied topics (review)" In *Journal of the University of Chemical Technology and Metallurgy,* **2007**, *42*, 4. [Online]

[18] Chaplin, R. P. S.; Wragg, A. A. *J. Appl. Electrochem.* **2003**, *33*, 1107.

[19] (a) Amatore, C.; Savéant, J.-M. *J. Am. Chem. Soc.* **1981**, *103*, 5021; (b) Kushi, Y.; Nagao, H.; Nishioka, T.; Isobe, K.; Tanaka, K. *Chem. Commun.* **1995,** *1995*, 1223.

[20] Green, D.W.; Perry, R.H. "Perry's Chemical Engineer's Handbook", 6th ed. McGraw-Hill, **1984**.

[21] Hori, Y. "Electrochemical CO_2 Reduction on Metal Electrodes". In

Modern Aspects of Electrochemistry; Vayenas, C. G.; White, R. E.; Gamboa-Aldeco, M. E.; Eds.; Springer: New York, **2008**, *42*, 89.

[22] Ohta, K.; Suda, K.; Kaneco, S.; Mizuno, T. *J. Electrochem. Soc.* **2000**, *147*, 233.

[23] Mahmood, M. N.; Masheder, D.; Harty, C. J. *J. Appl. Electrochem.* **1987**, *17*, 1159.

[24] Hori, Y.; Wakebe, H.; Tsukamoto, T.; Koga, O. *Electrochim. Acta.* **1994**, *11-12*, 1833.

[25] Ikeda, S.; Takagi, T.; Ito, K. *Bull. Chem. Soc. Jpn.* **1987**, *60*, 2517.

[26] Haynes, L. V.; Sawyer, D. T. *Anal. Chem.* **1967**, *39*, 332.

[27] Tyssee, D. A.; Wagenknecht, J. H.; Baizer, M. M.; Chruma, J. L. *Tetrahedron Lett.* **1972**, *47*, 4809.

[28] Gressin, J. C.; Michelet, D.; Nadjo, L.; Savéant, J.-M. *Nouv. J. Chim.* **1979**, 545.

[29] Ogura, K.; Yoshida, I. *J. Mol. Catal.* **1988**, *47*, 51.

[30] Hammouche, M.; Lexa, D.; Savéant, J.-M. *J. Electroanal. Chem.* **1988**, *249*, 347.

[31] Christensen, P. A.; Hamnett, A.; Muir, A. V. G. *J. Electroanal. Chem.* **1988**, *241*, 361.

[32] Furuya, N.; Koide, S. *Electrochim. Acta.* **1991**, *36*, 1309.

[33] Mahmood, M. N.; Masheder, D.; Harty, C. J. *J. Appl. Electrochem.* **1987**, *17*, 1223.

[34] Fujihira, M.; Hirata, Y.; Suga, K. *J. Electroanal. Chem.* **1990**, *292*, 199.

[35] Christensen, P. A.; Higgins, S. J. *J. Electroanl. Chem.* **1995**, *387*, 127.

[36] Symaszek, A.; Pruchnik, F. P. *J. Organomet. Chem.* **1989**, *376*, 133.

[37] Rasmussen, S. C.; Richter, M. M.; Yi, E.; Place, H.; Brewer, K. J. *Inorg. Chem.* **1990**, *29*, 3926.

[38] Kushi, Y.; Nagao, H.; Nishioka, T.; Isobe, K.; Tanaka, K. *Chem. Lett.* **1994**, *23*, 2175.

[39] Komeda, N.; Nagao, H.; Matsui, T.; Adachi, G.; Tanaka, K. *J. Am. Chem. Soc.* **1992**, *114*, 3625.

[40] Sánchez-Sánchez, C. M.; Montiel, V.; Tryk, D. A.; Aldaz, A.; Fujishima, A. *Pure Appl. Chem.* **2001**, *73*, 1917.

[41] Beley, M.; Collin, J.-P.; Ruppert, R.; Sauvage, J. P. *J. Am. Chem. Soc.* **1986**, *108*, 7461.

[42] Beley, M.; Collin, J.-P.; Ruppert, R.; Sauvage, J. P. *Chem. Commun.* **1984**, 1315.

[43] Hawecker, J.; Lehn, J.-M.; Ziessel, R. *Chem. Commun.* **1984**, 328.

[44] (a) Sullivan, B. P.; Bolinger, C. M.; Conrad, D.; Vining, W. J.;. Meyer, T. J. *Chem. Commun.* **1985**, 1414; (b) Deronzier, A., Moutet, J.-C. "Electrochemical Reactions Catalyzed by Transition Metal Complexes". In *Compreh. Coord. Chem. II.;* Elsevier Ltd. **2003**, *9*, 471.

[45] Ishida, H.; Tanaka, K.; Tanaka, T. *Chem. Lett.* **1985**, 405.

[46] Bolinger, C. M.; Sullivan, B. P.; Conrad, D.; Gilbert, J. A.; Story, N.; Meyer, T. J. *Chem. Commun.* **1985**, 796.

[47] (a) Kapusta, S.; Hackennan, N. *J. Electrochem. Soc.* **1984**, *131*, 1511, (b)Takahashi, K.; Hiratsuka, K.; Sasaki, H.; Toshima, S. *Chem. Lett.* **1979**, 305.

[48] Ishida, H., Tanaka, H.; Tanaka, K.; Tanaka, T. *Chem.Commun.* **1987**, 131.

[49] Sullivan, B. P.; Meyer, T. J. *Organometallics* **1986**, *5*, 1500.

[50] (a) Pugh, J. R.; Bruce, M. R. M.; Sullivan, B. P.; Meyer, T. J. *Inorg. Chem.* **1991**, *30,* 86; (b) Chardon-Noblat, S.; Cripps, G. H.; Deronzier, A.; Field, J. S.; Gouws, S.; Heines, R. J.; Southway, F. *Organometallics* **2001**, *20*, 1668; (c) Hayashi, H.; Ogo, S.; Abura, T.; Fukuzumi, S. *J. Am. Chem. Soc.* **2003**, *125*, 14266. (d) Tanaka, H.; Nagao, H.; Peng, S.-M.; Tanaka, K. *Organometallics* **1992**, *11*, 1450; (e) Tanaka, H.; Tzeng, B.-C.; Nagao, H.; Peng, S.-M.; Tanaka, K. *Organometallics* **1992**, *11*, 3171; (f) Toyohara, K.; Tsuge, K.; Tanaka, K. *Organometallics* **1995**, *14*, 5099; (g) Fujita, E.; Chou, M.; Tanaka, K.; *Appl. Organomet. Chem.* **2000**, *14*, 844.

[51] (a) Alessio, E.; Zassinovich, G.; Mestroni, G. *J. Mol. Catal.* **1983**, *18*, 3; Alessio, E.; Clauti, G.; Mestroni, G. *J. Mol. Catal.* **1985**, *29*, 77; (b) Hamnett, A.; Christensen, P. *J. Electroanal. Chem.* **1995**, *395*, 195; (c) Christensen, P.; Hamnett, A.; Muir, A. V. G. J.; Timney, A. *J.*

Chem. Soc. Dalton Trans. **1992**, 1455.

[52] Meshitsuka, S.; Ichikawa, M.; Tamaru, K. *Chem. Commun.* **1974**, 158.

[53] Fisher, B.; Eisenberg, R. *J. Am. Chem. Soc.* **1980**, *102*, 7361.

[54] Collin, J.-P.; Jouaiti, A.; Sauvage, J. P. *Inorg. Chem.* **1988**, *27*, 1986.

[55] Kevin, S. R.; Rebecca, E. L.; Clifford, P. K. *Organometallics* **1992**, *11*, 1986.

[56] Ishida, H.; Tanaka, K.; Tanaka, T. *Organometallics* **1987**, *6*, 181

[57] Ishida, H.; Fujiki, K.; Ohba, T.; Ohkubo, K.; Tanaka, K.; Tereda, T.; Tanaka, T. *J. Chem. Soc., Dalton Trans.* **1990**, 2155.

[58] Sylvie, C.-N.; Collomb-Dunand-Sauthier, M.-N.; Deronzier, A.; Ziessel, R.; Zsoldos, D. *Inorg. Chem.* **1994**, *33*, 4410.

[59] (a) Sears, W. M.; Morrison, S. R. *J. Phys. Chem.* **1985**, *89*, 3295; (b) Ito, K.; Ikeda, S.; Yoshida, M.; Ohta, S.; Iida, T. *Bull. Chem. Soc. Jpn.* **1984**, *57*, 583; (c) Taniguchi, Y.; Yoneyama, H.; Tamura, H.; *Bull. Chem. Soc. Jpn.* **1982**, *55*, 2034; (d) Inoue, T.; Fujishima, A.; Konishi, S.; Honda, K.; *Nature* **1979**, *277*, 637.

[60] (a) Ogura, K.; Takamagari, K. *J. Chem. Soc. Dalton Trans.* **1986**, 1519; (b) Fresejun, K. W.; Canfield, D. *J. Electrochem. Soc.* **1984**, *131*, 2581; (c) Canfield, D.; Frese, K. W. *J. Electrochem. Soc.* **1983**, *130*, 1772.

[61] (a) Hori, Y.; Kohi, K.; Mura, A.; Suzuki, S. *Chem. Lett.* **1986**, 897; (b) Frese, J.; K, W.; Leach, S. *J. Electrochem. Soc.* **1985**, *132*, 259.

[62] Zlessel, R.; Hawecker, J.; Lehn, J.-M. *Helv. Chim. Acta.* **1986**, *69*, 1065.

[63] (a) Hawecker, J.; Lehn, J.-M.; Ziessel, R. *Chem. Commun.* **1983**, 536; (b) Hawecker, J.; Lehn, J.-M.; Ziessel, R. *Helv. Chim. Acta.* **1986**, *69*, 1990.

[64] Kutal, C.; Corbin, A. J.; Ferraudi, G. *Organometallics* **1987**, *6*, 553.

[65] Kalyanasundaram, K. *J. Chem. Soc. Faraday Trans.* **1986**, *82*, 2401.

[66] Hukkanen, H.; Pakkanen, T. T. *Inorg. Chim. Acta.* **1986**, *114*, 43.

[67] Nagao, H.; Mizukawa, T.; Tanaka, K. *Chem. Lett.* **1993**, *22*, 955.

[68] (a) Nagao, H.; Mizukawa, T.; Tanaka, K. *Inorg. Chem.* **1994**, *33*, 3415; (b) Toyohara, K.; Nagao, H.; Mizukawa, T.; Tanaka, K. *Inorg. Chem.* **1995**, *34*, 5399.

[69] Nakajima, H.; Mizukawa, T.; Nagao, H.; Tanaka, K. *Chem. Lett.* **1995**, *24*, 251.

[70] Nakajima, H.; Kushi, Y.; Nagao, H.; Tanaka, K. *Organometallics* **1995**, *14*, 5093.

[71] Mizukawa, T.; Tsuge, K.; Nakajima, H.; Tanaka, K. *Angew. Chem. Int. Ed.* **1999**, *38*, 362.

[72] Tanaka, K. *Bull. Chem. Soc. Jpn.* **1998**, *71*, 17.

[73] Tanaka, K.; Mizukawa, T. *Appl. Organomet. Chem.* **2000**, *14*, 863.

[74] Tomon, T.; Koizumi, T-A.; Tanaka, K.; *Angew. Chem. Int. Ed.* **2005**, *117*, 2269.

[75] Bolinger, C. M.; Story, N.; Sullivan, B. P.; Meyer, T. J. *Inorg. Chem.* **1988**, *27*, 4582.

[76] Bruce, M. R. M.; Megehee, E.; Sullivan, B. P.; Thorp, H.; Toole, T.R.O.; Downard, A.; Meyer, T. J. *Organometallics* **1988**, *7*, 238.

[77] Ali, M. M.; Sato, H.; Mizukawa, T.; Tsuge, K.; Haga, M.-A.; Tanaka, T. *Chem. Commun.* **1998**, 249.

[78] Rau, S.; Ruben, M.; Büttner, T.; Temme, C.; Dautz, S.; Görls, H.; Rudolph, M.; Walther, D.; Brodkorb, A.; Duati, M.; O'Connor, C.; Vos, J. G. *J. Chem. Soc. Dalton Trans.* **2000**, 3649.

[79] Koizumi, T.-A.; Tomon, T.; Tanaka, K. *J. Organomet. Chem.* **2005,** *690*, 4272.

[80] Seddon, E. A.; Seddon, K. R. "The Chemistry of Ruthenium". Elsevier, Amsterdam, **1984**. Copyright © Elsevier all rights reserved.

[81] Haga, M.-A.; Ano, T.-A.; Kano, K.; Yamabe, S. *Inorg. Chem.* **1991**, *30*, 3843.

[82] Cole, E. B.; Lakkaraju, P. S.; Rampulla, D. M.; Morris, A. J.; Abelev, E.; Bocarsly, A. B. *J. Am. Chem. Soc.* **2010**, *132*, 11539.

[83] Crabtree, R. H. "The Organometallic Chemistry of the Transition Metals" 4th ed.; Wiley: New York , **2005**.

[84] Haga, M.-A.; Ali, M. M.; Koseki, S.; Fujimoto, K.; Yoshimura, A.; Nozaki, K.; Ohno, T.; Nakajima, K.; Stufkens, D. *J. Inorg. Chem.* **1996**, *35*, 3335.

[85] Browne, W. R.; Hage, R.; Vos, J. G. *Coord. Chem. Rev.* **2006**, *250*, 1653.

[86] Lapinte, C. *J. Organomet. Chem.* **2008**, *693*, 793.

[87] Cameron, C. G.; Pittman, T. J.; Pickup, P. G. *J. Phys. Chem. B.* **2001**, *105*, 8838.

[88] Crutchley, R. J. "Intervalance Charge Transfer and Electron Exchange Studies of Dinuclear Ruthenium Complexes" In *Advantages of Inorg. Chem.* **1994**, *41*, 273.

[89] (a) Ruzic, I. *J. Electroanal. Chem.* **1974**, *52*, 331; (b) Ruzic, I. *J. Electroanal. Chem.* **1970**, *25*, 144.

[90] Hupp, J. T. "Mixed Valance Dinuclear Species". In *Compreh. Coord. Chem. II*; McCleverty, J. A.; Meyer, T. J.; Eds.; Elsevier Oxford, U.K., **2004**, *2*, 709.

[91] (a) Creutz, C.; Taube, H. *J. Am. Chem. Soc.* **1969**, *91*, 3988; (b) Creutz, C. "Mixed Valence Complexes of d^5-d^6 Metal Centres". In *Progress .in Inorg. Chem.*; Lippard, S. J.; Ed.; Wiley: New York, **1983**, *30*, 1.

[92] Richardson, D. E.; Taube, H. *Coord. Chem. Rev.* **1984**, *60*, 107.

[93] (a) Callahan, R. W.; Brown, G. M.; Meyer, T. J. *J. Am. Chem. Soc.* **1974**, *96*, 7829; (b) Callahan, R. W.; Brown, G. M.; Meyer, T. J. *Inorg. Chem.* **1975**, *14*, 1443.

[94] (a) Callahan, R. W.; Meyer, T. J. *J. Chem. Phys. Lett.* **1976**, *39*, 82; (b)

Demadis, K. D.; Neyhart, E. G. A.; Kober, M.; White, P. S.; Meyer, T. J. *Inorg. Chem.* **1999**, *38*, 5948; (c) Callahan, R. W.; Keene, F. R.; Meyer, T. J.; Salmon, D. J. *J. Am. Chem. Soc.* **1977**, *99*, 1064; (d) Powers, M. J.; Meyer, T. J. *J. Am. Chem. Soc.* **1980**, *102*, 1289.

[95] Adeyemi, S. A.; Braddock, J. N.; Brown, G. M.; Ferguson, J. A.; Meyer, T. J. *J. Am. Chem. Soc.* **1972**, *94*, 300.

[96] Powers, M. J.; Meyer, T. J. *Inorg. Chem.* **1978**, *17*, 2955.

[97] Marcaccio, M.; Paolucci, F.; Paradisi, C.; Roffia, S.; Fontanesi, C.; Yellowlees, L. J.; Serroni, S.; Campagna, S.; Denti, G.; Balzani, V. *J. Am. Chem. Soc.* **1999**, *121*, 10081.

[98] Giuffrida, G.; Campagna, S. *Coord. Chem. Rev.* **1994**, *135–136*, 517.

[99] (a) Ohno, T.; Nozaki, K.; Haga, M.-A. *Inorg. Chem.* **1992**, *31*, 548; (b) Ohno, T.; Nozaki, K.; Haga, M.-A. *Inorg. Chem.* **1992**, *31*, 4256; (c) Ali, M. M.; Sato, H.; Haga, M.-A.; Tanaka, K.; Yoshimura, A.; Ohno, T. *Inorg. Chem.* **1998**, *37*, 6176.

[100] Cameron, C. "Enhanced Rates of Electron Transport in Conjugated Redox Polymer Hybrids" PhD thesis, Memorial University of Newfoundland, **2000**.

[101] Nozaki, K.; Ohno, T. *J. Phys. Chem.* **1992**, *26*, 10880.

[102] Canty, A. J.; Chaichit, N.; Gatehouse, B. M.; George, E. E. *Inorg. Chem.* **1981**, *20*, 4293.

[103] Haga, M.-A.; Ali, M. M.; Koseki, S.; Yoshimura, A.; Nozaki, K.;

Ohno, T. *Inorg. Chim. Acta.* **1994**, *226*, 17.

[104] Sheldrick, G. M. *Acta Cryst.* **2008**, *A64*, 112-122.

[105] DIRDIF-99: Beurskens, P. T.; Admiraal, G.; Beurskens, G.; Bosman, W. P.; de Gelder, R.; Israel, R.; Smits, J. M. M. **1999**. "The DIRDIF-99 program system". In *Technical Report of the Crystallography Laboratory,* University of Nijmegen,The Netherlands.

[106] Cromer, D. T.; Waber, J. T. "*International Tables for X-ray Crystallography*", Vol. IV, The Kynoch Press, Birmingham, England, Table 2.2 A, **1974**.

[107] Ibers, J. A.; Hamilton, W. C. *Acta Crystallogr.* **1964**, *17*, 781.

[108] Creagh, D. C.; McAuley, W. J. "*International Tables for Crystallography*", Vol C, (A.J.C. Wilson, ed.), Kluwer Academic Publishers, Boston, Table 4.2.6.8, **1992**, 219.

[109] Creagh, D. C.; Hubbell, J. H. "*International Tables for Crystallography*", Vol C, (A. J. C. Wilson, ed.), Kluwer Academic Publishers, Boston, Table 4.2.4.3, **1992**, 200.

[110] Crystal Structure 3.7.0: Crystal Structure Analysis Package, Rigaku and Rigaku/MSC (**2000-2005**). 9009 New Trails Dr. The Woodlands TX 77381 USA.

[111] CRYSTALS Issue 10: Watkin, D. J.; Prout, C. K.; Carruthers, J. R.; Betteridge, P.W. Chemical Crystallography Laboratory, Oxford, UK. **1996**.

[112] Liu, Y.-J.; Chao, H.; Yu, H.-J.; Yuan, Y.-X.; Jia, L.-N. *Acta Cryst.* **2006**, *E62*, 585.

[113] Rillema, D. P.; Jones, D.; Woods, C.; Levy, H. A. *Inorg. Chem.* **1992**, *31*, 2935.

[114] Liu, Y.-J.; Chao, H.; Yu, H.-J.; Yuan, Y.-X.; Jia, L.-N. *Dalton Trans.* **2003**, 325.

[115] Gobetto, R.; Caputo, G.; Garino, C.; Ghiani, S.; Nervi, C.; Salassa, L.; Rosenberg, E.; Ross, J. B. A.; Viscardi, G.; Martra, G.; Miletto, I.; Milanesio, M. *Eur. J. Inorg. Chem.* **2006**, 2839.

[116] a) Templeton, J. L. *J. Am. Chem. Soc.* **1979**, *101*, 4906; (b) Eggleston, D. S.; Goldsby, K. A.; Hodgson, D. J.; Meyer, T. J. *Inorg. Chem.* **1985**, *24*, 4573; (c) Bolger, J. A.; Ferguson, G.; James, J. P.; Long, C.; McArdle, P.; Vos, J. G. *J. Chem. Soc. Dalton Trans.* **1993**, 1577; (d) Rillema, D. P.; Taghdiri, D. G.; Jones, D. S.; Keller, C. D. ; Worl, L. A.; Meyer, T. J. ; Levy, H. A. *Inorg.Chem.* **1987**, *26*, 578; (e) Fennema, B. D. J. R.; de Graaffi, R. A. G.; Hage, R.; Haasnoot, J. G.; Reedijk, J.; Vos, J. G. *J. Chem. Soc., Dalton Trans.* **1991**, 1043.

[117] Spek, A. L. *J. Appl. Cryst.* **2003**, *36*, 7.

[118] Constable, E. C.; Eriksson, H.; Housecroft, C. E.; Kariuki, B. M.; Nordlander, E.; Olsson, J. *Inorg. Chem. Commun.* **2001**, *4*, 749.

[119] Baitalik, S.; Flörke, U.; Nag, K. *J. Chem. Soc., Dalton Trans.* **1999**, 719.

[120] Zampese, J. A.; Keene, F. R.; Steel, P. J. *J. Chem. Soc., Dalton Trans.* **2004**, 4124.

[121] Ji, Z.; Huang, S. D.; Guadalupe, A. R. *Inorg. Chim. Acta.* **2000**, *305*, 127.

[122] Juris, A.; Balzan, V.; Barigelletti, F.; Campagna, S.; Belser, P.; Zelewsky, A.V. *Coord. Chem. Rev.* **1988**, *84*, 85.

[123] Dose, E. V.; Wilson, L. J. *Inorg. Chem.* **1978**, *17*, 2660.

[124] Rillema, D. P.; Mack, K. B. *Inorg. Chem.* **1982**, *21*, 3849.

[125] Rillema, D. P.; Allen, G.; Meyer, T. J.; Conrad, D. *Inorg. Chem.* **1983**, *22*, 1617.

[126] Ernst, S. D.; Kaim, W. *Inorg. Chem.* **1989**, *28*, 1520.

[127] Nicholson, R. S.; Shain, I. *Anal. Chem.* **1964**, *36*, 705.

[128] Sutton, J. E.; Taube, H. *Inorg. Chem.* **1981**, *20*, 3125.

[129] Richardson, D. E.; Taube, H. *J. Am. Chem. Soc.* **1983**, *105*, 40.

[130] Cooper, J. B.; MacQueen, D.B.; Petersen, J. D.; Wertz, D. W. *Inorg. Chem.* **1990**, *29*, 3701.

[131] Ernst, S.; Kasack, V.; Kaim, W. *Inorg. Chem.* **1988**, *27*, 1146.

[132] Richardson, D. E.; Taube, H. *Inorg. Chem.* **1981**, *20*, 1278.

[133] Launay, J.-P. *Chem. Soc. Rev.* **2001**, *30*, 386.

[134] Hage, R.; Haasnoot, J. G.; Reedijk, J.; Wang, R.; Vos, J. G. *Inorg. Chem.* **1991**, *30*, 3263.

[135] Hage, R.; Haasnoot, J. G.; Nieuwenhuis, H. A.; Reedijk, J.; Wang, R.;

Vos, J. G. *J. Chem. Soc., Dalton Trans.* **1991**, 3271.

[136] Braunstein, C. H.; Baker, A. D.; Stekas, T. C.; Gafney, H. D. *Inorg. Chem.* **1984**, *23*, 857.

[137] Toma, H. E.; Santos, P. S.; Lever, A. B. P. *Inorg. Chem.* **1988**, *27*, 3850.

[138] Allen, G. H.; White, R. P.; Rillema, D. P.; Meyer, T. J. *J. Am. Chem. Soc.* **1984**, *106*, 613.

[139] Strousse, G. F.; Anderson, P. A.; Schoonover, J. R.; Meyer, T. J.; Keene, F. R. *Inorg. Chem.* **1992**, *31*, 3004.

[140] Roundhill, D. M. "Photochemistry and photophysics of metal complexes". In *Modren Inorg. Chem.* **1994,** plenum press, New York and London. ISBN 0-306- 44694-4.

[141] Ioachim, E.; Madlycott, E. A.; Hanan, G. S.; Loiseau, F.; Campagna, S. *Inorg. Chim. Acta.* **2006**, *359*, 766.

[142] Jonathan, V. C.; Meyer, T. J. *J. Am. Chem. Soc.* **1983**, *105*, 5583.

[143] (a) Crosby, G. A.; Elfring, W. H. J. *J. Phys. Chem.* **1976**, *80*, 2206; (b) Cook, M. J.; Lewis, A. P.; McAuliffe, G. S. G.; Sharda, V.; Thomson, A. J.; Glasper, J. L.; Robbins, D. J.; *J. Chem. Soc. Perkin Trans.* **1984**, *2*, 1293.

[144] Orellana, G.; Quiroga, M. L. *Helv. Chim. Acta.* **1987**, *70*, 207.

[145] Juris, A.; Balzani, V.; Campagna, S.; Denti, G.; Serroni, S.; Frei, G.; Gudel, H. U. *Inorg. Chem.* **1994**, *33*, 1491.

[146] Balzani, V.; Scandola, F. "Supramolecular Photochemistry". Horwood, Chichester, U.K., **1991**.

[147] Arachchige, S. M.; Brewer, K. J. *Inorg. Chem. Commun.* **2007**, *10*, 1159.

[148] Shahidul, I. M.; Pickup, P. G.; Poirier, R. A. "A Computational Study of CO_2 Reduction by a Ruthenium Benzothiazole Complex" **CSC 2008** poster.

[149] Begum, A.; Pickup, P. G. *Electrochem. Commun.* **2007**, *9*, 2525.

[150] Thomas, H. A.; Walter S. R. *J. Biological Chem.* **1955**, 309.

[151] Arana, C.; Yan, S.; Keshavart-K, M.; Potts, K. T.; Abruna, H. D. *Inorg. Chem.* **1992**, *31*, 3680.

[152] Costamagna, J.; Ferraudi, G.; Canales, J.; Vargas, J. *Coord. Chem. Rev.* **1996**, *148*, 221.

[153] (a) Caballol, R.; Sanchez, M. E.; Barthelat, J. C. *J. Phys. Chem.* **1987**, *91*, 1328; (b) Jegat, C.; Fouassier, M.; Tranquille, M.; Mascetti, J.; Tommasi, I.; Aresta, M.; Ingold, F.; Dedieu, A. *Inorg. Chem.* **1993**, *32*, 1279; (c) Jegat, C.; Fouassier, M.; Mascetti, J. *Inorg. Chem.* **1991**, *30*, 1521; (d) Jegat, C.; Fouassier, M.; Tranquille, M.; Mascetti, J. *Inorg. Chem.* **1991**, *30*, 1529; (e) Nakajima, H.; Tsuge, K.; Toyohara, K.; Tanaka, K. *J. Organomet. Chem.* **1998**, *569*, 61.

[154] Tanaka, K. *Proc. Int. Conf. Coord. Chem.* **1994**, *30*, 104.

[155] Scialdone, O.; Amatore, C.; Galia, A.; Filardo, G. *J. Electroanal.*

Chem. **2006**, *592*, 163.

[156] Silvestri, G.; Gambino, S.; Filardo, G.; Aresta, M.; Schloss, J. V. "Enzymatic and Model Carboxylation and Reduction Reactions for Carbon Dioxide Utilisation". NATO ASI Ser. C, Kluwer Academic Publishers, Dordrecht, **1990**, *314*, 101.

[157] Wawzonek, S.; Gundersen, A. *J. Electrochem. Soc.* **1960**, *107*, 37.

[158] Scialdone, O.; Galia, A; Rocca, C. L; Filardo, G. *Electrochim. Acta.* **2005**, *50*, 3231.

[159] Isse, A. A.; Gennaro, A. *Czech. Chem. Commun.* **2003**, *68*, 1379.

[160] Isse, A. A.; Scialdone, O.; Galia, A.; Gennaro, A. *J. Electroanal. Chem.* **2005**, *585*, 220.

[161] Tyssee, D. A.; Baizer, M. M. *J. Org. Chem.* **1974**, *39*, 2819.

[162] Banderia, M. C. E.; Maia, G. *Electrochim. Acta.* **2008**, *53*, 4512.

[163] Ikeda, Y.; Manda, E. *Bull. Chem. Soc. Jpn.* **1985**, *58*, 1723.

[164] Filardo, G.; Silvestri, G.; Gambino, S. *Eur. Patent Appl.* **1986**, *EP* 86, 100496.

[165] Van, T.; Wilhelmus, J; Smit, C. J; Engels, R. *Eur. Patent Appl.* **1981**, *EP* 28430.

[166] Oettmeier, W.; Masson, K.; Donner, A. *Febs. Lett.* **1988**, *231*, 259.

[167] Kim, Y. M.; Lee, C. H.; Kim, H. G.; Lee, H. S. *J. Agric. Food Chem.* **2004**, *52*, 6096.

[168] Park, B. S.; Kim, J. R.; Lee, S. E.; Kim, K. S.; Takeoka, G. R.; Ahm,

Y. J.; Kim, J. H. *J. Agric. Food Chem.* **2005**, *53*, 1152.

[169] Sock, O.; Troupel, M.; Perichon, J. *Tetrahedron Lett.* **1985**, *26*, 1509.

[170] Silvestri, G.; Gambino, S.; Filardo, G.; Greco, G.; Gulotta, A. *Tetrahedron Lett.* **1984**, *25*, 4307.

[171] Silvestri, G.; Gambino, S.; Gulotta, A. *Tetrahedron Lett.* **1986**, *27*, 3429.

[172] Di Lorenzo, S.; Filardo, G.; Gambino, S.; Silvestri, G. *Chem. Eng. J.* **1989**, *40*, 187.

[173] Ikeda, Y.; Manda, E. *Chem. Lett.* **1984**, *13*, 453.

[174] Mcharek, S.; Heintz, M.; Troupel, M. *J. Perichon, Bull. Soc. Chim. Fr.* **1989**, 95.

[175] Scialdone, O.; Sabartino, M. A.; Belfiore, C.; Galia, A.; Paternostro, M. P.; Filardo, G. *Electrochim. Acta.* **2006**, *51*, 3500.

[176] Ardrade, A. R. D.; Boodts, J. F. C. "Electrochemical Behavior of 4-keto Isophorone in Non-Aqueous Medium in the Presence of Carbon Dioxide." In *J. Braz. Chem. Soc.* **1998**, *9*, 157. [online] DOI:10.1590/S0103- 50531998000200007.

[177] Gennaro, A.; Isse, A. A.; Savéant, J.-M.; Severin, M.-G; Vianello, E. *J. Am. Chem. Soc.* **1996**, *118*, 7190.

[178] Koshechko, V. G.; Lopushanskaya, V. A. *Theoretical and Experimental Chem.* **2006**, *42*, 33.

[179] Gamerith, S.; Gadermaier, C.; Scherf, U.; List, E. J. W. *Phys. Stat. Sol.*

A. **2004**, *201*, 1132.

[180] Lineares, M.; Scifo, L.; Demadrille, R.; Brocorens, P.; Beljonne, D.; Lazzaroni, R.; Grevin, B. *J. Phys. Chem. C*. **2008**, *112*, 6850.

[181] Mano, N.; Kuhn, A. *Electrochem. Commun.* **1999**, *1*, 497.

[182] Mano, N.; Kuhn, A. *J. Electroanal. Chem.* **1999**, *477*, 79.

[183] Elving, P. J.; Leone, J. T. *J. Am. Chem. Soc.* **1958**, *80*, 1021.

[184] Tsierkezos, N. G. *J. Solution Chem.* **2007**, *36*, 1301.

[185] Lehmann M. W.; Evans, D. H. *J. Electroanal. Chem.* **2001**, *500*, 12.

[186] (a) Savéant, J.-M.; Vianello, E. "Advances in Polarography". Longmuir, 1. S.; Ed.; Pergamon Press: New York, **1960**, Vol. 1, 367. (b) Andrieux, C. P.; Savéant, J.-M. "Electrochemical Reactions in Investigation of Rates and Mechanisms of Reactions, Techniques of Chemistry". Bernasconi, C. F.; Ed.; Wiley: New York, **1986**, *VI/4E*, Part 2, 305.

[187] Mizen, M. B.; Wrighton, M. S. *J. Electrochem. Soc.* **1989**, *136*, 941.

[188] Pletcher, D.; Slevin, L. *J. Chem. Soc., Perkin Trans.* **1996**, *2*, 217.

[189] Isse, A. A.; Galia, A.; Belfiore, C.; Silvestri, G.; Gennaro, A. *J. Electroanal. Chem.* **2002**, *526*, 41.

[190] Scialdone, O.; Galia, A.; Isse, A. A.; Gennaro, A.; Sabatino, M. A.; Leone, R.; Filardo, G. *J. Electroanal. Chem.* **2007**, *609*, 8.

[191] Cheng, S. C.; Blaine, C. A.; Hill, M. G.; Mann, K. R. *Inorg. Chem.* **1996**, *35*, 7704.

Appendix A

IR Spectra

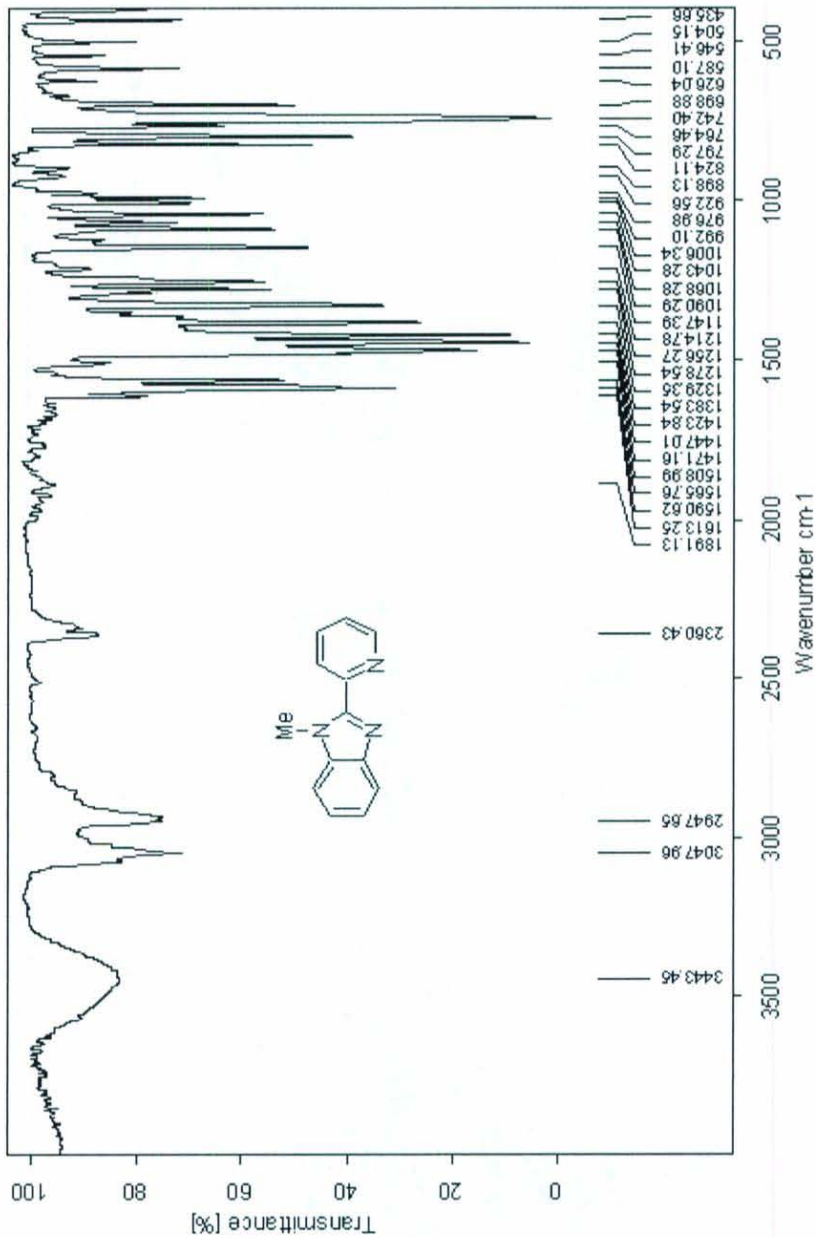
Transmittance [%]
0
20
40
60
80
100
Wavenumber cm-1
3500
3000
2500
2000
1500
1000
500
3443.46
3047.96
2947.55
2360.43
1891.13
1613.25
1590.62
1565.76
1508.99
1471.16
1447.01
1423.84
1383.54
1329.35
1278.54
1256.27
1214.78
1147.39
1090.29
1068.28
1043.28
1006.34
992.10
976.98
922.56
898.13
824.11
797.29
764.46
742.40
698.88
626.04
587.10
546.41
504.15
435.66
Me
N
N
N

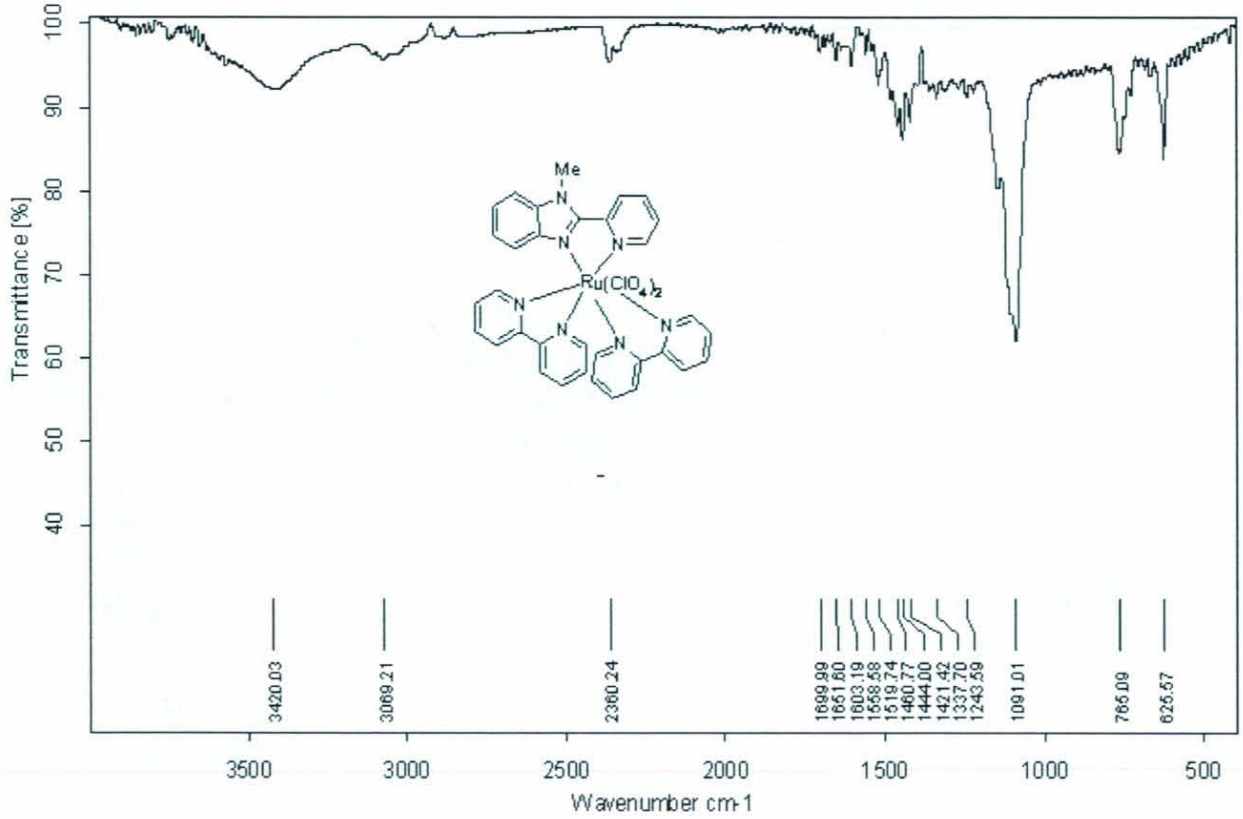
Transmittance [%]
100
90
80
70
60
50
40
Me
N
N
N
N
Ru(ClO4)2
N
N
N
3420.03
3069.21
2360.24
1699.99
1651.60
1603.19
1568.58
1519.74
1460.77
1444.00
1421.42
1337.70
1243.59
1091.01
765.09
626.57
3500
3000
2500
2000
1500
1000
500
Wavenumber cm-1

Transmittance [%]
100
90
80
70
60
3500
3000
2500
2000
1500
1000
500
Wavenumber cm-1
3051.42
1725.35
1661.74
1584.12
1565.36
1510.06
1466.21
1433.33
1316.50
1293.14
1265.12
1234.02
1154.22
1088.78
1014.90
996.01
979.02
897.47
866.81
783.07
758.47
740.48
727.72
703.27
619.63
571.70
550.93
465.92
426.82

Transmittance [%]
0
20
40
60
80
100
Wavenumber cm-1
3500
3000
2500
2000
1500
1000
500
3424.66
3074.59
2009.83
1603.11
1563.52
1464.61
1444.92
1423.46
1325.06
1243.41
1091.89
884.51
764.30
729.73
623.47
423.13
Ru(ClO4)2

Transmittance [%]
100
90
80
70
60
50
40
3500
3000
2500
2000
1500
1000
500
Wavenumber cm-1
3441.72
3064.62
2962.58
1723.40
1614.95
1587.93
1534.93
1477.25
1446.41
1425.64
1407.95
1384.59
1357.13
1335.72
1302.64
1284.39
1255.56
1206.77
1178.94
1125.79
1086.35
1025.89
1006.90
930.11
902.48
816.93
741.81
682.34
655.47
440.85
414.34
Me
N
N
N
N
Me
N
N

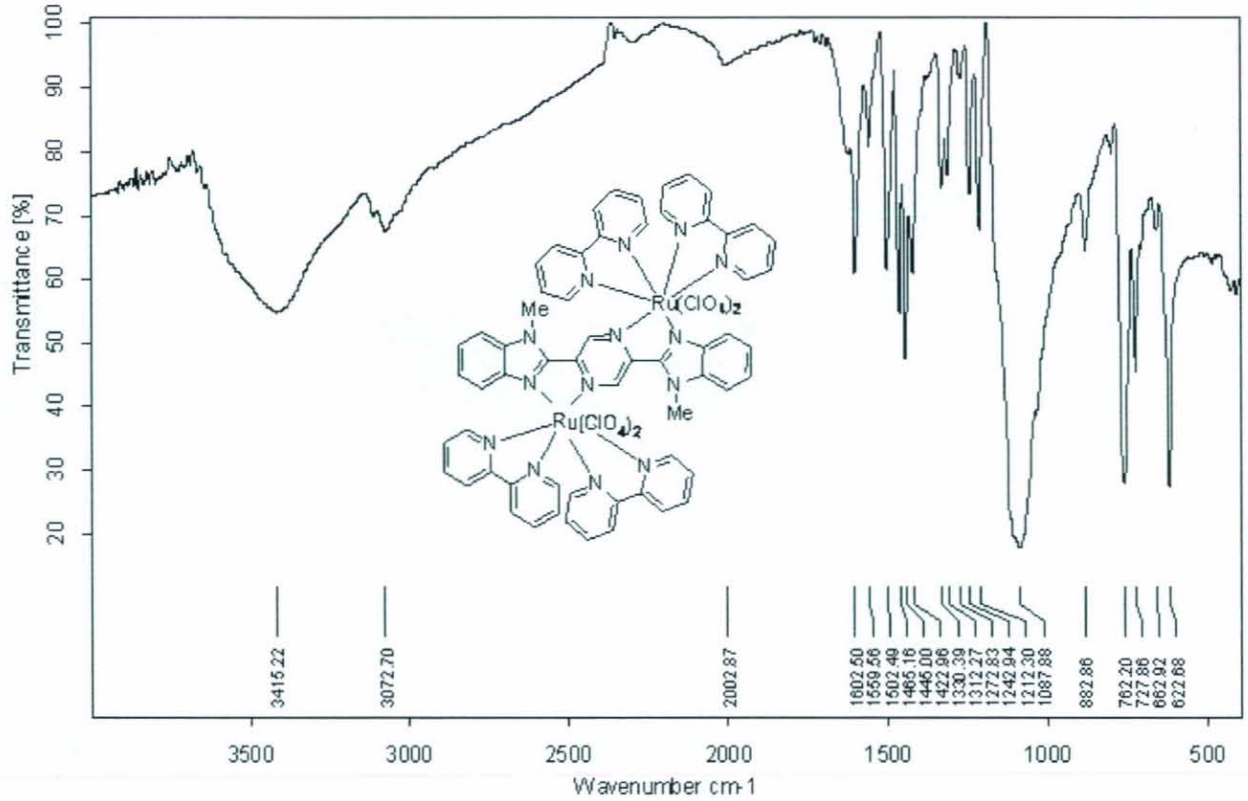
Transmittance [%]
100
90
80
70
60
50
40
30
20
3500
3000
2500
2000
1500
1000
500
Wavenumber cm-1
3415.22
3072.70
2002.87
1602.50
1559.56
1502.49
1465.16
1446.00
1422.96
1330.39
1312.27
1272.83
1242.94
1212.30
1087.88
882.86
762.20
727.86
662.92
622.68
Ru(ClO4)2
Me
Ru(ClO4)2
Me

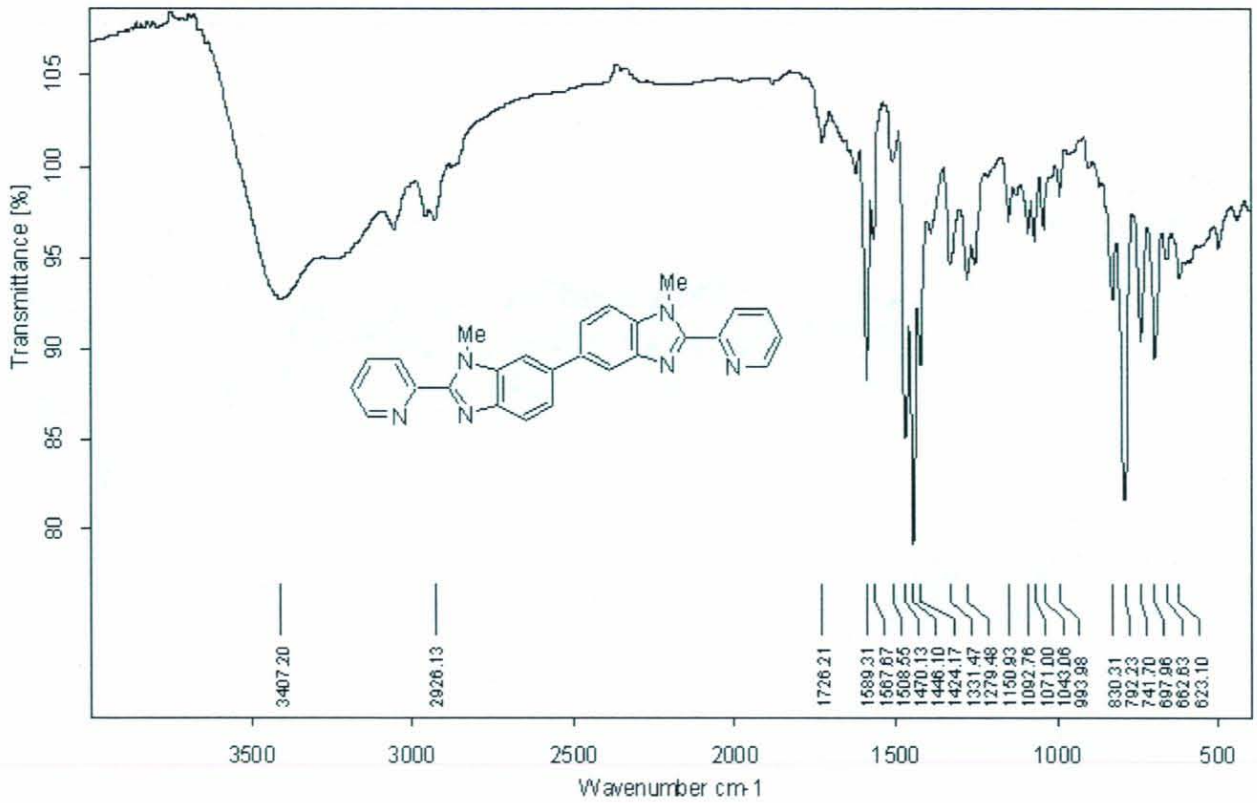
Transmittance [%]
105
100
95
90
85
80
Me
N
N
N
Me
N
N
N
3407.20
2926.13
1726.21
1589.31
1567.67
1508.55
1470.13
1446.10
1424.17
1331.47
1279.48
1150.93
1092.76
1071.00
1043.06
993.98
830.31
792.23
741.70
697.96
662.63
623.10
3500
3000
2500
2000
1500
1000
500
Wavenumber cm-1

Transmittance [%]
90
80
70
60
50
Wavenumber cm-1
3500
3000
2500
2000
1500
1000
500
3392.36
3069.85
1972.82
1602.09
1516.52
1481.17
1463.55
1444.81
1421.71
1333.22
1242.53
1089.42
764.77
729.61
622.96
Ru(ClO4)2
Me
Me
N

Transmittance [%]
100
90
80
70
60
50
40
30
20
Wavenumber cm-1
3500
3000
2500
2000
1500
1000
500
3048.95
3000.53
1742.97
1584.33
1564.37
1529.06
1466.33
1435.76
1400.17
1316.87
1290.13
1275.04
1246.08
1145.46
1091.54
996.82
980.16
869.85
846.26
783.71
740.37
715.96
689.18
619.40
603.82
S
S
N
N
N
N

Transmittance [%]
100
90
80
70
60
50
40
3500
3000
2500
2000
1500
1000
500
Wavenumber cm-1
3406.81
3070.07
1978.39
1601.90
1463.60
1444.60
1384.50
1341.36
1244.17
1088.77
767.63
730.63
624.96
Ru(ClO4)2
Ru(ClO4)2

Transmittance [%]
100
95
90
85
80
75
70
65
Wavenumber cm-1
3500
3000
2500
2000
1500
1000
500
3444.91
3057.78
2924.80
2360.62
1717.97
1618.05
1563.79
1522.80
1492.74
1461.94
1427.96
1384.28
1359.71
1310.13
1251.76
1198.06
1176.86
1074.87
1030.95
979.66
921.93
856.36
765.26
730.03
696.37
435.56

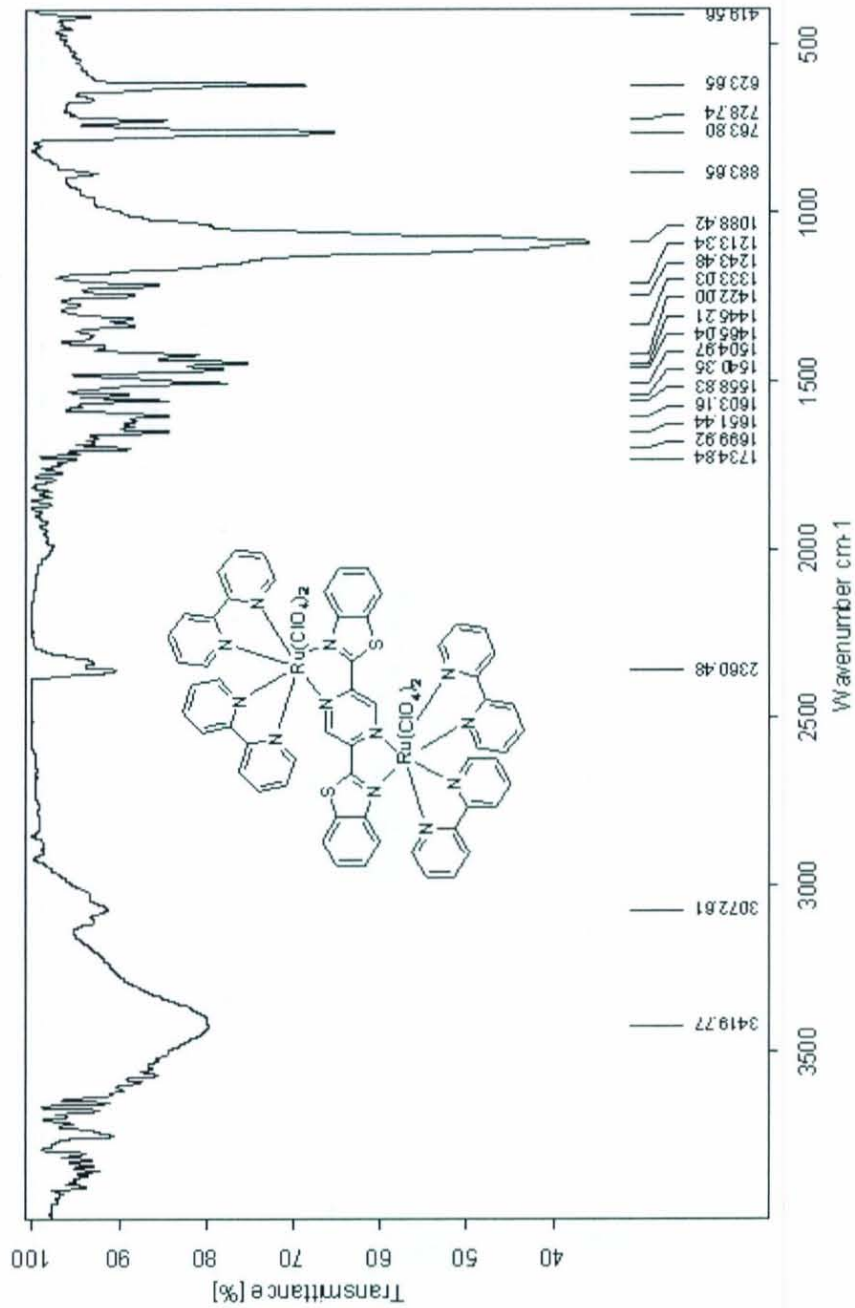
Transmittance [%]
100
90
80
70
60
50
40
3500
3000
2500
2000
1500
1000
500
Wavenumber cm-1
3419.77
3072.61
2360.48
1734.84
1699.92
1651.44
1603.16
1558.83
1504.97
1446.21
1313.34
1088.42
883.65
763.80
728.74
623.65
419.56
Ru(ClO4)2
Ru(ClO4)2

Transmittance [%]
70
75
80
85
90
95
100
105
Wavenumber cm-1
3500
3000
2500
2000
1500
1000
500
3052.30
2919.23
2850.34
2283.61
1725.46
1662.70
1600.32
1549.90
1529.47
1466.93
1449.39
1429.52
1397.54
1356.37
1326.90
1278.88
1257.90
1157.30
1075.21
1013.59
856.19
813.54
734.99
651.35
434.23
Me
N
N
N
N
Me

Transmittance [%]
100
95
90
85
80
75
70
65
Wavenumber cm-1
3500
3000
2500
2000
1500
1000
500
3385.22
2926.71
1868.26
1602.79
1463.55
1444.59
1384.82
1354.04
1145.00
1118.90
1088.48
767.51
626.15
Me
Me
Ru(ClO4)2

Appendix B

^{1}H NMR Spectra

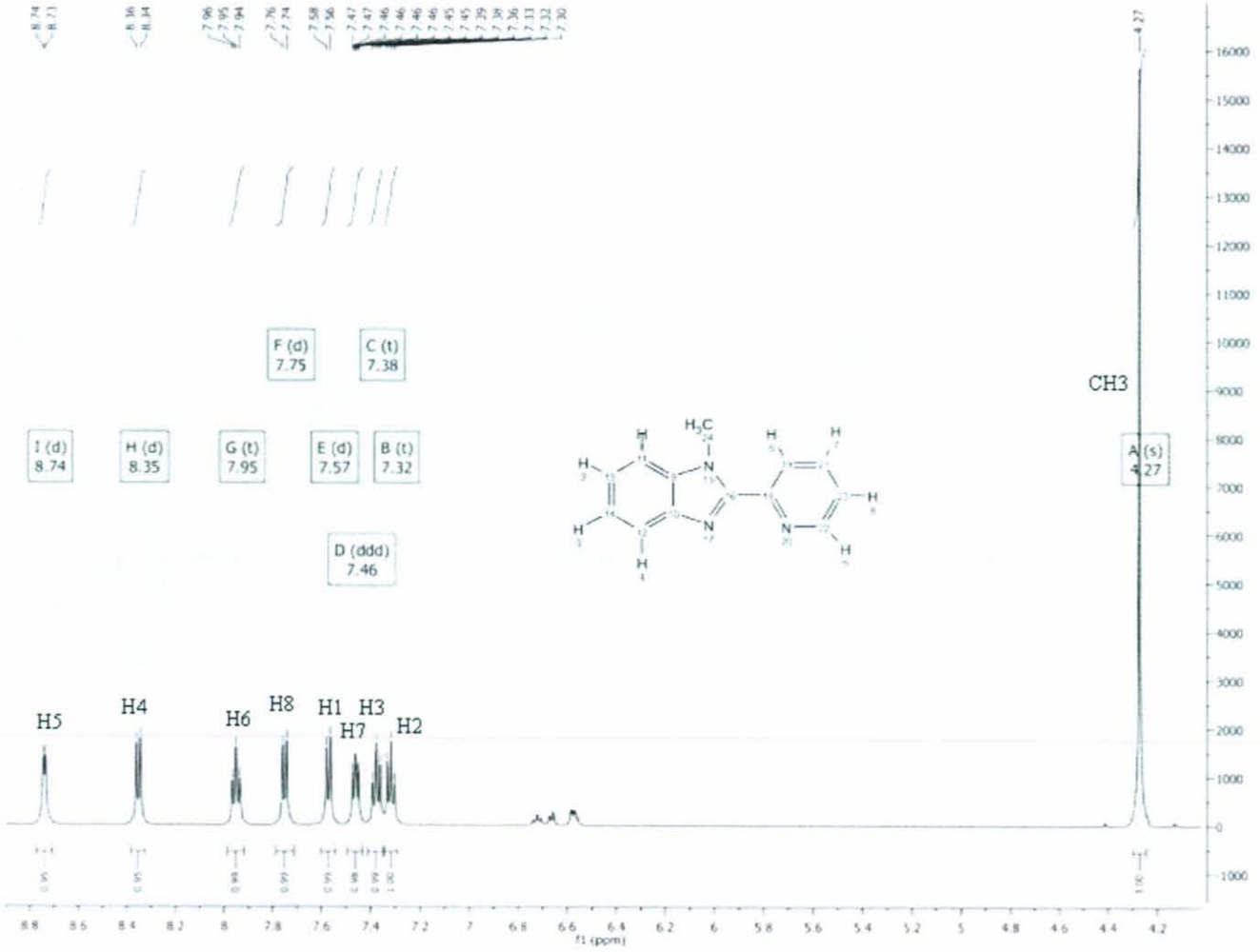
I (d)
8.74
H (d)
8.35
G (t)
7.95
F (d)
7.75
E (d)
7.57
C (t)
7.38
B (t)
7.32
D (ddd)
7.46
A (s)
4.27
CH3
H5
H4
H6
H8
H1
H7
H3
H2
f1 (ppm)

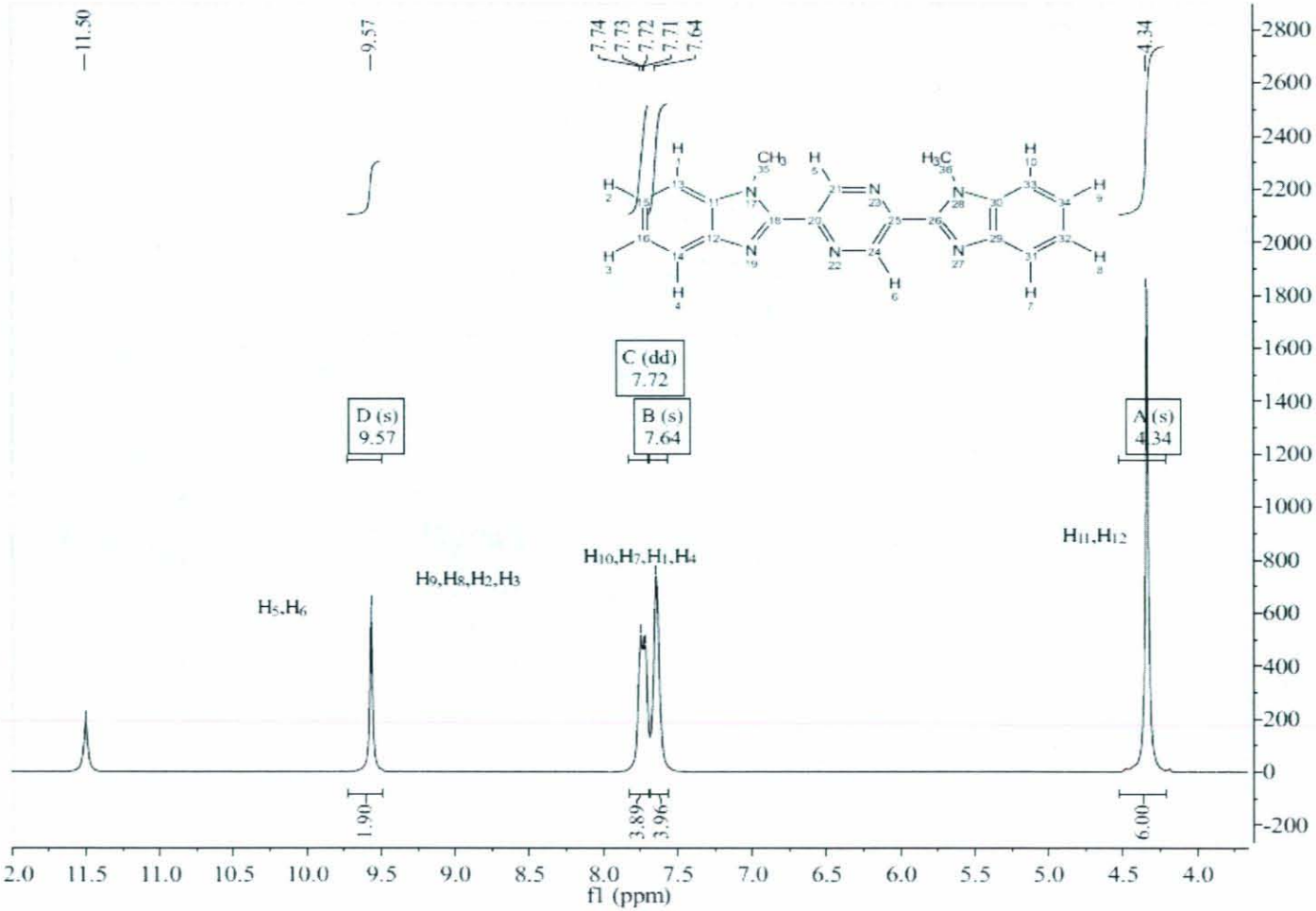
11.50
9.57
7.74
7.73
7.72
7.71
7.64
4.34
C (dd)
7.72
D (s)
9.57
B (s)
7.64
A (s)
4.34
H5,H6
H9,H8,H2,H3
H10,H7,H1,H4
H11,H12
1.90
3.89
3.96
6.00
f1 (ppm)

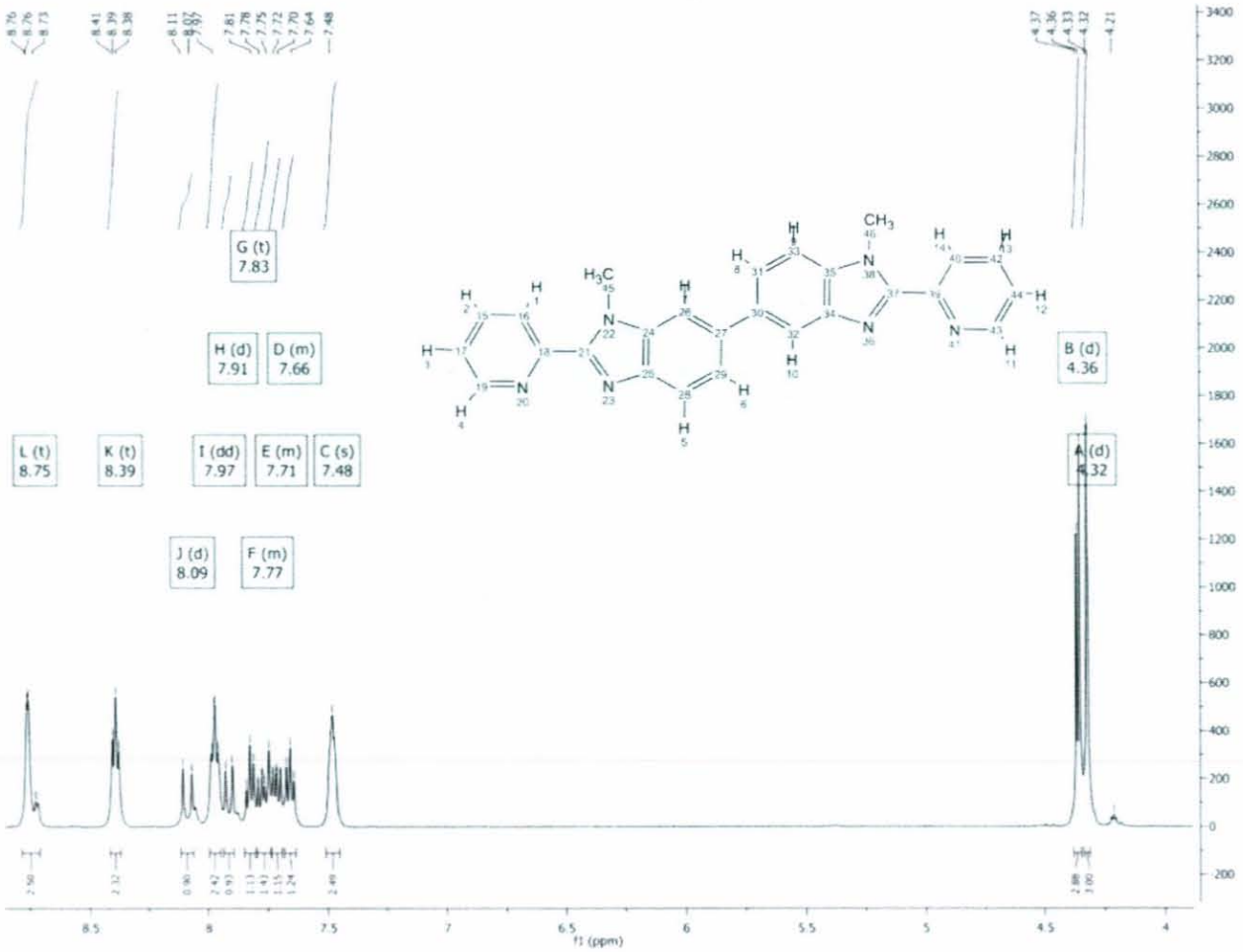
G (t)
7.83
H (d)
7.91
D (m)
7.66
B (d)
4.36
L (t)
8.75
K (t)
8.39
I (dd)
7.97
E (m)
7.71
C (s)
7.48
A (d)
4.32
J (d)
8.09
F (m)
7.77
f1 (ppm)

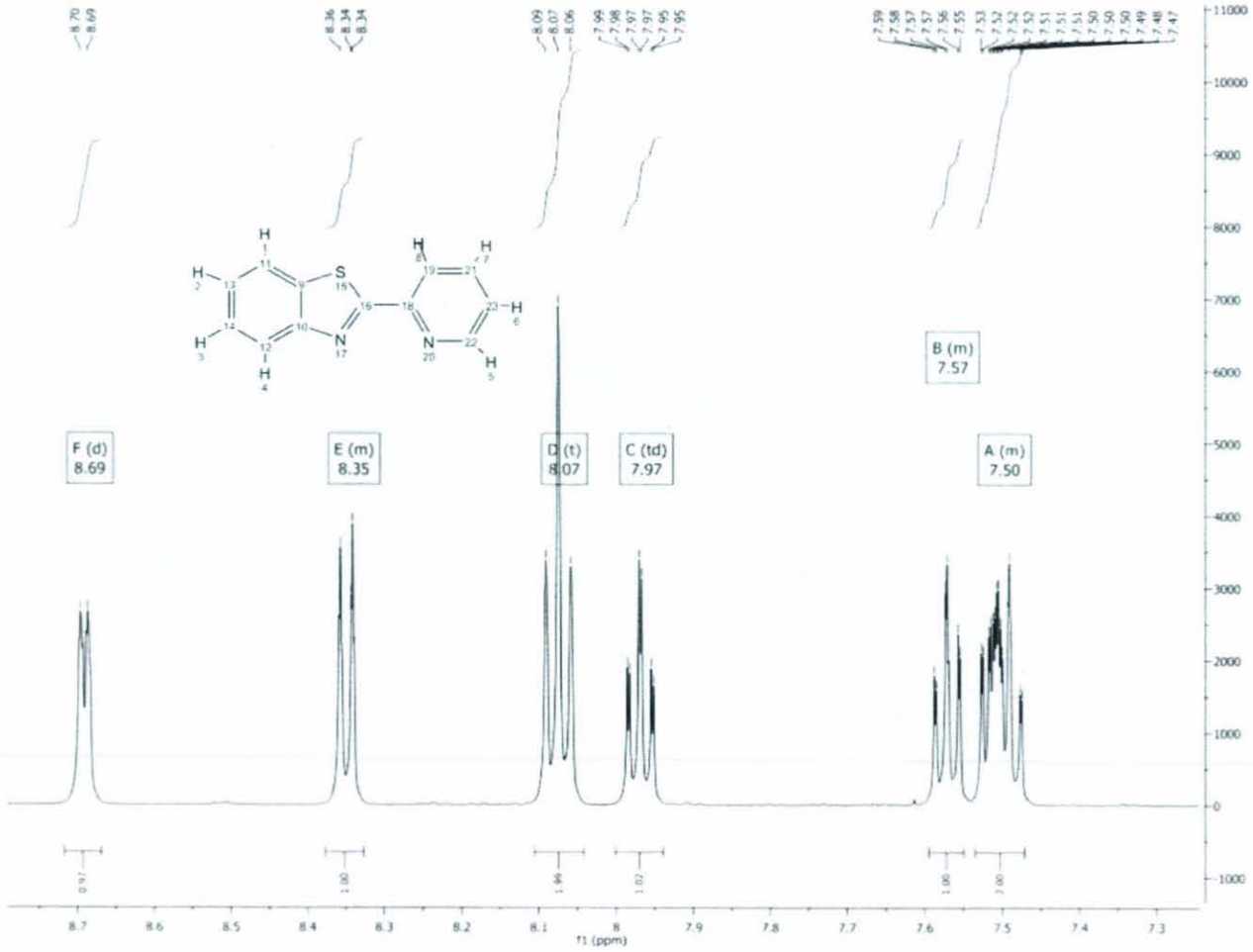
F (d)
8.69
E (m)
8.35
D (t)
8.07
C (td)
7.97
B (m)
7.57
A (m)
7.50
f1 (ppm)

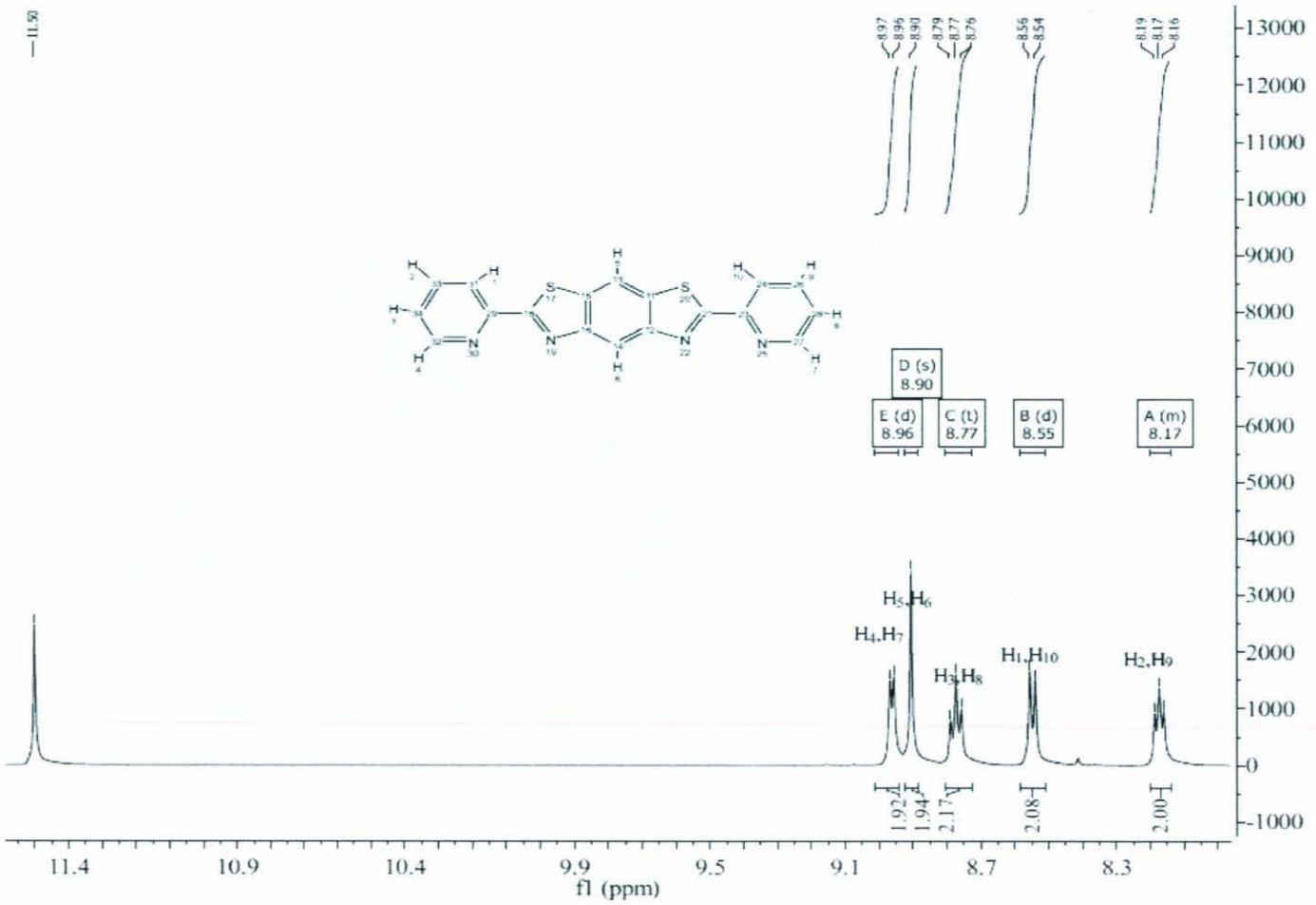
11.90
8.97
8.96
8.90
8.79
8.77
8.76
8.56
8.54
8.19
8.17
8.16
D (s)
8.90
E (d)
8.96
C (t)
8.77
B (d)
8.55
A (m)
8.17
H5,H6
H4,H7
H3,H8
H1,H10
H2,H9
1.92
1.94
2.17
2.08
2.00
13000
12000
11000
10000
9000
8000
7000
6000
5000
4000
3000
2000
1000
0
-1000
11.4
10.9
10.4
9.9
9.5
9.1
8.7
8.3
f1 (ppm)

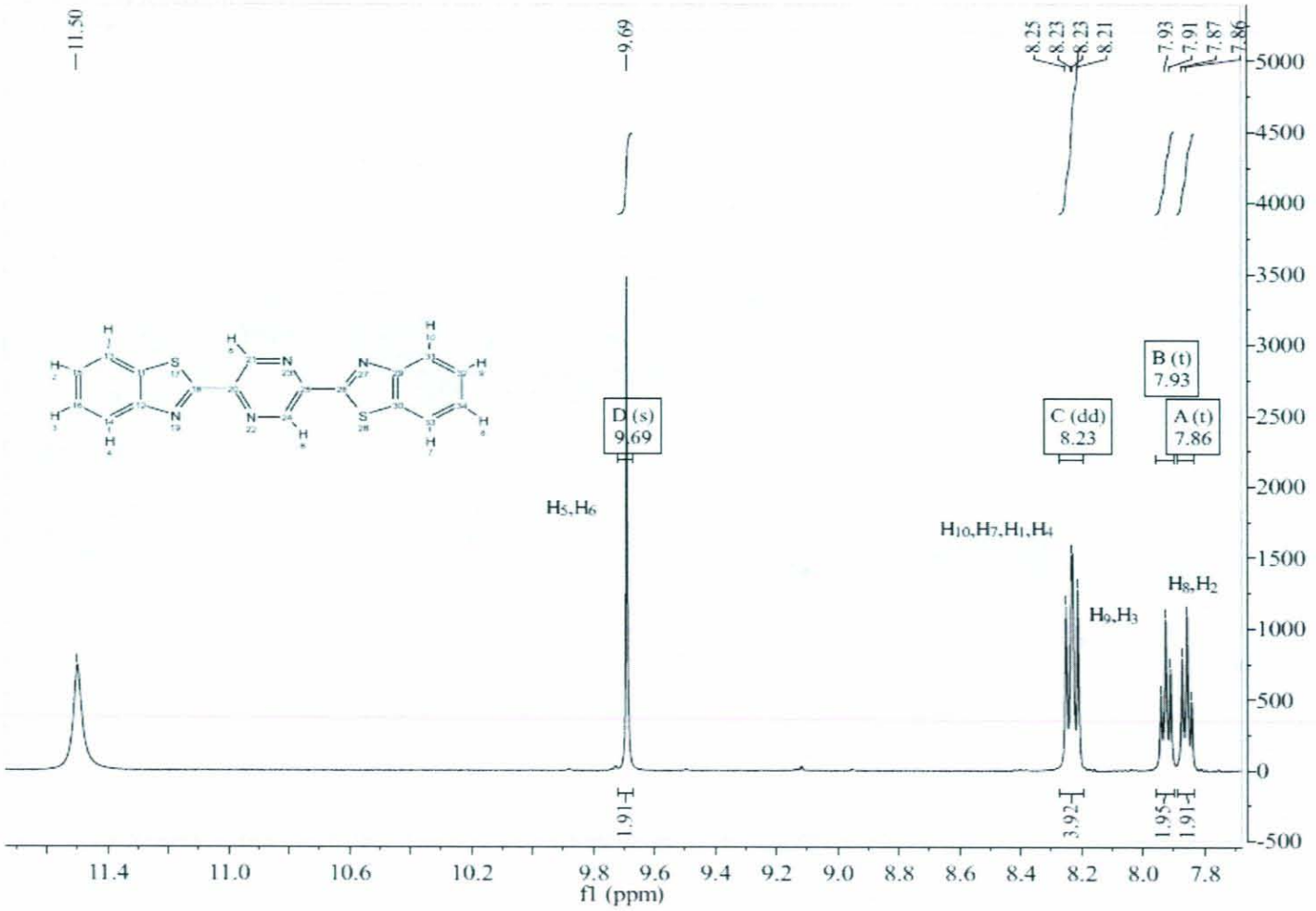
11.50
9.69
8.25
8.23
8.23
8.21
7.93
7.91
7.87
7.86
D (s)
9.69
C (dd)
8.23
B (t)
7.93
A (t)
7.86
H5,H6
H10,H7,H1,H4
H9,H3
H8,H2
1.91
3.92
1.95
1.91
f1 (ppm)

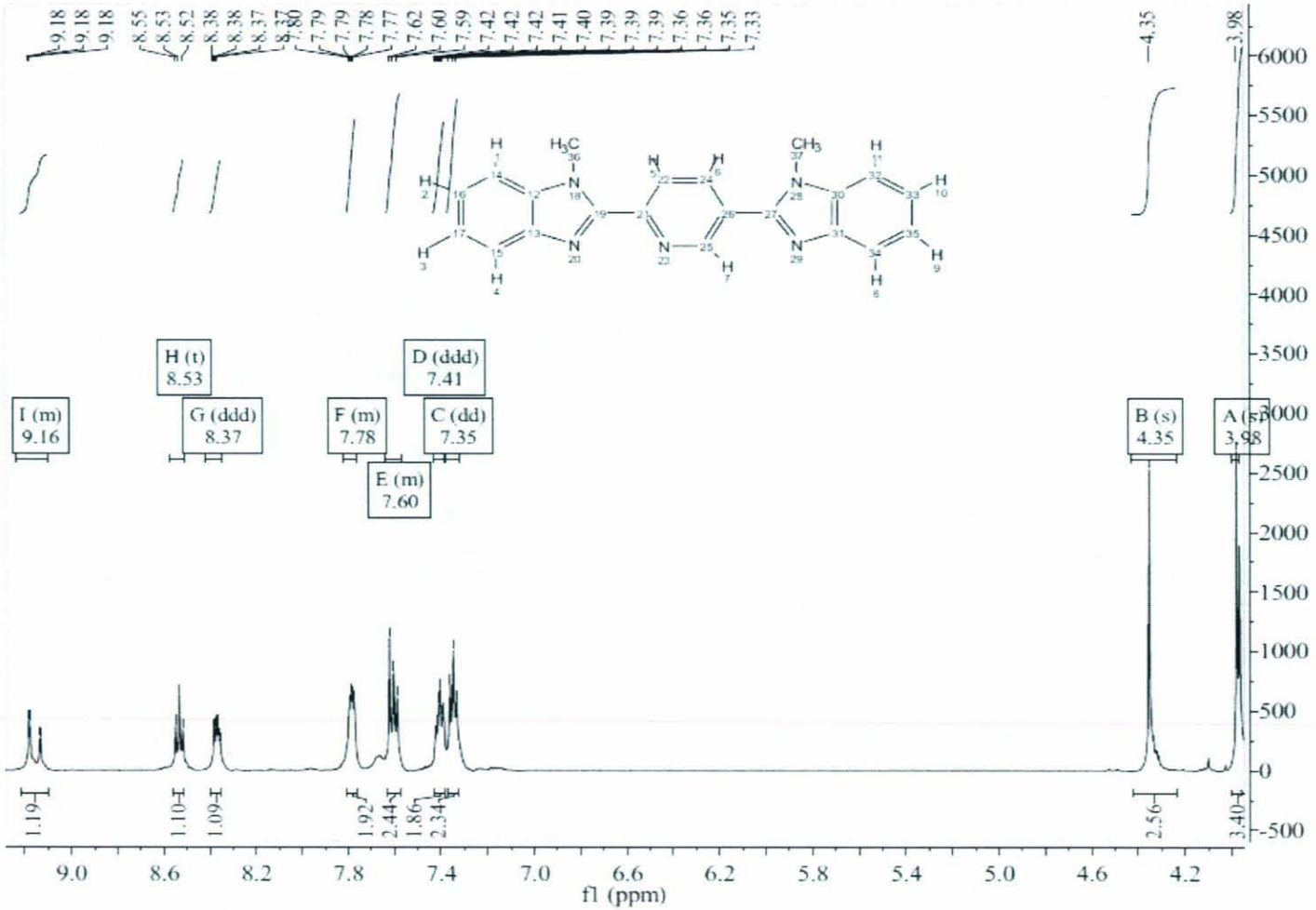
9.18
9.18
9.18
8.55
8.53
8.52
8.38
8.38
8.37
8.37
7.80
7.79
7.79
7.78
7.77
7.62
7.60
7.59
7.42
7.42
7.42
7.41
7.40
7.39
7.39
7.39
7.36
7.36
7.35
7.33
4.35
3.98
I (m)
9.16
H (t)
8.53
G (ddd)
8.37
F (m)
7.78
E (m)
7.60
D (ddd)
7.41
C (dd)
7.35
B (s)
4.35
A (s)
3.98
1.19
1.10
1.09
1.92
2.44
1.86
2.34
2.56
3.40
9.0
8.6
8.2
7.8
7.4
7.0
6.6
6.2
5.8
5.4
5.0
4.6
4.2
f1 (ppm)
6000
5500
5000
4500
4000
3500
3000
2500
2000
1500
1000
500
0
-500

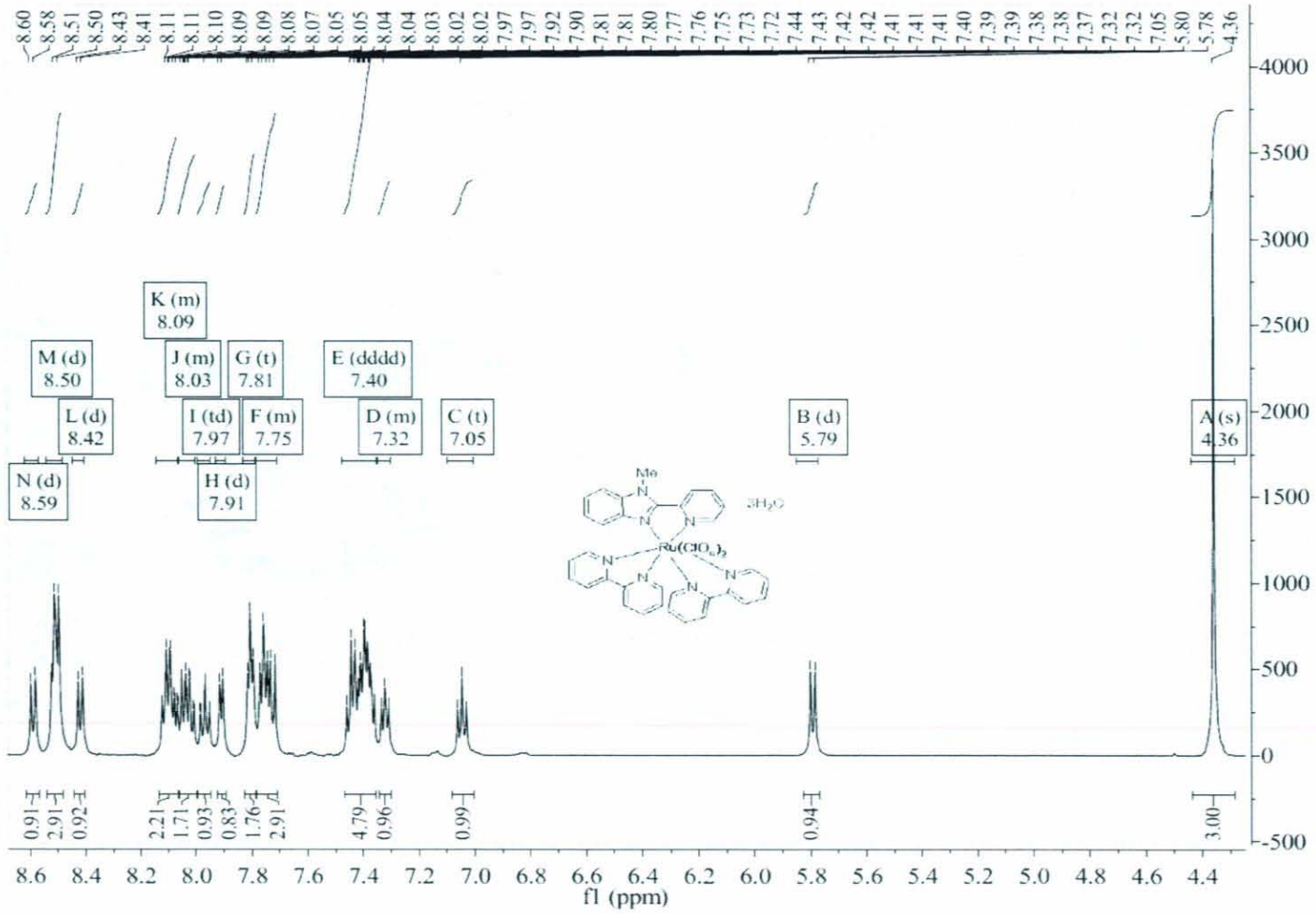
8.60 8.58 8.51 8.50 8.43 8.41 8.11 8.11 8.10 8.09 8.09 8.08 8.07 8.05 8.05 8.04 8.04 8.03 8.02 8.02 7.97 7.97 7.92 7.90 7.81 7.81 7.80 7.77 7.76 7.75 7.73 7.72 7.44 7.43 7.42 7.42 7.41 7.41 7.41 7.40 7.39 7.39 7.38 7.38 7.37 7.32 7.32 7.05 5.80 5.78 4.36
K (m) 8.09
M (d) 8.50
J (m) 8.03
G (t) 7.81
E (dddd) 7.40
L (d) 8.42
I (td) 7.97
F (m) 7.75
D (m) 7.32
C (t) 7.05
B (d) 5.79
A (s) 4.36
N (d) 8.59
H (d) 7.91
Me
3H2O
Ru(C2O4)2
0.91 2.91 0.92 2.21 1.71 0.93 0.83 1.76 2.91 4.79 0.96 0.99 0.94 3.00
8.6 8.4 8.2 8.0 7.8 7.6 7.4 7.2 7.0 6.8 6.6 6.4 6.2 6.0 5.8 5.6 5.4 5.2 5.0 4.8 4.6 4.4
f1 (ppm)
4000 3500 3000 2500 2000 1500 1000 500 0 -500

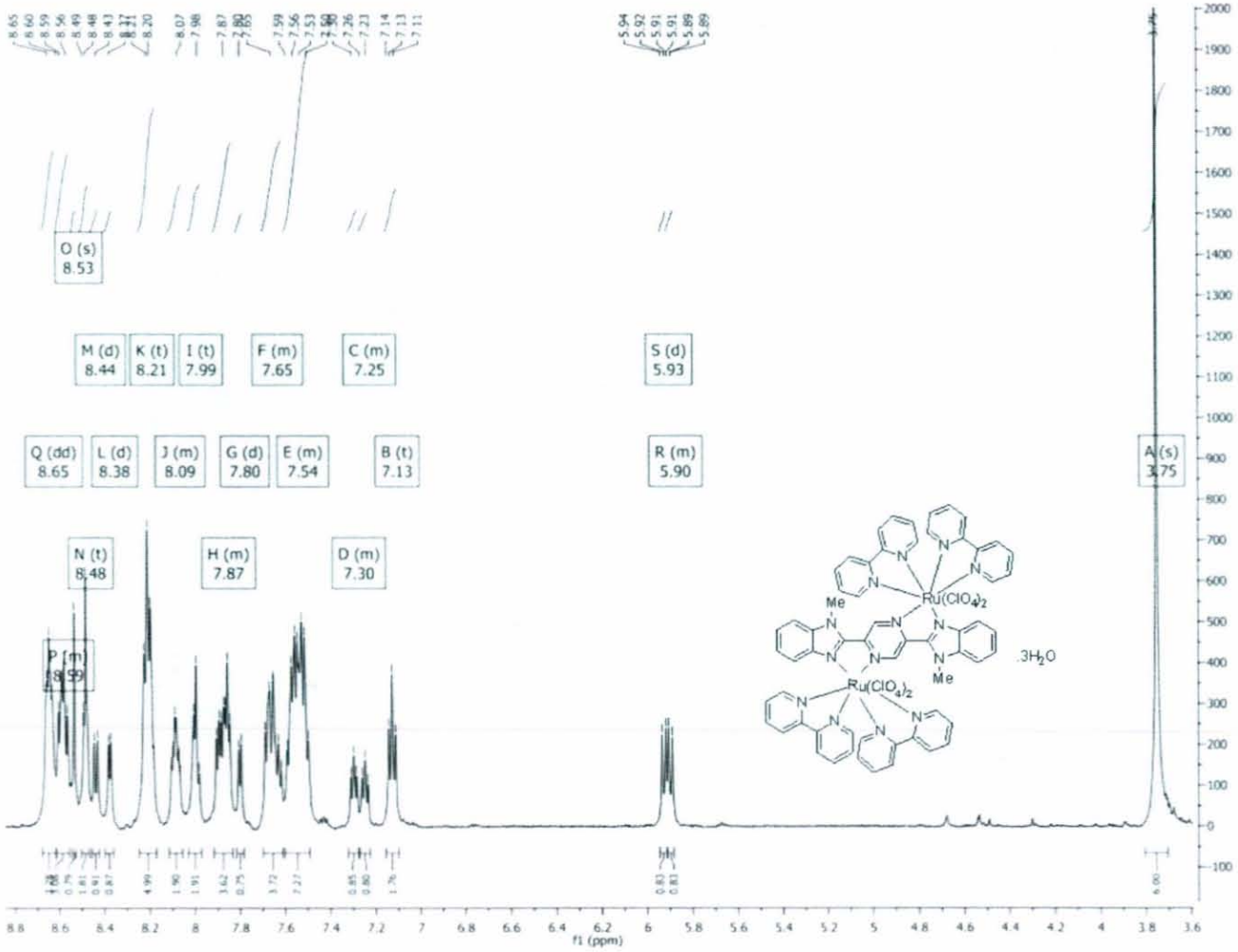
O (s) 8.53
M (d) 8.44
K (t) 8.21
I (t) 7.99
F (m) 7.65
C (m) 7.25
S (d) 5.93
Q (dd) 8.65
L (d) 8.38
J (m) 8.09
G (d) 7.80
E (m) 7.54
B (t) 7.13
R (m) 5.90
A (s) 3.75
N (t) 8.48
H (m) 7.87
D (m) 7.30
P (m)
Me
Ru(ClO4)2
Me
Ru(ClO4)2
3H2O
f1 (ppm)

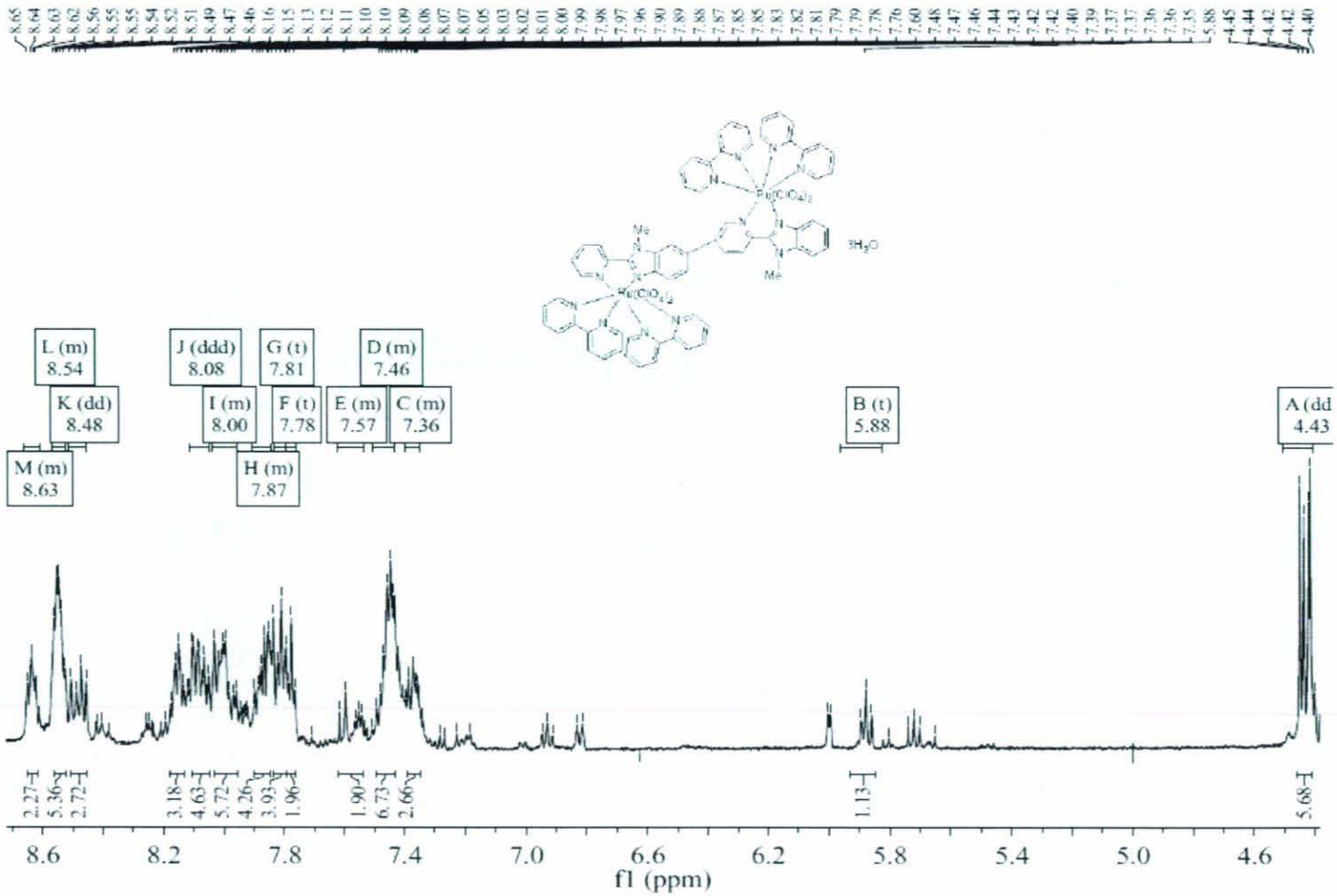
L (m) 8.54
K (dd) 8.48
M (m) 8.63
J (ddd) 8.08
I (m) 8.00
G (t) 7.81
F (t) 7.78
H (m) 7.87
D (m) 7.46
E (m) 7.57
C (m) 7.36
B (t) 5.88
A (dd 4.43
3H2O
8.6
8.2
7.8
7.4
7.0
6.6
6.2
5.8
5.4
5.0
4.6
f1 (ppm)

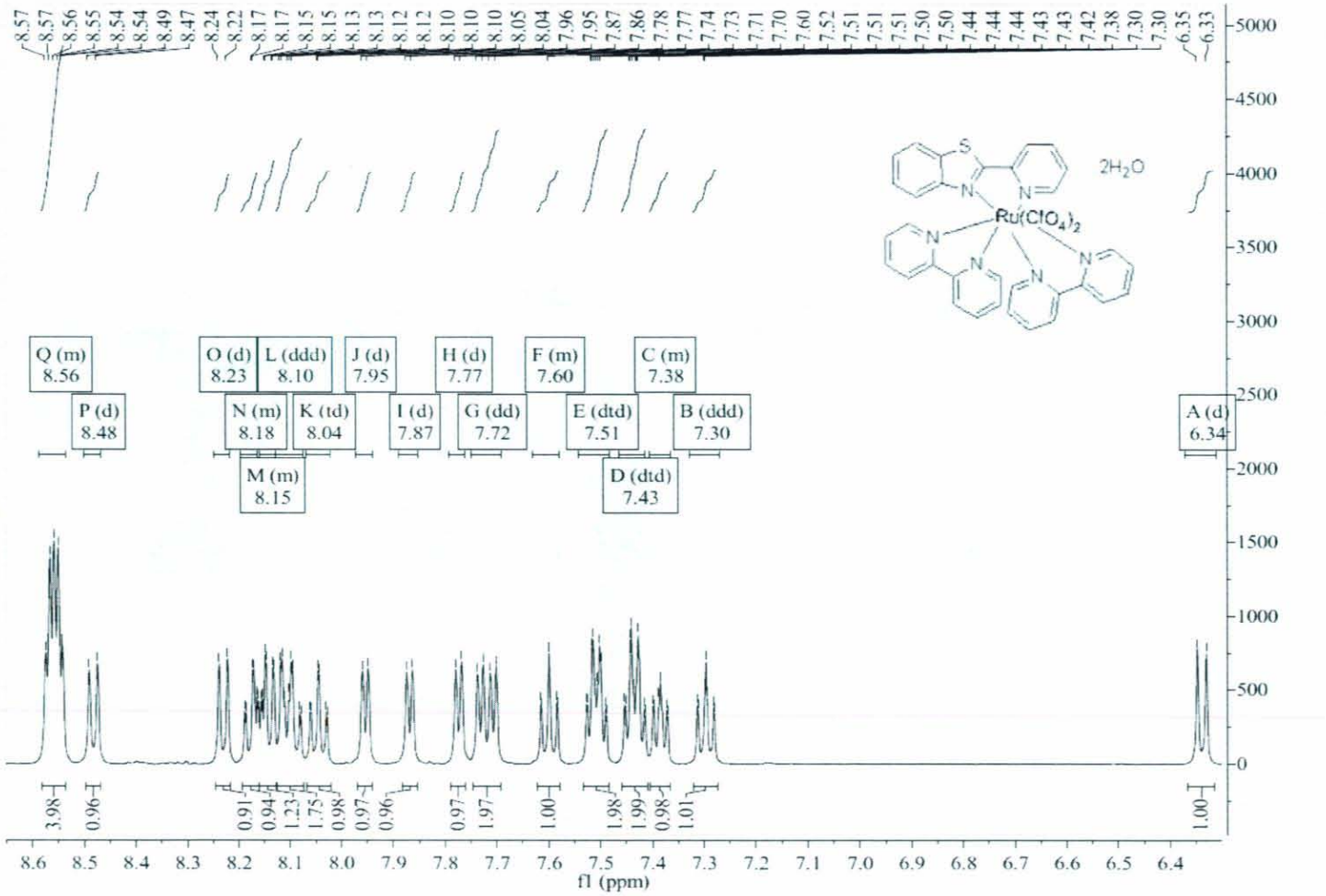
Q (m) 8.56
P (d) 8.48
O (d) 8.23
L (ddd) 8.10
J (d) 7.95
H (d) 7.77
F (m) 7.60
C (m) 7.38
N (m) 8.18
K (td) 8.04
I (d) 7.87
G (dd) 7.72
E (dtd) 7.51
B (ddd) 7.30
M (m) 8.15
D (dtd) 7.43
A (d) 6.34
2H2O
Ru(ClO4)2
f1 (ppm)

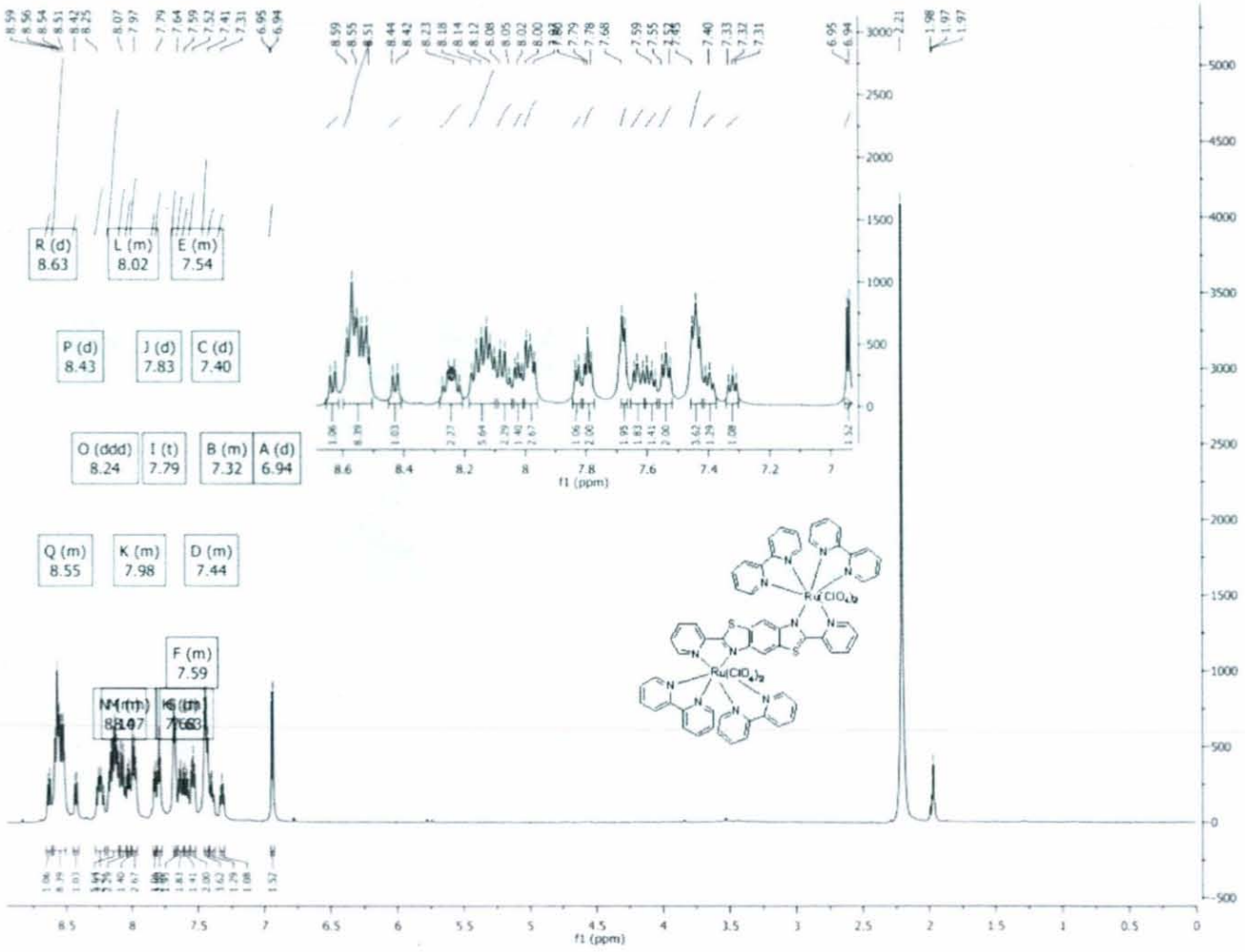
R (d) 8.63
L (m) 8.02
E (m) 7.54
P (d) 8.43
J (d) 7.83
C (d) 7.40
O (ddd) 8.24
I (t) 7.79
B (m) 7.32
A (d) 6.94
Q (m) 8.55
K (m) 7.98
D (m) 7.44
F (m) 7.59
f1 (ppm)

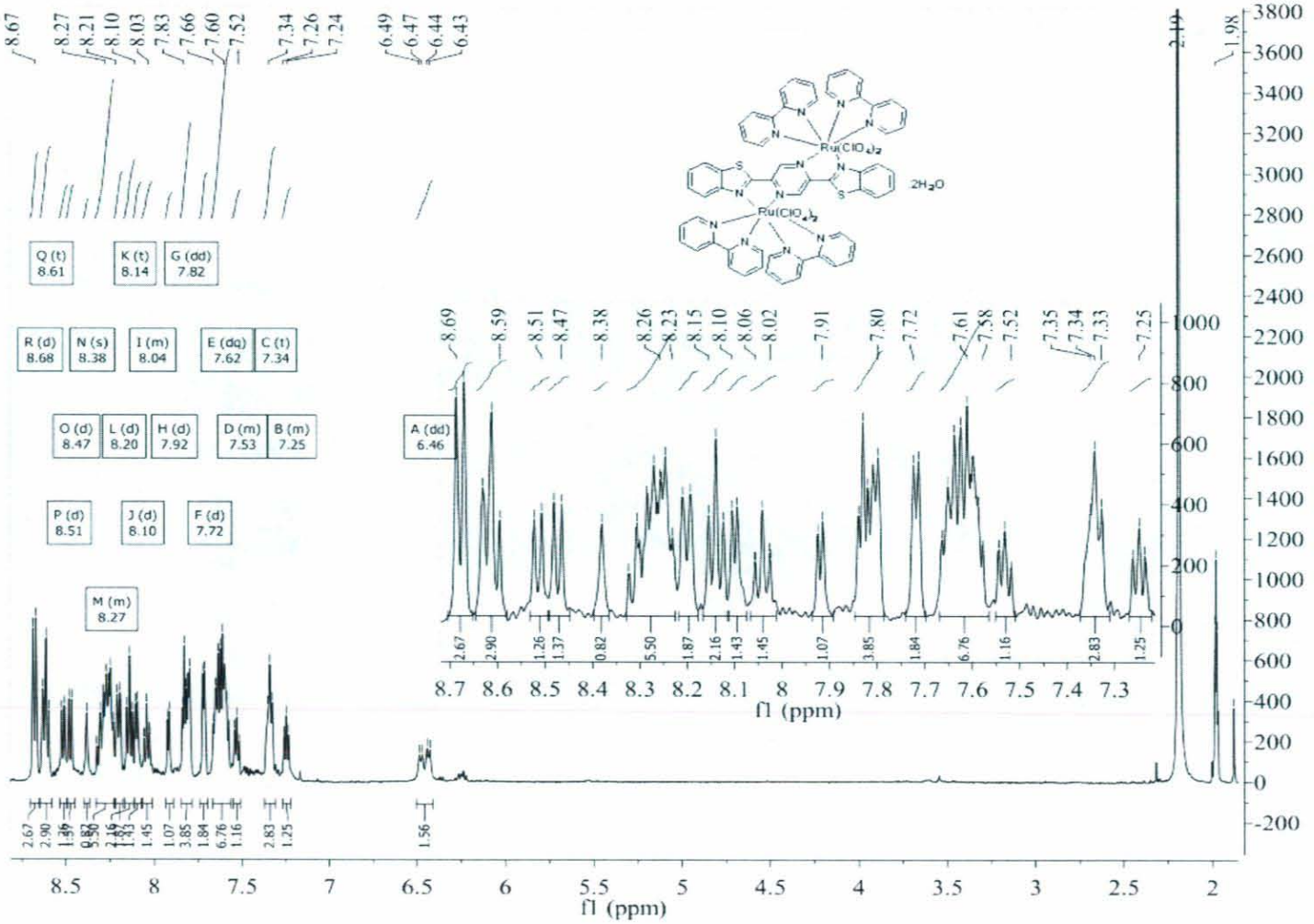
8.67
8.27
8.21
8.10
8.03
7.83
7.66
7.60
7.52
7.34
7.26
7.24
6.49
6.47
6.44
6.43
2.19
1.98
Q (t) 8.61
K (t) 8.14
G (dd) 7.82
R (d) 8.68
N (s) 8.38
I (m) 8.04
E (dq) 7.62
C (t) 7.34
O (d) 8.47
L (d) 8.20
H (d) 7.92
D (m) 7.53
B (m) 7.25
A (dd) 6.46
P (d) 8.51
J (d) 8.10
F (d) 7.72
M (m) 8.27
Ru(ClO4)2
2H2O
f1 (ppm)

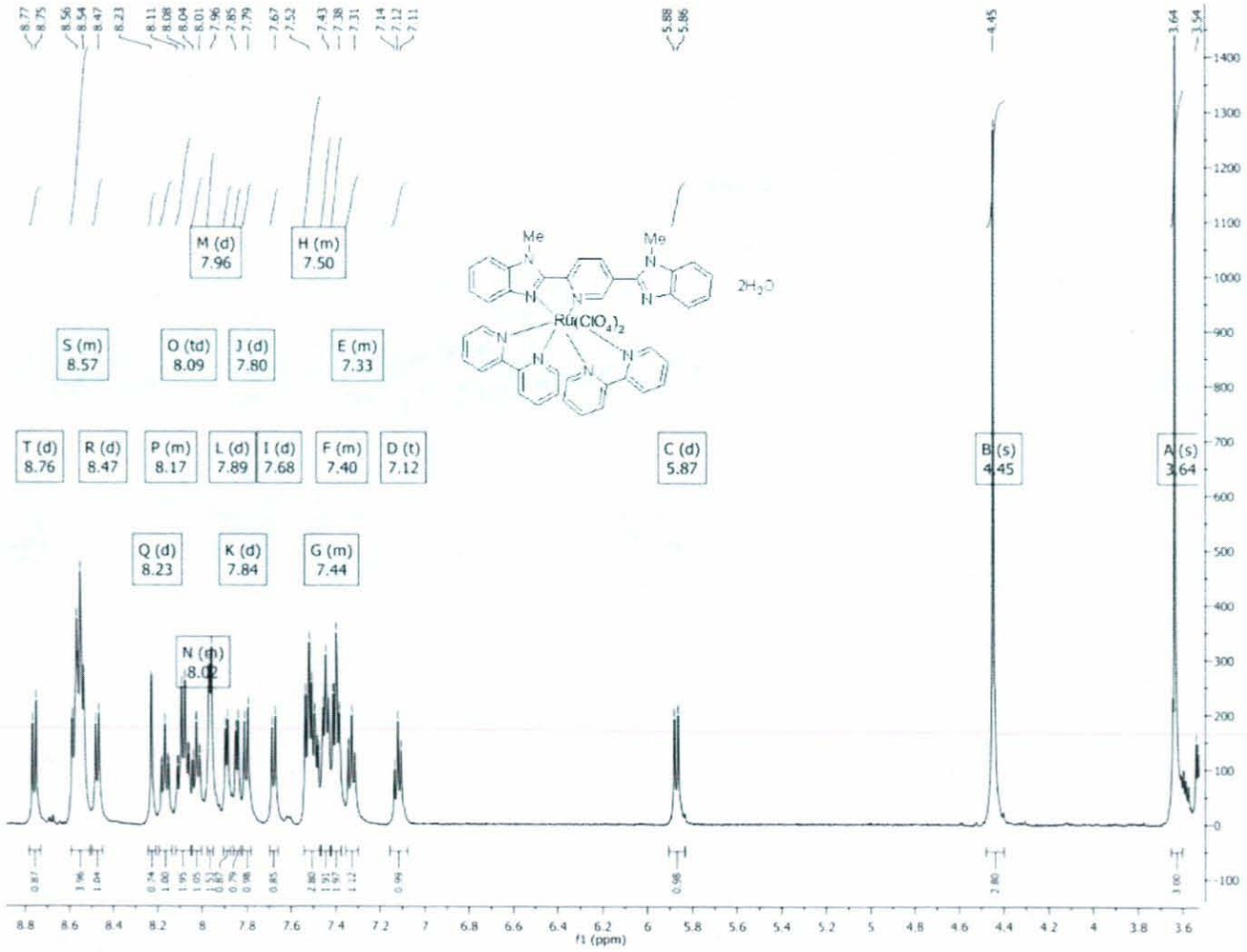
8.77
8.75
8.56
8.54
8.47
8.23
8.11
8.08
8.04
8.01
7.96
7.85
7.79
7.67
7.52
7.43
7.38
7.31
7.14
7.12
7.11
5.88
5.86
4.45
3.64
3.54
M (d)
7.96
H (m)
7.50
Me
Me
2H2O
Ru(ClO4)2
S (m)
8.57
O (td)
8.09
J (d)
7.80
E (m)
7.33
T (d)
8.76
R (d)
8.47
P (m)
8.17
L (d)
7.89
I (d)
7.68
F (m)
7.40
D (t)
7.12
C (d)
5.87
B (s)
4.45
A (s)
3.64
Q (d)
8.23
K (d)
7.84
G (m)
7.44
N (m)
8.02
f1 (ppm)

Appendix C

^{13}C NMR Spectra

[Ru(**btz**)(bpy)$_2$](ClO$_4$)$_2$, CH_3CN-d_3

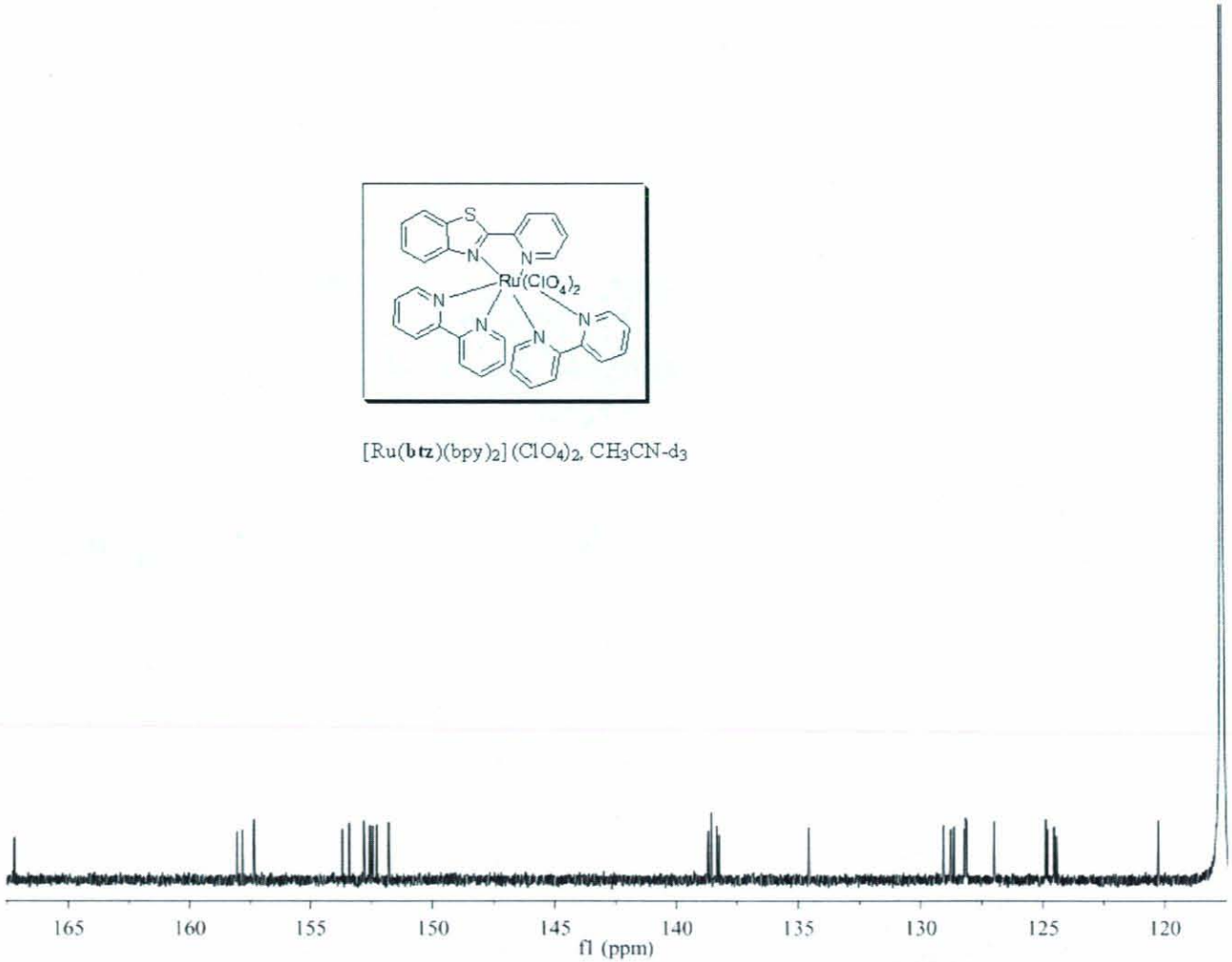

[Ru(**pbim**)(bpy)$_2$] (ClO_4)$_2$, CH_3CN-d_3

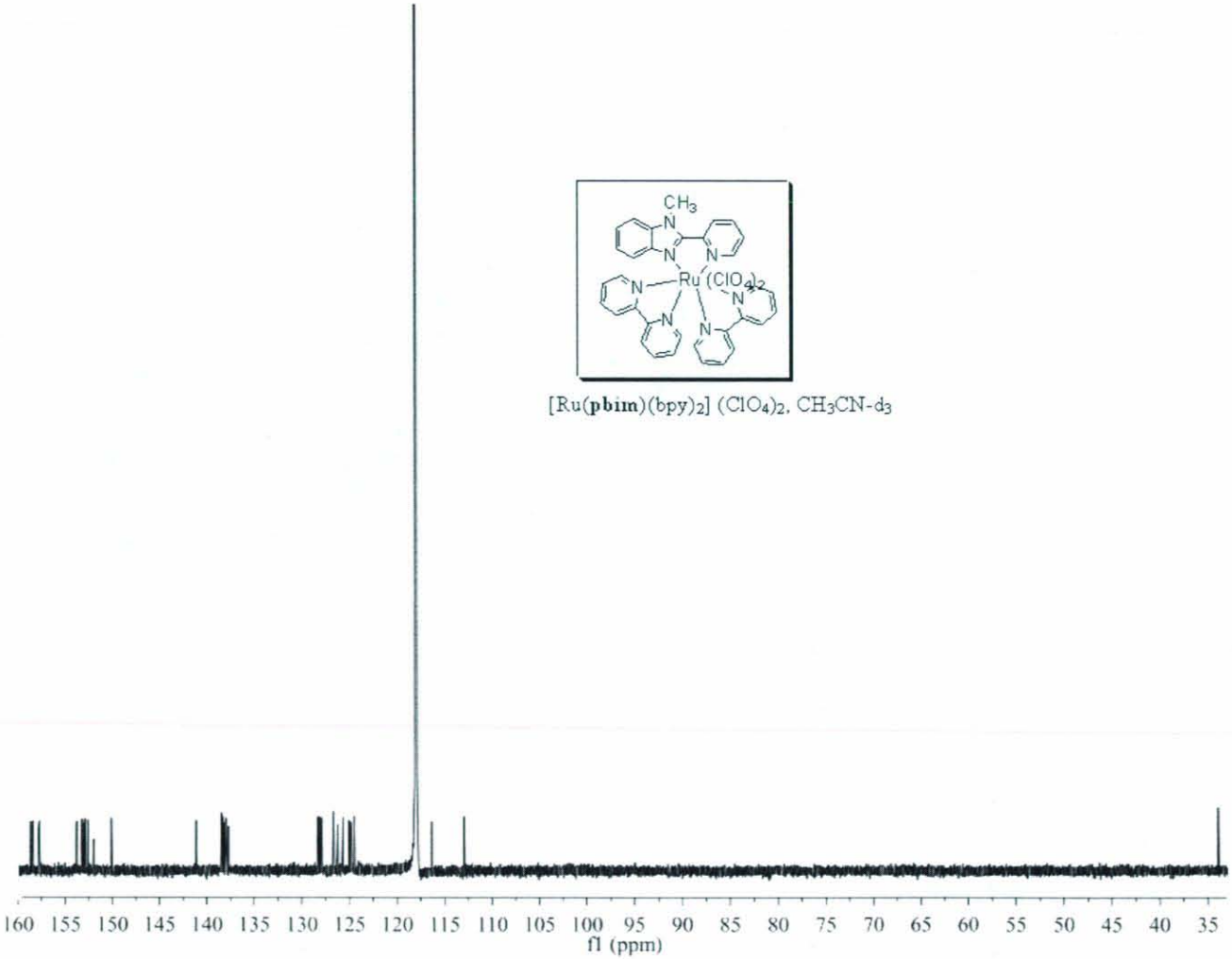

[Ru(**pdbim**)(bpy)$_2$](ClO$_4$)$_2$, CH$_3$CN-d$_3$

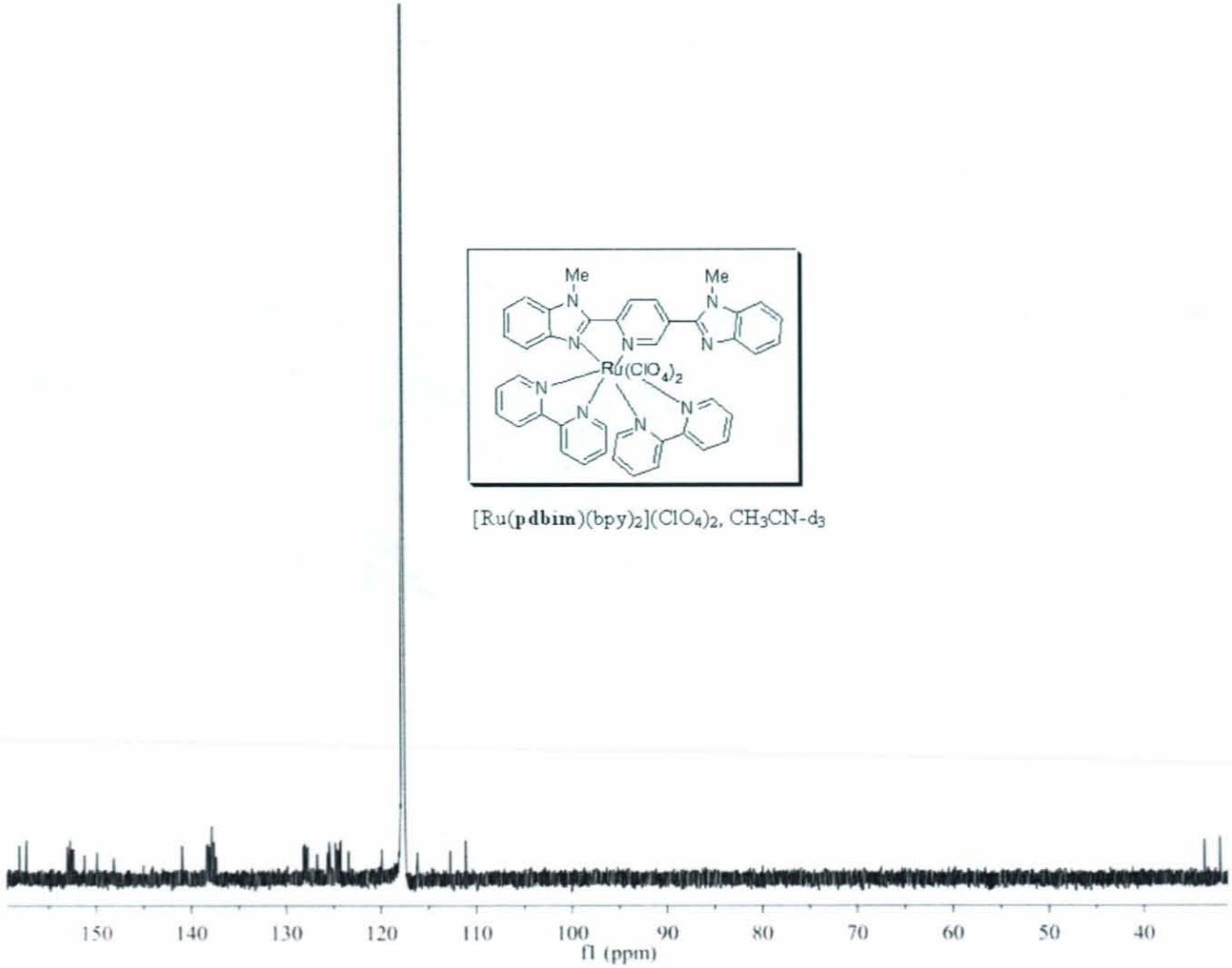

$[(bpy)_2Ru(\mathbf{bptb})(bpy)_2](ClO_4)_4$, CH_3CN-d_3

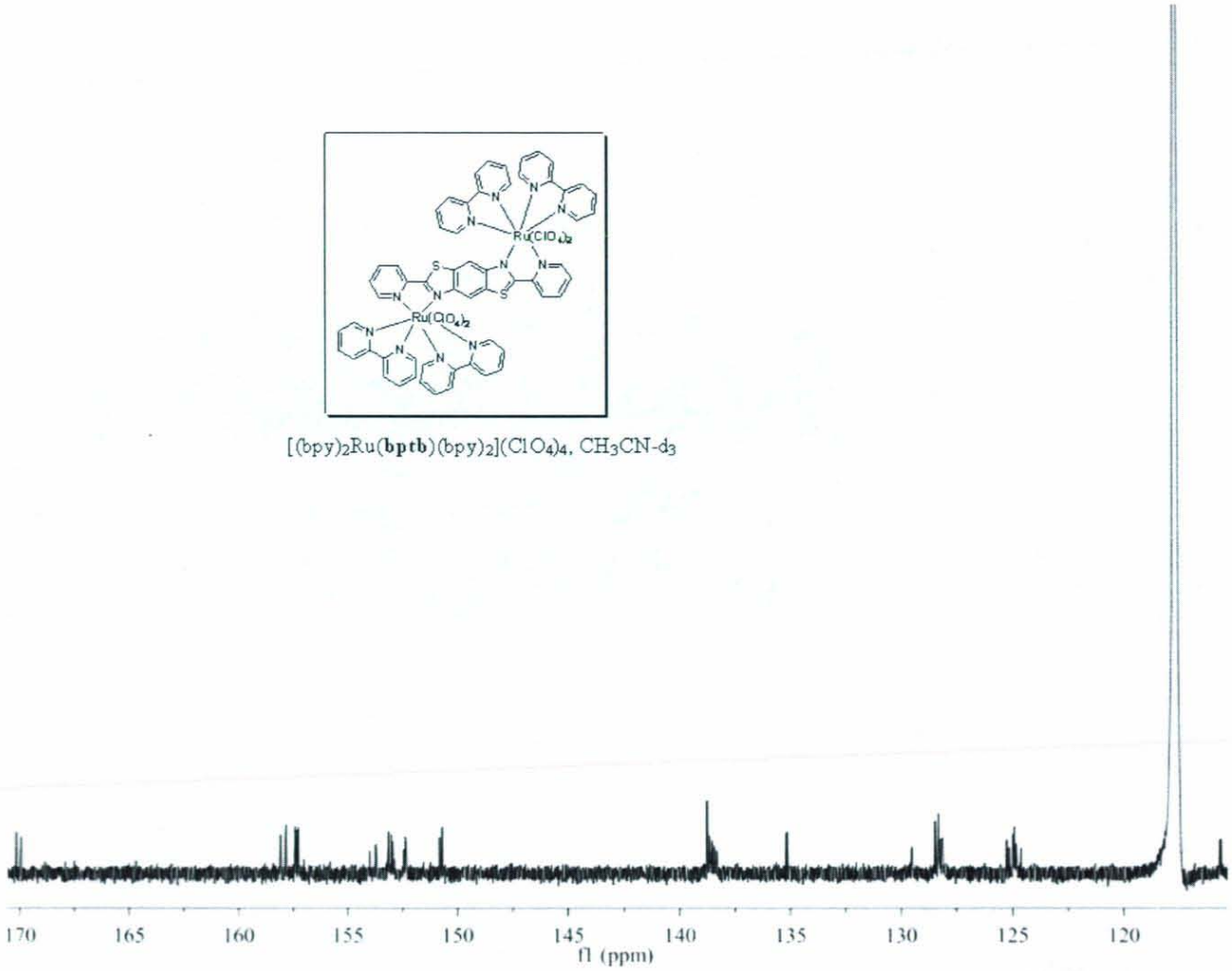

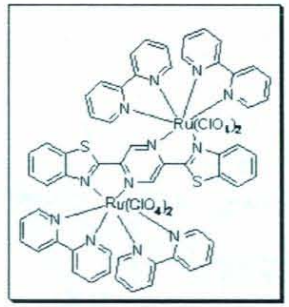

$[(bpy)_2Ru(\mathbf{pybbtz})(bpy)_2](ClO_4)_4$, CH_3CN-d_3

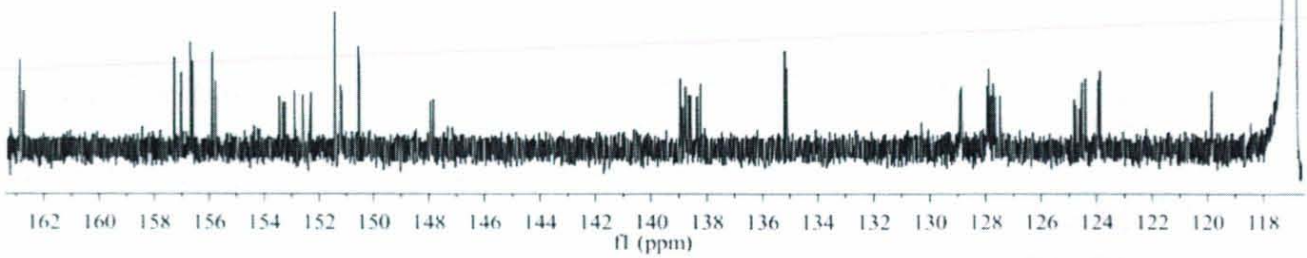

$[(bpy)_2Ru(\mathbf{bpbim})(bpy)_2](ClO_4)_4$, CH_3CN-d_3

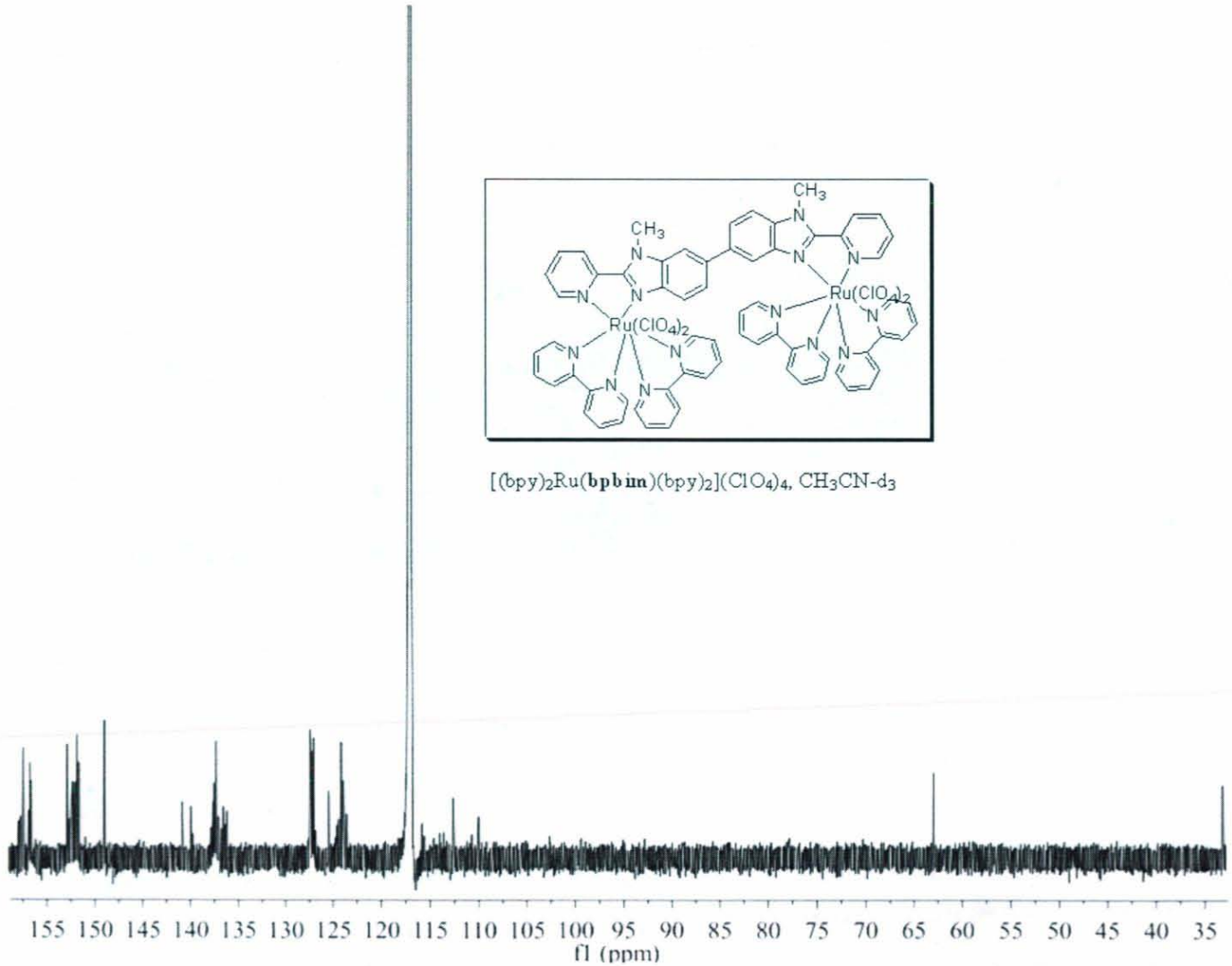

Appendix D

X-ray Crystallography Data

X-ray crystallography data for Ru(**pybtz**)$(bpy)_2(ClO_4)_2$

Experimental

Collection, solution and refinement proceeded normally. Hydrogen atoms were introduced in calculated positions with isotropic thermal parameters set twenty percent greater than those of their bonding partners. They were refined on the riding model. All other atoms were refined anisotropically.

Two perchlorate ions and one lattice solvent molecule of $CHCl_3$ and one of CH_3CN are present for each mononuclear ruthenium complex. The Z-value was therefore set to 4 in order to reflect one formula unit of the following:

$[(C_{12}H_8N_2S)(C_{10}H_8N_2)_2Ru](ClO_4)_2(CHCl_3)(CH_3CN)$

Data Collection

A red chip crystal of $C_{35}H_{28}Cl_5N_7O_8RuS$ having approximate dimensions of 0.33 x 0.20 x 0.20 mm was mounted on a low temperature diffraction loop. All measurements were made on a Rigaku Saturn CCD [1] area detector equipped with a Rigaku SHINE optic, with Mo-Kα radiation.

Indexing was performed from 360 images that were exposed for 14 seconds. The crystal-to-detector distance was 40.11 mm.

Cell constants and an orientation matrix for data collection corresponded to a primitive monoclinic cell with dimensions:

a = 19.432(3) Å
b = 8.8126(14) Å β = 111.760(3)°
c = 24.654(4) Å
V = 3921.1(12) $Å^3$

For Z = 4 and F.W. = 985.04, the calculated density is 1.668 g/cm^3. The systematic absences of:

h0l: h+l ± 2n
0k0: k ± 2n

uniquely determine the space group to be:

$P2_1/n$ (#14)

The data were collected at a temperature of -120 ± 1°C to a maximum 2θ value of 61.7°.

Data Reduction

Of the 72920 reflections that were collected, 8054 were unique (R_{int} = 0.0469); The linear absorption coefficient, μ, for Mo-Kα radiation is 8.54 cm^{-1}. A numerical absorption correction was applied which resulted in transmission factors ranging from 0.8215 to 0.9191. The data were corrected for Lorentz and polarization effects.

Structure Solution and Refinement

The structure was solved by direct methods [2] and expanded using Fourier techniques [3]. The non-hydrogen atoms were refined anisotropically. Hydrogen atoms were refined using the riding model. The final cycle of full-matrix least-squares refinement [4] on F^2 was based on 8054 observed reflections and 515 variable parameters and converged (largest parameter shift was 0.00 times its esd) with unweighted and weighted agreement factors of:

$$R1 = \Sigma \, ||Fo| - |Fc|| \, / \, \Sigma \, |Fo| = 0.0712$$

$$wR2 = [\Sigma \, (\, w \, (Fo^2 - Fc^2)^2 \,) / \, \Sigma \, w(Fo^2)^2]^{1/2} = 0.1869$$

The standard deviation of an observation of unit weight [5] was 1.11. Unit weights were used. The maximum and minimum peaks on the final difference Fourier map corresponded to 2.02 and -1.46 $e^-/Å$ [3], respectively.

Neutral atom scattering factors were taken from Cromer and Waber [6]. Anomalous dispersion effects were included in Fcalc [7]; the values for Δf' and Δf'' were those of Creagh and McAuley [8]. The values for the mass attenuation coefficients are those of Creagh and Hubbell [9]. All calculations were performed using the CrystalStructure [10, 11] crystallographic software package except for refinement, which was performed using SHELXL-97 [2].

References

[1] CrystalClear: Rigaku Corporation, 1999. CrystalClear Software User's Guide, Molecular Structure Corporation, (c) 2000.J.W.Pflugrath (1999) Acta Cryst. D55, 1718-1725.

[2] SHELX97: Sheldrick, G.M. (1997).

[3] DIRDIF99: Beurskens, P.T., Admiraal, G., Beurskens, G., Bosman, W.P., de Gelder, R., Israel, R. and Smits, J.M.M.(1999). The DIRDIF-99 program system, Technical Report of the Crystallography Laboratory, University of Nijmegen, The Netherlands.

[4] Least Squares function minimized: (SHELXL97)
$\Sigma w(F_O^2-F_C^2)^2$ where w = Least Squares weights.

[5] Standard deviation of an observation of unit weight:
$[\Sigma w(F_O^2-F_C^2)^2/(N_O-N_V)]^{1/2}$
where: N_O = number of observations
N_V = number of variables

[6] Cromer, D. T. & Waber, J. T.; "International Tables for X-ray Crystallography", Vol. IV, The Kynoch Press, Birmingham, England, Table 2.2 A (1974).

[7] Ibers, J. A. & Hamilton, W. C.; Acta Crystallogr., 17, 781 (1964).

[8] Creagh, D. C. & McAuley, W.J .; "International Tables for Crystallography", Vol C, (A.J.C. Wilson, ed.), Kluwer Academic Publishers, Boston, Table 4.2.6.8, pages 219-222 (1992).

[9] Creagh, D. C. & Hubbell, J.H..; "International Tables for Crystallography", Vol C, (A.J.C. Wilson, ed.), Kluwer Academic Publishers, Boston, Table 4.2.4.3, pages 200-206 (1992).

[10] CrystalStructure 3.7.0: Crystal Structure Analysis Package, Rigaku and Rigaku/MSC (2000-2005). 9009 New Trails Dr. The Woodlands TX 77381 USA.

[11] CRYSTALS Issue 10: Watkin, D.J., Prout, C.K. Carruthers, J.R. & Betteridge, P.W. Chemical Crystallography Laboratory, Oxford, UK. (1996)

EXPERIMENTAL DETAILS

A. Crystal Data

Empirical Formula	$C_{35}H_{28}Cl_5N_7O_8RuS$
Formula Weight	985.04
Crystal Color, Habit	red, chip
Crystal Dimensions	0.33 X 0.20 X 0.20 mm
Crystal System	monoclinic
Lattice Type	Primitive
Detector Position	40.11 mm
Pixel Size	0.137 mm
Lattice Parameters	a = 19.432(3) Å b = 8.8126(14) Å c = 24.654(4) Å β = 111.760(3)° V = 3921.1(12) Å^3
Space Group	$P2_1/n$ (#14)
Z value	4
D_{calc}	1.668 g/cm^3
F_{000}	1984
μ(MoKα)	8.54 cm^{-1}

B. Intensity Measurements

Detector	Rigaku Saturn
Goniometer	Rigaku AFC8
Radiation	MoKα (λ = 0.71075 Å) Rigaku SHINE Optic
Detector Aperture	70 mm x 70 mm
Data Images	1800 exposures
ω oscillation Range (χ=45.0, ϕ=90.0)	-75.0 - 105.0°
Exposure Rate	28.0 sec./°
Detector Swing Angle	15.07°
ω oscillation Range (χ=0.0, ϕ=0.0)	-75.0 - 105.0°
Exposure Rate	28.0 sec./°
Detector Swing Angle	15.07°
ω oscillation Range (χ=45.0, ϕ=180.0)	-75.0 - 105.0°
Exposure Rate	28.0 sec./°
Detector Swing Angle	15.07°
ω oscillation Range (χ=0.0, ϕ=90.0)	-75.0 - 105.0°
Exposure Rate	28.0 sec./°
Detector Swing Angle	15.07°
ω oscillation Range (χ=45.0, ϕ=0.0)	-75.0 - 105.0°
Exposure Rate	28.0 sec./°

Detector Swing Angle	15.07°
Detector Position	40.11 mm
Pixel Size	0.137 mm
$2\theta_{max}$	61.7°
No. of Reflections Measured	Total: 72920 Unique: 8054 (R_{int} = 0.0469) I>2σ(I): 7322
Corrections	Lorentz-polarization (trans. factors: 0.8215 - 0.9191)

C. Structure Solution and Refinement

Structure Solution	Direct Methods (SHELX97)
Refinement	Full-matrix least-squares on F^2
Function Minimized	$\Sigma\, w\,(Fo^2 - Fc^2)^2$
Least Squares Weights	$w = 1/[\,\sigma^2(Fo^2) + (0.0937 \cdot P)^2 + 13.6853 \cdot P\,]$ where $P = (Max(Fo^2,0) + 2Fc^2)/3$
$2\theta_{max}$ cutoff	53.0^o
Anomalous Dispersion	All non-hydrogen atoms
No. Observations (All reflections)	8054
No. Variables	515
Reflection/Parameter Ratio	15.64
Residuals: R1 ($I>2.00\sigma(I)$)	0.0712
Residuals: R (All reflections)	0.0765
Residuals: wR2 (All reflections)	0.1869
Goodness of Fit Indicator	1.106
Max Shift/Error in Final Cycle	0.002
Maximum peak in Final Diff. Map	2.02 $e^-/Å^3$
Minimum peak in Final Diff. Map	-1.46 $e^-/Å^3$

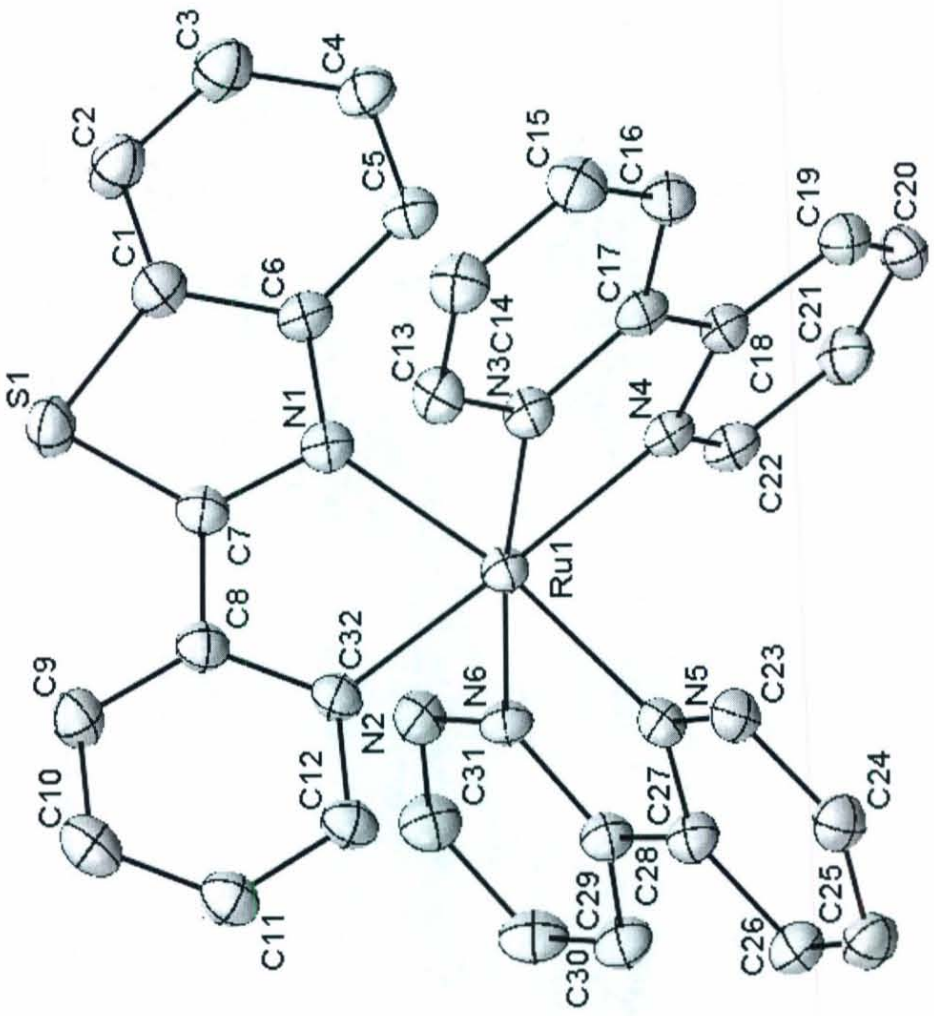

Figure D1: X-ray crystal structure for Ru(**pybtz**)$(bpy)_2(ClO_4)_2$. Anions and hydrogen atoms omitted for clarity.

Table 1: Bond lengths (Å) for Ru(**pybtz**)$(bpy)_2(ClO_4)_2$

atom	atom	distance	atom	atom	distance
Ru(1)	N(1)	2.078(4)	Ru(1)	N(2)	2.084(3)
Ru(1)	N(3)	2.060(3)	Ru(1)	N(4)	2.058(3)
Ru(1)	N(5)	2.055(4)	Ru(1)	N(6)	2.065(3)
Cl(1)	O(1)	1.433(3)	Cl(1)	O(2)	1.442(4)
Cl(1)	O(3)	1.435(4)	Cl(1)	O(4)	1.444(3)
Cl(2)	O(5)	1.392(5)	Cl(2)	O(6)	1.349(8)
Cl(2)	O(7)	1.421(5)	Cl(2)	O(8)	1.444(7)
Cl(3)	C(33)	1.765(6)	Cl(4)	C(33)	1.754(7)
Cl(5)	C(33)	1.771(8)	S(1)	C(1)	1.736(5)
S(1)	C(7)	1.712(5)	N(1)	C(6)	1.392(7)
N(1)	C(7)	1.324(5)	N(2)	C(8)	1.354(6)
N(2)	C(12)	1.352(7)	N(3)	C(13)	1.347(5)
N(3)	C(17)	1.367(5)	N(4)	C(18)	1.362(5)
N(4)	C(22)	1.354(5)	N(5)	C(23)	1.349(5)
N(5)	C(27)	1.348(6)	N(6)	C(28)	1.360(7)
N(6)	C(32)	1.343(5)	N(7)	C(35)	1.149(11)
C(1)	C(2)	1.396(9)	C(1)	C(6)	1.407(6)
C(2)	C(3)	1.372(8)	C(3)	C(4)	1.393(6)
C(4)	C(5)	1.371(8)	C(5)	C(6)	1.402(6)
C(7)	C(8)	1.453(7)	C(8)	C(9)	1.388(6)
C(9)	C(10)	1.378(8)	C(10)	C(11)	1.393(8)
C(11)	C(12)	1.384(6)	C(13)	C(14)	1.376(7)
C(14)	C(15)	1.387(6)	C(15)	C(16)	1.378(6)
C(16)	C(17)	1.388(7)	C(17)	C(18)	1.474(6)
C(18)	C(19)	1.388(5)	C(19)	C(20)	1.379(7)
C(20)	C(21)	1.380(7)	C(21)	C(22)	1.369(6)
C(23)	C(24)	1.378(7)	C(24)	C(25)	1.378(8)
C(25)	C(26)	1.391(7)	C(26)	C(27)	1.391(8)
C(27)	C(28)	1.473(6)	C(28)	C(29)	1.387(7)
C(29)	C(30)	1.377(7)	C(30)	C(31)	1.381(9)
C(31)	C(32)	1.376(7)	C(34)	C(35)	1.450(12)

Table 2: Bond angles (°) for Ru(**pybtz**)$(bpy)_2(ClO_4)_2$

atom	atom	atom	angle	atom	atom	atom	angle
N(1)	Ru(1)	N(2)	78.44(15)	N(1)	Ru(1)	N(3)	88.94(15)
N(1)	Ru(1)	N(4)	100.85(15)	N(1)	Ru(1)	N(5)	171.06(14)
N(1)	Ru(1)	N(6)	95.35(15)	N(2)	Ru(1)	N(3)	97.34(14)
N(2)	Ru(1)	N(4)	175.98(16)	N(2)	Ru(1)	N(5)	94.62(15)
N(2)	Ru(1)	N(6)	88.69(14)	N(3)	Ru(1)	N(4)	78.67(14)
N(3)	Ru(1)	N(5)	97.60(15)	N(3)	Ru(1)	N(6)	173.21(12)
N(4)	Ru(1)	N(5)	86.46(15)	N(4)	Ru(1)	N(6)	95.32(14)
N(5)	Ru(1)	N(6)	78.73(15)	O(1)	Cl(1)	O(2)	109.9(2)
O(1)	Cl(1)	O(3)	109.8(2)	O(1)	Cl(1)	O(4)	109.7(2)
O(2)	Cl(1)	O(3)	109.1(2)	O(2)	Cl(1)	O(4)	109.0(2)
O(3)	Cl(1)	O(4)	109.4(2)	O(5)	Cl(2)	O(6)	112.8(5)
O(5)	Cl(2)	O(7)	111.0(3)	O(5)	Cl(2)	O(8)	104.3(5)
O(6)	Cl(2)	O(7)	112.8(4)	O(6)	Cl(2)	O(8)	107.4(7)
O(7)	Cl(2)	O(8)	108.0(5)	C(1)	S(1)	C(7)	89.4(2)
Ru(1)	N(1)	C(6)	135.4(2)	Ru(1)	N(1)	C(7)	113.5(3)
C(6)	N(1)	C(7)	110.9(3)	Ru(1)	N(2)	C(8)	115.6(3)
Ru(1)	N(2)	C(12)	126.4(2)	C(8)	N(2)	C(12)	118.0(3)
Ru(1)	N(3)	C(13)	125.8(2)	Ru(1)	N(3)	C(17)	115.6(2)
C(13)	N(3)	C(17)	118.5(4)	Ru(1)	N(4)	C(18)	115.8(2)
Ru(1)	N(4)	C(22)	125.8(3)	C(18)	N(4)	C(22)	118.3(3)
Ru(1)	N(5)	C(23)	125.4(3)	Ru(1)	N(5)	C(27)	115.9(3)
C(23)	N(5)	C(27)	118.7(4)	Ru(1)	N(6)	C(28)	115.5(2)
Ru(1)	N(6)	C(32)	125.9(3)	C(28)	N(6)	C(32)	118.6(4)
S(1)	C(1)	C(2)	128.1(3)	S(1)	C(1)	C(6)	110.1(4)
C(2)	C(1)	C(6)	121.8(4)	C(1)	C(2)	C(3)	117.6(4)
C(2)	C(3)	C(4)	121.0(6)	C(3)	C(4)	C(5)	122.1(4)
C(4)	C(5)	C(6)	118.1(4)	N(1)	C(6)	C(1)	113.5(4)
N(1)	C(6)	C(5)	127.2(4)	C(1)	C(6)	C(5)	119.3(5)
S(1)	C(7)	N(1)	116.0(4)	S(1)	C(7)	C(8)	124.8(3)
N(1)	C(7)	C(8)	119.2(4)	N(2)	C(8)	C(7)	113.1(3)
N(2)	C(8)	C(9)	122.9(5)	C(7)	C(8)	C(9)	124.0(4)
C(8)	C(9)	C(10)	119.2(4)	C(9)	C(10)	C(11)	118.0(4)
C(10)	C(11)	C(12)	120.6(5)	N(2)	C(12)	C(11)	121.3(4)
N(3)	C(13)	C(14)	122.3(4)	C(13)	C(14)	C(15)	119.4(4)
C(14)	C(15)	C(16)	119.0(5)	C(15)	C(16)	C(17)	119.5(4)
N(3)	C(17)	C(16)	121.3(3)	N(3)	C(17)	C(18)	114.7(3)
C(16)	C(17)	C(18)	123.8(3)	N(4)	C(18)	C(17)	114.4(3)
N(4)	C(18)	C(19)	121.8(4)	C(17)	C(18)	C(19)	123.7(4)
C(18)	C(19)	C(20)	118.5(4)	C(19)	C(20)	C(21)	119.7(4)
C(20)	C(21)	C(22)	119.4(4)	N(4)	C(22)	C(21)	122.1(4)

Table 2: Bond angles (°) for Ru(**pybtz**)(bpy)$_2$(ClO_4)$_2$ (Continued)

atom	atom	atom	angle	atom	atom	atom	angle
N(5)	C(23)	C(24)	122.6(4)	C(23)	C(24)	C(25)	119.0(4)
C(24)	C(25)	C(26)	119.1(5)	C(25)	C(26)	C(27)	119.2(5)
N(5)	C(27)	C(26)	121.4(4)	N(5)	C(27)	C(28)	115.3(4)
C(26)	C(27)	C(28)	123.3(4)	N(6)	C(28)	C(27)	114.5(4)
N(6)	C(28)	C(29)	121.0(4)	C(27)	C(28)	C(29)	124.5(4)
C(28)	C(29)	C(30)	120.0(5)	C(29)	C(30)	C(31)	118.4(5)
C(30)	C(31)	C(32)	119.7(4)	N(6)	C(32)	C(31)	122.2(5)
Cl(3)	C(33)	Cl(4)	107.8(4)	Cl(3)	C(33)	Cl(5)	110.0(3)
Cl(4)	C(33)	Cl(5)	110.8(3)	N(7)	C(35)	C(34)	172.1(9)

X-ray crystallography data for Ru(**Me$_2$-pybbim**)(bpy)$_2$(ClO$_4$)$_2$

Experimental

Collection, solution and refinement proceeded normally. Hydrogen atoms were introduced in calculated positions with isotropic thermal parameters set twenty percent greater than those of their bonding partners. All hydrogen atoms were refined on the riding model.

The Platon [12] Squeeze procedure was applied to recover 104 electrons per unit cell in one void (total volume 369 Å^3); that is 52 electrons per formula unit (~5 H_2O). Several partial-occupancy solvent lattice water molecules were present, prior to the application of Squeeze however, a good point atom model could not be achieved. The application of Squeeze gave a good improvement in the data statistics and allowed for a full anisotropic refinement of the structure.

The formula for this model, which includes the Squeezed lattice water molecules, is:

$[(C_{21}H_{17}N_5)(C_{10}H_8N_2)_2Ru](ClO_4)_2(H_2O)_5$

Data Collection

A red prism crystal of $C_{41}H_{43}Cl_2N_9O_{13}Ru$ having approximate dimensions of 0.26 x 0.19 x 0.04 mm was mounted on a low temperature diffraction loop. All measurements were made on a Rigaku Saturn CCD [1] area detector, equipped with a SHINE optic, with Mo-Kα radiation.

Indexing was performed from 360 images that were exposed for 35 seconds. The crystal-to-detector distance was 49.94 mm.

Cell constants and an orientation matrix for data collection corresponded to a primitive triclinic cell with dimensions:

a = 9.313(6) Å α = 103.50(2)°
b = 14.766(10) Å β = 104.18(3)°
c = 17.970(12) Å γ = 104.12(4)°
V = 2208(3) Å^3

For Z = 2 and F.W. = 1041.82, the calculated density is 1.567 g/cm^3. Based on a statistical analysis of intensity distribution, and the successful solution and refinement of the structure, the space group was determined to be:

P-1 (#2)

The data were collected at a temperature of -120 ± 1°C to a maximum 2θ value of 60.0°.

Data Reduction

Of the 18276 reflections that were collected, 9011 were unique (R_{int} = 0.0387). The linear absorption coefficient, μ, for Mo-Kα radiation is 5.519 cm^{-1}. A numerical absorption correction was applied which resulted in transmission factors ranging from 0.8898 to 0.9832 respectively. The data were corrected for Lorentz and polarization effects.

Structure Solution and Refinement

The structure was solved by direct methods[2] and expanded using Fourier techniques [3]. The non-hydrogen atoms were refined anisotropically. Hydrogen atoms were refined using the riding model. The final cycle of full-matrix least-squares refinement [4] on F^2 was based on 9011 observed reflections and 550 variable parameters and converged (largest parameter shift was 0.00 times its esd) with unweighted and weighted agreement factors of:

$$R1 = \Sigma \, ||Fo| - |Fc|| \, / \, \Sigma \, |Fo| = 0.1180$$

$$wR2 = [\Sigma (w (Fo^2 - Fc^2)^2) / \Sigma \, w(Fo^2)^2]^{1/2} = 0.3055$$

The standard deviation of an observation of unit weight [5] was 1.06. Unit weights were used. The maximum and minimum peaks on the final difference Fourier map corresponded to 3.18 and -1.49 $e^-/Å^3$, respectively.

Neutral atom scattering factors were taken from Cromer and Waber [6]. Anomalous dispersion effects were included in Fcalc [7]; the values for $\Delta f'$ and $\Delta f''$ were those of Creagh and McAuley [8]. The values for the mass attenuation coefficients are those of Creagh and Hubbell [9]. All calculations were performed using the CrystalStructure [10, 11] crystallographic software package except for refinement, which was performed using SHELXL-97 [2].

References

[1] CrystalClear: Rigaku Corporation, 1999. CrystalClear Software User's Guide, Molecular Structure Corporation, (c) 2000.J.W.Pflugrath (1999) Acta Cryst. D55, 1718-1725.

[2] SHELX97: Sheldrick, G.M. (1997).

[3] DIRDIF99: Beurskens, P.T., Admiraal, G., Beurskens, G., Bosman, W.P., de Gelder, R., Israel, R. and Smits, J.M.M.(1999). The DIRDIF-99 program system, Technical Report of the Crystallography Laboratory, University of Nijmegen, The Netherlands.

[4] Least Squares function minimized: (SHELXL97)
$\Sigma w(F_O^2-F_C^2)^2$ where w = Least Squares weights.

[5] Standard deviation of an observation of unit weight:
$[\Sigma w(F_O^2-F_C^2)^2/(N_O-N_V)]^{1/2}$
where: N_O = number of observations
N_V = number of variables

[6] Cromer, D. T. & Waber, J. T.; "International Tables for X-ray Crystallography", Vol. IV, The Kynoch Press, Birmingham, England, Table 2.2 A (1974).

[7] Ibers, J. A. & Hamilton, W. C.; Acta Crystallogr., 17, 781 (1964).

[8] Creagh, D. C. & McAuley, W.J .; "International Tables for Crystallography", Vol C, (A.J.C. Wilson, ed.), Kluwer Academic Publishers, Boston, Table 4.2.6.8, pages 219-222 (1992).

[9] Creagh, D. C. & Hubbell, J.H..; "International Tables for Crystallography", Vol C, (A.J.C. Wilson, ed.), Kluwer Academic Publishers, Boston, Table 4.2.4.3, pages 200-206 (1992).

[10] CrystalStructure 3.7.0: Crystal Structure Analysis Package, Rigaku and Rigaku/MSC (2000-2005). 9009 New Trails Dr. The Woodlands TX 77381 USA.

[11] CRYSTALS Issue 10: Watkin, D.J., Prout, C.K. Carruthers, J.R. & Betteridge, P.W. Chemical Crystallography Laboratory, Oxford, UK. (1996)

[12] Spek, A.L. (2003), J.Appl.Cryst. 36, 7-13.

EXPERIMENTAL DETAILS

A. Crystal Data

Empirical Formula	$C_{41}H_{43}Cl_2N_9O_{13}Ru$
Formula Weight	1041.82
Crystal Color, Habit	red, prism
Crystal Dimensions	0.26 X 0.19 X 0.04 mm
Crystal System	triclinic
Lattice Type	Primitive
Detector Position	49.94 mm
Pixel Size	0.137 mm
Lattice Parameters	a = 9.313(6) Å b = 14.766(10) Å c = 17.970(12) Å α = 103.50(2) ° β = 104.18(3) ° γ = 104.12(4) ° V = 2208(3) Å^3
Space Group	P-1 (#2)
Z value	2
D_{calc}	1.567 g/cm^3
F_{000}	1068
μ(MoKα)	5.52 cm^{-1}

B. Intensity Measurements

Detector	Rigaku Saturn
Goniometer	Rigaku AFC8
Radiation	MoKα (λ = 0.71075 Å) graphite monochromated-Rigaku
SHINE	
Detector Aperture	70 mm x 70 mm
Data Images	880 exposures
ω oscillation Range (χ=45.0, ϕ=0.0)	-70.0 - 110.0°
Exposure Rate	70.0 sec./°
Detector Swing Angle	20.23°
ω oscillation Range (χ=45.0, ϕ=90.0)	-70.0 - 92.0°
Exposure Rate	70.0 sec./°
Detector Swing Angle	20.23°
ω oscillation Range (χ=45.0, ϕ=180.0)	-70.0 - -2.0°
Exposure Rate	70.0 sec./°
Detector Swing Angle	20.23°
ω oscillation Range (χ=0.0, ϕ=180.0)	-50.0 - -20.0°
Exposure Rate	70.0 sec./°
Detector Swing Angle	20.23°
Detector Position	49.94 mm

Pixel Size	0.137 mm
$2\theta_{max}$	60.0^{o}
No. of Reflections Measured	Total: 18276 Unique: 9011 (R_{int} = 0.0387) I>2σ(I): 7997
Corrections	Lorentz-polarization (trans. factors: 0.8898 - 0.9832)

C. Structure Solution and Refinement

Structure Solution	Direct Methods (SHELX97)
Refinement	Full-matrix least-squares on F^2
Function Minimized	Σ w $(Fo^2 - Fc^2)^2$
Least Squares Weights	$w = 1/ [\sigma^2(Fo^2) + (0.1076 \cdot P)^2 + 39.7151 \cdot P]$ where $P = (Max(Fo^2,0) + 2Fc^2)/3$
$2\theta_{max}$ cutoff	53.0°
Anomalous Dispersion	All non-hydrogen atoms
No. Observations (All reflections)	9011
No. Variables	550
Reflection/Parameter Ratio	16.38
Residuals: R1 ($I>2.00\sigma(I)$)	0.1180
Residuals: R (All reflections)	0.1247
Residuals: wR2 (All reflections)	0.3055
Goodness of Fit Indicator	1.058
Max Shift/Error in Final Cycle	0.000
Maximum peak in Final Diff. Map	3.18 $e^-/Å^3$
Minimum peak in Final Diff. Map	-1.49 $e^-/Å^3$

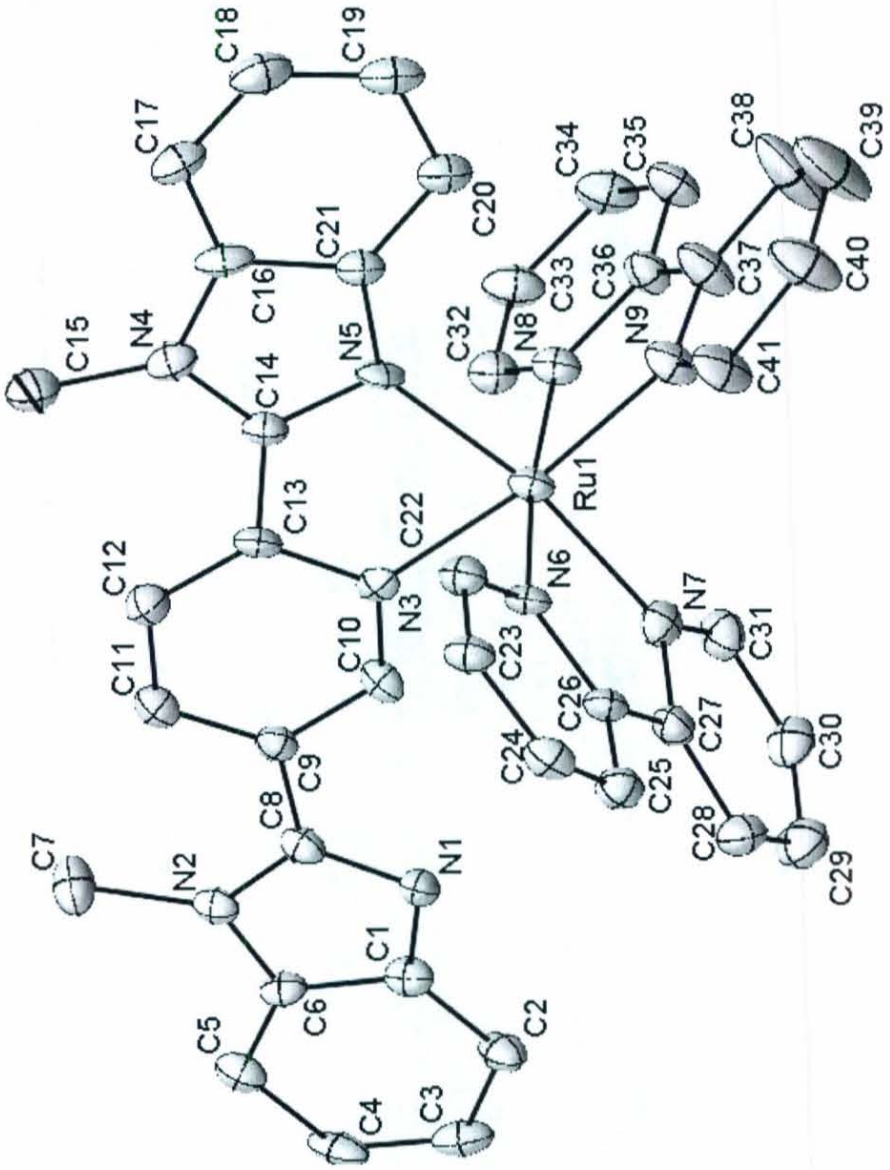

Figure D3: X-ray crystal structure for Ru(**Me$_2$pybbim**)(bpy)$_2$(ClO$_4$)$_2$. Anions and hydrogen atoms omitted for clarity.

Table 3: Bond lengths (Å) for Ru(**Me_2-pybbim**)$(bpy)_2(ClO_4)_2$

atom	atom	distance	atom	atom	distance
Ru(1)	N(3)	2.068(8)	Ru(1)	N(5)	2.056(5)
Ru(1)	N(6)	2.062(8)	Ru(1)	N(7)	2.053(6)
Ru(1)	N(8)	2.046(8)	Ru(1)	N(9)	2.040(10)
Cl(1)	O(1)	1.413(11)	Cl(1)	O(2)	1.343(13)
Cl(1)	O(3)	1.40(2)	Cl(1)	O(4)	1.438(13)
Cl(2)	O(5)	1.431(11)	Cl(2)	O(6)	1.456(16)
Cl(2)	O(7)	1.441(12)	Cl(2)	O(8)	1.392(17)
N(1)	C(1)	1.385(12)	N(1)	C(8)	1.312(9)
N(2)	C(6)	1.364(8)	N(2)	C(7)	1.503(11)
N(2)	C(8)	1.367(13)	N(3)	C(10)	1.330(11)
N(3)	C(13)	1.383(9)	N(4)	C(14)	1.360(9)
N(4)	C(15)	1.477(14)	N(4)	C(16)	1.349(14)
N(5)	C(14)	1.343(13)	N(5)	C(21)	1.374(10)
N(6)	C(22)	1.342(11)	N(6)	C(26)	1.360(9)
N(7)	C(27)	1.383(14)	N(7)	C(31)	1.336(12)
N(8)	C(32)	1.351(14)	N(8)	C(36)	1.359(14)
N(9)	C(37)	1.326(18)	N(9)	C(41)	1.390(18)
C(1)	C(2)	1.416(10)	C(1)	C(6)	1.373(13)
C(2)	C(3)	1.379(16)	C(3)	C(4)	1.348(17)
C(4)	C(5)	1.424(10)	C(5)	C(6)	1.376(14)
C(8)	C(9)	1.457(11)	C(9)	C(10)	1.380(14)
C(9)	C(11)	1.389(10)	C(11)	C(12)	1.395(13)
C(12)	C(13)	1.376(15)	C(13)	C(14)	1.438(12)
C(16)	C(17)	1.362(11)	C(16)	C(21)	1.452(12)
C(17)	C(18)	1.361(19)	C(18)	C(19)	1.402(16)
C(19)	C(20)	1.409(12)	C(20)	C(21)	1.401(16)
C(22)	C(23)	1.381(15)	C(23)	C(24)	1.360(11)
C(24)	C(25)	1.413(13)	C(25)	C(26)	1.382(15)
C(26)	C(27)	1.487(12)	C(27)	C(28)	1.368(11)
C(28)	C(29)	1.362(15)	C(29)	C(30)	1.385(18)
C(30)	C(31)	1.367(12)	C(32)	C(33)	1.371(16)
C(33)	C(34)	1.386(19)	C(34)	C(35)	1.385(19)
C(35)	C(36)	1.369(17)	C(36)	C(37)	1.466(18)
C(37)	C(38)	1.40(2)	C(38)	C(39)	1.37(3)
C(39)	C(40)	1.33(2)	C(40)	C(41)	1.44(2)

Table 4: Bond angles (°) for Ru(**Me_2-pybbim**)$(bpy)_2(ClO_4)_2$

atom	atom	atom	angle	atom	atom	atom	angle
N(3)	Ru(1)	N(5)	78.1(2)	N(3)	Ru(1)	N(6)	90.2(3)
N(3)	Ru(1)	N(7)	93.6(2)	N(3)	Ru(1)	N(8)	95.5(3)
N(3)	Ru(1)	N(9)	172.0(3)	N(5)	Ru(1)	N(6)	93.2(2)
N(5)	Ru(1)	N(7)	168.9(3)	N(5)	Ru(1)	N(8)	90.6(2)
N(5)	Ru(1)	N(9)	96.2(3)	N(6)	Ru(1)	N(7)	79.2(3)
N(6)	Ru(1)	N(8)	173.7(3)	N(6)	Ru(1)	N(9)	95.8(3)
N(7)	Ru(1)	N(8)	97.7(3)	N(7)	Ru(1)	N(9)	92.6(3)
N(8)	Ru(1)	N(9)	78.7(3)	O(1)	Cl(1)	O(2)	111.0(9)
O(1)	Cl(1)	O(3)	111.6(10)	O(1)	Cl(1)	O(4)	113.8(7)
O(2)	Cl(1)	O(3)	108.0(10)	O(2)	Cl(1)	O(4)	104.7(8)
O(3)	Cl(1)	O(4)	107.4(11)	O(5)	Cl(2)	O(6)	107.8(7)
O(5)	Cl(2)	O(7)	114.5(8)	O(5)	Cl(2)	O(8)	108.5(9)
O(6)	Cl(2)	O(7)	106.0(9)	O(6)	Cl(2)	O(8)	111.2(9)
O(7)	Cl(2)	O(8)	108.8(8)	C(1)	N(1)	C(8)	105.2(8)
C(6)	N(2)	C(7)	124.1(8)	C(6)	N(2)	C(8)	107.0(6)
C(7)	N(2)	C(8)	128.9(6)	Ru(1)	N(3)	C(10)	126.7(5)
Ru(1)	N(3)	C(13)	116.1(6)	C(10)	N(3)	C(13)	117.2(8)
C(14)	N(4)	C(15)	127.4(9)	C(14)	N(4)	C(16)	109.4(8)
C(15)	N(4)	C(16)	123.2(7)	Ru(1)	N(5)	C(14)	114.3(5)
Ru(1)	N(5)	C(21)	137.7(6)	C(14)	N(5)	C(21)	106.9(6)
Ru(1)	N(6)	C(22)	125.9(5)	Ru(1)	N(6)	C(26)	115.8(5)
C(22)	N(6)	C(26)	118.2(8)	Ru(1)	N(7)	C(27)	115.6(5)
Ru(1)	N(7)	C(31)	127.1(7)	C(27)	N(7)	C(31)	116.8(7)
Ru(1)	N(8)	C(32)	127.0(7)	Ru(1)	N(8)	C(36)	115.8(7)
C(32)	N(8)	C(36)	117.2(9)	Ru(1)	N(9)	C(37)	115.8(8)
Ru(1)	N(9)	C(41)	123.6(8)	C(37)	N(9)	C(41)	120.4(11)
N(1)	C(1)	C(2)	130.8(9)	N(1)	C(1)	C(6)	109.8(6)
C(2)	C(1)	C(6)	119.3(9)	C(1)	C(2)	C(3)	117.8(9)
C(2)	C(3)	C(4)	121.5(7)	C(3)	C(4)	C(5)	122.6(10)
C(4)	C(5)	C(6)	114.9(9)	N(2)	C(6)	C(1)	106.0(8)
N(2)	C(6)	C(5)	130.1(8)	C(1)	C(6)	C(5)	123.9(6)
N(1)	C(8)	N(2)	111.9(7)	N(1)	C(8)	C(9)	121.2(9)
N(2)	C(8)	C(9)	126.9(6)	C(8)	C(9)	C(10)	115.9(6)
C(8)	C(9)	C(11)	126.7(9)	C(10)	C(9)	C(11)	117.4(8)
N(3)	C(10)	C(9)	124.7(6)	C(9)	C(11)	C(12)	119.7(9)
C(11)	C(12)	C(13)	119.0(7)	N(3)	C(13)	C(12)	121.7(7)
N(3)	C(13)	C(14)	112.0(8)	C(12)	C(13)	C(14)	126.3(7)

Table 4: Bond angles (°) for Ru(**Me_2-pybbim**)(**bpy**)$_2$(ClO_4)$_2$ (continued)

atom	atom	atom	angle	atom	atom	atom	angle
N(4)	C(14)	N(5)	110.8(8)	N(4)	C(14)	C(13)	130.7(9)
N(5)	C(14)	C(13)	118.5(6)	N(4)	C(16)	C(17)	135.1(10)
N(4)	C(16)	C(21)	105.1(6)	C(17)	C(16)	C(21)	119.8(10)
C(16)	C(17)	C(18)	120.1(9)	C(17)	C(18)	C(19)	121.4(9)
C(18)	C(19)	C(20)	121.1(11)	C(19)	C(20)	C(21)	116.9(9)
N(5)	C(21)	C(16)	107.8(8)	N(5)	C(21)	C(20)	131.6(7)
C(16)	C(21)	C(20)	120.5(7)	N(6)	C(22)	C(23)	122.8(7)
C(22)	C(23)	C(24)	118.7(8)	C(23)	C(24)	C(25)	120.5(10)
C(24)	C(25)	C(26)	117.0(7)	N(6)	C(26)	C(25)	122.8(7)
N(6)	C(26)	C(27)	114.9(8)	C(25)	C(26)	C(27)	122.4(6)
N(7)	C(27)	C(26)	113.8(6)	N(7)	C(27)	C(28)	121.9(9)
C(26)	C(27)	C(28)	124.3(10)	C(27)	C(28)	C(29)	120.1(11)
C(28)	C(29)	C(30)	118.5(8)	C(29)	C(30)	C(31)	119.5(9)
N(7)	C(31)	C(30)	123.1(11)	N(8)	C(32)	C(33)	123.2(11)
C(32)	C(33)	C(34)	118.7(12)	C(33)	C(34)	C(35)	119.0(12)
C(34)	C(35)	C(36)	119.2(12)	N(8)	C(36)	C(35)	122.6(11)
N(8)	C(36)	C(37)	113.4(10)	C(35)	C(36)	C(37)	123.8(11)
N(9)	C(37)	C(36)	116.0(12)	N(9)	C(37)	C(38)	120.7(14)
C(36)	C(37)	C(38)	123.2(14)	C(37)	C(38)	C(39)	119.9(19)
C(38)	C(39)	C(40)	120.6(19)	C(39)	C(40)	C(41)	119.7(17)
N(9)	C(41)	C(40)	118.2(12)				

X-ray crystallography data for $[\{(bpy)_2Ru\}_2(\mathbf{py_2tbtz})]^{4+}$

Experimental

Collection, solution and refinement proceeded normally. All hydrogen atoms were introduced in calculated positions with isotropic thermal parameters set twenty percent greater than those of their bonding partners and were refined on the riding model.

The Platon [12] Squeeze procedure was applied to recover 65 electrons per unit cell in two voids (total volume 228 $Å^3$); that is 65 electrons per formula unit (with Z = 1 in this model). Disordered solvent lattice water molecules were present prior to the application of Squeeze, however, a satisfactory point atom model could not be achieved. The application of Squeeze gave a good improvement in the data statistics and allowed for a full anisotropic refinement of the structure.

The formula, which includes protons and solvent molecules omitted from the model, is: $[(C_{58}H_{42}S_2O_{16}Ru_2](ClO_4)_4(H_2O)_6$

Data Collection

A red prism crystal of $C_{58}H_{54}Cl_4N_{12}O_{22}Ru_2S_2$ having approximate dimensions of 0.28 x 0.27 x 0.18 mm was mounted on a low temperature diffraction loop. All measurements were made on a Rigaku Saturn CCD [1] area detector with a SHINE optic and Mo-Kα radiation.

Indexing was performed from 360 images that were exposed for 25 seconds. The crystal-to-detector distance was 40.06 mm.

Cell constants and an orientation matrix for data collection corresponded to a primitive triclinic cell with dimensions:

a = 12.0249(11) Å α = 93.388(18)°
b = 12.75010(10) Å β = 112.8809(13)°
c = 13.9516(14) Å γ = 117.909(18)°
V = 1663.4(2) $Å^3$

For Z = 1 and F.W. = 1679.20, the calculated density is 1.676 g/cm^3. Based on a statistical analysis of intensity distribution, and the successful solution and refinement of the structure, the space group was determined to be:

P-1 (#2)

The data were collected at a temperature of -120 $\pm$ 1°C to a maximum 2θ value of 61.8°.

Data Reduction

Of the 12827 reflections that were collected, 6116 were unique (R_{int} = 0.0356). The linear absorption coefficient, μ, for Mo-Kα radiation is 7.64 cm^{-1}. A numerical absorption correction was applied which resulted in transmission factors ranging from 0.8731 to 0.9708. The data were corrected for Lorentz and polarization effects.

Structure Solution and Refinement

The structure was solved by direct methods [2] and expanded using Fourier techniques [3]. The non-hydrogen atoms were refined anisotropically. Hydrogen atoms were refined using the riding model. The final cycle of full-matrix least-squares refinement [4] on F^2 was based on 6116 observed reflections and 425 variable parameters and converged (largest parameter shift was 0.00 times its esd) with unweighted and weighted agreement factors of:

$$R1 = \Sigma \, ||Fo| - |Fc|| \, / \, \Sigma \, |Fo| = 0.0855$$

$$wR2 = [\Sigma (w (Fo^2 - Fc^2)^2) / \Sigma \, w(Fo^2)^2]^{1/2} = 0.2475$$

The standard deviation of an observation of unit weight [5] was 1.07. Unit weights were used. The maximum and minimum peaks on the final difference Fourier map corresponded to 2.18 and -1.62 $e^-/Å^3$, respectively.

Neutral atom scattering factors were taken from Cromer and Waber [6]. Anomalous dispersion effects were included in Fcalc [7]; the values for $\Delta f'$ and $\Delta f''$ were those of Creagh and McAuley [8]. The values for the mass attenuation coefficients are those of Creagh and Hubbell [9]. All calculations were performed using the CrystalStructure [10, 11] crystallographic software package except for refinement, which was performed using SHELXL-97 [2].

References

[1] Spek, A.L. (2003), J.Appl.Cryst. 36, 7-13

[2] CrystalClear: Rigaku Corporation, 1999. CrystalClear Software User's Guide, Molecular Structure Corporation, (c) 2000.J.W.Pflugrath (1999) Acta Cryst. D55, 1718-1725.

[3] SIR92: Altomare, A., Cascarano, G., Giacovazzo, C., Guagliardi, A., Burla, M., Polidori, G., and Camalli, M. (1994) J. Appl. Cryst., 27, 435.

[4] DIRDIF99: Beurskens, P.T., Admiraal, G., Beurskens, G., Bosman, W.P., de Gelder, R., Israel, R. and Smits, J.M.M.(1999). The DIRDIF-99 program system, Technical Report of the Crystallography Laboratory, University of Nijmegen, The Netherlands.

[5] Least Squares function minimized: (SHELXL97)
$\Sigma w(F_O^2-F_C^2)^2$ where w = Least Squares weights.

[6] Standard deviation of an observation of unit weight:
$[\Sigma w(F_O^2-F_C^2)^2/(N_O-N_V)]^{1/2}$
where: N_O = number of observations
N_V = number of variables

[7] Cromer, D. T. & Waber, J. T.; "International Tables for X-ray Crystallography", Vol. IV, The Kynoch Press, Birmingham, England, Table 2.2 A (1974).

[8] Ibers, J. A. & Hamilton, W. C.; Acta Crystallogr., 17, 781 (1964).

[9] Creagh, D. C. & McAuley, W.J .; "International Tables for Crystallography", Vol C, (A.J.C. Wilson, ed.), Kluwer Academic Publishers, Boston, Table 4.2.6.8, pages 219-222 (1992).

[10] Creagh, D. C. & Hubbell, J.H..; "International Tables for Crystallography", Vol C, (A.J.C. Wilson, ed.), Kluwer Academic Publishers, Boston, Table 4.2.4.3, pages 200-206 (1992).

[11] CrystalStructure 3.7.0: Crystal Structure Analysis Package, Rigaku and Rigaku/MSC (2000-2005). 9009 New Trails Dr. The Woodlands TX 77381 USA.

[12] CRYSTALS Issue 10: Watkin, D.J., Prout, C.K. Carruthers, J.R. & Betteridge, P.W. Chemical Crystallography Laboratory, Oxford, UK. (1996).

EXPERIMENTAL DETAILS

A. Crystal Data

Empirical Formula	$C_{58}H_{54}Cl_4N_{12}O_{22}Ru_2S_2$
Formula Weight	1679.20
Crystal Color, Habit	red, prism
Crystal Dimensions	0.28 X 0.27 X 0.18 mm
Crystal System	triclinic
Lattice Type	Primitive
Detector Position	40.06 mm
Pixel Size	0.137 mm
Lattice Parameters	a = 12.0249(11) Å b = 12.75010(10) Å c = 13.9516(14) Å α = 93.388(18) ° β = 112.8809(13) ° γ = 117.909(18) ° V = 1663.4(2) Å^3
Space Group	P-1 (#2)
Z value	1
D_{calc}	1.676 g/cm^3
F_{000}	850
μ(MoKα)	7.64 cm^{-1}

B. Intensity Measurements

Detector	Rigaku Saturn
Goniometer	Rigaku AFC8
Radiation	MoKα (λ = 0.71075 Å) graphite monochromated-Rigaku SHINE
Detector Aperture	70 mm x 70 mm
Data Images	680 exposures
ω oscillation Range (χ=45.0, ϕ=180.0)	-75.0 - 105.0°
Exposure Rate	50.0 sec./°
Detector Swing Angle	15.10°
ω oscillation Range (χ=45.0, ϕ=0.0)	-75.0 - 25.0°
Exposure Rate	50.0 sec./°
Detector Swing Angle	15.10°
ω oscillation Range (χ=0.0, ϕ=90.0)	-30.0 - 30.0°
Exposure Rate	50.0 sec./°
Detector Swing Angle	15.10°
Detector Position	40.06 mm
Pixel Size	0.137 mm
$2\theta_{max}$	61.8°
No. of Reflections Measured	Total: 12827 Unique: 6116 (R_{int} = 0.0356) I>2σ(I): 5467
Corrections	Lorentz-polarization (trans. factors: 0.8731 - 0.9708)

C. Structure Solution and Refinement

Structure Solution	Direct Methods (SIR92)
Refinement	Full-matrix least-squares on F^2
Function Minimized	Σ w $(Fo^2 - Fc^2)^2$
Least Squares Weights	$w = 1/ [\sigma^2(Fo^2) + (0.1560 \cdot P)^2 + 5.1289 \cdot P]$ where $P = (Max(Fo^2,0) + 2Fc^2)/3$
$2\theta_{max}$ cutoff	51.0^o
Anomalous Dispersion	All non-hydrogen atoms
No. Observations (All reflections)	6116
No. Variables	425
Reflection/Parameter Ratio	14.39
Residuals: R1 ($I>2.00\sigma(I)$)	0.0855
Residuals: R (All reflections)	0.0913
Residuals: wR2 (All reflections)	0.2475
Goodness of Fit Indicator	1.072
Max Shift/Error in Final Cycle	0.001
Maximum peak in Final Diff. Map	2.18 $e^-/Å^3$
Minimum peak in Final Diff. Map	-1.62 $e^-/Å^3$

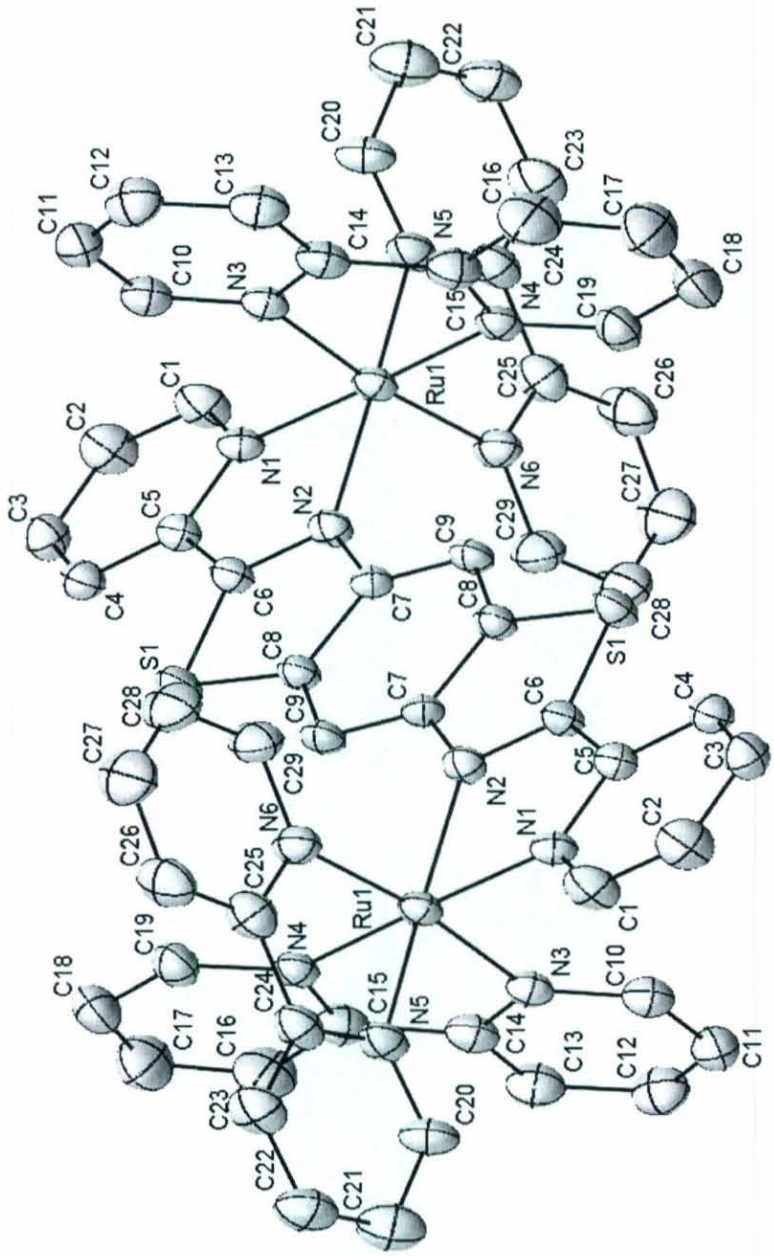

Figure D4: X-ray crystal structure for $[(\mathbf{bpy})_2Ru(\mathbf{py_2tbtz})Ru(bpy)_2]^{4+}$. Anions and hydrogen atoms omitted for clarity.

Table 5: Bond lengths (Å) for $[\{(bpy)_2Ru\}_2(\mathbf{py_2tbtz})]^{4+}$

atom	atom	distance	atom	atom	distance
Ru(1)	N(1)	2.054(6)	Ru(1)	N(2)	2.096(4)
Ru(1)	N(3)	2.056(7)	Ru(1)	N(4)	2.047(6)
Ru(1)	N(5)	2.053(5)	Ru(1)	N(6)	2.056(8)
Cl(1)	O(1)	1.430(8)	Cl(1)	O(2)	1.380(12)
Cl(1)	O(3)	1.443(8)	Cl(1)	O(4)	1.380(8)
Cl(2)	O(5)	1.51(2)	Cl(2)	O(6)	1.519(7)
Cl(2)	O(7)	1.39(2)	Cl(2)	O(8)	1.45(2)
S(1)	C(6)	1.714(6)	S(1)	C(8)	1.735(7)
N(1)	C(1)	1.350(9)	N(1)	C(5)	1.365(8)
N(2)	C(6)	1.329(9)	N(2)	C(7)	1.387(7)
N(3)	C(10)	1.326(10)	N(3)	C(14)	1.370(11)
N(4)	C(15)	1.360(14)	N(4)	C(19)	1.346(11)
N(5)	C(20)	1.304(9)	N(5)	C(24)	1.350(13)
N(6)	C(25)	1.367(10)	N(6)	C(29)	1.353(9)
C(1)	C(2)	1.365(13)	C(2)	C(3)	1.381(11)
C(3)	C(4)	1.378(10)	C(4)	C(5)	1.387(10)
C(5)	C(6)	1.464(9)	C(7)	C(8)	1.413(8)
C(7)	$C(9)^{1)}$	1.368(9)	C(8)	C(9)	1.400(8)
C(10)	C(11)	1.409(16)	C(11)	C(12)	1.312(16)
C(12)	C(13)	1.403(14)	C(13)	C(14)	1.387(16)
C(14)	C(15)	1.473(12)	C(15)	C(16)	1.413(16)
C(16)	C(17)	1.354(19)	C(17)	C(18)	1.37(2)
C(18)	C(19)	1.390(15)	C(20)	C(21)	1.419(10)
C(21)	C(22)	1.338(19)	C(22)	C(23)	1.372(13)
C(23)	C(24)	1.384(10)	C(24)	C(25)	1.488(10)
C(25)	C(26)	1.407(18)	C(26)	C(27)	1.365(13)
C(27)	C(28)	1.377(17)	C(28)	C(29)	1.377(19)

Table 6: Bond angles (°) for $[\{(bpy)_2Ru\}_2(\mathbf{py_2tbtz})]^{4+}$

atom	atom	atom	angle	atom	atom	atom	angle
N(1)	Ru(1)	N(2)	78.3(2)	N(1)	Ru(1)	N(3)	96.4(2)
N(1)	Ru(1)	N(4)	175.9(3)	N(1)	Ru(1)	N(5)	96.0(2)
N(1)	Ru(1)	N(6)	89.0(2)	N(2)	Ru(1)	N(3)	88.0(2)
N(2)	Ru(1)	N(4)	99.8(2)	N(2)	Ru(1)	N(5)	173.6(2)
N(2)	Ru(1)	N(6)	97.5(2)	N(3)	Ru(1)	N(4)	79.9(2)
N(3)	Ru(1)	N(5)	95.7(2)	N(3)	Ru(1)	N(6)	173.0(2)
N(4)	Ru(1)	N(5)	86.1(2)	N(4)	Ru(1)	N(6)	94.9(2)
N(5)	Ru(1)	N(6)	79.3(2)	O(1)	Cl(1)	O(2)	113.3(6)
O(1)	Cl(1)	O(3)	107.5(5)	O(1)	Cl(1)	O(4)	111.3(5)
O(2)	Cl(1)	O(3)	104.3(5)	O(2)	Cl(1)	O(4)	111.3(6)
O(3)	Cl(1)	O(4)	108.8(6)	O(5)	Cl(2)	O(6)	116.3(8)
O(5)	Cl(2)	O(7)	104.3(12)	O(5)	Cl(2)	O(8)	80.3(12)
O(6)	Cl(2)	O(7)	102.7(9)	O(6)	Cl(2)	O(8)	119.2(6)
O(7)	Cl(2)	O(8)	130.8(10)	C(6)	S(1)	C(8)	88.6(3)
Ru(1)	N(1)	C(1)	127.6(4)	Ru(1)	N(1)	C(5)	116.7(4)
C(1)	N(1)	C(5)	115.7(6)	Ru(1)	N(2)	C(6)	112.9(3)
Ru(1)	N(2)	C(7)	135.6(4)	C(6)	N(2)	C(7)	111.1(5)
Ru(1)	N(3)	C(10)	126.7(6)	Ru(1)	N(3)	C(14)	114.5(5)
C(10)	N(3)	C(14)	118.8(8)	Ru(1)	N(4)	C(15)	115.1(5)
Ru(1)	N(4)	C(19)	126.5(6)	C(15)	N(4)	C(19)	118.3(7)
Ru(1)	N(5)	C(20)	126.2(7)	Ru(1)	N(5)	C(24)	115.8(4)
C(20)	N(5)	C(24)	118.0(6)	Ru(1)	N(6)	C(25)	115.6(5)
Ru(1)	N(6)	C(29)	126.7(6)	C(25)	N(6)	C(29)	117.7(9)
N(1)	C(1)	C(2)	123.5(6)	C(1)	C(2)	C(3)	119.9(7)
C(2)	C(3)	C(4)	118.7(8)	C(3)	C(4)	C(5)	118.2(6)
N(1)	C(5)	C(4)	123.9(6)	N(1)	C(5)	C(6)	112.1(6)
C(4)	C(5)	C(6)	123.8(5)	S(1)	C(6)	N(2)	116.5(4)
S(1)	C(6)	C(5)	124.7(5)	N(2)	C(6)	C(5)	118.8(5)
N(2)	C(7)	C(8)	112.6(5)	N(2)	C(7)	$C(9)^{1)}$	125.8(5)
C(8)	C(7)	$C(9)^{1)}$	121.6(5)	S(1)	C(8)	C(7)	111.2(4)
S(1)	C(8)	C(9)	126.4(5)	C(7)	C(8)	C(9)	122.4(6)
$C(7)^{1)}$	C(9)	C(8)	115.9(5)	N(3)	C(10)	C(11)	121.7(8)
C(10)	C(11)	C(12)	119.9(9)	C(11)	C(12)	C(13)	120.2(11)
C(12)	C(13)	C(14)	118.6(10)	N(3)	C(14)	C(13)	120.8(7)
N(3)	C(14)	C(15)	115.0(9)	C(13)	C(14)	C(15)	124.1(8)
N(4)	C(15)	C(14)	115.3(8)	N(4)	C(15)	C(16)	121.1(9)
C(14)	C(15)	C(16)	123.5(11)	C(15)	C(16)	C(17)	118.5(14)

Table 6: Bond angles (°) for $[\{(bpy)_2Ru\}_2(\mathbf{py_2tbtz})]^{4+}$ (continued)

atom	atom	atom	angle	atom	atom	atom	angle
C(16)	C(17)	C(18)	121.4(13)	C(17)	C(18)	C(19)	117.7(10)
N(4)	C(19)	C(18)	122.9(10)	N(5)	C(20)	C(21)	123.3(10)
C(20)	C(21)	C(22)	116.8(8)	C(21)	C(22)	C(23)	121.9(8)
C(22)	C(23)	C(24)	117.3(10)	N(5)	C(24)	C(23)	122.5(7)
N(5)	C(24)	C(25)	115.1(6)	C(23)	C(24)	C(25)	122.3(9)
N(6)	C(25)	C(24)	114.1(9)	N(6)	C(25)	C(26)	121.8(6)
C(24)	C(25)	C(26)	124.1(7)	C(25)	C(26)	C(27)	118.8(10)
C(26)	C(27)	C(28)	119.6(14)	C(27)	C(28)	C(29)	119.9(9)
N(6)	C(29)	C(28)	122.2(8)				

X-ray crystallography data for $[\{(bpy)_2Ru\}_2(\mathbf{pzbbtz})]^{4+}$

Experimental

Collection, solution and refinement proceeded normally. Hydrogen atoms were introduced in calculated positions with isotropic thermal parameters set twenty percent greater than those of their bonding partners. They were refined on the riding model. One acetonitrile lattice solvent molecule was refined isotropically, while all other non-hydrogen atoms were refined anisotropically.

The formula for this model is:

$[(C_{18}H_{10}N_4S_2)(C_{10}H_8N_2)_4Ru_2](ClO_4)_4(CH_3CN)_4$

Data Collection

A black prism crystal of $C_{66}H_{54}Cl_4N_{16}O_{16}Ru_2S_2$ having approximate dimensions of 0.34 x 0.28 x 0.15 mm was mounted on a low-temperature diffraction loop. All measurements were made on a Rigaku Saturn CCD area detector equipped with a SHINE optic, with Mo-Kα radiation.

Indexing was performed from 360 images that were exposed for 20 seconds. The crystal-to-detector distance was 40.05 mm.

Cell constants and an orientation matrix for data collection corresponded to a primitive triclinic cell with dimensions:

a = 13.600(4) Å	α = 88.874(19)°
b = 16.050(5) Å	β = 86.357(19)°
c = 17.237(6) Å	γ = 70.514(13)°
V = 3539.6(19) Å^3	

For Z = 2 and F.W. = 1735.32, the calculated density is 1.628 g/cm^3. Based on a statistical analysis of intensity distribution, and the successful solution and refinement of the structure, the space group was determined to be:

P-1 (#2)

The data were collected at a temperature of -120 $\pm$ 1°C to a maximum 2θ value of 61.7°.

Data Reduction

Of the 32634 reflections that were collected, 14466 were unique (R_{int} = 0.0717). The linear absorption coefficient, μ, for Mo-Kα radiation is 7.17 cm^{-1}. A numerical absorption correction was applied which resulted in transmission factors ranging from 0.8354 to 0.9259. The data were corrected for Lorentz and polarization effects.

Structure Solution and Refinement

The structure was solved by direct methods [2] and expanded using Fourier techniques [3]. Some non-hydrogen atoms were refined anisotropically, while the rest were refined isotropically. Hydrogen atoms were refined using the riding model. The final cycle of full-matrix least-squares refinement [4] on F^2 was based on 14466 observed reflections and 940 variable parameters and converged (largest parameter shift was 0.00 times its esd) with unweighted and weighted agreement factors of:

$$R1 = \Sigma \, ||Fo| - |Fc|| \, / \, \Sigma \, |Fo| = 0.0850$$

$$wR2 = [\, \Sigma \, (\, w \, (Fo^2 - Fc^2)^2 \,) / \, \Sigma \, w(Fo^2)^2]^{1/2} = 0.2470$$

The standard deviation of an observation of unit weight [5] was 1.05. Unit weights were used. The maximum and minimum peaks on the final difference Fourier map corresponded to 3.36 and -1.15 $e^-/Å^3$ respectively.

Neutral atom scattering factors were taken from Cromer and Waber [6] . Anomalous dispersion effects were included in Fcalc [7]; the values for $\Delta f'$ and $\Delta f''$ were those of Creagh and McAuley [8]. The values for the mass attenuation coefficients are those of Creagh and Hubbell [9]. All calculations were performed using the CrystalStructure [10, 11] crystallographic software package except for refinement, which was performed using SHELXL-97 [2].

References

[1] CrystalClear: Rigaku Corporation, 1999. CrystalClear Software User's Guide, Molecular Structure Corporation, (c) 2000.J.W.Pflugrath (1999) Acta Cryst. D55, 1718-1725.

[2] SHELX97: Sheldrick, G.M. (1997).

[3] DIRDIF99: Beurskens, P.T., Admiraal, G., Beurskens, G., Bosman, W.P., de Gelder, R., Israel, R. and Smits, J.M.M.(1999). The DIRDIF-99 program system, Technical Report of the Crystallography Laboratory, University of Nijmegen, The Netherlands.

[4] Least Squares function minimized: (SHELXL97)
$\Sigma w(F_O^2-F_C^2)^2$ where w = Least Squares weights.

[5] Standard deviation of an observation of unit weight:
$[\Sigma w(F_O^2-F_C^2)^2/(N_O-N_V)]^{1/2}$
where: N_O = number of observations
N_V = number of variables

[6] Cromer, D. T.; Waber, J. T.; "International Tables for X-ray Crystallography", Vol. IV, The Kynoch Press, Birmingham, England, Table 2.2 A (1974).

[7] Ibers, J. A.; Hamilton, W. C.; Acta Crystallogr., 17, 781 (1964).

[8] Creagh, D. C.; McAuley, W.J .; "International Tables for Crystallography", Vol C, (A.J.C. Wilson, ed.), Kluwer Academic Publishers, Boston, Table 4.2.6.8, pages 219-222 (1992).

[9] Creagh, D. C.; Hubbell, J.H..; "International Tables for Crystallography", Vol C, (A.J.C. Wilson, ed.), Kluwer Academic Publishers, Boston, Table 4.2.4.3, pages 200-206 (1992).

[10] CrystalStructure 3.7.0: Crystal Structure Analysis Package, Rigaku and Rigaku/MSC (2000-2005). 9009 New Trails Dr. The Woodlands TX 77381 USA.

[11] CRYSTALS Issue 10: Watkin, D.J., Prout, C.K. Carruthers, J.R., Betteridge, P.W. Chemical Crystallography Laboratory, Oxford, UK.,**1996.**

EXPERIMENTAL DETAILS

A. Crystal Data

Empirical Formula	$C_{66}H_{54}Cl_4N_{16}O_{16}Ru_2S_2$
Formula Weight	1735.32
Crystal Color, Habit	black, prism
Crystal Dimensions	0.34 X 0.28 X 0.15 mm
Crystal System	triclinic
Lattice Type	Primitive
Detector Position	40.05 mm
Pixel Size	0.137 mm
Lattice Parameters	a = 13.600(4) Å b = 16.050(5) Å c = 17.237(6) Å α = 88.874(19)° β = 86.357(19)° γ = 70.514(13)° V = 3539.6(19) Å^3
Space Group	P-1 (#2)
Z value	2
D_{calc}	1.628 g/cm^3
F_{000}	1756
μ(MoKα)	7.17 cm^{-1}

B. Intensity Measurements

Detector	Rigaku Saturn
Goniometer	Rigaku AFC8
Radiation	MoKα (λ = 0.71075 Å) graphite monochromated – Rigaku SHINE
Detector Aperture	70 mm x 70 mm
Data Images	788 exposures
ω oscillation Range (χ=45.0, ϕ=0.0)	-75.0 - 105.0°
Exposure Rate	40.0 sec./°
Detector Swing Angle	14.70°
ω oscillation Range (χ=45.0, ϕ=180.0)	-75.0 - 105.0°
Exposure Rate	40.0 sec./°
Detector Swing Angle	14.70°
ω oscillation Range (χ=0.0, ϕ=0.0)	-75.0 - -41.0°
Exposure Rate	40.0 sec./°
Detector Swing Angle	14.70°
Detector Position	40.05 mm
Pixel Size	0.137 mm
$2\theta_{max}$	61.7°
No. of Reflections Measured	Total: 32634 Unique: 14466 (R_{int} = 0.0717) I>2σ(I): 12802
Corrections	Lorentz-polarization (trans. factors: 0.8354 - 0.9259)

C. Structure Solution and Refinement

Structure Solution	Direct Methods (SHELX97)
Refinement	Full-matrix least-squares on F^2
Function Minimized	$\Sigma\, w\,(Fo^2 - Fc^2)^2$
Least Squares Weights	$w = 1/[\,\sigma^2(Fo^2) + (0.1528 \cdot P)^2 + 4.6741 \cdot P\,]$ where $P = (Max(Fo^2,0) + 2Fc^2)/3$
$2\theta_{max}$ cutoff	53.0^o
Anomalous Dispersion	All non-hydrogen atoms
No. Observations (All reflections)	14466
No. Variables	940
Reflection/Parameter Ratio	15.39
Residuals: R1 ($I>2.00\sigma(I)$)	0.0850
Residuals: R (All reflections)	0.0912
Residuals: wR2 (All reflections)	0.2470
Goodness of Fit Indicator	1.048
Max Shift/Error in Final Cycle	0.001
Maximum peak in Final Diff. Map	3.36 $e^-/Å^3$
Minimum peak in Final Diff. Map	-1.15 $e^-/Å^3$

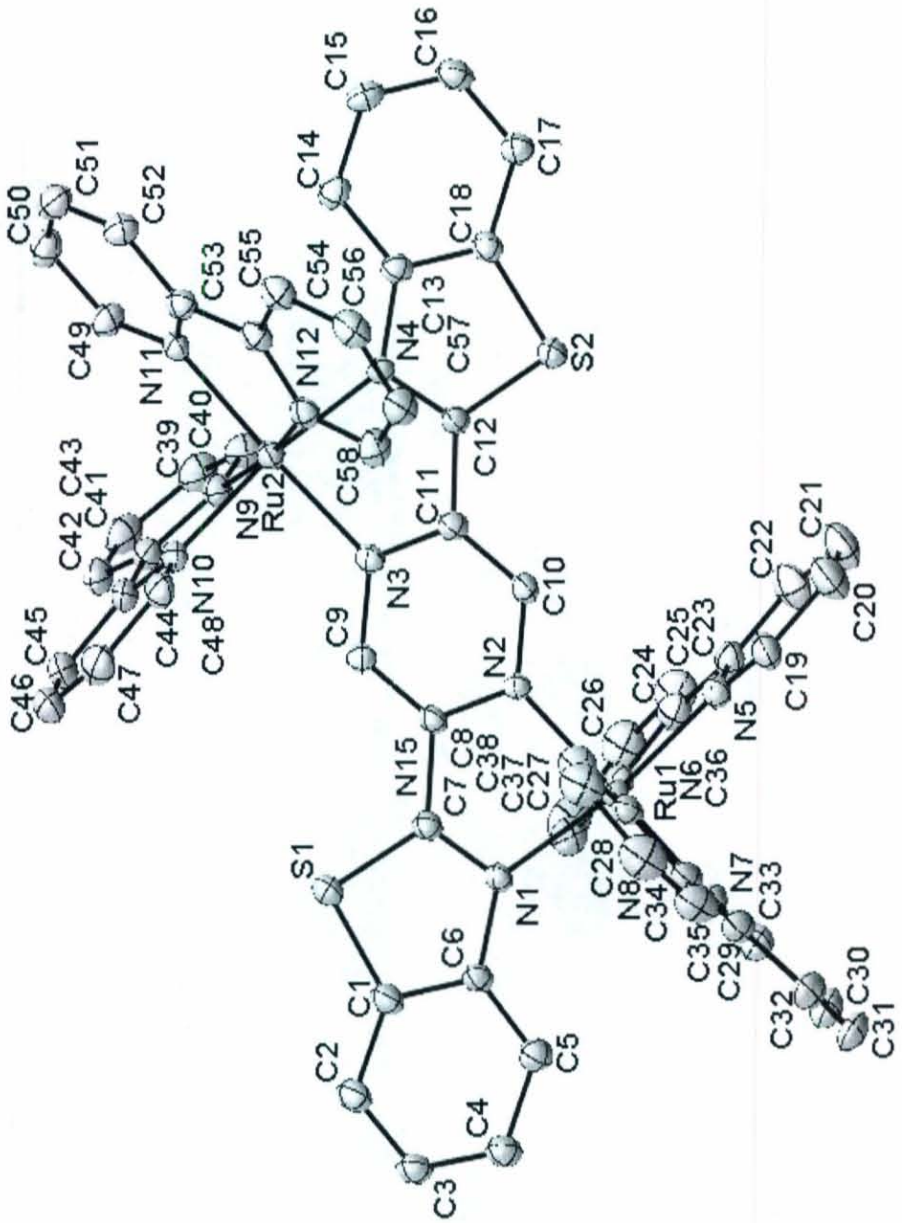

Figure D4: X-ray crystal structure for $[(bpy)_2Ru(\mathbf{pzbbtz})Ru(bpy)_2](ClO_4)_4$
Anions and hydrogen atoms omitted for clarity.

Table 7: Bond lengths (Å) for $[\{(bpy)_2Ru\}_2(\mathbf{pzbbtz})]^{4+}$

atom	atom	distance	atom	atom	distance
Ru(1)	N(1)	2.082(3)	Ru(1)	N(2)	2.052(4)
Ru(1)	N(5)	2.045(3)	Ru(1)	N(6)	2.065(4)
Ru(1)	N(7)	2.069(5)	Ru(1)	N(8)	2.075(4)
Ru(2)	N(3)	2.048(4)	Ru(2)	N(4)	2.084(3)
Ru(2)	N(9)	2.065(3)	Ru(2)	N(10)	2.041(3)
Ru(2)	N(11)	2.069(4)	Ru(2)	N(12)	2.062(3)
Cl(1)	O(1)	1.418(5)	Cl(1)	O(2)	1.395(6)
Cl(1)	O(3)	1.433(7)	Cl(1)	O(4)	1.413(6)
Cl(2)	O(5)	1.398(7)	Cl(2)	O(6)	1.429(4)
Cl(2)	O(7)	1.445(5)	Cl(2)	O(8)	1.391(5)
Cl(3)	O(9)	1.294(9)	Cl(3)	O(10)	1.353(9)
Cl(3)	O(11)	1.543(7)	Cl(3)	O(12)	1.345(9)
Cl(4)	O(13)	1.424(5)	Cl(4)	O(14)	1.419(5)
Cl(4)	O(15)	1.426(5)	Cl(4)	O(16)	1.442(6)
S(1)	C(1)	1.742(6)	S(1)	C(7)	1.736(4)
S(2)	C(12)	1.727(4)	S(2)	C(18)	1.731(6)
N(1)	C(6)	1.396(6)	N(1)	C(7)	1.303(7)
N(2)	C(8)	1.354(5)	N(2)	C(10)	1.343(6)
N(3)	C(9)	1.346(6)	N(3)	C(11)	1.358(5)
N(4)	C(12)	1.309(6)	N(4)	C(13)	1.401(6)
N(5)	C(19)	1.336(6)	N(5)	C(23)	1.372(6)
N(6)	C(24)	1.348(6)	N(6)	C(28)	1.350(6)
N(7)	C(29)	1.347(7)	N(7)	C(33)	1.359(6)
N(8)	C(34)	1.353(7)	N(8)	C(38)	1.334(8)
N(9)	C(39)	1.352(6)	N(9)	C(43)	1.346(5)
N(10)	C(44)	1.363(6)	N(10)	C(48)	1.352(6)
N(11)	C(49)	1.350(6)	N(11)	C(53)	1.347(6)
N(12)	C(54)	1.371(7)	N(12)	C(58)	1.342(6)
N(13)	C(64)	1.069(12)	N(14)	C(62)	1.151(11)
N(15)	C(60)	1.103(11)	N(16)	C(66)	1.169(10)
C(1)	C(2)	1.397(7)	C(1)	C(6)	1.400(6)
C(2)	C(3)	1.364(9)	C(3)	C(4)	1.389(7)
C(4)	C(5)	1.388(7)	C(5)	C(6)	1.383(8)
C(7)	C(8)	1.444(6)	C(8)	C(9)	1.362(7)
C(10)	C(11)	1.362(7)	C(11)	C(12)	1.451(7)
C(13)	C(14)	1.400(8)	C(13)	C(18)	1.395(6)
C(14)	C(15)	1.372(7)	C(15)	C(16)	1.388(7)

Table 7: Bond lengths (Å) for $[\{(bpy)_2Ru\}_2(\mathbf{pzbbtz})]^{4+}$ (continued)

atom	atom	distance	atom	atom	distance
C(16)	C(17)	1.373(9)	C(17)	C(18)	1.398(6)
C(19)	C(20)	1.374(7)	C(20)	C(21)	1.374(10)
C(21)	C(22)	1.356(9)	C(22)	C(23)	1.376(7)
C(23)	C(24)	1.470(7)	C(24)	C(25)	1.396(7)
C(25)	C(26)	1.350(9)	C(26)	C(27)	1.372(9)
C(27)	C(28)	1.390(7)	C(29)	C(30)	1.377(10)
C(30)	C(31)	1.370(10)	C(31)	C(32)	1.387(10)
C(32)	C(33)	1.386(9)	C(33)	C(34)	1.461(8)
C(34)	C(35)	1.396(7)	C(35)	C(36)	1.367(11)
C(36)	C(37)	1.399(10)	C(37)	C(38)	1.390(7)
C(39)	C(40)	1.392(7)	C(40)	C(41)	1.382(7)
C(41)	C(42)	1.355(7)	C(42)	C(43)	1.403(7)
C(43)	C(44)	1.466(7)	C(44)	C(45)	1.384(6)
C(45)	C(46)	1.380(9)	C(46)	C(47)	1.362(9)
C(47)	C(48)	1.373(7)	C(49)	C(50)	1.374(9)
C(50)	C(51)	1.385(8)	C(51)	C(52)	1.362(7)
C(52)	C(53)	1.401(8)	C(53)	C(54)	1.468(6)
C(54)	C(55)	1.375(7)	C(55)	C(56)	1.389(7)
C(56)	C(57)	1.372(9)	C(57)	C(58)	1.410(7)
C(59)	C(60)	1.501(14)	C(61)	C(62)	1.407(12)
C(63)	C(64)	1.51(2)	C(65)	C(66)	1.412(10)

Table 8: Bond angles (°) for $[\{(bpy)_2Ru\}_2(\mathbf{pzbbtz})]^{4+}$

atom	atom	atom	angle	atom	atom	atom	angle
N(1)	Ru(1)	N(2)	78.17(15)	N(1)	Ru(1)	N(5)	171.01(18)
N(1)	Ru(1)	N(6)	98.53(14)	N(1)	Ru(1)	N(7)	100.66(16)
N(1)	Ru(1)	N(8)	85.67(14)	N(2)	Ru(1)	N(5)	93.29(16)
N(2)	Ru(1)	N(6)	90.33(17)	N(2)	Ru(1)	N(7)	174.16(16)
N(2)	Ru(1)	N(8)	95.47(17)	N(5)	Ru(1)	N(6)	78.51(15)
N(5)	Ru(1)	N(7)	88.12(17)	N(5)	Ru(1)	N(8)	98.07(14)
N(6)	Ru(1)	N(7)	95.51(18)	N(6)	Ru(1)	N(8)	173.45(17)
N(7)	Ru(1)	N(8)	78.72(18)	N(3)	Ru(2)	N(4)	77.76(15)
N(3)	Ru(2)	N(9)	90.79(17)	N(3)	Ru(2)	N(10)	93.87(16)
N(3)	Ru(2)	N(11)	175.48(14)	N(3)	Ru(2)	N(12)	97.00(16)
N(4)	Ru(2)	N(9)	99.21(14)	N(4)	Ru(2)	N(10)	171.44(18)
N(4)	Ru(2)	N(11)	100.55(15)	N(4)	Ru(2)	N(12)	85.93(13)
N(9)	Ru(2)	N(10)	78.93(15)	N(9)	Ru(2)	N(11)	93.62(16)
N(9)	Ru(2)	N(12)	171.45(16)	N(10)	Ru(2)	N(11)	87.94(16)
N(10)	Ru(2)	N(12)	96.96(15)	N(11)	Ru(2)	N(12)	78.66(16)
O(1)	Cl(1)	O(2)	109.1(4)	O(1)	Cl(1)	O(3)	108.2(3)
O(1)	Cl(1)	O(4)	109.3(3)	O(2)	Cl(1)	O(3)	110.3(4)
O(2)	Cl(1)	O(4)	111.3(5)	O(3)	Cl(1)	O(4)	108.6(4)
O(5)	Cl(2)	O(6)	109.9(3)	O(5)	Cl(2)	O(7)	107.7(3)
O(5)	Cl(2)	O(8)	108.8(4)	O(6)	Cl(2)	O(7)	110.4(3)
O(6)	Cl(2)	O(8)	110.4(3)	O(7)	Cl(2)	O(8)	109.7(4)
O(9)	Cl(3)	O(10)	117.8(8)	O(9)	Cl(3)	O(11)	102.8(5)
O(9)	Cl(3)	O(12)	115.2(7)	O(10)	Cl(3)	O(11)	102.3(5)
O(10)	Cl(3)	O(12)	113.7(6)	O(11)	Cl(3)	O(12)	101.8(5)
O(13)	Cl(4)	O(14)	110.1(3)	O(13)	Cl(4)	O(15)	111.9(3)
O(13)	Cl(4)	O(16)	106.8(3)	O(14)	Cl(4)	O(15)	110.5(3)
O(14)	Cl(4)	O(16)	107.0(3)	O(15)	Cl(4)	O(16)	110.3(4)
C(1)	S(1)	C(7)	88.4(2)	C(12)	S(2)	C(18)	88.1(2)
Ru(1)	N(1)	C(6)	135.9(3)	Ru(1)	N(1)	C(7)	113.0(3)
C(6)	N(1)	C(7)	111.0(3)	Ru(1)	N(2)	C(8)	115.8(3)
Ru(1)	N(2)	C(10)	128.9(3)	C(8)	N(2)	C(10)	115.2(4)
Ru(2)	N(3)	C(9)	126.9(2)	Ru(2)	N(3)	C(11)	117.2(3)
C(9)	N(3)	C(11)	115.9(4)	Ru(2)	N(4)	C(12)	114.1(3)
Ru(2)	N(4)	C(13)	135.0(3)	C(12)	N(4)	C(13)	110.4(3)
Ru(1)	N(5)	C(19)	125.5(3)	Ru(1)	N(5)	C(23)	115.6(3)
C(19)	N(5)	C(23)	118.8(4)	Ru(1)	N(6)	C(24)	116.2(3)
Ru(1)	N(6)	C(28)	125.0(3)	C(24)	N(6)	C(28)	118.7(4)

Table 8: Bond angles (°) for $[\{(bpy)_2Ru\}_2(\mathbf{pzbbtz})]^{4+}$ (continued)

atom	atom	atom	angle	atom	atom	atom	angle
Ru(1)	N(7)	C(29)	125.8(3)	Ru(1)	N(7)	C(33)	115.1(3)
C(29)	N(7)	C(33)	119.1(5)	Ru(1)	N(8)	C(34)	115.1(3)
Ru(1)	N(8)	C(38)	125.8(3)	C(34)	N(8)	C(38)	118.8(4)
Ru(2)	N(9)	C(39)	125.7(2)	Ru(2)	N(9)	C(43)	115.1(3)
C(39)	N(9)	C(43)	119.1(4)	Ru(2)	N(10)	C(44)	115.8(3)
Ru(2)	N(10)	C(48)	125.0(3)	C(44)	N(10)	C(48)	119.1(3)
Ru(2)	N(11)	C(49)	126.0(3)	Ru(2)	N(11)	C(53)	115.2(3)
C(49)	N(11)	C(53)	118.6(4)	Ru(2)	N(12)	C(54)	115.9(2)
Ru(2)	N(12)	C(58)	125.6(3)	C(54)	N(12)	C(58)	118.2(4)
S(1)	C(1)	C(2)	127.4(4)	S(1)	C(1)	C(6)	110.5(3)
C(2)	C(1)	C(6)	122.1(5)	C(1)	C(2)	C(3)	116.7(4)
C(2)	C(3)	C(4)	123.0(4)	C(3)	C(4)	C(5)	119.5(6)
C(4)	C(5)	C(6)	119.6(4)	N(1)	C(6)	C(1)	113.6(4)
N(1)	C(6)	C(5)	127.3(4)	C(1)	C(6)	C(5)	119.1(4)
S(1)	C(7)	N(1)	116.4(3)	S(1)	C(7)	C(8)	124.0(3)
N(1)	C(7)	C(8)	119.5(3)	N(2)	C(8)	C(7)	112.6(4)
N(2)	C(8)	C(9)	123.3(4)	C(7)	C(8)	C(9)	124.1(3)
N(3)	C(9)	C(8)	121.1(3)	N(2)	C(10)	C(11)	122.1(3)
N(3)	C(11)	C(10)	122.3(4)	N(3)	C(11)	C(12)	112.0(4)
C(10)	C(11)	C(12)	125.7(3)	S(2)	C(12)	N(4)	116.9(3)
S(2)	C(12)	C(11)	124.3(3)	N(4)	C(12)	C(11)	118.8(3)
N(4)	C(13)	C(14)	126.9(4)	N(4)	C(13)	C(18)	113.1(4)
C(14)	C(13)	C(18)	120.0(4)	C(13)	C(14)	C(15)	117.8(4)
C(14)	C(15)	C(16)	122.0(5)	C(15)	C(16)	C(17)	121.0(4)
C(16)	C(17)	C(18)	117.7(4)	S(2)	C(18)	C(13)	111.4(3)
S(2)	C(18)	C(17)	127.1(3)	C(13)	C(18)	C(17)	121.4(5)
N(5)	C(19)	C(20)	122.4(5)	C(19)	C(20)	C(21)	118.4(6)
C(20)	C(21)	C(22)	120.2(6)	C(21)	C(22)	C(23)	119.9(6)
N(5)	C(23)	C(22)	120.3(4)	N(5)	C(23)	C(24)	114.9(4)
C(22)	C(23)	C(24)	124.7(4)	N(6)	C(24)	C(23)	114.1(4)
N(6)	C(24)	C(25)	120.7(4)	C(23)	C(24)	C(25)	125.2(4)
C(24)	C(25)	C(26)	119.9(5)	C(25)	C(26)	C(27)	120.2(5)
C(26)	C(27)	C(28)	118.2(5)	N(6)	C(28)	C(27)	122.1(5)
N(7)	C(29)	C(30)	122.8(5)	C(29)	C(30)	C(31)	118.1(6)
C(30)	C(31)	C(32)	120.3(6)	C(31)	C(32)	C(33)	119.1(5)
N(7)	C(33)	C(32)	120.5(5)	N(7)	C(33)	C(34)	115.4(5)
C(32)	C(33)	C(34)	124.0(4)	N(8)	C(34)	C(33)	115.4(4)

Table 8: Bond angles (°) for $[\{(bpy)_2Ru\}_2(\mathbf{pzbbtz})]^{4+}$ (continued)

atom	atom	atom	angle	atom	atom	atom	angle
N(8)	C(34)	C(35)	121.3(5)	C(33)	C(34)	C(35)	123.2(5)
C(34)	C(35)	C(36)	119.0(6)	C(35)	C(36)	C(37)	120.4(5)
C(36)	C(37)	C(38)	117.0(6)	N(8)	C(38)	C(37)	123.4(6)
N(9)	C(39)	C(40)	121.6(4)	C(39)	C(40)	C(41)	118.7(5)
C(40)	C(41)	C(42)	120.1(5)	C(41)	C(42)	C(43)	119.4(4)
N(9)	C(43)	C(42)	121.2(4)	N(9)	C(43)	C(44)	115.4(4)
C(42)	C(43)	C(44)	123.4(3)	N(10)	C(44)	C(43)	114.5(3)
N(10)	C(44)	C(45)	120.2(4)	C(43)	C(44)	C(45)	125.3(4)
C(44)	C(45)	C(46)	120.4(5)	C(45)	C(46)	C(47)	118.3(5)
C(46)	C(47)	C(48)	120.7(5)	N(10)	C(48)	C(47)	121.2(5)
N(11)	C(49)	C(50)	122.4(4)	C(49)	C(50)	C(51)	118.3(5)
C(50)	C(51)	C(52)	120.5(6)	C(51)	C(52)	C(53)	118.5(5)
N(11)	C(53)	C(52)	121.5(4)	N(11)	C(53)	C(54)	116.2(4)
C(52)	C(53)	C(54)	122.2(4)	N(12)	C(54)	C(53)	113.7(4)
N(12)	C(54)	C(55)	122.1(4)	C(53)	C(54)	C(55)	124.2(5)
C(54)	C(55)	C(56)	119.3(5)	C(55)	C(56)	C(57)	119.6(4)
C(56)	C(57)	C(58)	118.8(5)	N(12)	C(58)	C(57)	122.1(5)
N(15)	C(60)	C(59)	174.6(10)	N(14)	C(62)	C(61)	178.8(6)
N(13)	C(64)	C(63)	170.1(10)	N(16)	C(66)	C(65)	179.3(9)